Identification and Validation of Target Receptors/Transporters for AAV9

By

Matthew Alberto Roach

May 2023

A thesis submitted for the degree of Doctor of Philosophy (PhD)

Sheffield Institute for Translational Neuroscience

Supervisors:

Professor Mimoun Azzouz

Dr. Christopher Webster

Professor Guillaume Hautbergue

Abstract

Background: Adeno-Associated Virus Serotype 9 (AAV9) is the gold standard viral vector for the treatment of monogenic central nervous system (CNS) disorders as a result of its strong neurotropism and its ability to transverse the blood-brain barrier (BBB). Although AAV9 has been used in recent human clinical trials, our understanding of its interactome, which controls its tropism, is limited. As a result, its therapeutic potential is restricted. A greater understanding of AAV9s interaction partners and pathways will enable the development of more efficient vectors with enhanced therapeutic potential. Preliminary data showed an upregulation of SDC4, ICAM1 and SLC7A2 after cells were incubated with AAV9 *in vitro*. These targets were hypothesised to be involved in AAV9's transduction pathway.

Aims and objectives: I) To characterise the target proteins and identify AAV9 permissive and non-permissive cell lines. II) To investigate if modulating target protein expression in permissive and non-permissive cell lines can affect AAV9 transduction efficiency.

Results: Firstly, neuronal cell lines were screened and characterised based on target protein expression, and AAV9 transduction efficiency. HeLa and SHSY cell lines were identified as permissive cell lines, while N2A, NIH3T3, 1321N1 and b.End5's were classified as non-permissive. Overexpression of the positive control, AAVR, and also SLC7A2, in HeLa and 1321N1 cells resulted in a significant increase in AAV9 transduction efficiency, while overexpression of ICAM1 and SDC4 had no effect. Interestingly however, ICAM1 was shown to interact with the viral capsid protein VP1, similar to AAVR, despite having no effect on transduction. Finally, knockdown of AAVR, SDC4 and ICAM1 in permissive cells led to a significant reduction in AAV9 transduction efficiency. Generation of SDC4 and ICAM1 CRISPR knockout (KO) HeLa cells, however, showed the opposite effect, which was rescued upon reintroduction of the target proteins to KO cells. There was no observable effect on internalisation of AAV9 in these cells suggesting a role further into the transduction pathway.

Conclusion: These results indicate modulation of ICAM1, SDC4 and SLC7A2 can affect AAV9 transduction, with ICAM1 identified as a potential novel interacting partner of the AAV capsid. These findings expand our knowledge of the AAV9 interactome and may further improve our understanding of the AAV9 transduction pathway.

Acknowledgments

I am grateful to Professor Mimoun Azzouz who has been supportive throughout the 4 years of my PhD and provided me every opportunity to develop as a researcher. I am extremely grateful for all that you have done for me.

I would like to give the greatest thanks to Dr. Christopher Webster, who has been the most supportive and patient supervisor. Without his tutelage and guidance, my experience would have been astronomically different. His constant encouragement enabled me to thrive with my project and I cannot express enough in words how much I appreciate the amount of effort and time he has given to me over these past 4 years. I will forever be grateful for his support.

To all my friends and colleagues who I have shared this experience with, I could not have achieved this without you. I would like to specially give thanks to Dr. Tobias Moll, Dr. Emily Graves and Dr. Anushka Bhargava. Our friendship throughout this project meant that even a global pandemic could not stop us. Words cannot describe how much I love you all for your support and the laughs we have had so far. I cannot wait to see what lies in the future for us. I would also like to give an immense thanks to Jack Greenshields, John Knowles, Diviya Thevarajah and Alex Cave for all your support throughout these years and I cannot thank you all enough. You all mean the world to me.

Finally, one of the biggest thanks I can give is to my family for their love and support. I could never have achieved this without your support throughout my life. Mum and Dad, you both have been amazing and have always taught me to stay driven and to follow my passions. Alex, you have been the best sister a brother could ask for and you have always been there for me. I could not have reached this goal without you. I love you all so much and I hope I have made you all proud.

Table of Tables:

Table of Figures:

List of Abbreviations:

AAV	Adeno-Associated Virus
AAVR	Adeno-Associated Virus Receptor
ABE	Adenine Base Editor
ALS	Amyotrophic Lateral Sclerosis
AMT	Adsorptive-Mediated Transcytosis
ASO	Antisense Oligonucleotide
ATP2C1	ATP Synthase Type 2C Gamma Chain 1
BBB	Blood-Brain Barrier
Cas	CRISPR-Associated System
CBE	Cytidine Base Editors
cDNA	Complementary DNA
CLIC/GEEC	Clathrin Independent Carrier/ Glycosylphosphophotidylinositol-anchored protein enriched compartments
CMV	Cytomegalovirus
CNS	Central Nervous System
CpG	5' – C -Phosphate-G-3' sequence of nucleotides
Crb3	Crumbs 3
CREATE	Cre Recombinase-based Targeted Evolution
CRISPR	Clustered Regularly Interspaced Short Palindromic Repeats
DNA	Deoxyribonucleic Acid
DRG	Dorsal Root Ganglion
DSB	Double-Strand Break
EC	Endothelial Cell
EDTA	Ethylenediaminetetraacetic Acid
EGFP	Enhanced Green Fluorescent Protein
EV	Empty Vector
EV1	Human Enterovirus Echovirus 1
GFP	Green Fluorescent Protein
GM -CSF	Granulocyte macrophage colony stimulating factor
GOF	Gain-Of-Function

GPR108	G protein coupled receptor 108
gRNA	Guide RNA
HDR	Homology Directed Repair
HGF	Human Growth Factor
HVEM	Herpesvirus Entry Mediator
ICE	Inference of CRISPR Edits
ICAM1	Intracellular Adhesion Molecule 1
Ig	Immunoglobulin
ITR	Inverted Terminal Repeats
KD	Knockdown
kDa	Kilo-Dalton
KO	Knockout
LAT	Latency-Associated Transcript
LDL	Low Density Lipoprotein
LOF	Loss-Of-Function
LV	Lentivirus
LY6A	Lymphocyte Antigen 6 complex, locus A
MANEC	Motif at the end terminus with eight cysteines
M-CREATE	Multiplex Cre Recombinase-based Targeted Evolution
MOI	Multiplicity Of Infection
mRNA	Messenger RNA
NHEJ	Non-Homogenous End-Joining
NHP	Non-Human Primates
NTC	Non-Targeted Control
ORF	Open Reading Frame
p	Postnatal
PAM	Protospacer Adjacent Motif
PBS	Phosphate Buffer Saline
PCR	Polymerase Chain Reaction
PEBC	Porcine Endothelial Brain Cells
PEI	Polyethylenimine
PKD	Polycystic Kidney Disease
pre-crRNA	Pre-CRISPR RNA
Puro	Puromycin

RAN	Repeated-Associated Non-ATG
rAAV	Recombinant AAV
RF	Restriction Factor
RISC	RNA-Inducing Silencing Complex
RMT	Receptor-Mediated Transcytosis
RNA	Ribonucleic Acid
RNAi	RNA-interference
RNP	Ribonucleoprotein
scAAV	Self-Complementary AAV
SDC4	Syndecan-4
siRNA	Small-Interfering RNA
SLC7A2	Solute Carrier Family 7 Member 2
SSB	Single Stranded Break
ssAAV	Single Stranded AAV
ssDNA	Single Stranded DNA
ssRNA	Single Stranded RNA
TALEN	Transcription Activator-Like Effector Nucleases
TJ	Tight Junction
TSS	Transcription Start Site
U_L	Unique Long
U_S	Unique Short
VEGF-A	Vascular Endothelial Growth Factor A
VG	Viral Genomes
VP	Viral Protein
VR	Variable Regions
VSV-G	Vesicular Stomatitis Virus Glycoprotein
WT	Wild-Type
ZFN	Zinc Finger Nuclease

Table of Contents

1 Introduction

1.1 Gene Therapy Strategies

Gene therapy, the process of altering a dysfunctional genome via transfer of functional genes, is becoming a world-leading form of treatment for monogenic disorders. Recently, the goal of delivering therapeutic cargo to target cells to normalise overactive or underactive gene expression has become a reality (Naso, Tomkowicz et al. 2017). The ability of viruses to infect target cells and transfer their genetic material makes them ideal delivery systems for gene therapy applications (Nayerossadat, Maedeh et al. 2012). In an effort to enhance the transduction efficiency and therefore effectiveness of these treatments, recombinant viral vectors have been developed via the design and engineering of next-generation viral capsids. This genetic engineering of viral capsids has led to novel variants with improved phenotypes for more efficient targeted delivery of therapeutic cargo (Nayerossadat, Maedeh et al. 2012, Lundstrom 2018). Viral vectors and alternate delivery systems, such as nanoparticles, have achieved pre-clinical and clinical success in neurodegenerative gene therapy studies (Sung and Kim 2019). However, these alternate delivery systems lack the evolutionary advantage viral vectors have developed (Naso, Tomkowicz et al. 2017). While systemic delivery of gene therapy, predominately via the use of AAV9, has been proven possible (Gruntman and Flotte 2015), vector delivery to the CNS is hindered by the blood-brain barrier (BBB), the natural protective barrier of the CNS. Direct injection to the CNS can overcome the BBB but comes with inherent risk.

There are three major gene therapy strategies: 1.) Gene Replacement Therapy 2.) Gene Silencing Therapy and 3.) Gene Editing Therapy. All three methods are depicted in Figure 1.1.

1.1.1 Gene Replacement Therapy

Gene replacement therapy, as the name suggests, involves replacing a mutated, non-functional disease-causing gene with functional copies of the same gene to counter the disease-associated genes effects. Gene replacement therapies are often focused on loss-of-

function (LoF) gene mutations, where the mutation results in reduced protein expression or the production of a non-functional protein (Petrich, Marchese et al. 2020). An example of this form of therapy was the use of the neurotropic AAV9 packaged with full length *SMN1* to deliver the therapeutic transgene to motor neurones to treat Type I spinal muscular atrophy (SMA) (Dominguez, Marais et al. 2011, Mendell, Al-Zaidy et al. 2021). The therapy was shown to improve the survival of patients and improved clinical symptoms. Other deficiency disorders which are being investigated to be treated via this method of gene therapy include duchenne muscular dystrophy (DMD), N-glycanase 1 deficiency and surfeit locus protein-related Leigh syndrome (Ling, Rioux et al. 2021, Manini, Abati et al. 2021, Zhu, Tan et al. 2022).

1.1.2 Gene Silencing Therapy

Genetic mutations that convey a new or altered function can disrupt the normal functioning of a protein, leading to cellular toxicity and cell death. Silencing methods are designed to interfere with the expression of genes which have acquired a toxic gain of function (GoF) phenotype (Korobeynikov, Lyashchenko et al. 2022). Toxicity can occur due to dysregulation of the wild type of function, alterations in protein-protein interactions or even incorrect protein folding and aggregation (Gerasimavicius, Livesey et al. 2022). RNA interference (RNAi) uses RNA-induced silencing complexes to achieve downregulation of the mutated mRNA thus preventing translation and therefore reducing expression of the toxic GoF protein (Mocellin and Provenzano 2004). By silencing target protein expression, toxicity is repressed helping to prolong survival of diseased cells and tissue. There are several methods to suppress expression of a gene of interest: small-interfering RNA (siRNA), short-hairpin RNA (shRNA) and anti-sense oligonucleotides (ASOs).

1.1.2.1 Small interfering RNA (siRNA)

siRNA are dsRNA molecules which interact with the RNA-inducing silencing complex (RISC) which contains argonaute 2 (Ago-2) endonuclease activity and cleaves the duplex into a passenger strand and a guide strand, activating the RISC complex (Dana, Chalbatani et al.

2017). The guide strand directs the targeting of silencing by complementary base pairing of target mRNA resulting in silencing of the pathway. A major benefit to this system is that the siRNA process is catalytic and capable of dissociating from mRNA and continuously cleaving target sequences (Neumeier and Meister 2020). This makes the RISC-siRNA complex persistent during cell division which enables very low concentration for effective mRNA knockdown. This therapeutic approach is used to repress the expression level of the disease-associated protein and to improve the levels of other affected proteins related to the disease pathway (Hu, Zhong et al. 2020). An example of this form of therapy is the siRNA therapy, referred to as Bevasiranib, against vascular endothelial growth factor A (VEGF-A) in relation to diabetic retinopathy (Garba and Mousa 2010). This therapy has shown that it slows the growth of abnormal blood vessels and improves vision. Although siRNA treatment is promising, due to the guide sequence following base pairing targeting, off-targeting of alternate gene transcripts due to sequencing homology is known to occur and the molecule is known to be unstable in physiological conditions (Mahmoodi Chalbatani, Dana et al. 2019, Hu, Zhong et al. 2020). Methods to reduce the risk of off-targeting is to modify the siRNA with alterations, such as 2'-O-methylations, which make off-targeted interactions less tolerable (Elmen, Thonberg et al. 2005). Due to the weaker interaction, the only sequences effectively cleaved are the sequences of interest.

1.1.2.2 Short-hairpin RNA (shRNA)

shRNA are exogenous RNA molecules with a hairpin-like structure which, when delivered to target cells, via vector packaging systems, undergoes transcription via RNA polymerase III resulting in the expression of shRNA (Sheng, Flood et al. 2020). Like siRNA, the RNAse III enzyme Dicer cleaves the shRNA, removing the hairpin loop, generating duplexes to stimulate loading to the RISC complex. Literature has shown the specificity of this RNAi method and its efficiency in silencing gene expression due to its stable structure and being capable of being constantly generated intracellularly in host cells (Denise, Moschos et al. 2014). shRNA has also showed therapeutic success *in vivo* by improving the lifespan and symptoms of mice in relation to diseases such as amyotrophic lateral sclerosis (ALS) (Foust, Salazar et al. 2013, Thomsen, Gowing et al. 2014, Iannitti, Scarrott et al. 2018, Bravo-Hernandez, Tadokoro et al.

2020). However, shRNA's share the same limitation as siRNA which is the risk of off-targeted silencing due to sequence homology of alternate transcripts (Czarnek, Sarad et al. 2021).

1.1.2.3 Antisense Oligonucleotide (ASOs)

ASOs are single stranded oligodeoxynucleotides which are complementary to a target mRNA sequence resulting in silencing of expression via RNase H endonuclease cleavage (Shen and Corey 2018). This has been shown to be an effective method of RNAi in pre-clinical models and clinical trials in relation to ALS and SMA therapy (Jiang, Zhu et al. 2016, Mercuri, Darras et al. 2018). However, due to their single stranded nature, ASO are inherently unstable and are therefore susceptible to intracellular degradation. For this reason, second generation ASOs have been developed which contain a phosphonothioate backbone and 2'-substituted oligoribonucleotide segments to improve RNA affinity and resistance to nuclease and protein degradation (Rinaldi and Wood 2018). Recently, in a single patient, ASOs targeting the ALS associated gene *C9ORF72* reduced polyGP dipeptide repeat, toxic proteins generated from repeated-associated non-ATG (RAN) translation, levels by approximately 80% (Tran, Moazami et al. 2022). Because of this, ASO has become a leading candidate for the treatment of neurological diseases.

1.1.3 Gene Editing

Genome editing is the process of deleting and adding genetic sequences to the target hosts genome. Several genome editing systems have been developed which include zinc finger nuclease (ZFN) (Sander, Dahlborg et al. 2011), transcription activator-like effector nucleases (TALENs) (Christian, Cermak et al. 2010) and the RNA-guided CRISPR-Cas nuclease (Gaj, Ojala et al. 2017). CRISPR associated system (Cas) is a prokaryote intracellular defence system which can be used to target exogenous genetic sequences (Newsom, Parameshwaran et al. 2020). As part of its natural function, upon entry of foreign DNA, adaptation module proteins excise spacer-sized viral fragments to be used for immune memory in bacteria (Asmamaw and Zawdie 2021). These spacers are transcribed into pre-CRISPR RNA (pre-crRNA) that bind

to effector Cas/RNase III complex proteins to generate mature crRNA which associates itself with tracrRNA, also referred to as guide RNA (gRNA) (Newsom, Parameshwaran et al. 2020). The gRNA enables recognition of viral DNA introduces a double-strand break (DSB). As a result of this natural mechanism, it has been widely used as a tool for genetic manipulation.

Using this system, a complementary gRNA can be designed for a target sequence, typically 20-base pairs long, which contains a protospacer adjacent motif (PAM) binding site, to introduce genetic edits in experimental models (Yun and Ha, 2020). With the nuclease and the gRNA in the nucleus (via transfection or electroporation), the Cas nuclease cleaves the target PAM site, via the recognition of the gRNA bound to the complementary sequence, which results in a double-strand break (DSB). Following this, the cells natural process is to repair the cleaved site via two methods: non-homogenous end-joining (NHEJ) and homologous directed repair (HDR). NHEJ generates insertions and deletions (indels) which can have the chance to introduce a stop codon, referred to as a frameshift mutation, due to the repair system being error prone. As a result of this stop codon, the full genetic sequence is unable to be transcribed resulting in the target protein of interest being unable to be expressed (for a review, see Adli, 2018). The alternate repair strategy is HDR in which the cell attempts to repair the DSB. However, this process requires a donor sister chromatin sequence to guide the repair and as a result is the less frequent repair strategy in eukaryotic cells compared to NHEJ (Yang, Ren et al. 2020) . A major concern, similar to RNAi, is the frequency of off-targeted edits due to sequence homology targeting from the guides designed. To mitigate the potential of off target editing, an improved CRISPR strategy using the mutant Cas9 nickase system, which requires dual gRNA recognition in the target exon to generate two single-stranded breaks (SSBs) at alternate genome loci. Due to the dual guide recognition technology, off-targeting risk is minimal (Shen, Zhang et al. 2014, Chiang, le Sage et al. 2016, Gopalappa, Suresh et al. 2018). More recently it was discovered that adding a cytosine sequence to the 5'end of the designed gRNA acts as a 'safeguard gRNA' which improved the editing efficiency of the CRISPR system (Kawamata, Suzuki et al. 2023). SOD1-linked ALS pre-clinical models have shown success in genetically editing disease-associated genes resulting in improved lifespan of mice, delayed onset of symptoms and improved survival due to inhibiting the toxic pathway (Gaj, Ojala et al. 2017, Duan, Guo et al. 2019, Lim, Gapinske et al. 2020). Packaging a Cas9 sequence and appropriate guides into a neurotropic viral vector is

therefore an extremely promising form of genetic manipulation technique for the treatment of toxic GoF mutations.

A novel CRISPR method being developed is the use of base editors to generate point mutations in the target sequences without the introduction of DSBs (Kantor, McClements et al. 2020). There are two major classes of base editors: (i) cytidine base editors (CBEs) which convert cytosine to thymine bases; (ii) adenine base editors (ABEs) which convert adenine into guanine (Antoniou, Miccio et al. 2021). This novel technique has potential in the treatment of genetic diseases caused by point mutations. Due to the system not requiring a DSB, it is clinically safer to use and novel mutans of Cas9n variants are capable of editing non-NGG PAM sites which makes this method therapeutically flexible (Lahr, Sipe et al. 2023). A limitation to this method was high concentrations of the target base in the editing window can result in bystander edits. An improved strategy to this method is the substitution of the flexible linker which shortens the editing window which reduces the chances of off-target (Tan, Zhang et al. 2019).

Overall, these gene therapy strategies are proving to have therapeutic potential which are progressively leading to the treatment of monogenic disorders. However, a challenge all these methods must overcome is the presence of the blood-brain barrier, which restricts vector delivery due to its natural function of being highly selective.

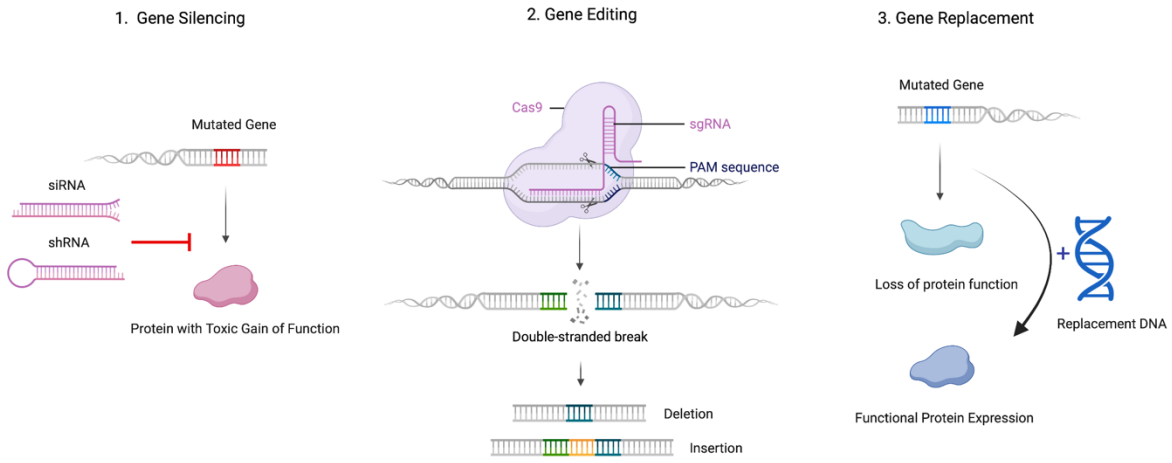

Figure 1.1: ***Gene Therapy Strategies –*** *1. Gene Silencing: The aim of this therapy is to silence the toxic pathways to improve symptoms via RNAi systems such as siRNA, shRNA and antisense oligonucleotides. 2. Gene Editing: The use of CRISPR-Cas9 to introduce genetic modifications to prevent the transcription of toxic genes. 3. Gene Replacement: The delivery of functional gene copies to deficient cells to rescue the cells of interest (Giovannelli, Higginbottom et al. 2023) (created by Biorender.com).*

1.1 Gene Therapy in the CNS

Neurogenetic disorders are commonly caused by genetic mutations in the CNS resulting in loss of limb function, loss of memory and more (Duarte and Deglon 2020). These disorders represent a major burden to healthcare, particularly in aging populations, and for this reason the use of gene therapy for the treatment of neurological disease is becoming an ever-increasing field of research. Recently, monogenic CNS disorders, neuronal diseases associated with a single mutation, have been targeted for gene therapy, via the methods described previously. However, a major obstacle in the treatment of the CNS is the blood-brain barrier (BBB). This is because the neurovascular unit of the BBB is highly selective and prevents the entry of macromolecules (Pardridge 2005). Because of this, most therapies targeted towards the CNS requires bypassing the BBB which makes therapeutic delivery more challenging.

1.1.4 Neurovascular Unit

The BBB refers to the microvasculature of the CNS. This protective selective permeable layer functions to maintain homeostasis within the CNS. This restrictive nature of the neurovascular unit preserves efficient neuronal function and prevents damage from peripheral toxins and/or pathogens (Abbott, Patabendige et al. 2010). The neurovascular unit is predominately made up of endothelial cells surrounded by the basal lamina, pericytes and astrocyte end-feet (Sofroniew and Vinters 2010, Greene and Campbell 2016) (Figure 1.2).

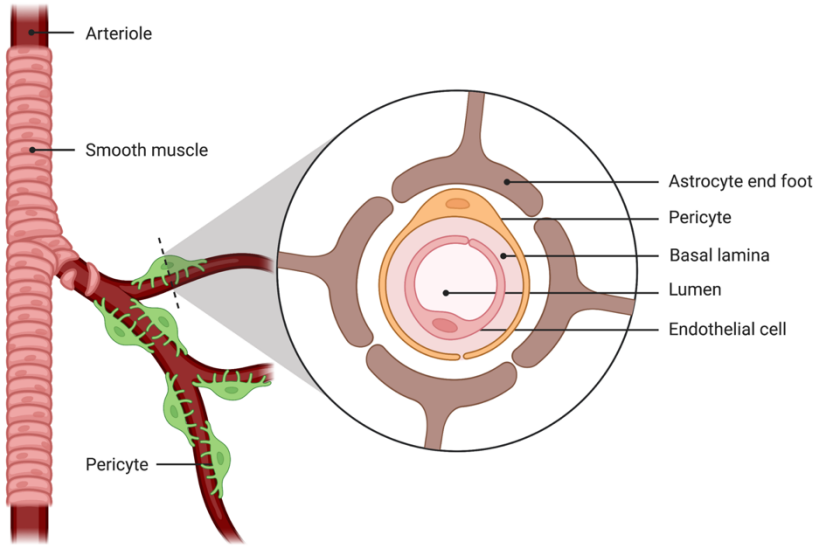

Figure 1.2: ***Model of the neurovascular unit***– *Neuronal capillaries composition (smooth muscle, arteriole and pericytes) with the neurovascular unit outlined with key cells labelled (astrocyte end feet, pericyte, basal lamina, capillary lumen and endothelial cells) (created by Biorender.com).*

1.1.4.1 Endothelial Cells

Endothelial cells (ECs), cells that line the interior surface of blood vessels, make up the apical layer of the BBB which is the main obstacle for most bioengineered vectors to reach the CNS. The cell walls of the CNS ECs are 40% thinner than other ECs (Merkel, Andrews et al. 2017). Therefore, due to the small diffusion distance from the capillary to CNS cells (~25μm), it is a preferred route for drug delivery as the therapeutic molecules can reach target cells rapidly (Stamatovic, Keep et al. 2008, Greene and Campbell 2016). CNS ECs are associated with tight junctions (TJs), the region where adjacent cells form a barrier limiting the paracellular flux of solutes and the vesicle-mediated transcellular pathways across endothelial cells (Daneman and Prat 2015). TJs are made up predominately of the integral plasma proteins occludin and claudin, which function to interact with cytoskeletal scaffold proteins (Luissint, Artus et al. 2012). As a result of these TJs, the BBB microvasculature is made-up of continuous non-fenestrated capillaries and form a physical barrier forcing molecules to predominately cross via transcellular routes (Pulgar 2019).

1.1.4.2 Astrocytes

Astrocytes are one of the predominant glial cells in the CNS. They function in the maintenance and homeostasis of the BBB by regulating the concentration of metabolites and ions, regulating blood flow and the development of the CNS (Serlin, Shelef et al. 2015). Astrocytes have protrusions, referred to as astrocyte end-feet, which extend from the cell body and attach to the basement membrane which surrounds the blood vessels and the rest of the microglia. These end-feet cover an estimated 80-90% of the basement membrane surrounding the CNS microvasculature (Kubotera, Ikeshima-Kataoka et al. 2019). Through their end-feet, astrocytes enable a pathway between the microvascular network and neurons of the CNS, enabling bidirectional signalling (Alvarez, Katayama et al. 2013, Cabezas, Ávila et al. 2014).

1.1.4.3 Pericytes

Pericytes, which are located in the neurovascular unit, play a key role in the development of the BBB and regulate cerebral blood-flow (De La Fuente et al., 2017). They are a class of perivascular cells and the coverage of these cells surrounding ECs varies between different micro-vessel types, although the CNS is where they are most abundantly found (Zheng, Chopp et al. 2020). Data suggests that pericytes may also have a role in the regulatory transport system across the BBB and the regulation of vascular permeability as a result of the direct physical contact and paracrine signalling pathways shared between pericytes and endothelial cells (Bergers and Song 2005). As a result of this signalling, pericytes are important for the regulatory function of the CNS.

1.1.5 Methods of Transfer Across the BBB

While inherently restrictive in nature, methods of transfer across the BBB are required to maintain neuronal homeostasis. There are five methods to cross the BBB. These are detailed in Figure 1.3.

1.1.5.1 Transcellular Lipophilic Pathway

An estimated 98% of small molecules are restricted from passing the barrier and only lipophilic and lipid-soluble molecules with a molecular mass under 400 Da can enter via the TJs or pass via transcellular diffusion through the endothelial cells from one region of high concentration to a region of low concentration (Lu, Zhao et al. 2014, Jamieson, Searson et al. 2017). Small hydrophobic molecules require alternate assistance to transverse the barrier due to the cellular membrane being a hydrophobic environment, preventing entry.

1.1.5.2 Paracellular Pathway

Paracellular transport refers to the transport of solutes in between adjacent cells through TJs, which control the permeability of the pathway. The inter-endothelial junctions are made up of TJs and adherent junctions (AJs) which function to restrict access between the vascular system and CNS (Luissint, Artus et al. 2012). Gap junction complexes form channels between adjacent cells which enables molecules of low molecular mass to transmit signals across rapidly (Komarova and Malik 2010). This process is passive and the permeability of the pathway can be altered via the stimulation of factors such as vascular endothelial growth factor (VEGF) (Daneman and Prat 2015).

1.1.5.3 Carrier-Mediated Pathway

The BBB contains a variety of different transporters and transport systems that facilitates the crossing of small molecules and substrates. There are three transport modes: blood-brain influx, drug-efflux pump and brain-to-blood pump, as described by Ohtsuki and Terasaki (2007). These systems function to help regulate and maintain nutrient levels in the CNS as well as protect the CNS by pumping out any metabolites or neurotoxic substances (Song, Lu et al. 2021). Examples of molecules which are regulated by this pathway include glucose via the GLUT1 transport system and large neutral amino acids via LAT1 systems (Ohtsuki and Terasaki 2007). Carrier-mediated transport can be passive or active, in which the latter process requires energy to travel against the concentration gradient (Zaragoza 2020).

1.1.5.4 Receptor-Mediated Transcytosis

Receptor-mediated transcytosis (RMT) refers to the process of macromolecules interacting with the endothelial layer resulting in the unidirectional transport of the macromolecules from the apical side to the basolateral side. This pathway involves the complementary binding of an extracellular ligand, resulting in the invagination of the extracellular membrane forming an endosome (Villaseñor *et al.*, 2019). This intracellular endosome is transported across the

cellular cytoplasm to the polar end of entry where the macromolecule cargo is released via exocytosis. Examples of molecules which require this pathway include hormones such as insulin and growth factors such as epidermal growth factors (EGF) (Islam and Mohamed 2015). The process of RMT occurs in all cell types, however the rate of transcytosis is much lower in CNS ECs compared to that of peripheral ECs (Daneman and Prat 2015). It is theorised that this pathway is hijacked by neuronal viral vectors, which enables entry into the CNS. However, the underlying molecular pathway is unknown.

1.1.5.5 Adsorptive-Mediated Transcytosis

Similar to RMT, molecules that enter ECs via adsorptive-mediated transcytosis (AMT) enter via the apical luminal side and are transported through the cytoplasm and undergo exocytosis on the basolateral side. However, the process differs from RMT as after binding to a ligand on the cell surface membrane, the opposing charges of the positively charged macromolecule and the negatively charged membrane triggers the encapsulation of the cargo (Hervé, Ghinea et al. 2008). This is described in literature as a non-specific process.

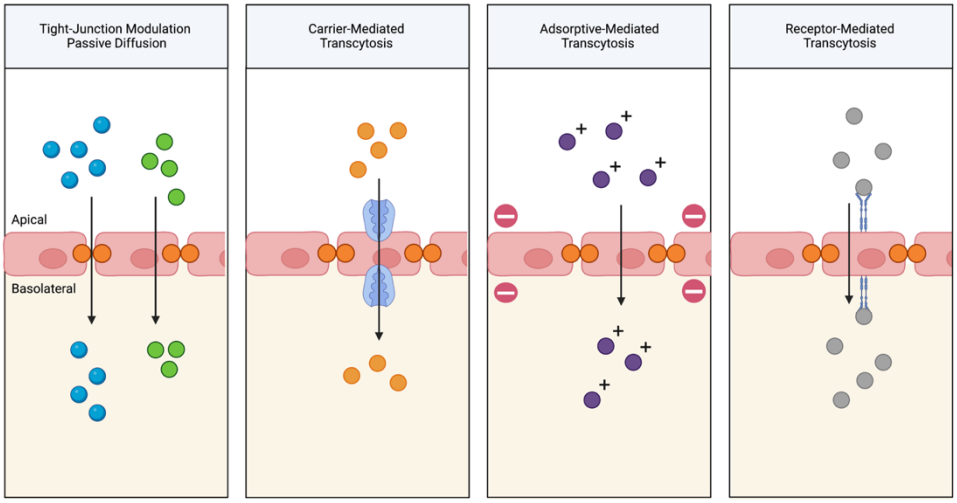

Figure 1.3: ***Model diagram of routes across the blood-brain barrier***– *Pathways across the blood brain barrier include: Tight Junction modulation and Passive Diffusion (molecules cross between cells or passively diffuse through the cell), Carrier-mediated transcytosis (molecules must bind to transport molecules which regulate and facilitate transport across), Adsorptive-mediated transcytosis (molecules polarity stimulates transport across the cell) and Receptor-mediated transcytosis (molecules bind to particular receptors and ligands which stimulates transport across the cell). (created in Biorender.com)*

1.1.6 Methods to Bypass the BBB

Due to its protective function, the BBB is a major obstacle towards systemic delivery methods to the CNS. Of course, direct delivery of a therapeutic compound to the CNS completely bypasses the BBB (Pardridge 2005), but comes with its own set of limitation and possible complications. Other strategies to bypass the BBB after systemic delivery of a compound, also come with a wide range of caveats, with many relying physical disruption of the BBB. For example, transient disruption of the BBB via the use of ultrasound to cause TJ dysregulation has been used to non-invasively permeabilise the BBB for drug delivery (Bellettato and Scarpa 2018), while hyperosmotic therapy, the osmotic shrinkage of endothelial cells via creating osmotic pressure across the BBB has been used for the treatment of cerebral oedema (Rodriguez, Tatter et al. 2015, Cook, Morgan Jones et al. 2020). These methods have been used to treat patients with severe conditions such as glioblastomas (Rodriguez, Tatter et al. 2015). However, the potential for complications and undesirable side effects mean these methods are not routinely used. The pathways across the BBB are highly-regulated processes and if altered, or consequently become uncontrolled, may lead to CNS disorders, including Alzheimer's and Tourette's, and affect the rest of the neurovascular unit, as described in the Villaseñor, Lampe et al. (2019) review. Comparatively, viral vector delivery systems, such as AAV9, cause no damage to the CNS and do not disrupt the homeostatic function of the BBB naturally (Merkel, Andrews et al. 2017). However, not all vector systems are capable of this.

1.2 Vector Delivery Systems

Vector systems are required to transport the desired therapeutic cassette to the tissue of interest to treat monogenic disorders. There are three clinical challenges a vector must overcome to be effective: 1. Deliver the therapeutic gene to the target tissue effectively with no off-targeting effect; 2. Achieve prolonged stable expression of the therapeutic gene; 3. Evade host-pathogen interactions (DiMattia, Nam et al. 2012). The predominant delivery vectors used in gene therapy are: Lentiviral vectors, Herpes Simplex Virus vectors and the AAV serotype vectors.

1.2.1 Lentivirus

The viral genome is made up of two single stranded positive sense RNA (ssRNA+) strands, referred to as a diploid genome, which encodes the genes *Gag, Pol* and *Env*. Lentivirus belongs to the *retroviridae* family of viruses which are enveloped virion particles with a diameter of 100 nm (Poletti and Mavilio 2021). Within the envelope, the capsid is made up of protein p24 which protects the viral DNA and viral enzymes required for viral replication. Due to the glycoproteins expressed in the envelope, the virus's cellular tropism is that of immune cells, specifically $CD4^{+,}$ monocytes, macrophages and dendritic cells (Froelich, Tai et al. 2010). Within the envelope, the nucleocapsid itself is made up of a protein matrix assembled by p17 which contains the viral genome and enzymes required for its replication cycle - reverse transcriptase (RT) enzyme, proteases and the integrase enzyme (IT) (Durand and Cimarelli 2011). The virus is capable of infecting both dividing and non-dividing cells which makes the virus less restricted compared to other vector systems (Anderson and Hope 2005).

1.2.1.1 LV Life Cycle

The cell surface interactome of lentiviruses includes the CD4 receptor and gp120 protein, which enable adsorption and anchoring to the cell surface (Parr-Brownlie, Bosch-Bouju et al. 2015). This enables a conformational change to occur in the viral capsid which enables an interaction with the host cell chemokine receptor CCR5 (Milone and O'Doherty 2018). As a result of this interaction, an alternate change occurs and the fusion peptide in the gp41 protein enables fusion between the envelope and the host cell membrane, enabling delivery of the viral capsid. Upon intracellular trafficking, the RT enzyme initiates reverse transcription within the capsid, referred to as the pre-integration complex, generating the single stranded complementary DNA (cDNA) (Endsley, Somasunderam et al. 2014). The next stage of reverse transcription occurs in the cytoplasm, in which the original ssRNA is degraded via ribonuclease activity post cDNA synthesis and the cDNA undergoes DNA-dependent DNA polymerase transcription forming a viral dsDNA, referred to as a provirus (Milone and O'Doherty 2018). The integrase enzyme then binds to the provirus and transports the genome into the nucleus

via a nuclear pore complex and inserts the provirus into the host genome. Upon integration, the provirus is naturally transcribed and the viral mRNA encoding the *Gag, Pol* and *Rev* ORF undergoes ribosomal translation which results in synthesis of the viral proteins (Dong and Kantor 2021). The Rev protein assembles and translocate the partially spliced viral mRNA to the cytoplasm to enable structural protein synthesis and the non-spliced RNA for genomic RNA packaging (Marchand, Lemay et al. 2019). The Gag protein binds to the generated genomic dimeric RNA and translocate the Gag-RNA complex to the cell membrane (Milone and O'Doherty 2018). The capsid and envelope proteins are constructed simultaneously, enabling the viral genome to be packaged as a result of the Psi packaging signal (Vink, Counsell et al. 2017). The capsid undergoes polyprotein processing, referred to as capsid maturation, resulting in the development of mature virions (Westerman, Ao et al. 2007). The mature virion is released from the cell via exocytosis, referred to as the budding process, and the capsid gains a lipid envelope to infect another target cell and repeat the cycle.

1.2.1.2 Recombinant LV

In the application of gene therapy, lentiviral vectors are used to deliver therapeutic transgenes and integrate the packaged cassette into specific host cells. The third-generation recombinant LV vector is replication-defective, containing a self-inactivating (SIN) deletion of the promoter sequence in 3' ITR and replacement of the actual viral genome with a therapeutic expression cassette (Poletti and Mavilio 2021). Additionally, the *Env* gene, which encodes the glycoproteins necessary for cellular tropism, was replaced with bovine vesicular stomatitis virus glycoprotein (VSV-G) which enables a broader range of tropism due to the targeted binding of low-density lipoproteins (LDL) receptors (Finkelshtein, Werman et al. 2013). Because of this, lentiviral vectors have become the predominant viral vector for *in vitro* studies for the design and generation of stable overexpression cell lines, particularly in the vectorology field (Pillay, Meyer et al. 2016, Madigan, Tyson et al. 2019, Dudek, Zabaleta et al. 2020). Due to the surface domain of the viral envelope, studies are attempting to insert ligands, peptides and single-chain antibodies to alter the tropism of the viral vector to make the delivery system flexible in its targeting strategy (Yang, Bailey et al. 2006). Clinical studies have also shown success in the vectors use in the treatment of HIV infection which have

showed no adverse effects (McGarrity, Hoyah et al. 2013). Other clinical trials include that of treatment of hematopoietic stem cells for disorders such as sickle cell disease (Kanter, Walters et al. 2022). A major limitation to this therapeutic vector is the potential random integration near cellular oncogenes which could result in the activation of the proto-oncogene and potential development of cancer (Modlich and Baum 2009). A method to improve the viral vectors safety in clinical applications is generating integrase deficient lentiviral vectors to reduce these clinical risks (Yew, Gurumoorthy et al. 2022).

Additionally, lentiviral vectors have shown success in the form of *ex vivo* therapy due to stable integrated transgene expression in transplanted cells from patients (Gowing, Svendsen et al. 2017). This has shown clinical progress in the treatment of cerebral adrenoleukodystrophy by transplanting lentiviral-induced hematopoietic stem cells for ABCD1 stable expression resulting in disease stabilisation in patients (Eichler, Duncan et al. 2017).

1.2.2 Herpes Simplex Virus (HSV)

The icosahedral capsid of the virus contains a large 150 kb linear dsDNA genome which is made up of two genomic elements referred to as unique long (U_L) and unique short (U_S) (McElwee, Vijayakrishnan et al. 2018). These genomic elements encode the majority of the viral proteins necessary for viral replication. HSV are enveloped virions with a diameter of 150 nm. The capsid envelope contains nine viral glycoproteins which are necessary for cellular tropism (Guo, Shen et al. 2010). A unique feature of the virus is the proteinaceous space between the envelope and the capsid, referred to as the tegument, which contains viral proteins that are necessary for viral infection. Following primary cell infection in epithelial cells, the virus target the CNS as a secondary target via sensory neurones and enables the virus to undergo latent infection in the nerve ganglia (Bello-Morales, Andreu et al. 2020). The viral circular episome, an extrachromosomal genetic element, is stably maintained as an episome in the nucleus of the neurones which enables immune evasion. The viral lifecycle undergoes reactivation from latency phase to lytic phase resulting in the progeny virus in the sensory neurones to traffic via retrograde transport to peripheral tissue (Maroui, Calle et al. 2016).

1.2.2.1 HSV Life Cycle

HSV adsorbs to the target cell via heparan sulphate and herpesvirus entry mediator (HVEM) cell surface proteins enabling anchoring on the plasma membrane to the gD and gM glycoproteins localised to the viral envelope (Kim, Chouljenko et al. 2013). Upon adsorbing to the cell surface and interacting with HVEM, the gB glycoprotein mediates membrane fusion enabling entry (Cooper and Heldwein 2015). The virus is capable of entering via direct fusion or via receptor-mediated endocytosis. The nucleocapsid is released into the cytoplasm and is transported across the cell via microtubule-mediated transport to the nucleus (Musarrat, Chouljenko et al. 2021). The nucleocapsid interacts with the nuclear pore complex which enables the delivery of the viral genome to the nucleus of the host cell. The linear genome become circularised via the cleavage of viral genomic elements (Strang and Stow 2005). Viral transcription can only occur after ICP0-mediated epigenetic regulation to repress the host intrinsic restriction factors such as nuclear domain 10 (ND10) (Gibeault, Conn et al. 2016). Viral transcription is divided into three phases – immediate early (IE) genes, early (E.) and late (L) phase genes (Alfonso-Dunn, Turner et al. 2017). The viral protein 16 (VP16) tegument protein drives the expression of the IE genes via interactions with the host cell factor 1 (HCF-1) and octamer binding protein-1 (Oct-1) (Wysocka and Herr 2003). This results in the transcription of the E genes which results in genome replication via the rolling circle mechanism (Muylaert, Tang et al. 2011). Following genome replication, the L genes are expressed which encode the viral proteins which are required for virion assembly. Capsid assembly occurs in the nucleus in regions referred to as the replication compartments, in which following capsid formation the dsDNA is incorporated into the capsid via a packaging signal A element sequence (Heming, Conway et al. 2017). The mature capsid then buds out of the nucleus, referred to as primary envelopment, and gains an envelope which enables fusion out of the perinuclear space, referred to as de-envelopment, thus releasing the naked capsid into the cytoplasm (Takeshima, Arii et al. 2019). This enables the capsid to be re-enveloped via the golgi, referred to as secondary envelopment, which enables the enveloped virion to be transported via *trans*-golgi vesicles to the cell membrane (Owen, Crump et al. 2015). During this translocation, the virion gains tegument proteins and viral glycoproteins before extracellular release.

1.2.2.2 Recombinant HSV

The HSV vector is replication-defective due to the deletion of immediate early (IE) genes which are required for viral replication. Deletion of the joint region between the two genome components U_L and U_S enables the insertion of an approximately 25 kb therapeutic expression cassette (Owen, Crump et al. 2015). The advantage of this vector is that it has a wide cellular tropism, capable of evading the immune system and it can transport large therapeutic cargo unlike other vectors. Clinically, the viral vector has been predominately used as an oncolytic vector for cancer immunotherapy (Carson, Haddad et al. 2010). Talimogene laherparepvec is an HSV-1 vector which packages granulocyte-macrophage colony-stimulating factor (GM-CSF) to lyse melanoma cells and stimulate an immune response (Ferrucci, Pala et al. 2021). Additionally, a clinical trial to treat dystrophic epidermolysis bullosa with HSV-based gene therapy has been designed to restore C7 protein, via the delivery of the *COL7A1* gene, and has shown success in improved wound healing via topical administration (Guide, Gonzalez et al. 2022). On the other hand, due to the majority of people having pre-existing immunity against the wild-type HSV virus, neutralising antibodies against the designed vector reduces its therapeutic efficiency (Brockman and Knipe 2002). Due to long-term expression being essential for an effective form of gene therapy, the latency phase of the virus which entails the stable expression of the HSV episome has been attempted to be utilised via the use of a latency-associated transcript (LAT) promoters. However, studies have shown the stable expression drops after 6-12 months and require further optimisation (Berges, Wolfe et al. 2005).

1.2.3 Adeno-Associated Virus (AAV)

The AAV virus is from the *Parvoviridae* family and is replication-dependent on co-infection with other viruses, including adenovirus, which supply multiple viral proteins to assist in AAV replication (Stracker, Cassell et al. 2004, Fragkos, Breuleux et al. 2008). Without viral proteins expressed by the helper virus upon infection, AAV cannot propagate (Matsushita, Okada et al. 2004). As a result, although AAV is a known human virus, it causes no known disease or

illness. AAVs are popular as delivery systems primarily due to their non-pathogenic nature, broad tropism between serotypes and their ability to infect both dividing and non-dividing cells. The latter ability is especially important in neuronal gene therapy due to the post mitotic nature of neurons. Although the vector is highly advantageous, the wild-type virus has been shown to integrate into the cell genome (Recchia and Mavilio 2011). The viral genome ITR and Rep sequences share sequence homology with a specific region of the host genome, referred to as locus AAVS1 (Hanlon, Kleinstiver et al. 2019). Due to this homology, during homology-directed repair, the viral genome can be mistaken for the cells donor chromatin. As a result, the ITR and Rep regions are integrated into the cells genome. Because of this, it has been shown in studies to induce hepatocellular carcinoma (de Jong and Herzog 2021).

1.2.3.1 AAV Viral Structure

The non-enveloped virus is a 26 nm icosahedral capsid containing single-stranded DNA (ssDNA) of ~4.7 kilobases (kb) which contains two open-reading frames (ORF) for three genes – *Rep* (Replication), *Cap* (Capsid) and *AAP* (Assembly) (Figure 1.4). The ORFs are flanked by two AAV-specific palindromic inverted terminal repeats (ITRs) (Colella, Ronzitti et al. 2018). The *Rep* gene encodes for viral proteins (Rep78, Rep68, Rep52 and Rep40*)* which function in genome replication and packaging. The *AAP* gene functions in capsid localisation and assembly (Earley, Powers et al. 2017). The *Cap* gene encodes three viral proteins (VP1, VP2 and VP3) which construct the viral icosahedral capsid in a predicted ratio of 1:1:10, respectively (DiMattia, Nam et al. 2012, Drouin and Agbandje-McKenna 2013). Although wild-type AAV and its lifecycle is not completely understood, more research is given towards recombinant AAV serotypes which are progressively being used in gene therapy.

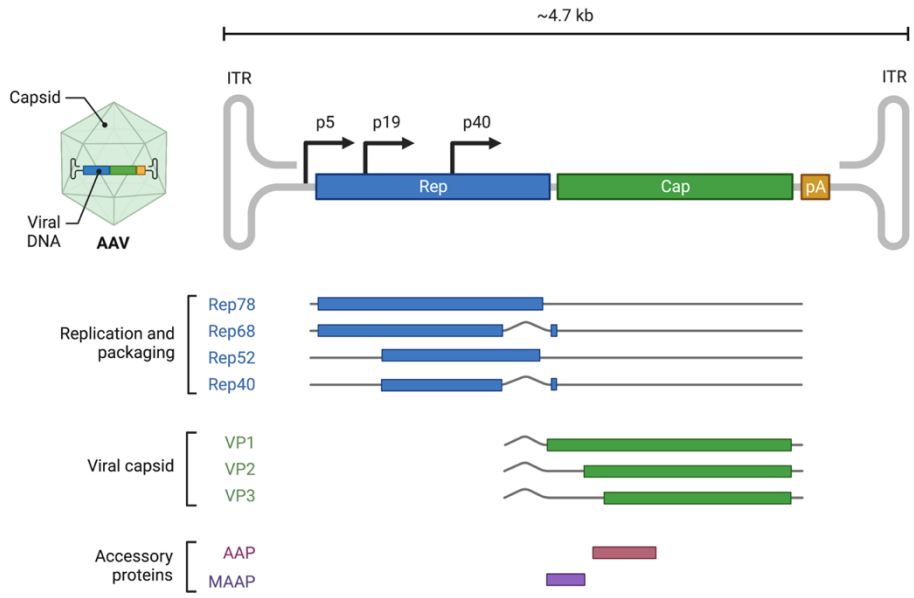

Figure 1.4: ***Model figure of the wild-type AAV genome–*** *A diagram of the AAV capsid with a detailed description of the viral genome and the viral genes required for viral replication. Viral genome containing the ITRs, Rep, Cap and PolyA tail genetic elements. All viral genes listed in relation to the Rep (Rep78/68/52/40), Cap (VP1/2/3) and accessory proteins (AAP and MAAP). (created by Biorender.com).*

1.2.3.2 Recombinant AAV Vector Design

Recombinant AAV (rAAV) is a delivery vector in which the AAV genome is replaced with a therapeutic cassette which contains no pathogenic viral DNA. Typically these recombinant vectors lack the *Rep* gene but retain the ITR-flanked ends which enable the formation of an episome as a result of their hairpin structure (Fragkos, Breuleux et al. 2008). The episome acts as an extrachromosomal element in the nucleus of the target cell which lowers the risk of vector-mediated insertional mutagenesis (0.1%-1% of transduction events) (Rodriguez, Tatter et al. 2015, Colella, Ronzitti et al. 2018). Between these rAAV ITRs resides the therapeutic cassette, consisting of a promoter to drive transcription, a gene of interest encoding the therapeutic protein, a poly A sequence and a terminator sequence to cleave the mRNA at the correct length, preventing the synthesis of a defective protein (Naso, Tomkowicz et al. 2017). However, for the therapeutic cassette to be packaged efficiently into new recombinant AAV viral particles, the entire sequence, including each ITR, must not exceed the wild type AAV genome size of approximately 4.7kb. If the genome package is over 5 kb, the episome cannot be packaged, resulting in genome fragmentation (Wu, Yang et al. 2010). This limited packaging capacity means only smaller therapeutic genes are appropriate for AAV mediated gene therapy techniques (Pryadkina, Lostal et al. 2015). To overcome the size limitation, current research has focused around delivering two halves of a therapeutic gene in two separate AAV gene therapy vectors (Carvalho, Turunen et al. 2017). However, this requires both vectors to transduce the same target cell simultaneously and for the separate fragments encoded within each therapeutic cassette to reform as a single gene. Regardless, these dual vector approaches are severely limited by the efficiencies of these processes.

The core of the AAV virion consists of β-barrel motifs, which are conserved among all parvovirus capsids, with loops inserted into β-strands which contain variable regions (VRs). These VRs facilitate cellular interactions and result in alternate cellular tropisms between serotypes (Bell, Gurda et al. 2012). AAV has several serotypes (1-9) with a variety of tropisms due to alternate primary and secondary cell-surface target receptors (Table 1.1). For example, AAV9 has a strong tropism for neurons and astrocytes as a result of alternate VR-I and VR-IV loop structures while AAV8 has a higher transduction efficiency in microglia (DiMattia, Nam et al. 2012, Stanimirovic, Sandhu et al. 2018).

Table 1.1*: List of known receptors for AAV receptor (Ellis, Hirsch et al. 2013, Lykken, Shyng et al. 2018). All glycan recognitions listed (except for AAV9) are from the Mietzsch, Broecker et al. (2014) study which details each N-glycan's specific structural chain differences.*

Serotype	Glycan Recognition	Co-Receptor
AAV1	N-Glycan	-
AAV2	6-O- and N-sulphated heparin	Fibroblast/hepatocyte growth factor receptor; laminin receptor; integrin αVβ5 and α5β1
AAV3	2-O- and N-sulphated heparin	Hepatocyte growth factor receptor; Laminin receptor
AAV4	N-Glycan	-
AAV5	N-Glycan	Platelet-derived growth factor receptor
AAV6	N-Glycan N-sulphated heparin	Epidermal growth factor receptor
AAV7	-	-
AAV8	-	Laminin Receptor
AAV9	Galactose	Laminin Receptor

In single-stranded AAV (ssAAV) transduction, transgene expression can only occur once the single stranded transgene undergoes second-strand synthesis to form double stranded DNA (Hauck, Zhao et al. 2004). This is a rate-limiting process. To increase the rate of transgene expression, self-complementary AAV (scAAV) has been designed in which both complementary ssDNA are packaged which allows optimised efficiency and increased speed of transgene expression. This method is time efficient as it avoids the ssDNA cellular conversion step into dsDNA to enable gene expression (Dominguez, Marais et al. 2011). Because of this, transduction and rate of transcription is improved which is optimal for transduction studies. Although it has improved transduction efficiency, due to the larger size of scAAV genome, the carrying capacity of the vector is reduced to 2.2 kB which limits transgene capacity (Raj, Davidoff et al. 2011).

1.2.3.3 AAV Transduction pathway

The viral vector of choice is selected based on its tropism for specific target tissue which is dependent on viral-protein interactions. Upon reaching the target cell, AAV interacts with cell surface receptors via glycan- and protein- interactions, in a process referred to as adsorption (Huang, Halder et al. 2014) (Figure 1.5). The known glycan and receptor interactions of each AAV serotype are detailed in Table 1.1. Once anchored to the cell surface, the virus hijacks specific endocytosis pathways, such as the clathrin-independent carriers/GPI-enriched endocytic compartment (CLIC/GEEC) pathway, via interacting with co-receptors on the cell surface resulting in the invagination of the plasma membrane and vector internalisation (Nonnenmacher and Weber 2011, Nonnenmacher and Weber 2012). Following intracellular scission of the endosome, the compartmentalised AAV capsid is transported across the cytoplasm with the assistance of transport proteins, such as Rab7 and Rab11 for AAV2 trafficking (Riyad and Weber 2021). This process has been shown to induce conformational changes to the viral capsid due to the acidic nature of the endosome and modifications which occur through the trans- Golgi network, resulting in efficient transduction (Sonntag, Bleker et al. 2006). Processing through the Golgi appears to be a particularly important step as disrupting the Golgi pathway results in reduced AAV transduction (Nonnenmacher, Cintrat et al. 2015). Following conformational changes, the capsid escapes the endosome via the phospholipase A2 (PLA2) domain located on VP1 of the AAV capsid and enters the nucleus via an importin beta-dependent process (Girod, Wobus et al. 2002). The capsid is then trafficked through the nucleolus to the nucleoplasm enabling the capsid to uncoat and release its ssDNA transgene (Bevington, Needham et al. 2007). Naturally, the cell detects the ssDNA and converts it into dsDNA which enables the formation of an episome. This episome is transcribed via polymerase II and the mRNA synthesised is transported through the nuclear pore to interact with ribosomes to undergo translation of the recombinant transgene. Due to the lack of the *Rep* gene, the viral vector does not replicate and has served its function when delivering and translating the therapeutic transgene.

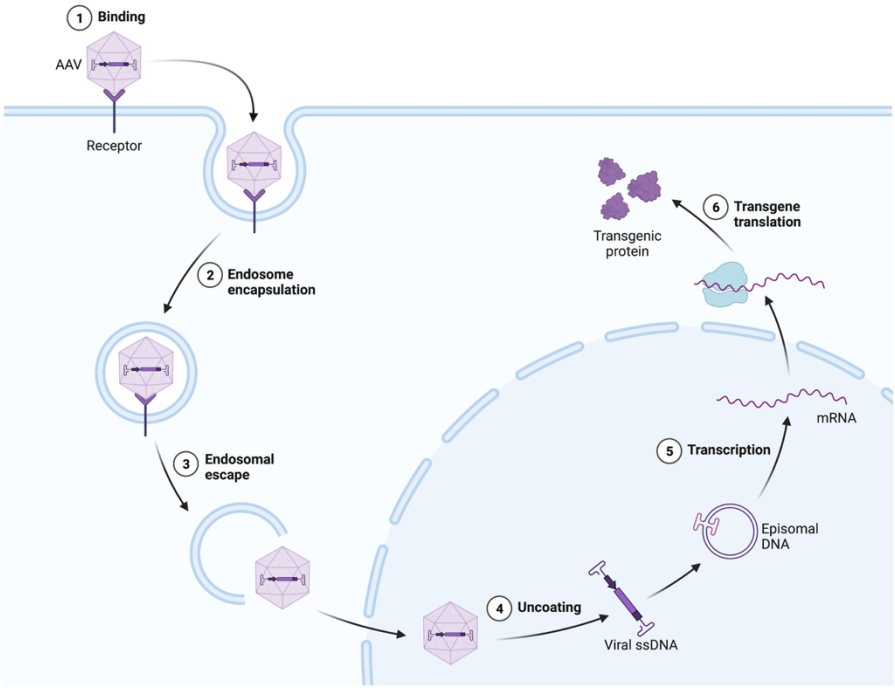

Figure 1.5: ***Model diagram of the AAV transduction pathway***– *Stages of AAV transduction: (i) Binding (ii) Endosome encapsulation (iii) Endosomal escape and nuclear entry (iv) uncoating and episome formation (v) transcription of the episome (vi) transport of transgene mRNA to the cytoplasm (vii) transgene translation and synthesis of transgene protein* (*created by Biorender.com*).

1.3 AAV9

Aside from its wide neural tropism, AAV9 also has the ability to cross the BBB after systemic administration by a mechanism not yet fully understood (Merkel, Andrews et al. 2017). Systemic administration of the vector is optimal as injection via the vasculature reduces surgical risks and clinical costs compared to other methods including local injection which is also limited to only transducing the areas surrounding the injection site (Zhang, Yang et al. 2011). However, although the virus can cross the BBB, the quantity of virions capable of penetrating the CNS via the vasculature is limiting (Song, Pekrun et al. 2022). Because of this, the efficiency of the virus to reach the CNS via the vasculature is restricted and the mechanism of AAV9s crossing across the BBB is unknown. To improve the therapeutic efficiency of AAV9 in its delivery, optimisation strategies have been designed to generate more efficient novel capsids variants.

1.3.1 AAV9 Optimisation

To achieve lower viral dosage, the use of cre-recombination-based adeno associated virus-targeted evolution (CREATE) strategy has enabled the synthesis of novel recombinant variants of AAV serotypes which have improved transduction efficiency and/or crossing of the BBB (Deverman, Pravdo et al. 2016, Ravindra Kumar, Miles et al. 2020). An AAV library was generated in which a range of capsid variants (each identified via genome packaged barcodes) with random peptides inserted into varied exposed regions of the capsid surface via PCR amplification, alter the capsids tropism and interacting pathways (Hanlon, Meltzer et al. 2019). After several rounds of forward evolution and selection *in vivo* in Cre-mice, the viral capsid variants which have maintained high delivery efficiency in target tissue are then further characterised. However, a major limitation of this process is that the selection process in the final read-out cannot distinguish capsids which mediate functional transgene expression as there are many steps involved in AAV transduction (Hanlon, Meltzer et al. 2019). To counter this limitation, an improved version of the method, referred to as multiplex-CREATE (M-CREATE) reduces the read-out of false positives via the use of next generation sequencing

(NGS) to screen multiple variants across a variety of Cre-transgenic cell lines (Ravindra Kumar, Miles et al. 2020). Because of these novel tools, several improved variants have been discovered.

1.3.1.1 PHP/PHP-eB

AAV capsid variant AAV-PHP-B (PHP-B) has AAV9 as a parent capsid. PHP-B has the novel 7-mer sequence TLAVPFK inserted between aa584-592 of the VP1 sequence resulting in enhanced transduction capability (Deverman, Pravdo et al. 2016). Although PHP-B efficiently transduces neurones and astrocytes compared to AAV9 across multiple regions of the brain after intravenous injection, it still requires a large viral dose (1 x 10^{12} vg per adult mice or higher) (Chan, Jang et al. 2017). CREATE was also used to develop an enhanced variant of PHP-B, referred to as AAV-PHP-eB (PHP-eB). It was proposed a DGT amino acid substitution enhanced transduction of the CNS compared to that of PHP-B and at a lower viral dose (1x10^{11} vg per adult mice) (Chan, Jang et al. 2017). Although these vectors have shown improved CNS transduction, multiple studies have shown both successful (Arotcarena, Dovero et al. 2021, Galvan, Petkau et al. 2021) and limiting (Hordeaux, Wang et al. 2018, Matsuzaki, Konno et al. 2018) transduction efficiency in NHPs models or specific strains of mice. The reason for this variation in efficiency was found to be due to the capsid modification leading to an interaction with a novel target receptor, the LY6A protein (Hordeaux, Yuan et al. 2019). Unfortunately, the polymorphisms in the *LY6A* gene in different mice strains meant that the improved transduction efficiency did not extend to all mice strains and NHP models (Batista, King et al. 2020).

1.3.1.2 AAV-F

A novel capsid variant, referred to as AAV-F, was found to mediate transgene expression in the brain cortex, hippocampus, striatum, cerebellum and olfactory bulb (Hanlon, Meltzer et al. 2019). The variant was made via the insertion of a 7-mer peptide sequence (FVVGQSY) between 588 and 589 nucleotides of AAV9 VP1. The vector showed a strong tropism for astrocytes and neurones in C57BL/6 and BALB/c mice strains compared to AAV9. AAV-F's

successful transduction is observed to be independent of strain and sex unlike PHP-B. In NHP studies, it was shown that AAV-F showed improved expression of the delivered transgene in the spinal cord compared to AAV9 at a lower transgene quantity, suggesting more efficient expression (Beharry, Gong et al. 2022). Additionally, the transduction of the dorsal root ganglion (DRG) was shown to be lower with AAV-F which is appealing due to DRG toxicity being a known side effect of AAV9 due to the high doses required for efficient transduction. There is limited literature on this novel capsid, however the capsids efficiency and capability to transduce NHPs CNS is a step in the right direction towards designing an improved viral capsid.

1.3.1.3 AAV-CAP-B10

Using PHP-eB as the parent capsid, the viral vector underwent M-CREATE selection which included the insertion of a 7-AA substitution library of the AA455 loop, between AA452 and AA460, found in VP1 which were functional and screened to be CNS specific and decreased specificity to the liver (Goertsen, Flytzanis et al. 2022). Of the capsid variants selected, the variant AAV9-CAP-B10 showed robust CNS expression and limited liver off-targeting in both rodent and non-human primate studies. By minimising off-target expression, side effects which are linked with the systemic delivery of AAV9 can be reduced.

By developing a more targeted AAV9 variant with further widespread neuronal transduction capability and decreased off-targeted risk, this elevates the possibility of treatment for neurological disorders (Foust, Nurre et al. 2009). Although the optimised variants have shown experimental success in their transduction efficiency, without understanding the pathways AAV9 and the viral variants undertake, the progression in experimental success will be limited. By developing our knowledge of the particular protein interactions of AAV9 and its variants, there is the potential for more directed forward evolution of these capsids, enabling enhanced capsid-protein interactions, and therefore, more specific, targeted therapeutic transgene delivery.

1.4 AAV9 Protein Factors

1.4.1 Restriction Factors (RFs)

A recognised advantage of AAV9 as a vector delivery system is its low level of immunogenicity (Ronzitti, Gross et al. 2020). However, that is not to say that AAV's do not elicit any immune response. Indeed, capsid specific antibody responses have been reported in many clinical trials using AAV vectors which have inflammatory effects mainly due to high levels of off target transduction resulting in hepatotoxicity and DRG toxicity (Hordeaux, Buza et al. 2020, Chand, Mohr et al. 2021, Emmanuel, Smith et al. 2022). There are also cellular antiviral mechanisms that seek to disrupt viral transgene expression. Restriction factors (RFs) are ubiquitously expressing proteins which function in interfering with the viral pathway. These factors can either be intrinsic in response to the presence of the viral protein/genome or as a response to an immune stimulated pathway (Coroadinha 2023). Only a few AAV9 restriction factors have been identified. Crumbs homologue-3 (Crb3) is a transmembrane protein which regulates cell surface polarity in relation to epithelial cells and retinal degeneration (Bulgakova and Knust 2009). In a CRISPR knockout screen to identify novel host restriction factors in relation to AAV9 transduction, the knockout of Crb3 had the highest increased AAV9 transgene expression in hepatocytes (Madigan, Tyson et al. 2019). The removal of Crb3 was shown to mis localise glycans and increase the expression of key viral biding partners, such as galactose, to the cell surface resulting in improved transduction efficiency. Other targets which have been shown to increase AAV9 transduction when downregulated via an siRNA screen include SETD8, SOX15, TROAP and WWC2 (Mano, Ippodrino et al. 2015). However, this study predominately focused on the transduction efficiency of AAV2. Research in identifying restriction factors is limited and further insight into these targets will help improve the therapeutic effectiveness of the viral vector. While restriction factors can limit AAV transduction and transgene expression, other host cell surface proteins help to govern AAV transduction and tropism via their interaction with the AAV capsid, these are termed entry factors.

1.4.2 Host Entry Factors

A number of AAV9 attachment receptors have been described and are discussed in detail below.

1.4.2.1 Terminal N-Linked Galactose

Virus-glycan interactions are essential for efficient host cell invasion. Predominately, viruses have a strong affinity to attachment receptors which enables them to adsorb to the surface of their target cell and interact with alternate co-receptors (Shen, Troupes et al. 2013). Several serotypes of AAV use sialyated glycans as a primary receptor which vary in N-acetylneuraminic acid linkage enabling varied tropisms due to the different capsid topology of each serotype (Shen, Bryant et al. 2011). Previous studies shown that AAV9 had a strong affinity to galactose; while the removal of siliac acid (SIA), the primary receptor for alternate serotypes, had no effect on AAV9 (Bell, Vandenberghe et al. 2011). By inhibiting N-linked and O-linked glycosylation there was a major decrease in AA9 infectivity, suggesting that the virus prefers N-linked glycans compared to other carbohydrates including SIA. In addition, the enzymatic removal of SIA resulted in a significant increase in galactose binding with AAV9 (Bell, Vandenberghe et al. 2011). The galactose binding domain on the AAV capsid is proposed to be found at the base of the protrusion of the 3-fold axis and it is suggested that N470, D271, and N272 found in the binding-pocket form hydrogen bonds with galactose enabling adsorption (Bell, Gurda et al. 2012). These data therefore indicates that AAV9 uses galactose as a primary receptor enabling the adsorption of the vector, possibly allows transcytosis to occur across the BBB.

1.4.2.2 Laminin

Once viruses have adsorbed to the cell membrane, they require further carbohydrate or proteomic interactions. These interactions are required for capsid conformational changes to enable fusion or by initiating an intracellular signalling cascade which enables the pathogen to enter the target cell via endocytosis. Because of this, co-receptors also determine a

pathogens tropism and vary across all viruses. In AAV serotypes this includes fibroblast growth factor receptor (FGFR) for AAV2, hepatocyte growth factor (HGF) for AAV3 and laminin receptor (LamR) for AAV9 (Mizukami, Young et al. 1996, Pillay and Carette 2017). LamR is a heterodimeric protein, composed of α, β and γ subunits, integrated into basement membranes and functions in cellular migration, tissue development and cellular communication (Hamill, Kligys et al. 2009, DiGiacomo and Meruelo 2016). It had been first put forward in the Akache, Grimm et al. (2006) study that LamR expression enhances several serotypes of AAV transduction, including AAV9. The results indicate that over-expression of LamR lead to an increase in AAV9 transduction while knocking-out LamR, via the use of RNAi, resulted in lower transduction efficiency suggesting a functional role in AAV9 transduction. Some studies have proposed that the plasma membrane receptor is located in concentrated regions of lipid rafts which could provide further indication of its role in the transcytosis stage as caveolae-associated lipid rafts have been hypothesised to be associated with the crossing of the BBB (Fujimura, Yamada et al. 2005, Hordeaux, Yuan et al. 2019).

1.4.2.3 AAVR

Recently, a non-biased haploid genome screening identified KIAA0319L, predominately referred to as AAVR, as a vital receptor for the transduction ability of a variety of AAV serotypes (Pillay *et al.*, 2016). AAVR is a type-1 glycosylated transmembrane protein which contains five polycystic kidney disease (PKD) Ig-like domains and a motif at the N-terminus with eight cysteines (MANEC) domain located on the ectodomain of the receptor (Dudek, Pillay et al. 2018) (Figure 1.6). MANEC-containing proteins are suggested to be linked with signalling peptides while the PKD Ig-like domains have been found to function in cellular adhesion and is often exploited by viruses in early stage infection, for example poliovirus and reovirus (Guo, Chen et al. 2004, Pillay, Meyer et al. 2016). Only two serotypes have been identified to be AAVR-independent, including AAV4 (Dudek, Pillay et al. 2018). By using AAVR knock out cell lines of AAVR, serotypes 1, 2, 3, 5 6, 7 and 9 all showed decreased transduction efficiency (Pillay *et* al., 2016). AAV susceptibility was restored in AAVR competent cells and in the presence of a minimal mutant AAVR, which only contained PKD 1-3. Alternate PKD domains were shown to have a preference between serotypes (Pillay and Carette, 2017).

PKD2 was the crucial binding domain for AAV2 while AAV5 required PKD1 for efficient transduction. The AAVR domain preference of AAV9 is unknown. AAVR was shown to undergo co-localisation with the *trans*-Golgi network, due to the receptor containing a carboxyl terminal cytoplasmic tail (C-tail) which may function in endocytosis and intracellular trafficking.

1.4.2.4 Lymphocyte Antigen 6 (LY6A)

LY6A, also referred to as SCA-1, is a GPI-anchor membrane protein which is expressed in a variety of organisms and is highly expressed in the brain microvasculature (Lang, Jenkins et al. 2017, Hordeaux, Yuan et al. 2019). These GPI-anchored proteins are known to associate with lipid rafts which are described as a subdomain enriched in cholesterol and glycosphingolipids and signalling molecules, such as protein tyrosine kinases (Hordeaux, Yuan et al. 2019). Due to these signalling properties and being associated with caveolin-1, the lipid raft is an important micro-domain in the process of caveolae/raft-dependent endocytosis and transcytosis (Nabi and Le 2003, Bian, Xiong et al. 2016). It was discovered recently that the novel AAV9 variants AAV-PHP-B and PHP-eB use LY6A as a primary receptor unlike its parent capsid which has an affinity for galactose (Huang, Chan et al. 2019). It is proposed that LY6A functions as an entry factor since by mutating a single amino acid on VP1 at position 592 prevented LY6A affinity with the viral vector variant (Hordeaux, Yuan et al. 2019). Although PHP-B and PHP-eB were initially identified as AAV9 variants with an enhanced ability to cross the BBB when delivered peripherally, it quickly became clear that these findings were strain and organism specific. PHP-B and PHP-eB were highly neurotropic in C57BL/6J mice, but this was not the case for the B6C3 strain (Mathiesen, Lock et al. 2020). These strains were shown to have a single nucleotide polymorphism (SNP) in LY6A thus prohibiting the interaction with the viral capsid (Batista, King et al. 2020).

Because of this altered tropism, PHP-B and PHP-eB have a significantly reduced BBB crossing to the CNS of certain murine models compared to others, for example BALB/cJ and C57BL/6J respectively (Hordeaux, Yuan et al. 2019, Batista, King et al. 2020). This further supports that LY6A functions as a predominant BBB crossing factor for PHP-B and PHP-eB, however *Ly6a*

gene variants appear to affect the viral variants tropisms in both mice and NHPs (Hordeaux, Yuan et al. 2019, Huang, Chan et al. 2019). This demonstrates the difficult in forward engineering AAV capsids for translation to human therapy. (Batista, King et al. 2020). These data suggest that LY6A functions as the predominant BBB crossing factor for PHP-B and PHP-eB, but also indicates the target receptor variants, in this case in *LY6A,* can drastically affect a viral variants tropism.

1.4.2.5 G protein-coupled receptor 108 (GPR108)

The encoded G-coupled protein (GPR108) is predicted to contain an amino-terminal signal peptide, a long extracellular domain and a carboxy-terminal segment containing seven transmembrane domains (Dong, Zhou et al. 2018). However, there is limited literature on this target proteins structure and function. Previously, before its association as a potential entry factor for AAV serotypes, GPR108 was shown to be a nuclear factor kB (NF-kB) activator that negatively regulates TLR signalling (Dong, Zhou et al. 2018).

Having first been identified as a potential target protein in the Pillay *et al.*, (2016) haploid genetic screen for potential target protein for AAV transduction, the Dudek, Zabaleta et al. (2020) study identified GPR108 as a crucial entry factor for all AAV serotypes except for AAV5. The chimeric construct data shows that both the N- and C-terminal domains of the target protein are essential for viral entry as defects in a single domain resulted in reduced viral transduction. In addition to this, it was shown via immunofluorescence that the target protein localises to the *trans*-Golgi network. All serotypes (which included AAV9 and PHP-B) except AAV5, were shown to have reduced viral entry in murine Hepa- and human Huh7 GPR108 knockout cells. This suggests that GPR108 is conserved across murine and human species and can be considered a homolog. GPR108 was further confirmed to be a key viral entry factor in the Meisen, Nejad et al. (2020) study. In this study, knockout of AAVR, GPR108 and TM9SF2 in U2-O2 cells were shown to reduce AAV transduction across all viral serotypes except AAV5, which was shown to be independent of GPR108 interaction. Although this data is strongly suggestive of GPR108 being a prospective target protein, its inability to rescue transduction via overexpression in both GPR108- and AAVR-knockout U2-O2 cell lines suggests it may have

an altered cell entry function compared to other target proteins. Further research is needed via the development of more knock-out cell lines and expanding the rescue study by over-expressing GPR108 in multiple poorly permissive cell lines.

1.4.2.6 ATP-powered calcium pump SPCA1 (ATP2C1)

Another target protein which was identified in the Pillay, Meyer et al. (2016) screen was the ATP2C1 protein. This calcium-transporting ATPase protein functions in the regulation of Ca^{2+} in the trans-golgi compartments and has been predominately researched in relation to Hailey-Hailey disease (Micaroni, Giacchetti et al. 2016). The knockout of the target protein was shown to significantly reduce the transduction efficiency and mRNA expression of AAV9 as well as alter the localisation of the virus (Madigan, Berry et al. 2020). The virus was also shown to not undergo necessary conformation changes due to the disrupted calcium influx which is believed to be required for effective transduction.

Overall, recent literature suggests we are making progress towards our understanding of AAV9's transduction pathway via identifying its entry interactome. Our understanding of the AAV9 viral transduction pathway is vital in the improvement of a variety of vectors and permit further treatment of neurological disorders. With a greater understanding of this pathway, we will gain access to enhanced potential in neurological viral delivery systems to the CNS and possibly develop even further improvements to the AAV9 serotype and its variants.

1.5 Preliminary Data

Preliminary studies from our lab sought to identify novel interactome targets for AAV9. Identifying vector-stimulated gene expression patterns could help identify target proteins in relation to the vector of interest. Due to gene transcription analysis recently becoming a novel approach for drug discovery (Ha, Park et al. 2021), we theorised the same could be used for identifying novel viral targets. Due to viruses' natural function to hijack cellular pathways to elicit entry into cells, the concept of these pathways being dysregulated as a result of viral interaction was tested. The preliminary data (Figure 1.6) showed that following porcine

endothelial brain cells (PEBCs) incubation with AAV9, there was an upregulation in gene expression of SDC4, ICAM1 and SLC7A2 via microarray and supported via qPCR.

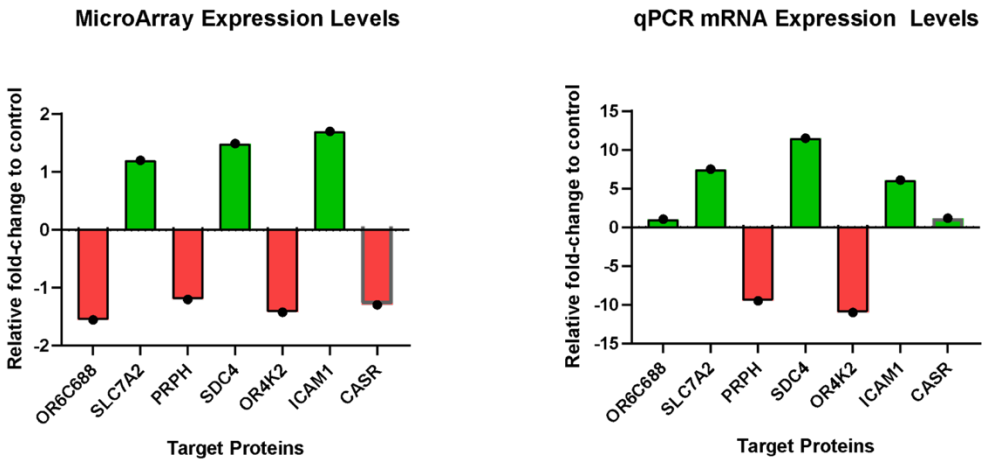

Figure 1.6: ***SDC4, ICAM1 and SLC7A2 have increased expression after introducing AAV9 to PEBCs –*** *PEBCs were treated with ssAAV9 and incubated for 48 hours. (A) Transduced cells RNA was collected which enabled cDNA conversion and then subjected to a (A) microarray hybridisation and (B) qPCR analysis. Graph depicts average mRNA fold-change of each gene relative to a non-treated condition.*

1.6 Preliminary Targets

There targets identified in the primary screen were carried forward for this study. These are detailed below and presented in Figure 1.7.

1.6.1 Syndecan-4 (SDC4)

Literature has shown that each AAV serotype tropism is as a result of carbohydrate specificity on the cell surface (Shen, Bryant et al. 2012). Syndecan-4 (SDC4) is a ubiquitously expressed transmembrane heparan sulphate proteoglycan which is localised to the cell membrane and functions in cellular migration, adhesion and intracellular signalling (Hudak, Roach et al. 2023). SDC4 has been shown to interact with signalling proteins, such as activate protein kinase C, and may have a potential role in immune signalling as well as interacting with intracellular networking proteins such as FGF2 and SDCBP (Lefevre, Felmlee et al. 2014). The *SDC4* gene is located on chromosome 20 (20q13.12) and contains 5 exons at a size of 23,137 base pairs. RNA-sequencing of tissue data shows that expression of SDC4 is highest in liver and lung tissue. The protein itself is predicted to have a molecular mass of 22 kDa (Lefevre, Felmlee et al. 2014). When expressed on the cell surface, the protein forms homodimers and its protein structure is made up of an extracellular domain (consisting of a sialic acid containing carbohydrate region, a cell binding domain region (CBD) and a GAG attachment site region), a transmembrane domain and a cytoplasmic domain (Hudak, Roach et al. 2023). Its predicated localisation as well as presence of the sialic acid region gave promise that SDC4 could be involved in the AAV transduction process.

1.6.2 Intracellular Adhesion Molecule 1 (ICAM1)

ICAM1 is an immunoglobulin-like (Ig) cell surface glycoprotein which is expressed on the cell surface of endothelial cells and immune-related cells (Figenschau, Knutsen et al. 2018). The *ICAM1* gene is located on Chromosome 19 (19p13.2) and contains 7 exons and has 5 splice

variants. The ICAM1 protein functions in cell-cell binding, it is associated with the extracellular matrix and for immune regulatory roles such as leukocyte recruitment and immune stimulation (Bui, Wiesolek et al. 2020). This target protein has been investigated for being an interacting partner with the coxsackievirus A21 capsid proteins (Xiao, Bator et al. 2001), supporting further its identification as a potential AAV interacting partner. The molecular weight of the protein is predated to be 80 kDa (Anbarasan, Bavanilatha et al. 2015) and has been shown to be predominately expressed in the liver and bone marrow via RNA-sequencing data.

1.6.3 Cationic Amino Acid Transporter 2 (SLC7A2)

SLC7A2 is a member of the amino acid-polyamine-organocation (APC) transporter family and functions in the regulation of the cationic amino acids arginine, lysine and orthenine (Xia, Wu et al. 2021). The *SLC7A2* gene is located on chromosome 8 (8p22) and contains 18 exons and has 5 splice variants. The molecular weight of the protein is predicted to be 76 kDa. RNA-sequencing data has shown that the target protein is predominately expressed in liver and thyroid tissue. A recent ATPase calcium pump target protein, ATP2C1, has been identified to be functionally relevant in the transduction pathway of AAV1 and AAV2 (Madigan, Berry et al. 2020). Because of this, SLC7A2 was carried through to validate if it shares a similar functionality to that of ATP2C1.

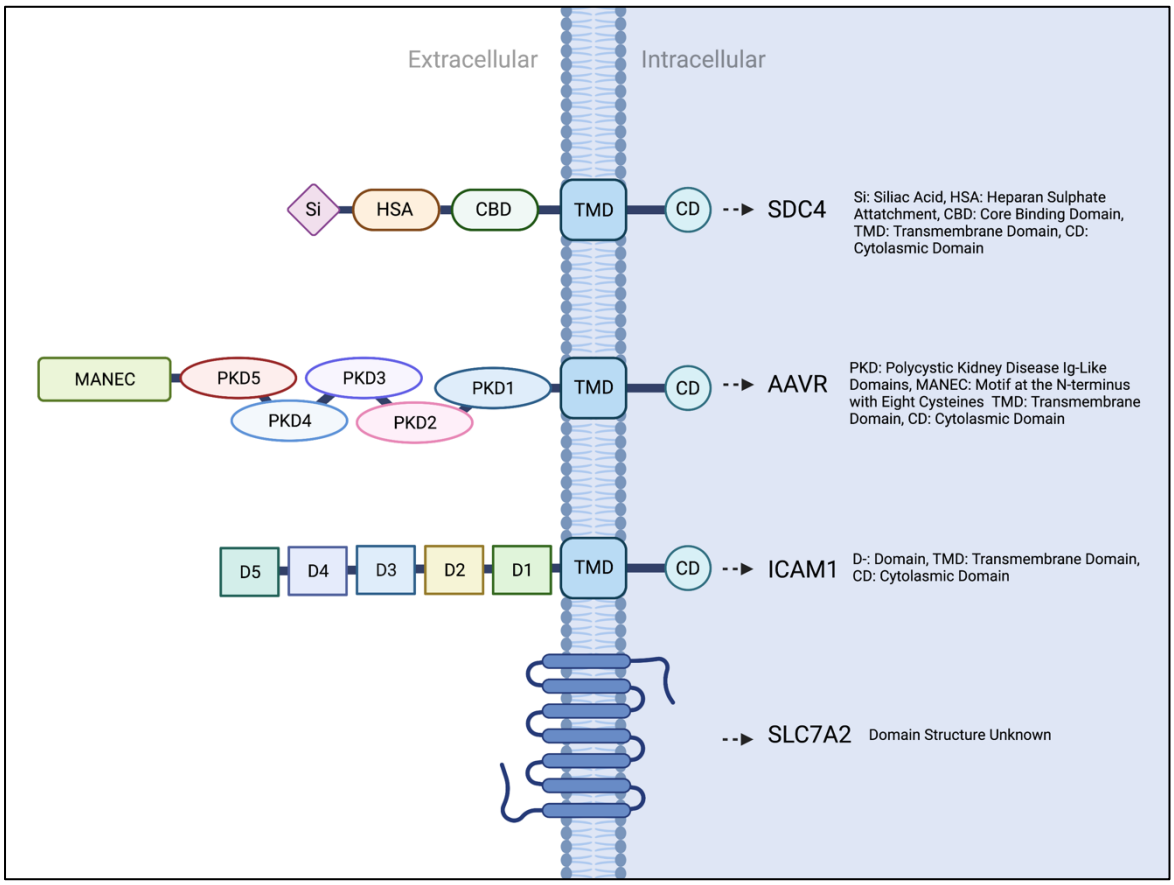

Figure 1.7: ***Model of each target protein identified in preliminary study with the positive control AAVR –*** *SDC4 structure (Si, HSA, CBD, TMD and CD), AAVR structure (MANEC, PKD5, PKD4, PKD3, PKD2, PKD1, TMD, CD), ICAM1 structure (D5, D4, D3, D2, D1, TMD, CD) and SLC7A2 structure.*

1.7 Hypothesis and Aims

Following our preliminary data, we hypothesised that by manipulating the protein expression of SDC4, ICAM1 and SLC7A2 would affect AAV9 transduction. AAVR, a known target protein of AAV9 (Pillay, Meyer et al. 2016), was used as a positive control. The aim of this project was to identify and characterise permissive lines as *in vitro* models to conduct an siRNA - knockdown and CRISPR-knockout screen to determine if loss of each target protein affected viral transduction. The non-permissive cell lines identified were used as *in vitro* models for

overexpression studies to determine if significantly increasing protein expression improved viral transduction. Additionally, with the tools generated, attempt to identify the functional nature of each protein in relation to AAV9s transduction pathway and validate if they were interacting with viral capsid.

2 Methodology

2.1 Materials

2.1.1 Stock Solutions

Acrylamide-bis-acrylamide (30%) (Thermo Fisher)

Ampicillin (100 mg/ml) (Thermo Fisher)

B-mercaptoethanol (Thermo fisher)

Bovine serum albumin (BSA) (Thermo Fisher)

Bradford reagent (5x stock) (Thermo Fisher)

Dimethyl sulphoxide (DMSO; 100%) (Thermo Fisher)

Ethanol (100%)

Ethidium Bromide (10 mg/ml) (Thermo Fisher)

Ethylenediaminetetraacetic acid (EDTA; 0.5 M)

Foetal bovine serum (100%) (Thermo Fisher)

Formaldehyde (37% (w/v))

Glycerol (100% (v/v))

Hydrochloric acid (HCl)

K-Piperazine-N,N'-bis (2-ethanesulphonic acid) buffered with potassium hydroxide to pH 6.8 (K-PIPES; 400 mM) (Sigma)

Magnesium chloride (MgCl2; 1 M) (Thermo Fisher)

Methanol (100%)

NP40 (Nonidet P-40) (100%) (Thermo Fisher)

Phosphate buffered saline (PBS; 137 mM NaCl, 2.7 mM KCl, 0.7 mM KH2PO4, 4 mM Na2HPO4)

Potassium chloride (Thermo Fisher)

Sodium dodecyl sulphate (SDS; 10% (w/v)) (Thermo Fisher)

Sodium chloride (NaCl; 5 M) (Thermo Fisher)

Sodium pyruvate (100 mM) (Thermo Fisher)

Trypsin-EDTA (Thermo Fisher)

Tris-buffered saline (TBS; 20 mM Tris (tris(hydroxymethyl)aminomethane) (Thermo Fisher)

Triton X-100 (100%) (Sigma)

Tween-20 (100%) (Sigma)

2.1.2 Microbiology Reagents

2.1.2.1 Plasmids

Plasmids purchased or generated in-house are detailed in table 2.1.

Table 2.1: List of plasmids - *A list of the plasmids which were generated and used for this project*

Name:	Expression:	Size:	Source:
AIO-Puro	Mammalian	~10 Kb	A gift from Steve Jackson (Addgene plasmid # 74630; http://n2t.net/addgene:74630; RRID: Addgene_74630).
AIO-Puro_SDC4	Mammalian	~10 Kb	In this study
AIO-Puro_ICAM1	Mammalian	~10 Kb	In this study
pCI_neo	Mammalian	~5.4 Kb	Promega, UK
pCI_neo-Myc-SDC4	Mammalian	~6 Kb	In this study
pCI_neo-HA-AAVR	Mammalian	~7 Kb	In this study
pCI_neo-FLAG-ICAM1	Mammalian	~7 Kb	In this study
pCI_neo_V5-SLC7A2	Mammalian	~7 Kb	In this study
LV_ Myc_SDC4	Mammalian	~7 Kb	Provided by VectorBuilder
LV_HA_AAVR	Mammalian	~7 Kb	Provided by VectorBuilder
LV_FLAG_ICAM1	Mammalian	~7 Kb	Provided by VectorBuilder
LV_V5_SLC7A2	Mammalian	~7 Kb	Provided by VectorBuilder

2.1.2.2 Bacterial Growth Media

Lysogeny (LB) Broth (25g/L) (Thermo Fisher)

Lysogeny (LB) Agar (32g/L) (Thermo Fisher)

Super Optimal Broth with Catabolite repression (SOC) medium (NEB)

2.1.2.3 Reagents for plasmid purification

Reagents used in plasmid extraction with QIAGEN Plasmid Kits were provided by the manufacturer:

Resuspension Buffer supplemented with Lyse Blue and RNase A

Lysis buffer

Neutralisation buffer

Wash buffer

Wash buffer A4 supplemented with ethanol

Elution buffer

2.1.3 Cloning

2.1.3.1 Reagents for cloning AAVR, SDC4, ICAM1 and SLC7A2 into pCI-neo

2.1.3.1.1 Primers

Primers were designed to add restriction sites to the 5' and 3' ends of AAVR, SDC4, ICAM1 and SLC7A2 to allow cloning into pCI-neo. The primers used for cloning are listed in table 2.2. Primers used for sequencing of these plasmids are listed in table 2.3.

Table 2.2: Designed PCR primers - *A list of the PCR primers which were generated and used for this project*

Primer	5'-3' Sequence
ICAM1_SalI	ATATGTCGACATGGCTCCCAGCAGCCCCC
ICAM1_EagI	ATATCGGCCGTCAGGGAGGCGTGGCTTGTGT
AAVR_SalI	ATATGTCGACATGGAAGGGAAACATTC
AAVR_EagI	ATATCGGCCGTCACAGGATCTCCTCCC
SDC4_NotI	ATCGCTCGAGATGGCCCCCGCCCGTCTGTTC
SDC4_XhoI	ATCGGCGGCCGCTCACGCGTAGAACTCATTGGTG
SLC7A2_NotI	ATATCTCGAGATGATTCCTTGCAGAGCCG
SLC7A2 XhoI	ATATGCGGCCGCTTAGAATTCACTTGTCTTTTC

Table 2.3: Sequencing PCR Primers - *A list of the sequencing primers which were generated and used for this project.*

Primer	5'-3' Sequence
AIO_Rev	GATTTTGAGACACGGGCCA
CMV Fw	CGCAAATGGGCGGTAGGCGTG
T7 EEV Fw	AAGGCTAGAGTACTTAATACGA
M13 Fw	TGTAAAACGACGGCCAGT
SDC4 Seq. Fw	AAGCAGCAAACAGCTTGTCC
SDC4 Seq. Rev	GACACGCGGTGAGTTAGAGG
AAVR Seq. Fw.	ACCTGTAGCCAAGAACCAGC
AAVR Seq. Rev	CAGGTATTGGGACTCTGCCC
ICAM1 Seq. Fw	TCCACATCGAAGGCAAAGTAT
ICAM1 Seq. Rev.	TCCAAGGATGTCCCCACCTG
SLC7A2 Seq. Fw.	CTGACTGCTCTGGGTCACTG
SLC7A2 Seq. Rev.	AGGGCTGCGATTTCTTCCAT

2.1.3.2 PCR Amplification

High Fidelity Phusion DNA polymerase (NEB) was used in all cloning. Phusion High-Fidelity Polymerase was supplied with:

5x Phusion HF buffer

10 mM dNTPs

Phusion HF Polymerase

2.1.3.3 Bacterial Transformation

Chemically competent cells were purchased from New England BioLabs (NEB):

5-alpha Competent E.coli

Stable Competent E.coli

2.1.3.4 Restriction Digest

Restriction Enzymes were purchase from New England BioLabs are listed in table 2.4.

Table 2.4: List of restriction enzymes and reaction buffer

Restriction Enzyme	**Reaction Buffer**	**Supplier**
NotI	Cutsmart	New England Biolabs
BbsI	Cutsmart	New England Biolabs
BsaI	Cutsmart	New England Biolabs
XhoI	Cutsmart	New England Biolabs
XbaI	Cutsmart	New England Biolabs
EagI	Cutsmart	New England Biolabs
SalI	Cutsmart	New England Biolabs
NheI	Cutsmart	New England Biolabs

2.1.3.5 Agarose Gel Electrophoresis and Gel Extraction

Tris Acetate EDTA (TAE) buffer:

Agarose

DNA was extracted from agarose gels using the Wizard SV Gel and PCR Clean Up gel extraction kit (Promgea). The reagents supplied were:

Membrane Binding Solution

Membrane Wash solution

2.1.3.6 Dephosphorylation of linearized plasmid DNA

10x Antarctic phosphatase buffer (NEB)

Antarctic Phosphatase (NEB)

Gel purified linearized vector

2.1.3.7 Ligation

Nuclease Free Water

2x Quick ligation buffer (NEB)

Quick T4 DNA ligase (NEB)

1:3 molar ration of plasmid to insert

2.1.4 Reagents for Mammalian cell culture

2.1.4.1 Mammalian cell culture

Dulbecco's Modified Eagles Medium (DMEM) with 4.5 g/L glucose supplemented with 10% (v/v) FBS (BioSera) and 1 mM Sodium Pyruvate

PBS

1x Trypsin-Versene (Lonza)

2.1.4.2 Mammalian cell lines

The mammalian cells lines purchased or generated in-house are listed in tables 2.5, 2.6 and 2.7.

Table 2.5: General Cell Lines - *A list of the cell lines which were used for this project.*

Cell Name:	Cell Line:	Provided by:
HEK293T	Embryonic Kidney Cells	SITraN
HeLa	Human Cervical Cancer	SITraN
N2A	Mouse Neuronal Cells	SITraN
NIH3T3	Mouse Embryonic Fibroblasts	SITraN
SHSY5Y	Neuroblastoma Cells	SITraN
1321N1	Astrocytoma Cells	SITraN
b.End5	Mouse Blood-Brain Barrier	SITraN

Table 2.6: CRISPR Cell Lines - *A list of the CRISPR cell lines purchased or generated which were used for this project.*

Cell Name:	Provided by:
HeLa - SDC4 CRISPR	In-House
HeLa – SLC7A2 CRISPR	In-House
HeLa – CRISPR Control	In-House
HeLa WT (AAVR isotype)	Prof Carrette (University of Stanford) (Pillay, Meyer et al. 2016)
HeLa AAVR-KO	Prof Carrette (University of Stanford) (Pillay, Meyer et al. 2016)
HeLa WT (ICAM1 isotype)	Abcam
HeLa ICAM1-KO	Abcam
SHSY5Y (SDC4 CRISPR)	In-House
SHSY5Y (AAVR CRISPR)	In-House
SHSY5Y (SLC7A2 CRISPR)	In-House

Table 2.7: Lentiviral Stable Cell Lines - *A list of the stable cell lines generated which were used for this project.*

Cell Name:	Provided by:
HeLa - Myc_SDC4	In-House
HeLa - HA_AAVR	In-House
HeLa - FLAG_ICAM1	In-House
HeLa - V5_SLC7A2	In-House
1321N1 - Myc_SDC4	In-House
1321N1 - HA_AAVR	In-House
1321N1 - FLAG_ICAM1	In-House
1321N1 - V5_SLC7A2	In-House

2.1.4.3 Transient DNA transfection

OptiMEM reduced serum media (Thermo Fisher)

Lipofectamine 2000 transfection reagent (Thermo Fisher)

Plasmid DNA

Polyethyleneimine (PEI) (stock 1 mg/ml) (Thermo Fisher)

2.1.4.4 siRNA transfection with Lipofectamine RNAiMax

OptiMEM reduced serum media

Lipofectamine RNAiMax transfection reagent (Thermo Fisher)

Nuclease Free water

siRNA pool (Dharmacon, Horizon Discovery and Sigma)

The sequences of the siRNA's used are listed in table 2.8

Table 2.8: siRNA products - *A list of the siRNA which were used for this project.*

siRNA:	Target Protein:	Sequences:	Provided by:
ON-TARGETplus Non-targeting Control siRNAs	Non-Targeted Control	UGGUUUACAUGUCGACUAA UGGUUUACAUGUUGUGUGA UGGUUUACAUGUUUUCUGA UGGUUUACAUGUUUUCCUA	Dharmacon
ON-TARGETplus Human SDC4 siRNA	SDC4	GAUCGGCCCUGAAGUUGUC GUGAGGAUGUGUCCAACAA GAAUCUCACCCGUUGAAGA UAGAGGAGAAUGAGGUUAU	Dharmacon
ON-TARGETplus Human KIAA0319L siRNA	AAVR	GUGAAUGACUCCAACGAAU AGGUAGUCCCAGUGACGUA GUGAGUGGAGCGUGUUAUA GGGAAGGCUAUGUGAACGU	Dharmacon
ON-TARGETplus Human ICAM1 siRNA	ICAM1	GGUAGCAGCCGCAGUCAUA GAGCCAAGGUGACGCUGAA CGGCUGACGUGUGCAGUAA GAAGAUAGCCAACCAAUGU	Dharmacon
ON-TARGETplus Human SLC7A2 siRNA	SLC7A2	GAGCAGAGCUGGUCAUCGU AAACAUUGAGAGAACGAAA GUAAAGAGGUUUCAUCUAU GGUAGGUGUUUAUUAAGCAA	Dharmacon
Human ICAM1 siRNA	ICAM1	GGAACAACCGGAAGGUGUA UACACCUUCCGGUUGUUCC	Sigma

2.1.4.5 CRISPR cell line generation

2.1.4.5.1 Transfection with AIO-Puro

Guide RNA sequences listed in Table 2.9 were cloned into AIO-Puro.

AIO-Puro containing gRNA's were transfected into mammalian cells with Lipofectamine 2000.

Table 2.9: Nickase CRISPR gRNA Sequences - *Nickase gRNAs designed for target protein knockout in vitro*

Sense/Antisense Targets	Sense Oligo	Antisense Oligo
SDC4 Sense gRNA	CCAGACGATGAGGATGTAGT	ACTACATCCTCATCGTCTGG
SDC4 Antisense gRNA	CGGAGAAGTATCGGCCTTCT	AGAAGGCCGATACTTCTCCG
ICAM1 Sense gRNA	GCCCGCGCTGCCCGCACTCC	GGAGTGCGGGCAGCGCGGGC
ICAM1 Antisense gRNA	GCTCGGGGCTCTGTTCCCAG	CTGGGAACAGAGCCCCGAGC

2.1.4.5.2 Ribonucleoprotein Electroporation of Cas9/gRNA

gRNAs, as listed in Table 2.10, and Cas9 were electroporated into mammalian cells using the Neon Transfection System (Invitrogen) and kit with reagents:

Alt-R V4 Cas9 Alt-RCas9 Electroporation Enhancer

Nuclease-Free IDT

Buffer R

Guide RNA's for use in RNP electroporation of Cas9/gRNA experiments are listed in Table 2.10.

Table 2.10: Ribonucleoprotein CRISPR gRNA Sequences - *RNP gRNAs designed for target protein knockout in vitro*

Guide RNA Target	5'-3' Sense
SDC4	CGGAGCCCTACCAGACGATG
	GACTGAGGTCATCGACCCCC
ICAM1	CAACTCCTTTTTAGGCAACG
	GCTATTCAAACTGCCCTGAT
AAVR	TATAGGTGTAACTACGTCAC
	AGTCAGACCACCTAATTCGT
SLC7A2	GGGCCCGTGTTCCCAAGACG
	ATCATTCTGACGTCTGACGA

2.1.4.5.3 DNA Extraction Kit

GenElute™ Mammalian Genomic DNA Miniprep Kit (Sigma) containing:

Resuspension Buffer

Lysis Solution T

Lysis Solution C

Column Preparation Solution

Wash Solution

Elution Solution

Proteinase K

RNAse A Solution

Binding Columns

2.1.5 General Biochemical reagents

2.1.5.1 Cell lysis

Radioimmunoprecipitation assay (RIPA) buffer:

50 mM Tris HCL ph 6.8, 150 mM NaCl, 1 mM EDTA, 1mM EGTA, 0.1% (w/v) SDS, 0.5% (w/v) deoxycholic acid, 1% (w/v) Triton X-100, 1x protease inhibitor cocktail (PIC) (ab271306)

5x Lamelli buffer:

250 mM Tris-HCL pH 6.8, 10% (w/v) SDS, 0.5% (w/v) Bromophenol blue, 50% (w/v) glycerol, 25% (v/v) Beta-mercaptoethanol

2.1.5.2 Tissue Lysis

Tissue Reporter Lysis Buffer:

1x Reporter Lysis Buffer (Promega) with 1x PIC (ab271306) and 1x phenylmethylsulphonyl fluoride (PMSF) protease inhibitor (Thermo Fisher).

2.1.5.3 BCA Assay

Pierce™ BCA Protein Assay Kit (Thermo Fisher):

Pierce™ BCA Reagent A

Pierce™ BCA Reagent B

2 mg/ml Bovine Serum Albumin (BSA)

2.1.5.4 Immunoprecipitation

BRB80 Lysis Buffer:

80 mM K-PIPES pH 6.8, 1 mM $MgCl_2$, 1 mM EDTA, 1% (v/v) NP40, 1 x Protease inhibitor cocktail,

Amersham Protein G-bead Mag agarose bead slurry (Scientific Laboratory Supplies)

2.1.5.5 SDS PAGE and Western blotting

2.1.5.5.1 SDS-PAGE

10, 12 and 15 well 4 – 20% (v/v) Mini-PROTEAN TGX Precast Protein gels (BioRad)

Running Buffer:

25 mM Tris, 192 mM glycine, 0.1% (w/v) SDS

2.1.5.5.2 Western blot

Transfer Buffer:

25 mM Tris, 192 mM Glycine, 20% (v/v) Methanol

Ponceau S:

5% (v/v) glacial acetic acid, 0.1% (w/v) Ponceau S

TBS-Tween (TBS-T):

0.1% (v/v) Tween-20 in TBS

Blocking Buffer:

0.1% (v/v) Tween-20 in TBS, 5% (w/v) dried milk powder

Enhanced Chemiluminescence (ECL) Reagent Kit (Bio-Rad):

Solution A (luminol solution)

Solution B (peroxide solution)

2.1.5.5.3 Antibodies

Table 2.11: ***Primary antibodies*** **-** *A list of the primary antibodies which were used for this project*

Antibody:	Company:	Concentration:	Species:	Catalogue Number:
SDC4	Genetex	1:500 (WB/IF)	Rabbit	GTX44511
SDC4	Abcam	1:500 (WB/IF)	Rabbit	ab24511
SDC4	Santa-Cruz	1:500 (WB/IF)	Mouse	sc-12766
AAVR	Abcam	1:1000 (WB/IF)	Mouse	ab105385
ICAM1	Abcam	1:500 (WB/IF)	Rabbit	ab53013
SLC7A2	Abcam	1:500 (WB/IF)	Rabbit	ab140831
Tubulin	Sigma	1:10,000 (WB)	Mouse	T9026
GAPDH	Cell Signalling	1:3,000 (WB)	Rabbit	2118S
Myc Tag	Cell Signalling	1:5,000 (WB) 1:500 (IF)	Mouse	2276
HA Tag	Sigma	1:5,000 (WB) 1:500 (IF)	Mouse	H9658
FLAG Tag	Sigma	1:5,000 (WB) 1:500 (IF)	Mouse	F1804
V5 Tag	Invitrogen	1:5,000 (WB) 1:500 (IF)	Mouse	R960-25
VP1/2/3	Progen	1:250 (WB)	Rabbit	61084

Table 2.12: *Secondary antibodies* *- A list of the secondary antibodies which were used for this project*

Antibody:	Company:	Concentration:	Species:	Catalogue Number:
Anti-Mouse IgG HRP	Invitrogen	1:5,000 (WB)	Goat	31430
Anti-Rabbit IgG HRP	Millipore	1:5,000 (WB)	Goat	12-348
Anti-Mouse Alexa 488	Invitrogen	1:500 (IF)	Goat	A28175
Anti-Rabbit Alexa 488	Invitrogen	1:500 (IF)	Donkey	A212206
Anti-Mouse Alexa 680 (Western	Jacksons Laboratory	1:50,000 (WB)	Donkey	715-655-150
Anti-Rabbit Alexa 790 (Western)	Jacksons Laboratory	1:50,000 (WB)	Donkey	711-625-152

2.1.5.6 RNA extraction and qPCR

2.1.5.6.1 RNA extraction

RNeasy Mini Kit (QIAGEN) containing:

RW1 Buffer

RPE Buffer

2.1.5.6.2 RT-qPCR

Superscript III reverse transcriptase kit (Invitrogen) containing:

Random Hexamers

10 mM Deoxynucleoside triphosphates (dNTPs)

Superscript III reverse transcriptase enzyme

0.1M DTT

5x Reaction Buffer

2.1.5.6.3 qPCR primer Design

qPCR primers were designed with cDNA target sequences, obtained via Ensembl software, which was incorporated into PrimerBlast program. PrimerBlast parameters included primer size of 20 bp, a PCR product between 100-200 bp, melting temperature to be optimally around 60 ^{o}C and to span from exon-exon junctions. 3 primer pairs generated from the program, optimally with a C-G lock, with a GC content below 60% and had low self-complementary risk were chosen, as listed in Table 2.13.

Table 2.13: Designed qPCR primers - *A list of the qPCR primers which were generated and used for this project.*

Primer	5'-3' Sequence
SDC4 mRNA Fw	GAGTCGCCGAGTCGATCC
SDC4 mRNA Rev	CCGGAGAAGTATCGGCCTTC
AAVR mRNA Fw	TGCAGGCCCAGATAAAGAGC
AAVR mRNA Rev	CTTGCAGCCCAGTCACAGTA
ICAM1 mRNA Fw	ACCATCTACAGCTTTCCGGC
ICAM1 mRNA Rev	GGACAATCCCTCTCGTCCAG
SLC7A2 mRNA Fw	CTGACCTTTGCCCGATGTCT
SLC7A2 mRNA Rev	GCAGCGGCATAATTTGGTGT
GAPDH mRNA Fw	CTGGTAAAGTGGATATTGTTGCCAT
GAPDH mRNA Rev	TGGAATCATATTGGAACATGTAAACC
GAPDH DNA Fw	GGTGAGACATTCTTGCTGGGGA
GAPDH DNA Rev	GATAGCCTAGGACTGGAGCGAG
mCherry DNA Fw	CACGAGTTCGAGATCGAGGG
mCherry DNA Rev	CAAGTAGTCGGGGATGTCGG
WPRE Fw Primer	CCCGTACGGCTTTCGTTTTC
WPRE Rev Primer	CAAACACAGAGCACACCACG
18S Fw	ATGGCCGTTCTTAGTTGGTG
18S Rev	CGCTGAGCCAGTCAGTGTAG

2.1.6 Microscopy

2.1.6.1 Immunofluorescence

Fixing solution:

3.7% (v/v) formaldehyde in PBS

Quenching solution:

50 mM NH_4CL in PBS

Permeabilization solution:

0.2% (v/v) Triton X-100 in PBS

Fluorescent mounting medium (Dako)

2.1.7 Lentiviral production

2.1.7.1 LV vector transfections with calcium chloride

2.5M Calcium Chloride:

2x HEPES Buffered Saline (HBS):

LV production plasmids listed in Table 2.14.

Table 2.14: Plasmids required for LV transfection

Plasmid:	Role:	Concentration (µg)
pCMV.delta8.2	Packaging	130
pRSV-REv	Packaging	30
pMD.G	Envelope	37.5
Vector Builder plasmid	Transgene	130

Gene of interest plasmids, to be packaged into LV are listed in Table 2.15

Table: 2.15: Viral vectors - *A list of the viral vectors which were generated and used for this project.*

Virus:	Produced:
scAAV9_GFP	Vector Builder
scAAV2_GFP	Vector Builder
AAV9_mCherry	Vector Builder
LV_GFP	Generated by Dr. Nelly Berreuta Ramirez and Dr. Eva Karyka
LV_Myc_SDC4	In-House
LV_HA_AAVR	In-House
LV_FLAG_ICAM1	In-House
LV_V5_SLC7A2	In-House

2.1.7.2 LV purification

0.45 µm filter

Beckman tubes (BECL343058)

1% BSA in PBS

2.2 Methods

2.2.1 General molecular biology

2.2.1.1 Bacterial culture

200 ng of plasmid DNA construct was added to 25 µl of DH5α/Stable3 E. coli strains (New England Biolabs, USA). This was left to incubate on ice for 30 minutes. Cells were transformed via heat shock by incubating the mixture at 42 ^{o}C for 30 secs in a heat block. The sample(s) were left on ice for 5 minutes. This was followed by the addition of 350 µl Super Optimal Broth with Catabolite repression (SOC) medium. Bacteria was left to grow for 1 hour at 37 ^{o}C in a shaking incubator. The bacteria were then plated on selective LB agar plates containing 50 µg/ml carbenicillin and left O/N at 37 ^{o}C. Resistant colonies were picked and added to 1 ml of LB broth supplemented with 50 µg/ml carbenicillin and left to grow and express the antibiotic resistant gene (located in the plasmid) in a shaking incubator at 37 ^{o}C for 7-8 hours. After this period of time, 100 µl of each sample was added to 5 ml of antibiotic supplemented LB broth. This was left to grow in a shaking incubator at 37 ^{o}C O/N. 500 µl of bacteria was added to 500 µl of 50% glycerol in a cryovial and organised in -80 storage while the rest of the bacteria was collected for DNA purification.

2.2.1.2 Purification of plasmid DNA

Bacteria was centrifuged at >8,000 rpm for 10 minutes to pellet cells. This was followed by resuspension 250 µl Buffer P1 and transferred to a microcentrifuge tube. 250 µl of Buffer P2 was added to lyse the cells and inverted four-six times for efficient lysis. 300 µl of Buffer N3 was added and inverted four-six times for efficient neutralisation of lysis. Samples were centrifuged at 13,000 rpm for 10 minutes to pellet debris and the 800 µl of supernatant was added to QIAprep spin columns and centrifuged for 60 seconds. 500 µl of Buffer PB was added to columns to wash the column and centrifuged. Flow through was removed and 750 µl of Buffer PE was added to the column and centrifuged again. Flow through was discarded and spin columns were centrifuged at 13,000 rpm for 2 minutes to remove any residual ethanol The spin column of each sample was removed and placed into a sterile 1.5 ml eppendorf and

50 µl of Buffer EB was added and left for 5 minutes before centrifugation and collection of elution.

2.2.1.3 Quantification of plasmid DNA

Purified DNA was measured using the nanodrop machine. 1 µl of elution buffer was used as a blank reading before 1 µl of experimental samples were analysed. The absorbance of DNA samples at 260 nm and 280 nm was recorded. Protein contaminants absorb at 280 and so the ratio of OD readings at 260 nm and 280 nm indicates purity of the sample (OD260/280). Pure DNA has an OD260/280 value of 1.8.

2.2.1.4 Agarose Gel Electrophoresis

Gels were made by boiling 1-2% agarose powder (w/v) in 1x Tris-acetate-EDTA (TAE) buffer. After boiling the dissolved agarose solution, it was supplemented with 0.5 – 2 µl of ethidium bromide and cast into a tray with the appropriate comb. This was left for 15 minutes and then placed into a submarine electrophoreses device filled with 1x TAE buffer. DNA samples were supplemented with 5x loading dye (Bioline, London) which were then loaded into wells and then were run at 100 v for 45 minutes. The gel was imaged by illumination UV light G-Box (Syngene, France). The gel was either removed or analysed on a UV illuminator (Spectroline, US) for gel excision.

2.2.2 Cloning AAVR, SDC4, ICAM1 and SLC7A2 into pCI-neo

2.2.2.1 PCR amplification of AAVR, SDC4, ICAM1 and SLC7A2

A 10 µl reaction mix of 5-50 ng of DNA template, 5x FIREpol Master Mix (Solis Boidyne, Estonia), 10 µM of forward and reverse primer (as listed in Table 2.13) and H_2O was made before undergoing a PCR program (Table 2.16). Amplified product was run on a 1-2.5% gel for gel electrophoresis (dependent on the size of the product) and analysed via the G-box. The PCR product was excised from the gel and then purified via Wizard SV Gel and PCR Clean Up gel extraction kit following manufacturer's instructions (Promgea).

Table 2.16: *Thermocycler conditions for PCR reaction*

Step:	Cycles:	Temperature (°C):	Time:
Initiation	1	95	2 minutes
Denaturing	35	96 (Denature)	10 seconds
		~65 (Annealing)	20 seconds
		72 (Extension)	10 seconds
Final Extension	1	72	10 minutes
Cooling	1	4	Hold

2.2.2.2 Restriction Digest

2 µg of plasmid DNA was digested with 20 units of appropriate restriction enzyme (list of restricted enzymes used listed in Table 2.4) and appropriate buffer (Cutsmart buffer, provided with the enzymes) in a total volume of 40-100 µl. This was left for 1 hour at 37 °C in a water bath. Digested DNA then undergoes agarose gel electrophoresis, as described in Section 1.2.1.4.

2.2.2.3 DNA Extraction

Two digested DNA extraction methods were used: (1.) Gel Extraction. 1x loading dye was added to samples which were run on an 1-2% agarose gel. The digested bands were excised via the use of a UV transilluminator (Spectroline) and the DNA was collected via the use of a Wizard SV Gel and PCR Clean Up gel extraction kit (Promgea, US) following manufacturer's instructions. Excised gel was incubated with 10 µl of membrane binding solution per 10 mg of agarose gel and incubated at 65 °C for until gel was completely dissolved. Dissolved gel mixture was transferred to a column and incubated at room temperature for 1 minute. Columns were centrifuged at 17,000 g for 1 minute and flowthrough was removed. 700 µl of Membrane Wash solution was added and centrifuged again. Flowthrough was removed and wash was repeated with 500 µl of Membrane Wash Solution and centrifuged for 5 minutes. Flowthrough was removed and the column was centrifuged again 2 minutes to remove

residual ethanol. Column was transferred to an eppendorf and 30 µl of nuclease free water was added for elution for 5 minutes before centrifuging the eluted DNA. Eluted DNA was nanodropped to quantify DNA concentration. (2.) Phenol-Chloroform Extraction. After digestion, the sample had 100 µl of phenol-chloroform added and then was centrifuged at 17,000 rpm for 15 minutes at 4 ^{o}C. The clear top layer was removed and an equal volume of 100% ethanol and (v/v) 0.5 M sodium acetate was supplemented. Samples were then left in -20 ^{o}C for 1-2 hours. These samples were then centrifuged down at 17,000 rpm for 20 minutes at 4 ^{o}C. Supernatant was removed and the DNA pellet was washed in 70% ethanol. After another 17,000 rpm centrifuge, the supernatant was removed and centrifuged again to make sure any excess is taken up. Pellets were dried for 5 minutes at 37 ^{o}C followed by adding 20 µl of EB buffer and was incubated the DNA in this solution at 37 ^{o}C for 5 minutes before nanodrop.

2.2.2.4 Dephosphorylation of linearized vector backbone

Following digestion of PCR products and vector backbone, 4 µl of 10x Antarctic Phosphatase reaction buffer and 1 µl of Antarctic Phosphatase was added to the 40 µl digestion reaction mix and left at 37 ^{o}C for 30 minutes. The samples are then incubated at 80 ^{o}C for 2 minutes for heat inactivation enabling effective ligation.

2.2.2.5 Ligation of AAVR, SDC4, ICAM1 and SLC7A2 digested products into pCI-neo

Following dephosphorylation, 50 ng of digested dephosphorylated plasmid was supplemented to a 3:1 ratio (calculated using the New England Biolabs, USA (NEB) Ligation calculator) of insert (or annealed oligonucleotides) with 0.5 µl of T4 Ligase (NEB) and appropriate buffer (provided with T4 ligase) in a total volume of 10 µl. This reaction was left for 30 minutes at RT before transformation in E. coli.

2.2.2.6 Transformation of NEB 5-alpha and NEB-stable competent cells

8.5 µl of ligated product was added to 25 µl of DH5α/Stable3 E. coli strains (NEB). This was left to incubate on ice for 30 minutes. Cells were transformed via heat shock by incubating the mixture at 42 ^{o}C for 30 secs in a heat block. The sample(s) were left on ice for 5 minutes.

This was followed by the addition of 350 µl Super Optimal Broth with Catabolite repression (SOC) medium. Bacteria was left to grow for 1 hour at 37 ^{o}C in a shaking incubator. The bacteria were then plated on selective LB agar plates containing 50 µg/ml carbenicillin and left O/N at 37 ^{o}C. Resistant colonies were picked and added to 1 ml of LB broth supplemented with 50 µg/ml carbenicillin and left to grow and express the antibiotic resistant gene (located in the plasmid) in a shaking incubator at 37 ^{o}C for 7-8 hours. After this period of time, 100 µl of each sample was added to 5 ml of supplemented LB broth. Different kits require different volumes of LB broth (Table 2.17). This was left to grow in a shaking incubator at 37 ^{o}C O/N. Plasmid DNA was collected following the QIAprep Spin Miniprep (Qiagen, Netherlands) following manufacturer's instructions. Samples were nanodropped for DNA concentration and purity.

Table 2.17: *Volumes of LB broth required for each QIAgen DNA kit*

Amount of DNA	**DNA Prep Kit**	**Volume of LB Broth (ml)**
<20 µg	Miniprep	5
>250 µg	Midiprep	50
>2500 µg	Megaprep	500

2.2.2.7 Plasmid Confirmation Digest

For ligated plasmids, once nanodropped, a diagnostic digest, as described in section 1.2.1.4., using the respective restriction enzymes used prior to ligation was conducted to validate the presence of an insert. This product was run and analysed on an agarose gel, as described in section 1.2.1.5. Once this confirmed successful integration (via the representation of a single digested band), the ligated plasmid was sent for Sanger Sequencing.

2.2.3 Cloning of CRSIPR gRNA into AIO_puro

2.2.3.1 gRNA Annealing

The gRNAs were ordered as single-stranded oligonucleotides (Table 2.9) which were then annealed following the Addgene Zhang Lab protocol (available at: https://www.addgene.org/crispr/zhang/).

Table 2.18: *Reaction mix for annealing of sense and antisense oligonucleotides*

Reagent	Volume (µl)
Oligo Sense	1 (100 µM)
Oligo Antisense	1 (100 µM)
10x T4 Ligation Buffer	1
T4 PNK	0.5
H_2O	6.5
Total	10

Table 2.19: *PCR steps for gRNA annealing*

Temperature Steps (^oC):	Time (Minutes)
37	30
95	5
25	5^0C/min

2.2.3.2 Digestion and Ligation into AIO_puro

Once annealed, the AIO_puro vector was digested with *BsaI (*for the sense gRNA scaffolding site) and *BsbI* (for the antisense gRNA scaffolding site). These digested products then underwent DNA extraction and ligation, as describe in section 1.2.1.4. and 1.2.1.5 before confirmation digest. Due to *BbsI* and *BsaI* destroying their restriction sites upon ligation, a confirmation digest of the constructs was conducted in which non-linearised plasmids were positive for gRNA integration, as shown in Figure 2.1 in samples #2, #3 and #7.

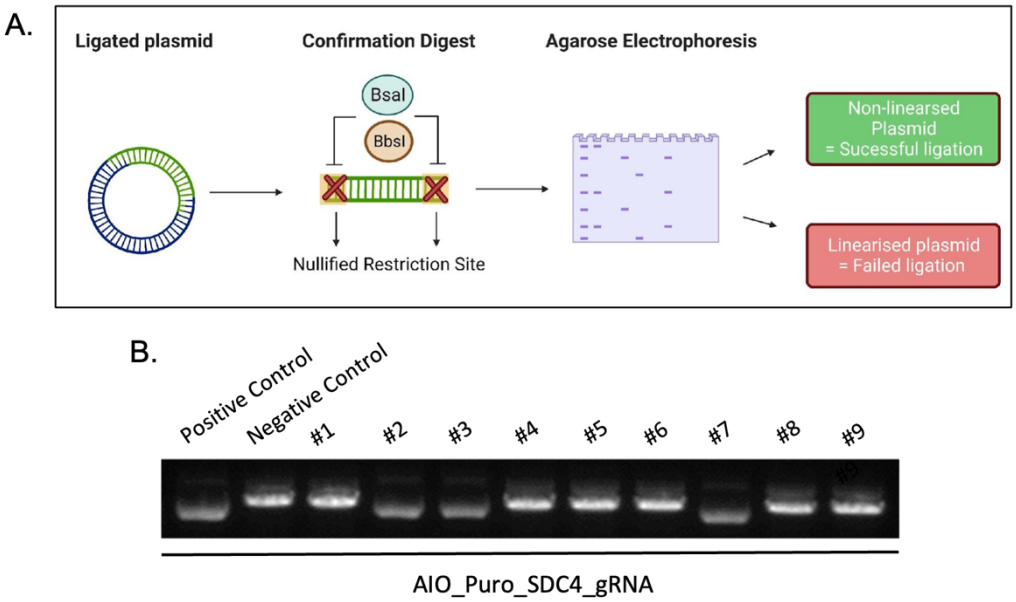

Figure 2.1: ***Generation of AIO_puro_SDC4 CRISPR constructs*** *– (A) Model of the validation experiment due to nullified restriction site from successful ligation. (B) DNA of AIO_puro_SDC4 colonies was digested with BbsI and BsaI and run on a 1% agarose gel.*

2.2.4 Mammalian cell culture and transfection

2.2.4.1 Cell Culture and Maintenance

Immortalised cell lines were cultured in Dulbecco's modified Eagle's medium (DMEM, Sigma) supplemented with 10% FBS (BioSera) and 1% penicillin streptomycin (Lonza), referred to as complete-DMEM. Cells were maintained at 37 ^{o}C in a 5% CO_2 atmosphere. Upon reaching 80-100% confluency, cells were passaged. Cells were washed once in PBS before incubation with

1x trypsin or 5 mM EDTA:PBS for 5 minutes at 37^{o}C. Cells were agitated and quenched with complete-DMEM. Following trituration, the cell suspension was split to new flasks and vessels for further culture and experimentation.

2.2.4.2 Plasmid DNA transfection

Cells were transfected with plasmid DNA using Polyethyleneimine (PEI) (stock 1 mg/ml) (provided by SITraN) at a 1:3 weight ratio (DNA:PEI) or Lipofectamine 2000 transfection reagent at 1:2 weight ratio in serum-free media (SFM) (DMEM without FBS added). Concentrations and volumes are listed in Table 2.20. Transfection reagent (PEI or Lipofectamine 2000) volume was diluted in serum-free media (SFM) and incubated for 5 minutes at room temperature, referred to as Mix A. Plasmid DNA was diluted in SFM, referred to as Mix B. After the incubation period, Mix A and Mix B are combined and vortexed. The transfection solution was incubated at room temperature for 15-20 minutes before being added dropwise to the 70% confluent cells. After 6 hours, the media was replaced. Cells were kept at 37 ^{o}C in a 5% CO_2 atmosphere for 24 hours post transfection before cells were harvested for downstream analysis.

Table 2.20: PEI and Lipofectamine 2000 - *Transfection volumes and quantities for DNA delivery to cells of PEI (1:3* µg/ µl) *and Lipofectamine (1:2* µg/ µl)

Plate	DNA (µg)	PEI (µl)	Serum-free media (µl)
6-well	2	6	200
12-well	1	3	100
24-well	0.5	1.5	50

Plate	DNA (µg)	Lipofectamine 2000 (µl)	Serum-free media (µl)
6-well	2	4	100
12-well	1	2	50
24-well	0.5	1	25

2.2.4.3 siRNA transfection with Lipofectamine RNAiMax

Cells were transfected with siRNA for 4 days using Lipofectamine RNAiMax transfection reagent according to manufacturer's instructions. At day 0 cells were seeded such that they would be 100% confluent 4 days post transfection. 24 h after seeding cells were transfected as detailed in Table 2.21 below.

Table 2.21: siRNA Transfection - *Transfection volumes and quantities for siRNA delivery to cells with RNAiMAX*

Plate	siRNA (µM)	RNAiMAX (µM)	Serum-free media (µl)
6-well	2	6	200
12-well	1	3	100
24-well	0.5	1.5	50

Lipofectamine RNAiMax was diluted in serum-free media (Mix A) and incubated for 5 minutes at room temperature. During this incubation, the correct volume of siRNA was diluted separately and added to serum-free media (Mix B). After incubation, Mix A was combined with Mix B and vortexed before a 20 minute incubation period at room temperature. Transfection mixes were then added dropwise to cells. After 6-hours, the media was replaced and the cells were left at 37 ^{o}C in 5% CO2 atmosphere for 4 days before harvesting for downstream experimentation and analysis.

2.2.4.4 CRISPR Cell Line Generation and Maintenance

2.2.4.4.1 Design of gRNA's for CRISPR Knockout

The sequence for human target genes were found on the Ensembl database and used the Breaking-Cas software for selection of sense and antisense guides (available at: http://bioinfogp.cnb.csic.es/tools/breakingcas/) (Table 2.9). Guides designed for ribonucleoprotein CRISPR were generated in the web tool CRISPOR (available at: http://crispor.tefor.net) (Table 2.10).

2.2.4.4.2 Generation of CRISPR edited cells via AIO_Puro transfection

Cells were seeded into a 6-well plate and left for overnight at 37^{o}C. As cells reached 70-80% confluence they were transfected with 2 µg of AIO-Puro DNA plasmid using Lipofectamine 2000 transfection reagent, as described in section 2.2.4.2. 24 h post transfection cells were lifted and replated in complete-DMEM supplemented with 3 µg/ml of puromycin. Once the negative control wells were completely killed and clear of surviving cells, the transfected wells containing puromycin-resistant cells were collected via trypsinisation and counted via haemocytometer. 4.0 x 10^3 of these resistant cells in 200 µl of complete-DMEM media were seeded in well A1 of 96-well plate and serially diluted 1:2 down the column. The first column (rows A-H) was then serial diluted 1:2 across the plate from column 1-12 in order to produce single colony wells. 100 µl of cell solution in well A4 (approximately 100 cells) was then mixed in 10ml of complete DMEM before re-plating on a fresh 96-well plate (100 µl/well). This limiting dilution was effectively equal to less than 1 cell per well increasing the chance of

obtaining single colony wells. These 96-well plates were incubated at 37 ^{o}C for 1-5 days. After this period of time, single colonies were labelled and after 7-10 days, all confluent single colonies were collected and moved into a 6-well plate containing complete-DMEM. Cells were left to grow until confluent and were expanded into T25 and T75 flasks before screening.

2.2.4.4.3 Ribonucleoprotein electroporation Cas9/gRNA Transfection

For the transfection of gRNAs and Cas9 in the generation of CRISPR cell lines, electroporation was performed using the Neon Transfection System (Invitrogen) according to the manufacturer's instructions. Neon tube was filled with 3 ml of electrolytic buffer and placed into the Neon Pipette Station. CRISPR-Cas9 ribonucleoproteins were formed by complexing 240 ng of gRNA duplex with 1250 ng Alt-R V4 Cas9 protein (IDT) in 10 µl of Buffer R at a 1:1 molar ration for 10 minutes. Confluent cells were harvested, as described in section 2.2.4.1. and washed with PBS followed by centrifugation at 400 xg for 4 minutes at RT. 1 x 10^5 of cells were aliquoted and centrifuged before being resuspended with Buffer R containing Cas9 and gRNA duplexes. 10 µl of this mixture was loaded into a Neon transfection system and electroporated according to manufacturer's instructions at 2 pulses at 1200 V with pulse widths of 20ms. Following electroporation, cells were seeded into a well of a 6-well containing pre-warmed DMEM media (10% FBS) and was incubated at 37 ^{o}C/5% CO_2. Once expanded, the cells were single seeded as described previously in Section 2.2.5.4.2.

2.2.4.4.4 Determining CRISPR Editing Efficiency

Genomic DNA was extracted from the CRISPR edited cells via the Sigma Mammalian DNA Miniprep Kit (Sigma) according to manufacturer's instructions. Pelleted cells are resuspended with the 200 µl Resuspension Buffer and 20 µl of RNAse A solution which was incubated at room temperature for 2 minutes. Following this, 20 µl of Proteinase K was added to the sample before adding 200 of Lysis Solution C and vortexed for 15 seconds. Solution was incubated at 70 ^{o}C for 10 minutes. During this incubation period, the binding columns were prepared by adding 500 µl of the Column Preparation Solution and centrifuged at 12,000 g for 1 minute. Flowthrough was removed. 200 µl of 100% ethanol was added to the samples

and vortexed for 10 seconds. The sample volume was added to the prepared columns and centrifuged at 6,500 g for 1 minute. Flowthrough was discarded and 500 µl of Wash Solution (previously diluted with ethanol) was added to the columns and centrifuged. The second wash step has an extended centrifugation for 3 minutes at 17,000 g. Flowthrough was removed and columns underwent an additional spin for.1 minute at 17,000g to remove any residual ethanol. Columns were transferred to an eppendorf and 200 µl of elution buffer was added to the binding column and left for 5 minutes at room temperature before final centrifugation. DNA was quantified via a nanodrop. 50 ng of DNA underwent a PCR with designed primers, as listed in Table 2.3, across the Cas9 cut site for each target . Amplified PCR product was validated via gel electrophoresis and the product was then cleaned via Wizard SV Gel and PCR Clean Up gel extraction kit following manufacturer's instructions (Promgea). Eluted product was sent off for sanger sequencing (Eurofins, Germany). Sequencing trace files were uploaded to Synthego ICE (available at: https://www.synthego.com/products/bioinformatics/crispr-analysis) to confirm indel.

2.2.4.4.5 Flow Cytometry Single Cell Sorting

Cells were lifted and centrifuged at 400 xg for 4 minutes to pellet cells. Cell pellet was washed 3 times in 1x PBS and re-centrifuged prior to being suspended in 500 µl of PBS. Suspended cells were transported to the Flow Cytometry department and single seeded into each well of a 96-well (I would like to thank the University of Sheffield Flow Group and Dr. Susan Clark for her assistance in this process).

2.2.5 General Biochemistry

2.2.5.1 Cell lysis

For protein extraction, cells were collected following dissociation and then centrifuged at 400 x g for 5 minutes. After a wash in 1x PBS and re-pelleting at 400 xg, the cells were lysed in radioimmunoprecipitation (RIPA) lysis buffer for 1 hour on ice. These samples were pelleted

at 17,000 x g for 20 minutes and the lysis supernatant was collected prior to protein quantification.

2.2.5.2 BCA assay

Pierce™ BCA Protein Assay Kit (Thermofisher, Catalogue number: 23227) was used as a protein quantification assay following the manufacturer's instructions. The standard curve was made (following the concentrations detailed in Table 2.22) to create a linear regression fit.

Table 2.22: BCA Standard Curve volumes

BSA (µg/ml)	Volume of BSA (µl)	Volume of PBS (µl)
2	50	0
1.5	37.5	12.5
1	25	25
0.75	18.8	31.2
0.5	12.5	37.5
0.25	6.3	43.7
0.125	3.1	46.9
0	0	50

Each BSA concentration had two replicates in a 96-well plate. The pre-cleared cellular lysate was diluted 1:10 in 1x PBS it was added in a 96-well plate in duplicate. 50:1 ratio of Reagent A and B, respectively, were mixed together at a volume which was suitable for 200 µl per well. Once the reagent solution was added to each well, this was then left for 30 minutes in the dark at 37 ^{o}C. The plate was then analysed via a Pherastar microplate reader (BMG Labtech, Germany) at 560 nm. A stock of 2-4 µg/µl of pre-cleared protein lysate was generated with 1x laemmli loading dye t and ddH_2O added. Samples were placed in a 95 ^{o}C heat block for 5 minutes to denature sample(s).

2.2.5.3 Immunoprecipitation

For each condition, a 10-cm^2 was used. Cells were dissociated via 5 mM EDTA-PBS and pelleted at 400 *g* for 4 minutes. Pellets were then washed in 1x PBS. Cells were lysed at 4 ^oC for 1 hour in cold BRB80 lysis buffer. Lysate was centrifuged at 15,000 *g* for 30 minutes at 4 ^oC. Supernatant protein concentration was measured via a BCA assay (section 2.19). 2 mg of supernatant was diluted in a total volume of 500 µl of BRB80 buffer and 3.1 x 10^{11} was added to the solution for viral capsid disassembly and rotated for 2 hours at 4 ^oC. 120 µg of protein was kept as an input sample with 5x lamelli buffer and boiled for 5 minutes. The rest of the protein was then incubated with 2 µg of primary antibody for 16 hours rotating at 4 ^oC. 10 µl of 50% magnetic G-Sepharose bead slurry (Sigma, US) was added to each sample for 2 hours at 4 ^oC while rotating the samples to capture the antibodies. Using a magnetic eppendorf holder, flow through was collected and beads were washed with cold BRB80 lysis buffer five times. After the final wash, the remaining BRB80 buffer was removed and the proteins were eluted from the G-beads in 2x lamelli buffer and boiled at 95 ^oC for 5 minutes. The eluted samples were then analysed via SDS-PAGE and immunoblot. Nitrocellulose membranes were imaged via the Licor system.

2.2.5.4 SDS-PAGE and Western blot

2.2.5.4.1 SDS-PAGE

The 4-20% Mini-PROTEAN TGX precast gel cassette (Bio-rad, California) was clamped into a chamber and placed into a tank filled with 1x Tris-Glycine SDS-PAGE (TGS) running buffer which was added to the recommended volume on the tank. 5 µl pre-stained protein ladder (Abcam) comprising of pre-stained proteins of 11kDa – 245 kDa was used to determine molecular weights of proteins of interest. Each protein-laemmli sample was added to each well of the pre-made gel and ran at 150 v between 1-2 hours until the loaded solution(s) had run to the end.

2.2.5.4.2 Western blot

After SDS-PAGE, proteins were transferred from the gel onto PVDF membranes (pre-activated in 100% methanol) or nitrocellulose membranes using the Criterion®™ blotting system (BioRad). Cassettes were fully submerged 1x Transfer Buffer (20% methanol, 20% Tris-base with ddH_2O) and proteins transferred at 100 V for 30 minutes or over-night at 30 V. After transfer membranes were stained Ponceau S solution (0.1% Ponceau S, 5% acetic acid) to determine efficient transfer and allow trimming of the membrane. Membrane were blocked 5% blocking buffer (non-fat milk in 1x TBS supplemented with 0.1% Tween-20 (TBS-T)) for 1 hour at room temperature (RT). After blocking, the membrane was incubated with primary antibody at the recommended concentration (Table 2.11) in blocking buffer O/N on a haematology mixer at 4 ^{o}C. The membrane was then washed three times in 1x TBS-T for 10 minutes per wash. The membrane was then incubated with secondary antibody at the recommended concentration (Table 2.12) with TBS-T for 1 hour at RT. After a final wash, the signal was developed using Pierce™ ECL Western Blotting Substrate (Thermofisher Scientific, UK) following the manufacturer's instructions, membranes were incubated in the ECL solution for 3 minutes prior to imaging using a G-Box Imaging System (Syngene).

2.2.5.4.3 Densitometry analysis of Western blots

Blots were quantified using ImageJ. A region of interest was drawn around the signal and a histogram constructed using the plot lanes tool. The area under the histogram was indicated density of the band and therefore level of the protein. Data was normalised to the loading control.

2.2.5.5 RNA extraction and cDNA synthesis

RNA was extracted from pelleted cells via the use of the RNeasy Mini Kit (Qiagen) following the manufacturer's instructions. Cells were resuspended in 350 µl of Buffer RLT and vortexed for 5 seconds. An equal volume of 70% ethanol was added to the sample and vortexed again for 5 seconds. 700 µl of sample was added to the columns provided and centrifuged at 8,000 g for 15 seconds. Flowthrough was removed and 500 µl of Buffer RPE was added and centrifuged. This wash was repeated once more and centrifuged for 2 minutes. Flowthrough

was removed and the spin column was centrifuged again for 2 minutes at 17,000 g to remove any residual ethanol. 30 µl of nuclease-free water was added to the membrane of the column and left for 5 minutes prior to centrifugation and elution of RNA. RNA was quantified via nanodrop analysis to measure RNA concentration and purity. Extracted RNA was reverse transcribed into cDNA using Superscript III reverse transcriptase (Invitrogen) following manufactures instructions. 2 µg of RNA was incubated with a range of reagents (Table 2.23).

Table 2.23: *Reaction mix for stage one of cDNA synthesis*

Reagent	Volume (µl)
2 µg RNA	*a*
50 ng/µl Random Hexamers	1
10 mM dNTPs	1
DEPC-treated H_2O	<13
Total	13

This solution was then incubated at 70 ^{o}C for 5 minutes before leaving on ice for at least 1 minute. A cDNA mastermix was then added to each RNA solution (Table 2.24). 7 µl of mastermix was added to each RNA solution and vortexed for 5 seconds. The reaction was run on a thermocycler according to the parameters in Table 2.25.

Table 2.24: *Master mix for stage two of cDNA synthesis*

Reagents:	Volume (µl)
5x Buffer	4
0.1 mM DTT	2
200 U/µl SuperScript III RT	1
Total	7
Total (with first step)	20

Table 2.25: *Thermocycler conditions for cDNA synthesis*

Temperature Steps (°C):	Time (Minutes)
25	10
50	50
85	5

2.2.5.6 Quantitative Polymerase Chain Reaction (qPCR)

A qPCR was performed using the CFX96 Real-Time System (Bio-rad). 9 µl of mastemix (Table 2.26) was added for each replicate and 1 µl of stock cDNA (2 µg) was added to each replicate. Samples were amplified in triplicate in 10 µl volumes. Cycling conditions for qPCR were as follows in the Table 2.27. Levels of mRNA were quantified relative to housekeeping gene mRNA levels according to the ΔΔCt method (Livak and Schmittgen 2001).

Table 2.26: *qPCR Mastermix per well*

Component :	Volume (µl):
Forward Primer (5mM)	1
Reverse Primer (5mM)	1
ddH_2O	2
2x SYBR	5
Total	9
Total (with cDNA)	10

Table 2.27: *Thermocycler conditions for qPCR analysis*

Step:	Temperature (°C):	Cycles:	Time:
Initiation	95	1	10 minutes
PCR	96 (Denature)		30 seconds
	65 (Annealing)	39	1 minute
	72 (Extension)		10 seconds
Melt curve analysis	95	1	1 minute
Melt curve analysis	60	1	5 seconds
Melt curve analysis	Ramp	1	(+0.5°C/5s)
Melt curve analysis	95	1	
Storage	10	-	Hold

2.2.5.6.1 Primer Optimisation

Primers (at a stock concentration of 100 µM) were diluted to make 1 µM, 0.5 µM, 0.25 µM, and 0.125 µM in the final 10 µl reaction mix with 10 ng of wild-type HeLa cDNA. This reaction was run according to the parameters in Table 2.16. The PCR products were run on a 2.5% gel agarose gel to observe a clear product of the correct size and that no primer dimers were formed during the cycle.

Following this, the optimal primer concentration identified previously, the standard curve of the primer was checked to ensure the amplification of the product was linear across a range of cDNA concentrations. The standard curve was generated by diluting the 2 µg stock of cDNA from 2000 ng – 0.128 ng (assuming 100% conversion during cDNA production). These samples were run in duplicate and with a no-template control for each reaction. These reactions were run on the thermocycler program outlined in Table 2.27.

2.2.6 Lentiviral production and purification

2.2.6.1 LV plasmid transfection with calcium chloride

HEK293T/T17 cells were used for lentiviral production. 10 x 10 cm^2 dishes were seeded with 3 x 10^6 cells per dish in DMEM-Complete media. After 24 hours, the cells were transfected with a calcium chloride ($CaCl_2$) mix containing the four lentiviral component plasmids (Table 2.14), 0.5 M calcium chloride and 2x HBS.

5 ml of 0.5 M $CaCL_2$ was added to 5 ml of the DNA mixture dropwise. Following this, 10 ml of 2x HBS was then aerated continuously while adding the DNA-$CaCl_2$ solution in a dropwise manner. This was then left at room temperature for 10 minutes which resulted in white precipitate to form over time in the solution. 1 ml of this mixture was then added to each 10 cm dish dropwise. Plates were then incubated overnight before changing media. The plates were then incubated at 37 ^oC for an additional 48 hours. Three days post transfection the media containing the virus was pooled into a T175 flask and filtered using a 0.45 µM filter on a 50 ml syringe. This filtered media was then split equally across 6 Beckman tubes and spun at 19,000 x rpm for 90 minutes at 4 ^oC in a Beckman Ultracentrifuge using a SW-28 rotor. After this spin, supernatant was discarded, and each pellet was resuspended with 280 µl of 1% BSA in PBS and left for 1 hour on ice before combining into one tube. Tubes were thoroughly mixed and then aliquoted for storage at -80 ^oC.

2.2.6.2 Lentiviral Titration

HEK293T/T17 were transduced with set volumes of a control virus whose titre was known by fluorescence activated cell sorting (FACs) (LV-GFP produced by Dr. Nelly Berreuta Ramirez and Dr. Eva Karyka; titre of 4.71 x 10^8 TU/ml) compared to the viruses made in the previous step. Dilution of control virus and newly generated viruses were – 1:50, 1:100 and 1:200. Media was changed after 6 hours after transduction. After 72 hours, cells were harvested and genomic DNA was extracted. Titre of the virus was analysed by qPCR using a woodchuck hepatitis virus post transcriptional regulatory element (WPRE) primer for lentiviral quantification and a housekeeping 18S control primer to enable normalisation of results. Relative gene expression values were quantified using the ΔΔCt method and the titre was calculated by comparing the expression levels relative to that of the known virus (LV-GFP).

Lentiviral multiplicity of infection (MOI) dosage was confirmed through immunocytochemistry.

2.2.6.3 LV Transduction and Generation of Stable Cell Lines

Cells were seeded at 1 x 10^5 and left for 6-hours for cell adhesion in a 6-well plate. Cells were then transduced at an optimised MOI (1-20 vg/cell) with lentiviral vectors and left at 37^{o}C for 48-hours. Transduced cells were selected in 3 µg/ml puromycin containing complete-DMEM until non-transduced control cells were completely killed and no surviving cells remained. Once confluent, puromycin resistant transduced cells were moved to a T75 with puromycin-DMEM. When confluent, cells were harvested for characterisation via immunoblot and immunofluorescence.

2.2.6.4 Viral Transduction Efficiency Assay

Cells were seeded in a black 96-well Phenoplate (PerkinElmer) at 5 x 10^3 - 1 x 10^4 (depending on cells growth rate) and left for 6-hours for cell adhesion. Virus was added to DMEM media at desired MOI titres and added to cells before desired incubation period (24-hours or 48-hours). Once confluent, the media was removed and 4% of formaldehyde with 1:10,00 hoechst was gently added and left for 15 minutes. Formaldehyde was removed and 200 µl of 1x PBS was added to each well before imaging via the Incell.

2.2.6.5 Viral Internalisation Assay

Cells were seeded at 5 x 10^5 cells per well on a 6-well plate and left for 24-hours at 37^{o}C and 5% CO_2. The AAV9_mCherry was suspended in complete-DMEM at an MOI of 5000 and was added to cells via a drop-wise manner and left for another 24-hours. Following this, cells were dissociated with trypsin to remove any surface bound virions and the cells were washed four timers with PBS and centrifuged at 500 xg, After the final wash and centrifugation, the Sigma DNA Isolation Kit was used per manufacturer's instructions. Once collected, the DNA was quantified via nanodrop to validate purity and DNA concentration. A stock dilution of 2 µg of DNA was generated to be used in quantitative PCR, as described in section 2.21, using the

primers mCherry and GAPDH DNA. Levels of DNA were quantified relative to GAPDH DNA levels according to the ΔΔCt method.

2.2.7 Microscopy

2.2.7.1 Immunofluorescence Confocal Microscopy

Cells were grown and fixed on glass coverslips in a 24-well plate. At optimal confluency, media was removed and 4% paraformaldehyde was added for 15 minutes at RT. These wells are then washed 3 times with 1x PBS. The paraformaldehyde was quenched via the addition of 50 mM ammoniochloride for 15 minutes at RT, followed by another round of washing. To permeabilise the cells, 0.2% Triton X-100 was added and left for 3 minutes, followed by its removal and another round of washing. Blocking occurred via the addition of 3% BSA for 1 hour at RT. After another wash, the primary antibody was added in 3% BSA at the recommended concentration and kept O/N on the fixed slides at 4 ^{o}C. Following another round of washing, the coverslips were incubated with secondary antibody at the recommended concentration in 3% BSA for 1 hour at RT. After another wash, the cells were then incubated in Hoechst staining (1:10,000) for 5 minutes before requiring a final set of washes. The coverslips were then mounted using fluorescence mounting medium (Dako, US) and analysed using the Leica SP5 confocal microscope. Slides were imaged with the Leica software in which cells volume was estimated via locking the nuclear signal into the program and selecting a Z-stack of 12 layers through the field of cells. Once done, using a FITC and DAPI channel, the program imaged the field of view through each Z-stack for each channel. Once complete, the image was exported into Fiji imaging software and analysed in max projection (all stacks quashed).

2.2.7.2 Opera Phenix Imaging

Following Section 2.2.7.1., cells seeded in Greiner 96-well culture plates were visualised within a high-resolution Z-stack of 10 layers consisting of images at 0.5 µm intervals through the entire nuclear volume of the cell. Per well, 10-fields of view were imaged at a 100 µm magnification for DAPI filter (exposure of 0.240 seconds) to detect nuclear staining and FITC

filter (at an exposure of 0.300 seconds) to detect 488 signals. Once confirming clarity of image per field of view across the plate, the imaging program was run. Once complete, the data was uploaded to Columbus software for analysis, as shown in Figure 2.2.

2.2.7.3 Incell Imaging

Following Section 2.2.7.1., the Greiner 96-well plate was imaged in the Incell machine. Per well, 10-fields of view were imaged at a magnification of 200 µm for DAPI filter (exposure of 0.240 seconds) to detect nuclear staining and FITC filter (at an exposure of 0.300 seconds) to detect GFP signal. Once confirming clarity of image per field of view across the plate, the imaging program was run. Once complete, the data was uploaded to Columbus software for analysis, as shown in Section 2.2.10.

2.2.8 In Vivo Tissue Preparation

2.2.8.1 Sample Collection

C57BL/6 mice were bred and were sacrificed at the ages required for our age study (postnatal (p) 5, p15 and p45). The brain, spine and liver tissue were collected by our technical team (I would like to thank Mr. Ian Coldicott for his assistance in maintaining the mice and collecting the tissue when necessary). Once extracted, tissue was kept at -80 ^{o}C till protein extraction was required.

2.2.8.2 Tissue Protein Extraction

Homogeniser screw-closed tubes (Precellys) were filled with 10 homogeniser beads (Precellys) and filled with 250-700 µl (dependent on density of tissue, as shown in Table 2.28) of tissue lysis buffer (as listed in section 2.1.5.2). Samples were homogenised (as listed in Table 2.29) and the supernatant was removed and protein quantification was achieved by BCA (as described in section 2.2.5.2.) followed by Western Blot analysis (as described in section 2.2.5.4.)

Table 2.28: *Table of tissue sizes and volume of lysis buffer required for protein extraction.*

p2 Tissue Size:	Volume of Lysis Buffer (µl):
Full spinal cord	200
½ brain	350
Full liver	250
p15/45 Tissue Size:	Volume of Lysis Buffer (µl):
½ spinal cord	250
½ brain	600
¼ liver	500

Table 2.29: *Tissue homogenising program and steps prior to protein extraction.*

Step:	Time:
Homogenise at 5,500 rpm	20 seconds (x2)
Leave at 4 °C	10 minutes
Homogenise at 5,500 rpm	20 seconds (x2)
Centrifuge at 17,000 xg at 4 °C	10 minutes
Remove supernatant	-

2.2.9 Equipment List

Table 2.30: *Table of equipment used in this project*

Equipment :	**Manufacturer:**
Nanodrop 1000	LabTech
G.Box Gel Imaging Machine	SynGene
Pherastate Plate Reader	BMG LabTech
PCR Machine	G-Storm
CFX96 RealTime System C1000 Touch Thermal Cycler	Bio-Rad
Confocal Microscope	Leica SPS Microscope System
OPERA PHENix High Throughput Imaging System	Perkin-Elmer
Optima L-100K Ultracentrifuge	Beckmann Coulter
In Cell Analyser 2200	GB Healthcare
Tissue Homogeniser	Precellys

2.2.10. Statistical Analysis

Three biological repeats were attempted with each experiment and referred to as N=3 in figure legends. Calculations of data from experiments was performed using Excel (Microsoft Corporation, Redmond, WA) and Prism 6 software (GraphPad Software Inc., San Diego, CA). A two-tailed t-tail test was conducted to determine significance of two experimental conditions. An ANOVA test was conducted to determine significance of three or more experimental conditions. Following ANOVA analysis, a Tukey post-hoc test was conducted to determine significance of differences between pairs of group means.

Columbus software was used to quantify GFP positive cells using a designed program (Figure 2.2). At maximum projection, the program had a selected method to outline and quantify the nuclei of cells via Hoechst/DAPI staining and a selected method was chosen for the outline of the cytoplasm. Once confirmed that the nuclei and cytoplasm were accurately selected, the region of quantification was selected as the cytoplasmic region. Intensity properties were selected for the FITC filter to detect GFP signal and the population of selected cells was nuclei with the region of quantification being the cytoplasm. Finally, the FITC mean intensity quantification for population selection was optimised so that background signal could not be detected. Following this, the program was run and number of GFP positive cells was quantified.

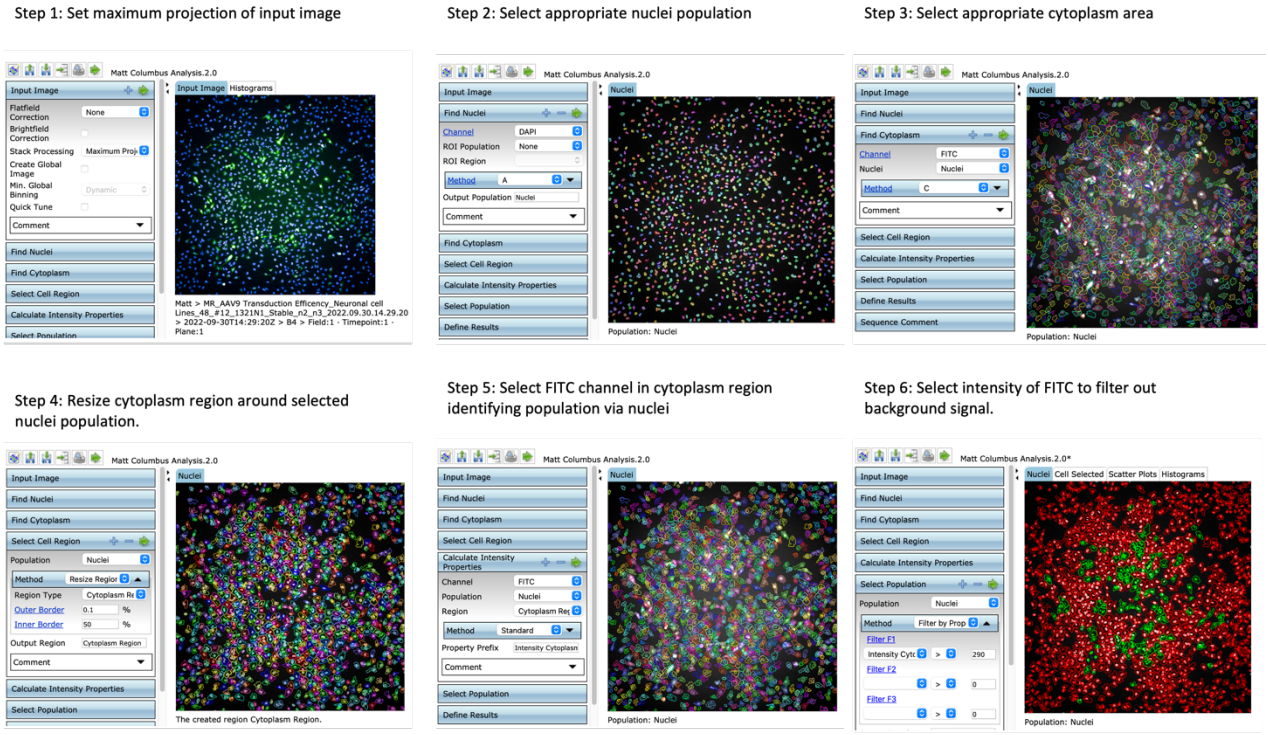

Figure 2.2: ***Columbus workflow to identify GFP positive cells*** *– Once uploaded to Columbus, the selected well had maximum projection selected followed by nuclei and cytoplasm filter selection methods. Once the most appropriate regions was selected and FITC intensity was chosen (based on removal of FITC background signal detected in the control wells), the program selected positive cells (green signal). Cells below intensity selected were selected as negative (red signal). Once this was confirmed, the program ran through the entire plate with each field in each well. Data was exported into an excel spreadsheet for data analysis.*

3 Characterisation of potential AAV9 receptor proteins

3.1 Introduction

AAV tropism is dependent on cell surface protein and glycan interactions with the viral capsid (Bell, Vandenberghe et al. 2011). These events enable the virus to anchor to the plasma membrane of target cells which stimulates the hijacking of a cellular internalisation pathway (Tosolini and Sleigh 2020). Differences in capsid shape and protein sequence between AAV serotypes leads to differences in cell surface protein and glycan interactions. The differences in protein and glycan specificity between serotypes, means each capsid has varied, and somewhat unique, cellular and tissue tropism (Li and Samulski 2020). This broad range of tropism makes the AAV family of viral vectors highly advantageous for therapeutic approaches. AAV9 is considered the gold standard viral vector for neurological gene therapy due to its tropism for CNS tissue, its low immunotoxicity and its ability to cross the BBB (Weinberg, Samulski et al. 2013). However, the capsids protein interactome is not well understood therefore limiting the therapeutic potential of the vector.

Due to varied tropism between serotypes, there is a need to identify *in vitro* models for each capsid as particular cellular models may be only experimentally optimal for specific capsids (Westhaus, Cabanes-Creus et al. 2020). *In vitro* screening studies have been conducted on the AAV serotypes which highlight major transduction variability between serotypes and cell lines (Ellis, Hirsch et al. 2013, Westhaus, Cabanes-Creus et al. 2020). In particular, AAV9 is notorious for having a limited selection of permissive cell lines due to its unknown interactome. Characterisation of *in vitro* models would therefore provide insight into the proteins required for effective AAV9 transduction.

Preliminary data indicated that AAV9 transduction in porcine endothelial brain cells (PEBCs) led to an upregulation of gene expression in SDC4, ICAM1 and SLC7A2 (Figure 1.6). This chapter sought to identify novel permissive and non-permissive cell lines and investigate the expression levels of these targets to validate if the expression pattern of these identified proteins regulates the cellular tropism of AAV9. To achieve this, characterisation of multiple antibodies, siRNA and mammalian expression constructs was required followed by the

characterisation of neuronal cell lines. These cell lines were then screened with AAV9 to identify permissive and non-permissive cellular models. In these studies, the recently identified AAV receptor protein (AAVR) was used as a positive control.

3.2 Results

3.2.1 Characterisation of antibodies and siRNA

As a result of preliminary data indicating that SDC4, ICAM1 and SLC7A2 are upregulated in AAV9 transduction, these targets were taken forward for further studies. Experiments to generate overexpression mammalian constructs and to determine if endogenous expression of these targets could be detected via western blot and immunofluorescence were performed.

3.2.1.1 Characterisation of AAVR Antibody and siRNA

Given that AAVR was being used as a positive control in these studies, it was initially decided to characterise and optimise an AAVR specific antibody for the necessary assays required for future work. As a method to confirm the specificity of endogenous AAVR protein signal, a commercially available anti-AAVR antibody was tested on HeLa cells transfected with non-targeting control (NTC) siRNA and AAVR-targeting siRNA to reduce AAVR expression. The commercial AAVR antibody detected signal at 140 kDa as similarly shown in literature (Figure 3.2A) (Pillay, Meyer et al. 2016). Supporting the specificity of this band, cells transfected with AAVR-targeting siRNA showed a reduced expression relative to that of the NTC transfected condition. The levels of AAVR knockdown were confirmed by quantitative PCR using designed primers, which confirmed a significant knockdown of AAVR mRNA (82% of mRNA knocked down relative to that of the NTC control, $p \leq 0.001$) (Figure 3.2B). Following this, the antibody was tested in immunocytochemistry experiments to investigate the localisation of AAVR. Transfected HeLa cells were fixed and stained with the commercial antibody (Figure 3.2C). Immunostained NTC-treated HeLa cells exhibited antibody signal in the predicted Golgi region of the cells, as previously reported (Pillay, Meyer et al. 2016). Specificity of signal was again verified in AAVR-siRNA treated cells which showed a significant reduction in fluorescent signal. As a result, it was concluded that the antibody was versatile in the necessary assays and had been shown to be specific in detecting endogenous expression. Following the positive control characterisation, the other targets antibodies and siRNAs were similarly characterised and optimised.

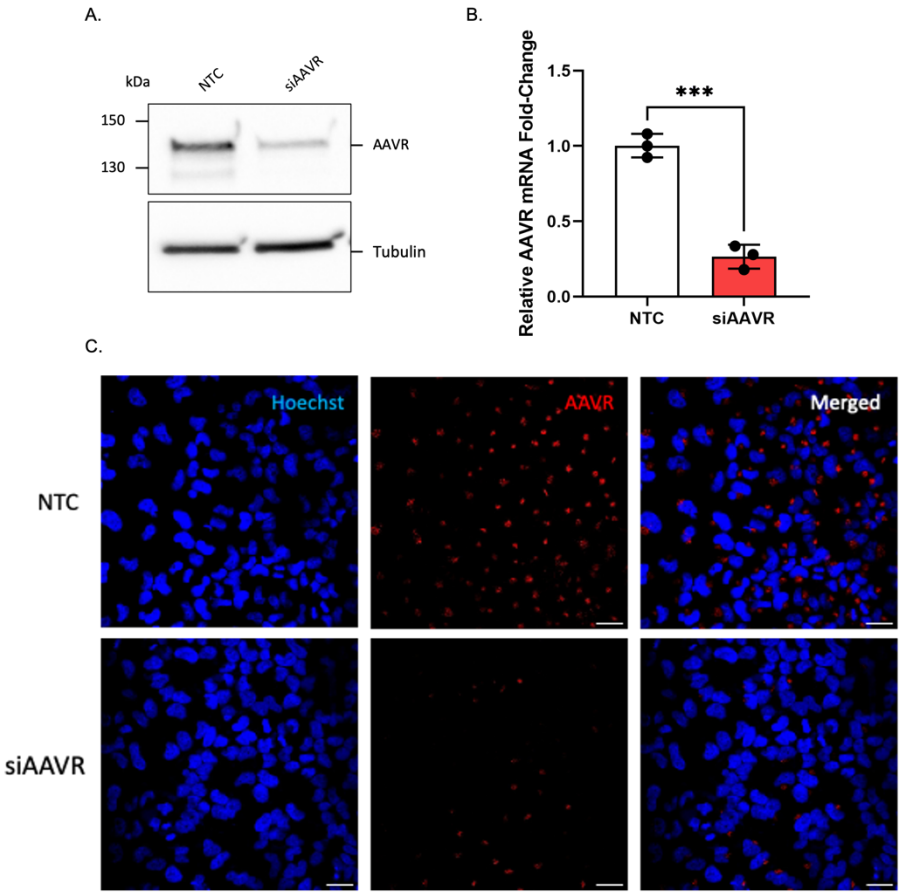

Figure 3.1: ***siRNA knock-down of endogenous expression of AAVR could be detected in all experimental methods*** *– HeLa cells were transfected with non-targeting control (NTC) and AAVR-targeted siRNA. (A) Transfected cells were subjected to an SDS-PAGE and immunoblot. Blots were probed with AAVR Abcam antibody at the recommended dilution. Tubulin was used as a loading control. (B) Transfected cells RNA was collected enabling cDNA to be generated and assessed by qPCR using optimised AAVR primers. Graph represents mean relative level of AAVR mRNA levels after siRNA transfection relative to the NTC dataset (Mean*±SEM; *t*-test, * * * p≤0.001, biological N=3). *(C) Treated cells were fixed with 4% paraformaldehyde and immunostained with AAVR Abcam antibody and anti-mouse Alexa488 (false coloured red). Cover slips were imaged via confocal microscopy (63x). Scale bar is at 38 µm.*

3.2.1.2 Generation and Validation of pCI_neo_HA_AAVR

Due to the success in antibody characterisation, a mammalian overexpression construct was generated for future experimental studies. Transient AAVR gene expression was controlled via an upstream CMV promoter (Figure 3.3A). The AAVR cDNA sequence was amplified to incorporate *Not* and *NheI* restriction sites onto the 5' and 3' ends, respectively. This PCR product and pCI_neo_HA tagged construct were digested with the mentioned restriction enzymes and ligated. This ligated product underwent a confirmation digest to cut out the 3,150 kB AAVR sequence from the linearised backbone (Figure 3.3B). The plasmids expression was validated via immunoblotting, using the HA antibody, which showed signal at the previously confirmed height of 140 kDa and an additional signal at the 75 kDa marker (Figure 3.3C). Although the 75 kDa signal was unexpected, due to its presence in only the overexpressed condition, it was accepted as a potential degradation product of overexpressed full length AAVR. The constructs transient expression was also confirmed by immunostaining in which transfected cells were identified overexpressing the target protein unlike the empty-vector control (Figure 3.3D).

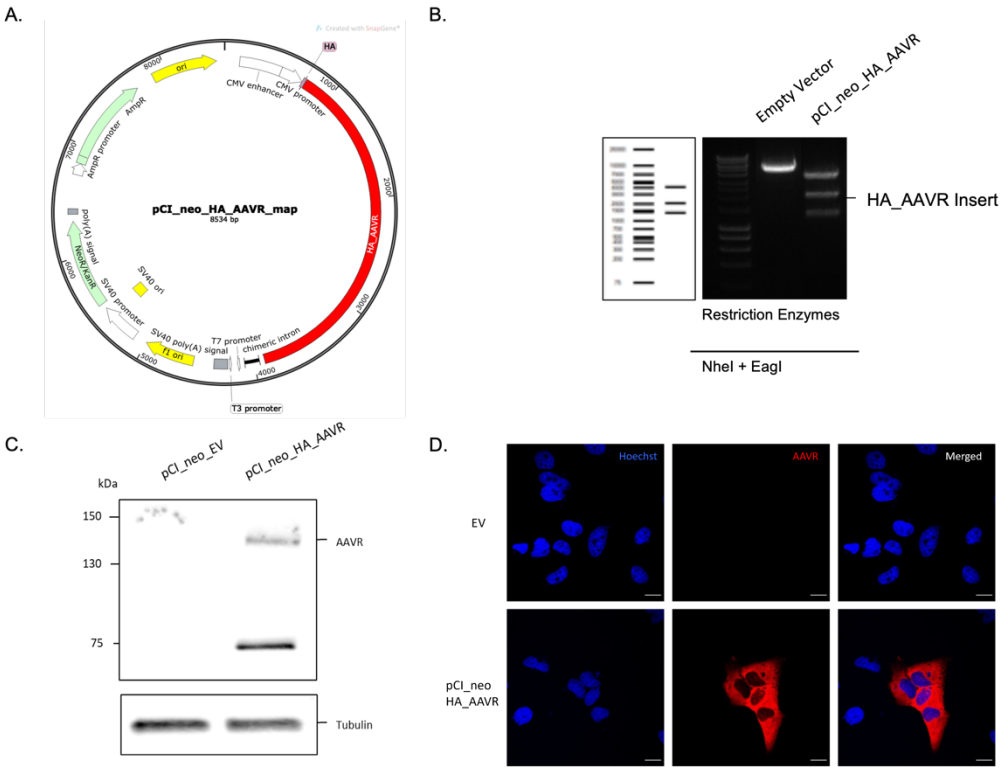

Figure 3.2: ***Generation of pCI_neo_HA_AAVR construct*** *– (A) Snapgene construct map of pCI_neo_HA_AAVR (B) Generated DNA was digested with restriction enzymes NheI and EagI which was run on a 1% agarose gel to validate insert (AAVR sequence contains an internal EagI restriction site). Predicted digested bands were generated on Serial Cloner. HeLa cells were transfected and left for 48 hours before: (C.) Transfected cells were subjected to an SDS-PAGE and immunoblot. Blots were incubated with HA antibody. Tubulin was used as a loading control. (D) Cells were fixed with 4% paraformaldehyde and immunostained with HA antibody and anti-mouse Alexa488 (false-coloured red). imaged via confocal microscopy (63x). Scale bar is at 38 µm*

3.2.1.3 Characterisation of SDC4 Antibody and siRNA

Having optimised a commercial antibody for the positive control AAVR, a commercial antibody against SDC4 from Genetex was validated to determine if endogenous SDC4 signal was detectable in the HeLa cell line. As a method to confirm the specificity of protein signal relative to endogenous SDC4, the antibody was tested on HeLa cell samples transfected with non-targeting control (NTC) siRNA and SDC4-targeting siRNA to reduce SDC4 expression on an mRNA level. The predicted height of SDC4 is approximately 22 kDa (Yang, Liu et al. 2021). However, following immunoblotting with the commercial antibody, no signal could be detected in the control cells (Figure 3.3A). As a result, no reduced signal could be detected in the siRNA treated cells to validate specificity. To confirm siRNA-induced mRNA knockdown, a quantitive PCR was conducted using designed primers. This confirmed significant depletion in SDC4 mRNA (76% of mRNA was reduced relative to that of the NTC control, $p \leq 0.01$) (Figure 3.3B). Having confirmed successful knockdown, immunocytochemistry experiments were conducted to investigate the localisation of SDC4. Transfected HeLa cells were fixed and stained with the commercial SDC4 antibody (Figure 3.3C). Only background signal could be detected in either the NTC- or siRNA-treated cells which prevented the identification of protein localisation.

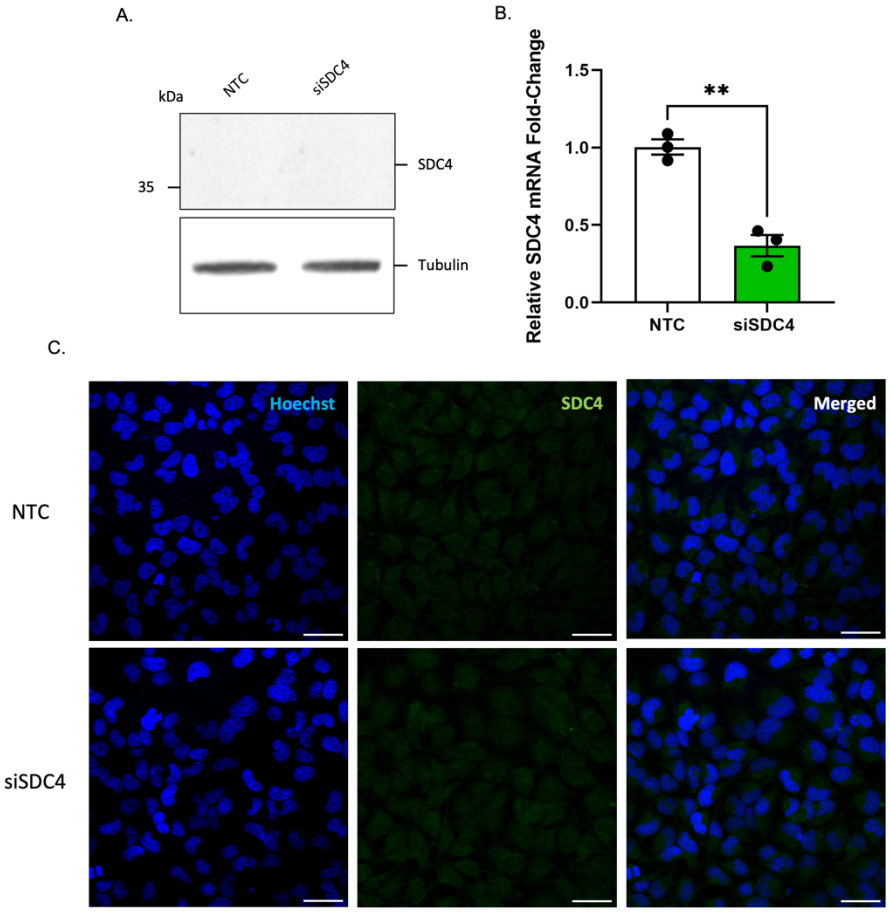

Figure 3.3: ***siRNA knock-down of endogenous expression of SDC4 could be detected via qPCR*** *–HeLa cells were treated with non-targeting control (NTC) and SDC4-targeted siRNA. (A) Treated cells were analysed by SDS-PAGE and immunoblotted with Genetex SDC4 antibody at the recommended dilution (see Methods). Tubulin was used as a loading control. (B) Treated cells RNA was collected enabling cDNA to be generated and used in a qPCR with optimised primers. Graph represents mean relative level of SDC4 mRNA levels after siRNA transfection (Mean*±SEM; *t*-test, * * p≤0.01, biological N=3) *(C.) Treated cells were fixed with 4% paraformaldehyde and immunostained with Genetex SDC4 antibody. Images captured via confocal microscopy (64x). Scale bar is at 38 µm*

3.2.1.4 Generation and Validation of pCI_neo_Myc_SDC4

Due to the lack of signal via immunocytochemistry, an SDC4 mammalian expression vector was generated to determine cellular localisation. The SDC4 cDNA sequence was amplified from the MGC Fully Sequenced Human SDC4 cDNA (Dharmacon, US) vector to incorporate *NotI* and *NheI* restriction sites onto the 5' and 3' ends, respectively. This PCR product was digested with *NotI* and *NheI* along with the pCI_neo mammalian expression vector. Digested products were gel purified and the SDC4 insert was ligated into pCI_neo_Myc. Transient SDC4 gene expression was controlled via an upstream CMV promoter (Figure 3.4A). This construct was screened by restriction digest of *NotI* and *NheI* to cut out the 597 kb SDC4 fragment from the linearised pCI_neo_Myc_SDC4 plasmid (Figure 3.4B). The generated plasmid was transfected into HeLa cells to validate if transient overexpression could be detected with an anti-Myc antibody. The overexpression of Myc_SDC4 could be detected at approximately 35 kDa and 75 kDa in the pCI_neo_Myc_SDC4 treated cells compared to the empty-vector (EV) control (Figure 3.4C) which was higher than the predicted height of 22 kDa. Transient expression was also confirmed via immunostaining in which strong cytoplasmic signalling could be detected in the pCI_neo_Myc_SDC4 transfected cell (Figure 3.4D).

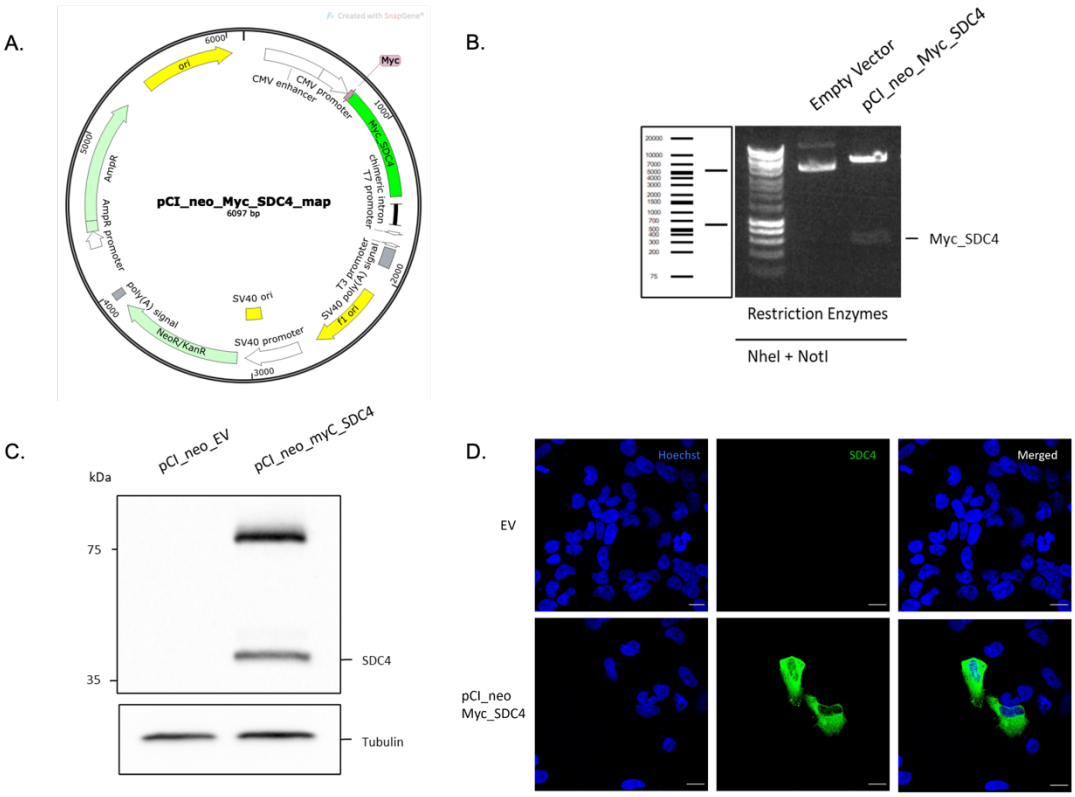

Figure 3.4: ***Generation of pCI_neo_Myc_SDC4 construct*** *– (A) Snapgene construct map of pCI_neo_Myc_SDC4. (B) Generated DNA was digested with restriction enzymes NheI and NotI which was run on a 1% agarose gel for DNA electrophoresis. Predicted digested bands were generated on Serial Cloner (C.) HeLa cells were transfected with empty vector and pCI_neo_Myc_SDC4 and subjected to an SDS-PAGE and immunoblot. SDC4 was detected with anti-Myc antibody. Tubulin was used as a loading control. (D) Treated cells were fixed with 4% paraformaldehyde and immunostained with Myc antibody and Anti-Mouse Alexa488. Imaged via confocal microscopy (63x). Scale bar is at 38 µm*

3.2.1.5 Determining SDC4 overexpression and reduced protein levels via siRNA knock-down in vitro

Due to confirming SDC4 overexpression signal was observable with the anti-Myc antibody, it was determined with a commercial anti-SDC4 antibody screen if the selected antibodies could detect endogenous SDC4 and overexpressed Myc_SDC4. In an attempt to detect endogenous SDC4 signal via immunoblot, two further commercially available SDC4 antibodies were tested in cells treated with control (NTC) or SDC4-targeting siRNA and transfected with empty vector control, or the Myc_SDC4 construct. HeLa cells were transfected with siRNA against SDC4 and 24-hours later transfected with the pCI_neo_Myc_SDC4 plasmid. Three commercially available antibodies (Genetex, Abcam and Santa-Cruz) were tested.

All commercial antibodies showed a similar signal pattern by detecting the strong 35 kDa signal in control siRNA (NTC) treated cells (Figure 3.5). The Abcam and Genetex antibodies also presented an additional signal at 17 kDa. When transfected with SDC4-targeting siRNA, the overexpressed 35 kDa and 17 kDa bands were both abolished. All three antibodies showed no detection of endogenous signal and were only capable of detecting overexpressed SDC4 which was reduced via siRNA. This led to the conclusion that it was impracticable to use these commercial antibodies for endogenous detection and signal may require alternate optimisation to these methods. Due to the Santa-Cruz antibody having clear signal at the 35 kDa height and no additional products at the 17 kDa marker, this antibody was chosen for future overexpression experiments.

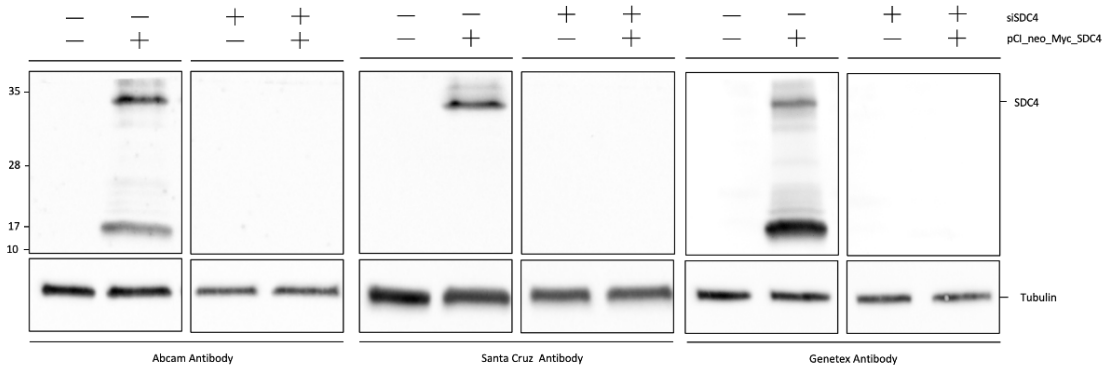

Figure 3.5: ***Transient overexpression of SDC4 is knocked down using SDC4-targeted siRNA*** *–HeLa cells were transfected with non-targeting control (NTC) and SDC4-targeted siRNA and then transfected with pCI_neo_Myc_SDC4. (A.) Transfected cells were subjected to an SDS-PAGE and immunoblot. Commercial antibodies used were (A) Abcam (B) Santa Cruz SDC4 and (C) Genetex. Tubulin was used as a loading control.*

3.2.1.6 Characterisation of ICAM1 antibody and siRNA

The next protein target to be screened was ICAM1. As a method to confirm the specificity of protein signal relative to endogenous ICAM1, the antibody was tested on HeLa cells transfected with NTC siRNA or ICAM1-targeting siRNA. The commercial ICAM1 antibody detected signal at the predicted 80 kDa marker (Figure 3.6A). Supporting the specificity of this signal, in cells transfected with ICAM1-targeting siRNA this signal was completely abolished. Quantitive PCR using designed primers confirmed a significant depletion of ICAM1 mRNA (55% knockdown of mRNA relative to that of the NTC control cells, $p \leq 0.001$) (Figure 3.6B). Following this, the antibody was tested in immunocytochemistry experiments to investigate the localisation of ICAM1. Transfected HeLa cells were fixed and stained with the commercial anti-ICAM1 antibody (Figure 3.6C). Immunostained NTC and siRNA-treated cells showed only background signal which prevented the assessment of protein localisation.

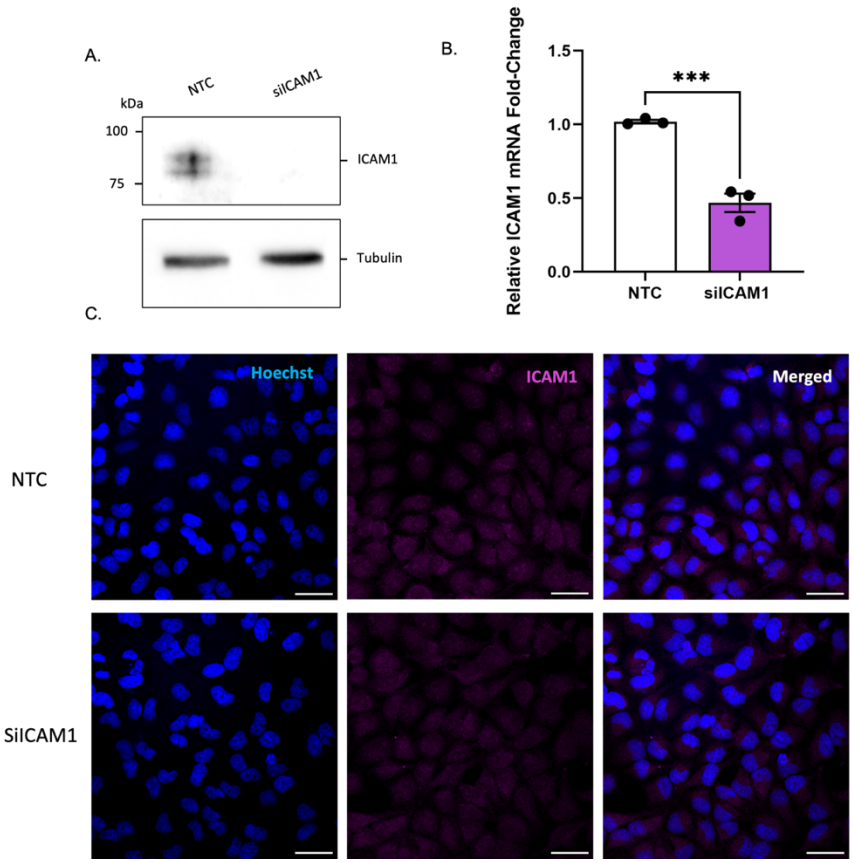

Figure 3.6: ***siRNA knock-down of endogenous expression of ICAM1*** *–HeLa cells were transfected with non-targeting control (NTC) and ICAM1-targeted siRNA. (A) Transfected cells were subjected to SDS-PAGE and immunoblot. Blots were incubated with ICAM1 Abcam antibody at the recommended dilutions. Tubulin was used as a loading control. (B) Transfected cells RNA was collected enabling cDNA conversion and used in a qPCR using optimized ICAM1 primers. Graph represents mean relative level of ICAM1 mRNA levels after siRNA transfection (Mean*±SEM; *t*-test, * * * p≤0.001, biological N=3) *(C.) Treated cells were fixed with 4% paraformaldehyde and immunostained with ICAM1 Abcam antibody and anti-rabbit Alexa488 (false-coloured magenta). Coverslips were imaged vis confocal microscopy (63x). Scale bar is at 38 µm*

3.2.1.7 Generation and Validation of pCI_neo_ICAM1

Due to the lack of signal via immunocytochemistry, an ICAM1 mammalian expression vector was generated to determine the cellular localisation of ICAM1. The ICAM1 cDNA sequence was amplified via a PCR reaction from the MGC Fully Sequenced Human ICAM1 cDNA (Dharmacon, US) vector. This PCR product was digested along with the digested pCI_neo mammalian expression vector and gel purified. The ICAM1 insert was ligated into a linearised pCI_neo via complimentary sticky ends. The ligated ICAM1 gene expression is controlled via an upstream CMV promoter (Figure 3.7A). Clones were screened by restriction digest of *EagI* and *SalI* to cut out the 1,599 kb ICAM1 fragment from the linearised pCI_neo_ICAM1 plasmid (Figure 3.7B). The generated plasmid was transfected into HeLa cells to validate if transient overexpression could be detected with the commercial ICAM1 antibody. Overexpression of ICAM1 signal could be detected at approximately 60 kDa in pCI_neo_ICAM1 transfected cells (Figure 3.7C). Transient overexpression was also confirmed via immunostaining which showed strong cytoplasmic and membrane signal in the cells transfected with pCI_neo_ICAM1 (Figure 3.7D).

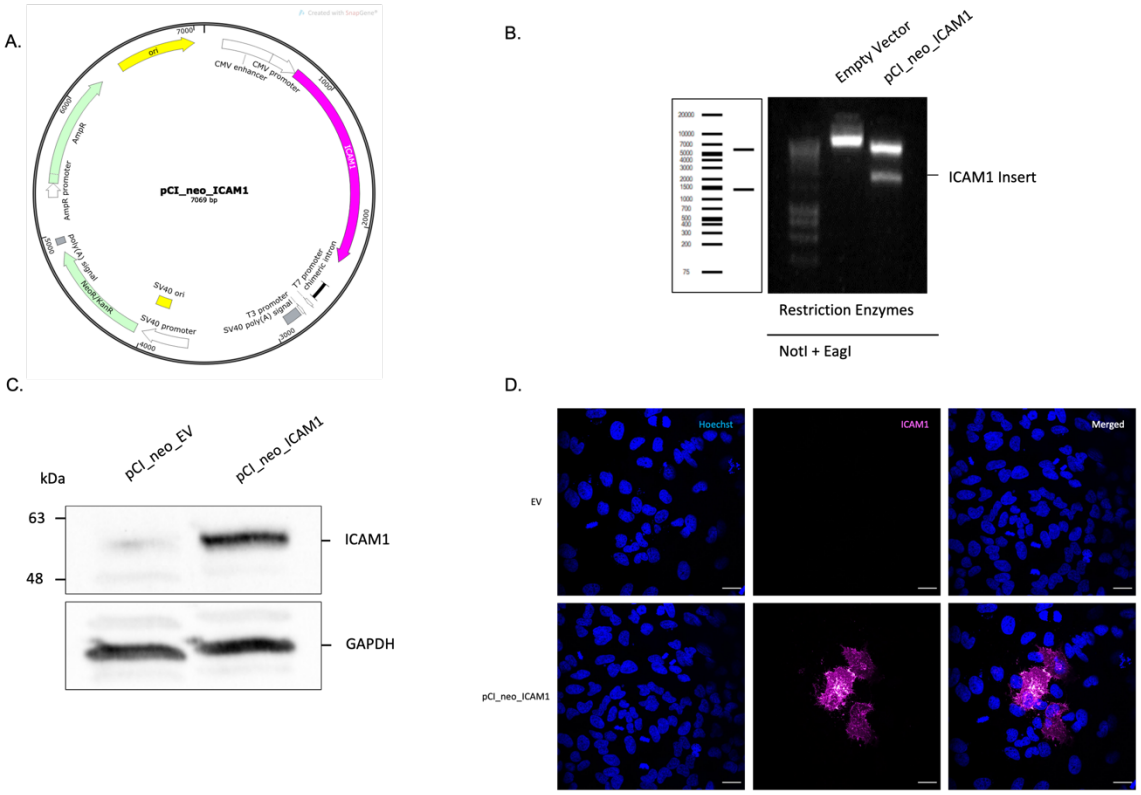

Figure 3.7: ***Generation of pCI_neo_ICAM1 construct*** *– (A) Snapgene construct map of pCI_neo_ICAM1 (B) Generated DNA was digested with restriction enzymes NheI and EagI and was run on a 1% agarose gel (AAVR sequence contains an internal EagI restriction site). Predicted digested bands were generated on Serial Cloner (C.) HeLa cells were transfected and left for 48 hours before being subjected to an SDS-PAGE and immunoblotted with Abcam ICAM1. Tubulin was used as a loading control. (D) Cells were fixed with 4% paraformaldehyde and immunostained with Abcam ICAM1 and anti-rabbit Alexa488 (false-coloured magenta). Imaged via confocal microscopy (63x). Scale bar is at 38 µm*

3.2.1.8 Characterisation of SLC7A2 Antibody and siRNA

The final commercial antibody to be characterised was anti-SLC7A2. To confirm the specificity of protein signal relative to endogenous SLC7A2, the antibody was tested on HeLa cells transfected with NTC siRNA and SLC7A2-targeted siRNA to reduce SLC7A2 expression on an mRNA level. The SLC7A2 antibody detected signal at 170 kDa, which was higher than the predicted height of 70 kDa (Figure 3.8A). This could be as a result of the target protein being highly glycosylated (Tsuji 2020). Supporting the specificity of this higher band, transfected cells with SLC7A2-targeting siRNA showed a reduced expression relative to that of the NTC control. The levels of SLC7A2 knockdown were confirmed by quantitative PCR using designed primers, which confirmed a significant depletion of SLC7A2 mRNA (73% mRNA knockdown relative to that of the NTC control, $p \leq 0.01$) (Figure 3.8B). Following this, the antibody was tested in immunocytochemistry experiments to investigate the localisation of SLC7A2. Transfected HeLa cells were fixed and stained with the commercial anti-SLC7A2 antibody (Figure 3.8C). Immunostained NTC and SDC4 siRNA treated cells showed only background signal which prevented the identification of endogenous protein localisation.

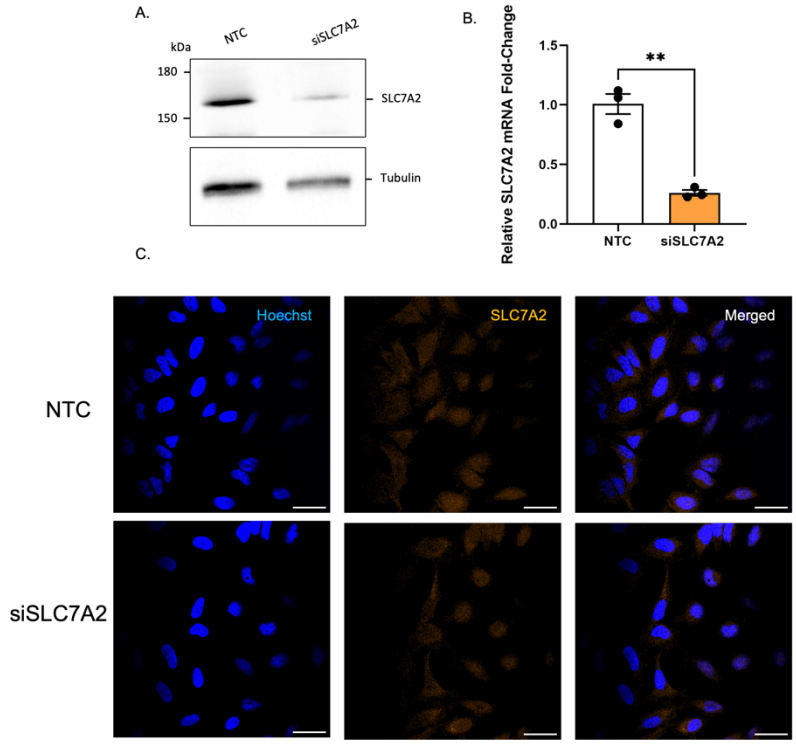

Figure 3.8: ***siRNA knock-down of endogenous expression of SLC7A2*** *–HeLa cells were transfected with non-targeting control (NTC) and SLC7A2-targeted siRNA. (A) Transfected cells were subjected to SDS-PAGE and immunoblot. Blots were incubated with Abcam SLC7A2 antibody at the recommended dilutions. Tubulin was used as a loading control. (B) Transfected cells RNA was collected enabling cDNA conversion and used in a qPCR using optimized ICAM1 primers. Graph represents mean relative level of SLC7A2 mRNA levels after siRNA transfection (Mean*±SEM; *t*-test, * * p≤0.01, biological N=3) *(C.) Treated cells were fixed with 4% paraformaldehyde and immunostained with Abcam SLC7A2 antibody and anti-rabbit Alexa488* (false-colour orange)*). Coverslips were imaged vis confocal microscopy (64x). Scale bar is at 38 µm*

3.2.1.9 Generation and Validation of pCI_neo_V5_SLC7A2

Due to the lack of signal via immunocytochemistry, an SLC7A2 mammalian expression vector was generated to determine the localisation of SLC7A2. The SLC7A2 ORF sequence was amplified from the MGC Fully Sequenced Human SLC7A2 cDNA (Dharmacon, US) vector using designed primers to incorporate *NotI* and *XhoI* restriction sites onto the 5' and 3' ends, respectively. This PCR product was digested with *NotI* and *XhoI* along with the pCI_neo mammalian expression vector. Digested and linearised products were gel purified and the SLC7A2 ORF insert was ligated into a linearised pCI_neo. The ligated pCI_neo_V5_SLC7A2 plasmid's gene expression was controlled via an upstream CMV promoter (Figure 3.9A). Clones were screened by restriction digest of *NotI* and *XhoI to* cut out the 2,097 kb SLC7A2 fragment from the linearised pCI_neo_V5_SLC7A2 plasmid (Figure 3.9B). The generated plasmid was transfected into HeLa cells to validate if its transient overexpression could be detected with the anti-V5 antibody. The overexpression of SLC7A2 signal was detected at approximately 70 kDa appearing as a smear in the pCI_neo_V5_SLC7A2 treated cells, again hinting at possible post translational modifications, including glycosylation (Figure 3.9C). Overexpression was further validated via immunocytochemistry by fixing cells transfected with pCI_neo_V5_SLC7A2. Transient overexpression was confirmed with cytoplasmic and membrane labelling in transfected cells (Figure 3.9D).

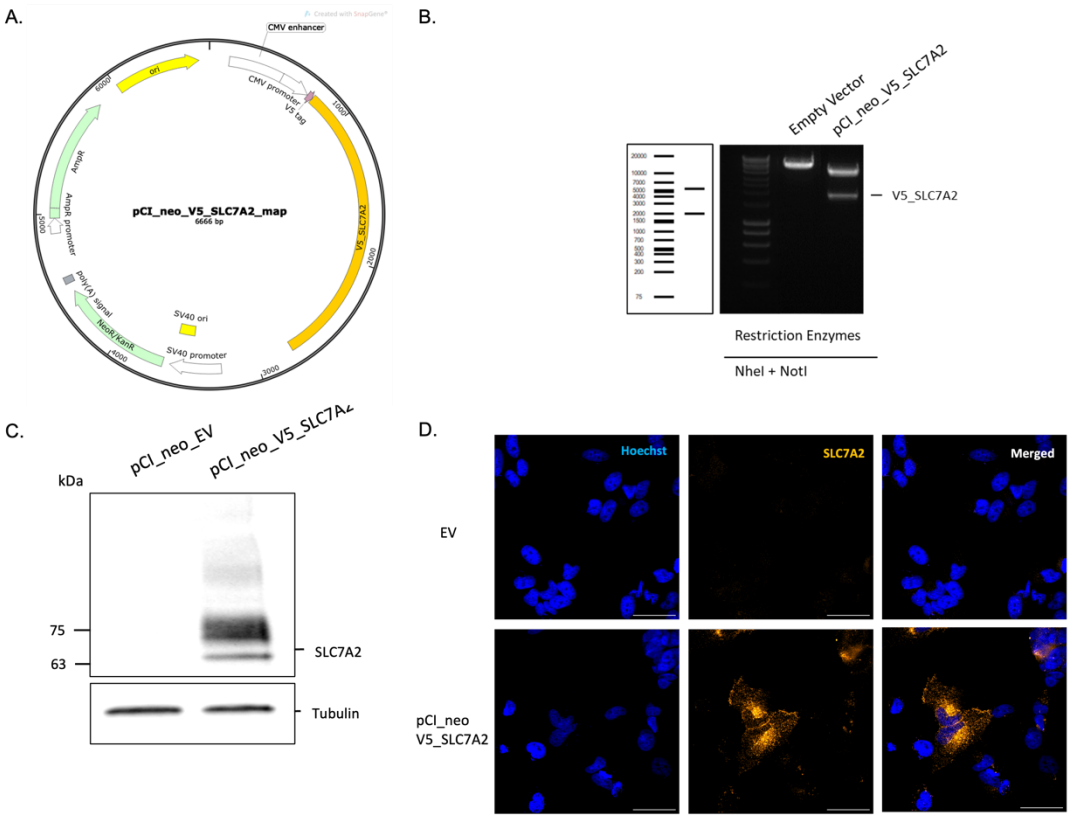

Figure 3.9: ***Generation and validation of pCI_neo_V5_SLC7A2 construct*** *– (A) Snapgene construct map of pCI_neo_V5_SLC7A2 (B) Generated DNA was digested with restriction enzymes NheI and NotI and was run on a 1% agarose gel Predicted digested bands were generated on Serial Cloner (C.) HeLa cells were transfected and left for 48 hours before being subjected to an SDS-PAGE and immunoblotted with Invitrogen V5 antibody. Tubulin was used as a loading control. (D) Treated cells were fixed with 4% paraformaldehyde and immunostained with Invitrogen V5 antibody and anti-mouse Alexa488 (false-colour orange). Coverslips were imaged via confocal microscopy (63x). Scale bar is at 20 µm.*

3.2.2 Target Protein Characterisation of Neurovascular Cell lines

Due to AAV9's neurotropism, it was hypothesised that a screening of neurovascular cell lines could identify more permissive cell lines to be used for future studies investigating AAV9 cell surface interaction. As a result, the selected cell lines to be tested were HeLa, Neuro-2A (N2A), SH-SY-5Y (SHSY), NIH3T3, 1321N1 and b.End5 (Table 1.1). Each cell line was characterised for the protein expression level of each target protein.

Table 3.1: ***List of cell lines used.***

Cell Line:	Cell Type:
HeLa	*Human cervix epithelioid carcinoma*
Neuro-2A	Mouse neuroblastoma
SH-SY-5Y	Human neuroblastoma
NIH3T3	Mouse Fibroblasts
1321N1	Human Astrocytoma
b.End5	Mouse brain endothelial cells

AAVR protein expression could be detected at the previously validated height in the HeLa and SHSY cell lines (Figure 3.10). The SHSY cell line had the highest expression of AAVR when compared to HeLa cells (approximately a 1.2-fold increase in SHSYs AAVR expression compared to HeLa's). However, the other cell lines had no detectable endogenous levels of AAVR (Figure 3.10A). Due to the lack of SDC4 endogenous signal seen previously in the HeLa cell line, it was hypothesised that one of these cell lines could have had a detectable expression level of SDC4. However, no endogenous SDC4 signal could be observed in any of the neurovascular cell lines (Figure 3.10B). Endogenous ICAM1 and SLC7A2 expression could be detected at the validated height at 80 kDa and 170 kDa, respectively, in the HeLa cell line (Figure 3.10C and 3.10D). SLC7A2 signal could also be observed in the 1321N1 cell line but in none of the other cell lines. Due to absence of SDC4 signal in any of the screened neuronal cell lines, a final optimisation was attempted to determine if the stability of SDC4 was affected by certain stages of protein extraction and SDS-PAGE.

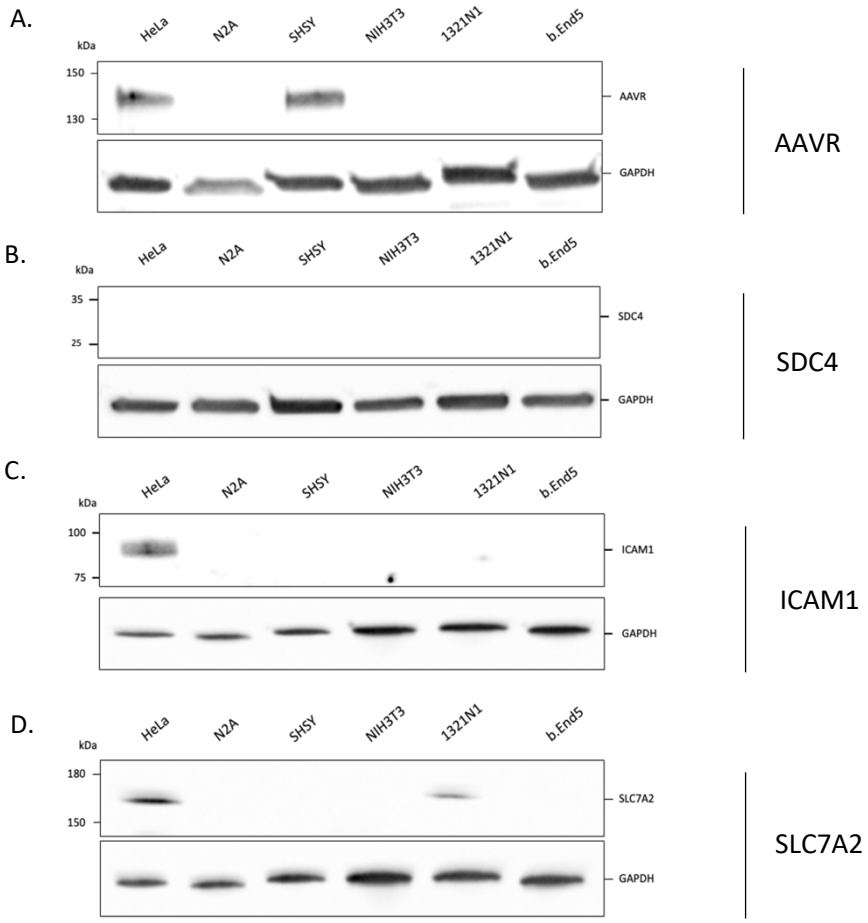

Figure 3.10: ***Characterisation of neuronal cell lines for all targets*** **–** *Neuronal cell lines lysates were subjected by SDS-PAGE and immunoblot. Blots were incubated with commercial antibodies (A) Abcam AAVR (B) Santa Cruz SDC4 (C.) Abcam ICAM1 and (D) Abcam SLC7A2. GAPDH was used as a loading control. (Biological N=3)*

3.2.3 Optimisation of lifting and temperature conditions to detect SDC4 levels in neurovascular cell lines.

Previous studies have shown that trypsin proteolysis cleaves surface proteins which results in cell dissociation (Huang, Hsing et al. 2010). Due to the lack of detectable endogenous SDC4 expression in any of the screened neurovascular cell lines, the experimental process of disassociating cells was optimised to evaluate if trypsin was affecting SDC4's epitope region and protein-antibody interactions. EDTA-PBS was used as an alternate non-enzymatic disassociation reagent compared to that of the serine protease trypsin. In addition to this, temperature is known to affect protein folding (Schön, Clarkson et al. 2017). Boiling treatment is typically required for the epitope region to be exposed for antibody binding. However, it can potentially be detrimental to epitope stability and alter the shape of the protein on which antibody binding may rely on. As a result, boiled and non-boiled samples were tested to validate if endogenous signal could be observed.

No endogenous SDC4 expression could be detected in any of the neuronal cell lines incubated with EDTA-PBS or trypsin (Figure 3.11A and 3.11B). Cell samples which had been boiled or had been maintained at room temperature (Figure 3.11C and 3.11D) also showed no SDC4 detection. To conclude, the SDC4 antibody was unable to detect endogenous SDC4 expression in a variety of conditions across multiple tested cell lines and was only capable of detecting expression when transfected with a mammalian SDC4 expression vector as shown in Figure 3.4.

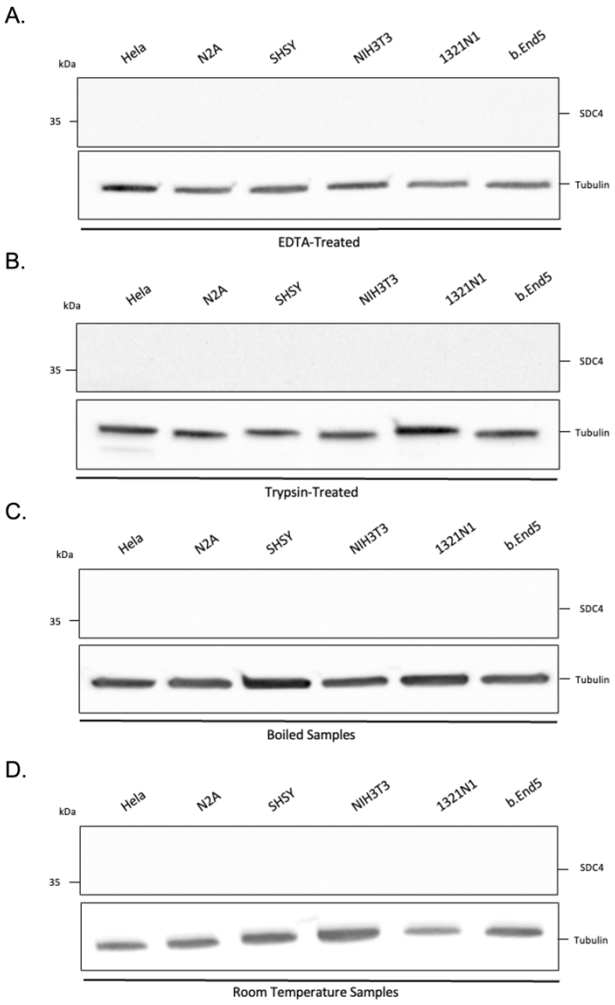

Figure 3.11: ***Optimisation of lifting agent and temperature conditions led to no detection of endogenous SDC4*** *- Neuronal cell lines were lifted with (A) 5mM PBS-EDTA or (B) 1x trypsin and then were subjected to SDS-PAGE and immunoblot. Blots are incubated with Santa Cruz SDC4 at the recommended dilutions. Lysates were also lysed at (C.) 95 °C (D) room temperature before subjected by SDS-PAGE and immunoblotted with Santa Cruz SDC4 at the recommended dilutions. Tubulin was used as a loading control.*

3.2.4 Assessing target receptor expression in neuronal tissue targets *in vivo*

Literature indicates that neonatal mice displays high transduction efficiency after intravascular delivery compared to that of adult mice (Yang, Li et al. 2014). Because of this, it was hypothesised that neonatal mice have a higher expression level of AAV9 target receptor proteins than that of adult mice, resulting in more efficient transduction. Brain, spinal cord and liver tissue were taken from p2, p15 and p45 mice to validate this hypothesis. Brain and spinal cord were used for CNS characterisation while the liver was used as an off-target tissue characterisation.

Figure 3.12: ***Model of hypothesis of alternate expression pattern based on age***

AAVR signal could not be detected in the p2 brain samples (Figure 3.13A). However, expression was increasingly detected in the p15 and p45 brain tissue, respectively. In spinal tissue AAVR protein expression could not be observed in the p2 and p15 tissue but was detectable at p45 age (Figure 3.13B), while in liver tissue, no AAVR expression could be detected at any age (Figure 3.13C). Intriguingly, unlike *in vitro*, an endogenous SDC4 signal could be detected at 35 kDa in the p2 brain tissue and expression increased in the p15 and p45 aged mice (Figure 3.14A). SDC4 could not be detected in the p2 spinal tissue but expression levels could be detected at p15 and p45 (Figure 3.14B). SDC4 expression was observed in p2 liver tissue and expression levels peaked at p15 mice before decreasing in p45 tissue (Figure 3.14C). No ICAM1 signal could be detected in the brain tissue of all mice tested

(Figure 3.15A). In the p2 spinal tissue, no ICAM1 signal was detected but expression increased with age in the p15 and p45 groups (Figure 3.15B). Similarly, to SDC4, ICAM1 expression could be detected at p2 liver tissue and expression levels peaked at p15 before decreasing at p45 (Figure 3.15C). SLC7A2 signal could not be detected in the p2 brain tissue, however, it was detectable in the p15 and p45 brain tissue and increase in expression respectively (Figure 3.16A). This expression pattern is similar in the spinal tissue across all ages (Figure 3.16B). This study also revealed that SLC7A2 was expressed in the p2 liver tissue and its expression increased in aged mice, maintaining its expression at p15 and p45 ages (Figure 3.16C). Unexpectedly, the height of the SLC7A2 signal observed was at a much lower molecular weight at 70 kDa compared to the signal height of 170 kDa *in vitro*.

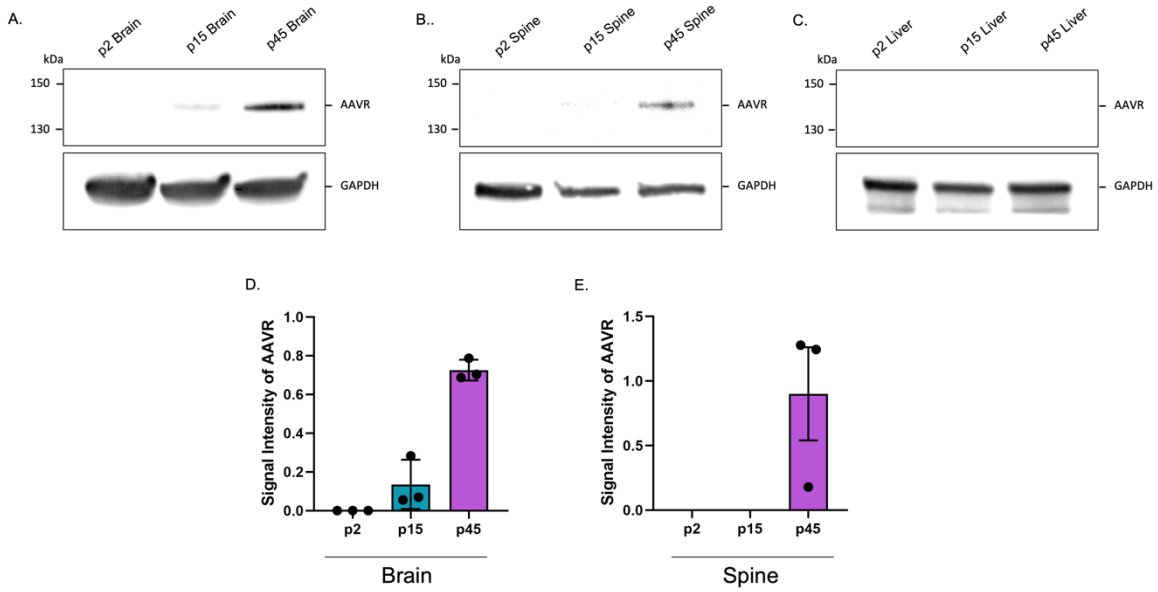

Figure 3.13: ***AAVR protein expression increases in age in mice brain and spine*** **–** *Tissue from postnatal day 2, 14 and 45 mice was subjected to SDS-PAGE and immunoblot. Blots were incubated with Abcam AAVR antibody for (A) brain, (B) spinal cord and (C.) liver tissue (biological N=3). Blots were quantified for levels in brain (D), spinal cord (E).*

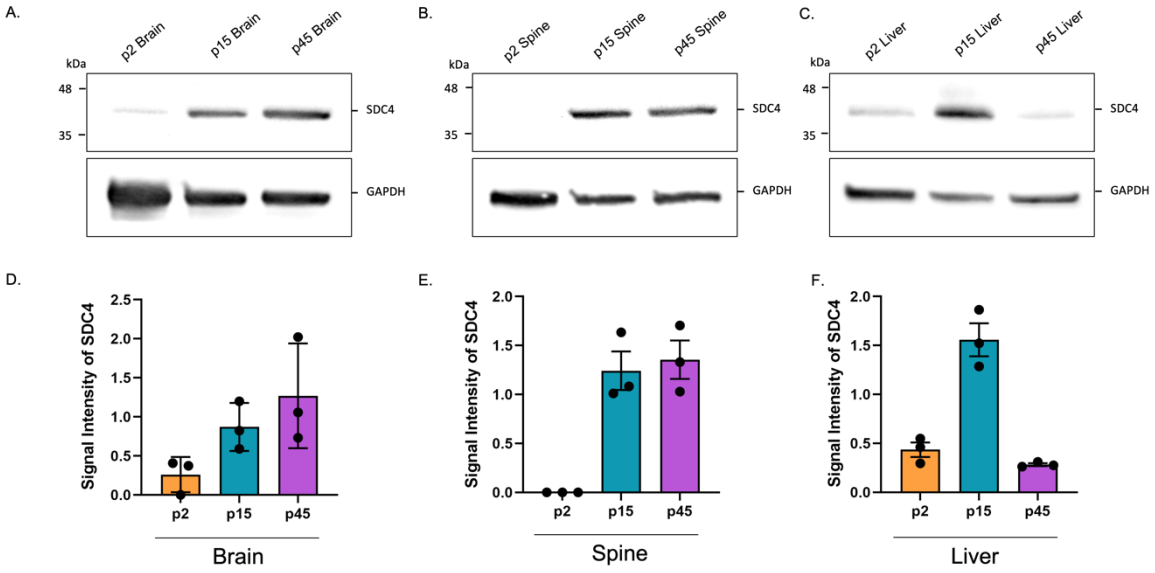

Figure 3.14: ***SDC4 protein expression increases with age in mice brain and spine –*** *Tissue from postnatal day 2, 14 and 45 mice was subjected to SDS-PAGE and immunoblot. Blots were incubated with Santa Cruz SDC4 antibody for (A) brain, (B) spinal cord and (C) liver tissue (biological N=3). Blots were quantified for levels in brain (D), spinal cord (E) and liver (F).*

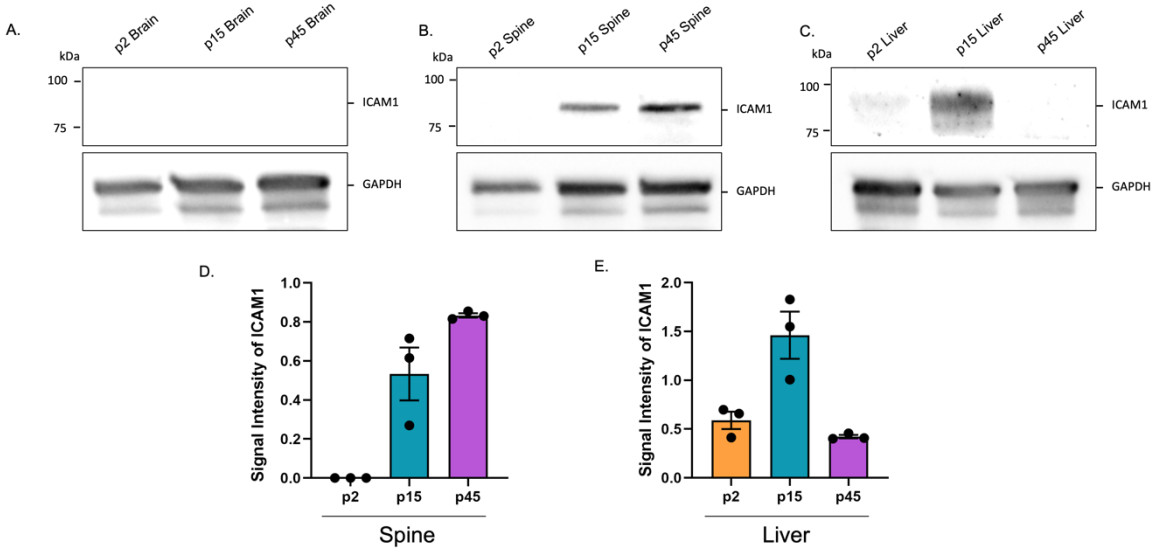

Figure 3.15: ***ICAM1 protein expression increases in age in mice brain and spinal cord*** **–** *Tissue from postnatal day 2, 14 and 45 mice was subjected to SDS-PAGE and immunoblot. Blots were incubated with Abcam ICAM1antibody for (A) brain, (B) spinal cord and (C.) liver tissue (biological N=3). Blots were quantified for levels in spinal cord (D) and liver (E).*

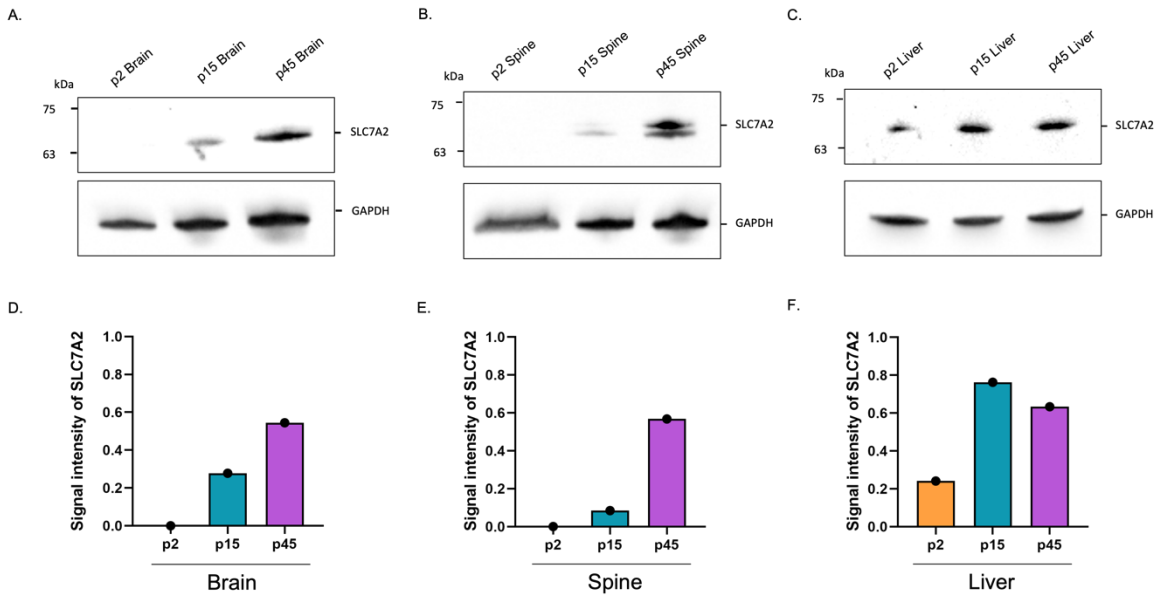

Figure 3.16: ***SLC7A2 protein expression increases with age in mice brain and spine*** **–** *Tissue from postnatal day 2, 14 and 45 mice was subjected to SDS-PAGE and immunoblot. Blots were incubated with Abcam SLC7A2 antibody for (A) brain, (B) spine and (C.) liver tissue (biological N=1). Blots were quantified for levels in Brain (D), Spinal cord (E) and Liver (F).*

3.2.5 AAV9 Transduction Efficiency in Neuronal Cell Lines

Following the characterisation of target protein expression of the selected neuronal cell lines, the transduction efficiency of AAV9 was investigated in the selected cell lines. Self-complementary AAV9 (scAAV9) was used due to its elevated transduction efficiency (McCarty, Monahan et al. 2001). scAAV9-EGFP was tested by using a multiplicity of infection (MOI) ranging from 5 x 10^4, 1 x 10^5 and 2 x 10^5 vector genomes per cell (vg/cell) in a 24-hour and 48-hour incubation period to determine the optimal experimental method for transduction efficiency. Self-complementary AAV2-EGFP (scAAV2-EGFP) at 3 x 10^3 vg/cell was used as a positive vector control due to its renowned wide tropism (Ellis, Hirsch et al. 2013).

The HeLa cell line was optimised first. Following 24-hour incubation, no scAAV9-GFP positive cells were identified at the MOI of 5 x 10^4 (Figure 3.17A). However, GFP positive cells could be detected at 1 x 10^5 and 2 x 10^5 MOI (average of 2% of total cells for each MOI). While the scAAV2-GFP control vector showed effective transduction with 100% scAAV2-GFP positive cells. Due to the low AAV9 transduction efficiency after 24 hours, 48-hour incubation was investigated at the same MOI's. After 48-hour incubation, the 5 x 10^4 MOI demonstrated improved but limited GFP positive cells (average of 2% of total cells) and efficiency in transduction increased at 1x 10^5 and 2 x 10^5 (average of 10% and 20% of total cells, respectively) (Figure 3.17B). The scAAV2-GFP vector maintained effective transduction efficiency at 100% GFP-positive cells. As a result, the optimal transduction method for scAAV9-GFP was 48-hours at an MOI of 2 x 10^5 in the HeLa cell line.

The N2A cell line was the first neuronal cell line to be evaluated. Following 24-hour incubation, no scAAV9-GFP positive cells were detected at any of the MOI tested. Intriguingly, the scAAV2-GFP positive control vector exhibited limited transduction (an average of 3% of GFP positive cells relative to total cells) (Figure 3.18A). After 48-hour incubation, no scAAV9-GFP positive cells could be observed at 5 x10^4 and 1 x 10^5 MOI (Figure 3.18B). However, at an MOI of 2 x 10^5 cells showed limited but improved transduction efficiency of 3% of GFP positive cells relative to total cells. The scAAV2-GFP vector showed an elevation in positive cells which increased to 7% GFP positive cells relative to total cells.

The SHSY cell line was next to be investigated. Following 24-hour incubation, SHSY's at an MOI of 5 x 10^4 showed 10% of scAAV9-GFP positive cells which increased with MOI concentration (increase at 33% and 59%, respectively) (Figure 3.19A). In the same time frame, the scAAV2-GFP vector showed 100% transduction efficiency. Due to limited transduction efficiency with scAAV9, 48-hour incubation was investigated at the same MOI's. At 48-hour incubation, the MOI of 5 x 10^4 showed improved transduction efficiency with 50% of total cells being GFP positive which increased with MOI titre (increase at 85% with the MOI of 1 x 10^5 and 96% of total cells with the MOI of 2 x 10^5 (Figure 3.19B). The scAAV2-GFP vector was shown to consistently transduce 100% of cells. These data indicated that SHSY-5Y cells were therefore the most permissive to scAAV9.

Following 24-hour incubation, NIH3T3's and 1321N1s at all MOI titres showed no scAAV9-GFP positive cells (Figure 3.20 and Figure 3.21). Similarly, no transduction was observed with scAAV2-GFP. Because of this, 48-hour incubation was investigated at the same MOI's. After 48-hour incubation, across all MOI conditions no GFP-positive cells were observed after either scAAV9-GFP or scAAV2-GFP transduction. These results therefore identified NIH3T3 and the 1321N1 cell lines as non-permissive to AAV9.

The final cell line to be investigated was the b.End5 cell line. Following 24-hour incubation, b.End5's at all MOI titres showed no scAAV9-GFP positive cells (Figure 3.22A). scAAV2-GFP could be identified at 1% of GFP positive cells relative to total cells. Due to limited transduction efficiency with scAAV9, 48-hour incubation was investigated at the same MOI's. After 48-hour incubation, across all MOI conditions, only at the 2 x 10^5 titre showed 1% of scAAV9-GFP positive cells detected (Figure 3.22B). scAAV2-GFP cells increased at 48-hours to 4% of GFP positive cells relative to total cells.

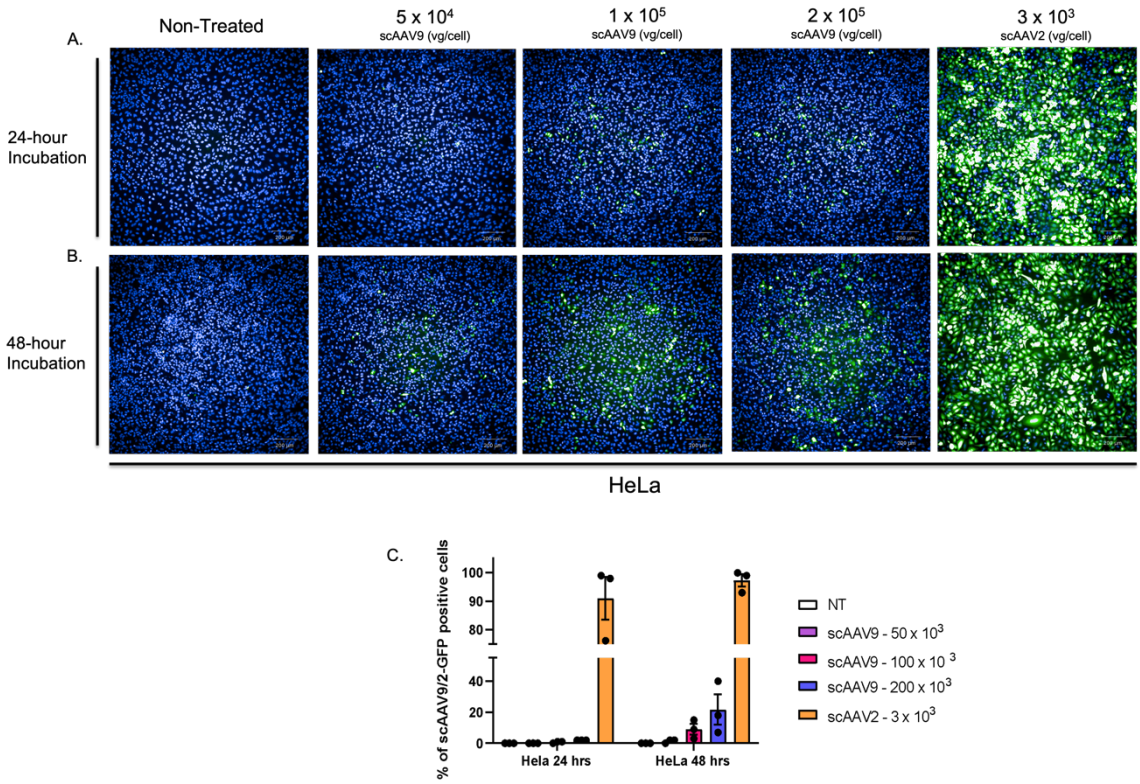

Figure 3.17: ***2 x 10^5 of scAAV9-GFP shows highest count of GFP positive cells in the HeLa cell line after 48 hours*** *– HeLa cells were transduced with scAAV9-GFP across a range of MOI's (5 x 10^4 – 2 x 10^5) over a (A). 24-hour and (B) 48-hour period. Cells were fixed with 4% paraformaldehyde before being imaged on the Incell microscope (10x). Scale bar is at 200 µm. (C). Percentage of scAAV-GFP positive cells was counted via Columbus analysis software and percentage to that of total cells was plotted on the graph (biological N=3).*

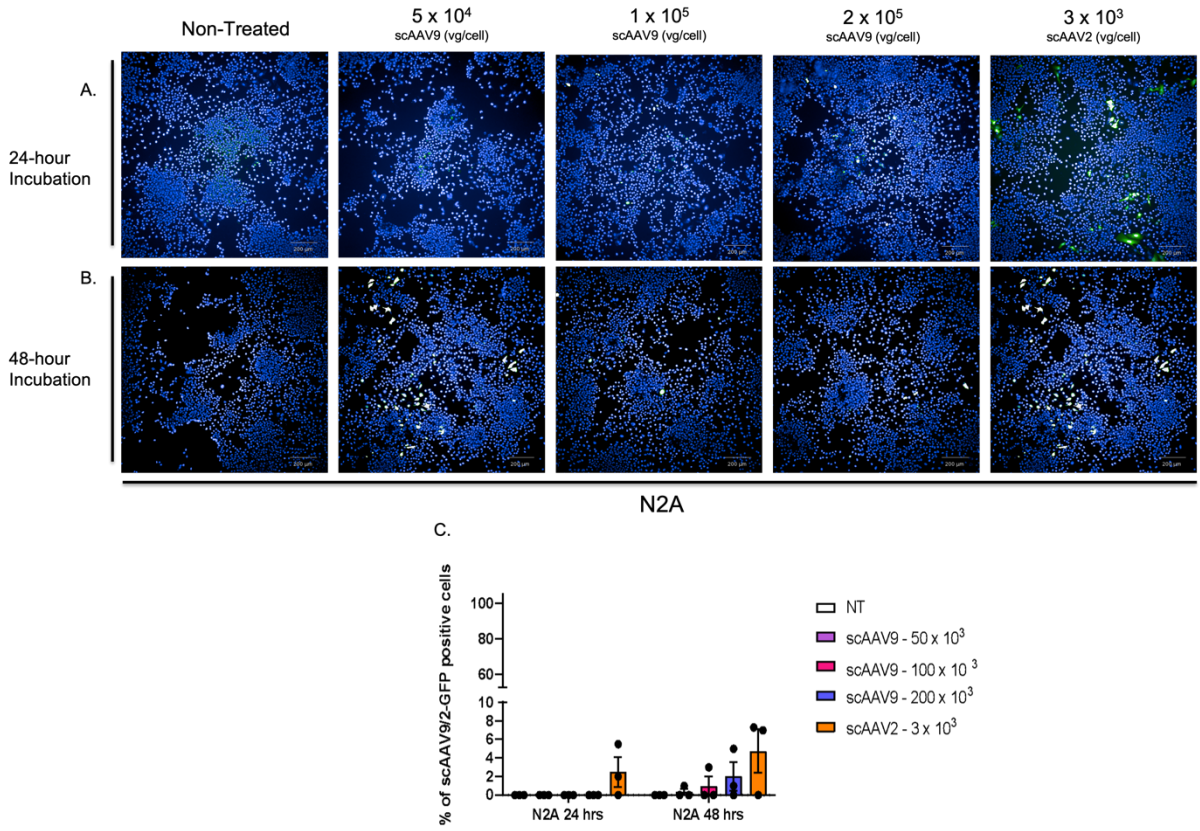

Figure 3.18: ***scAAV9-GFP transduction efficiency was limiting in N2A cell line across all conditions*** *– N2A cells were transduced with scAAV9-GFP across a range of MOI's (5 x 10^4 – 2 x 10^5) over a (A). 24-hour and (B) 48-hour period. Cells were fixed with 4% paraformaldehyde before being imaged on the Incell microscope (10x). Scale bar is at 200 µm. (C) Percentage of scAAV-GFP positive cells was counted on Columbus software and percentage to that of total cells was plotted on the graph (biological N=3).*

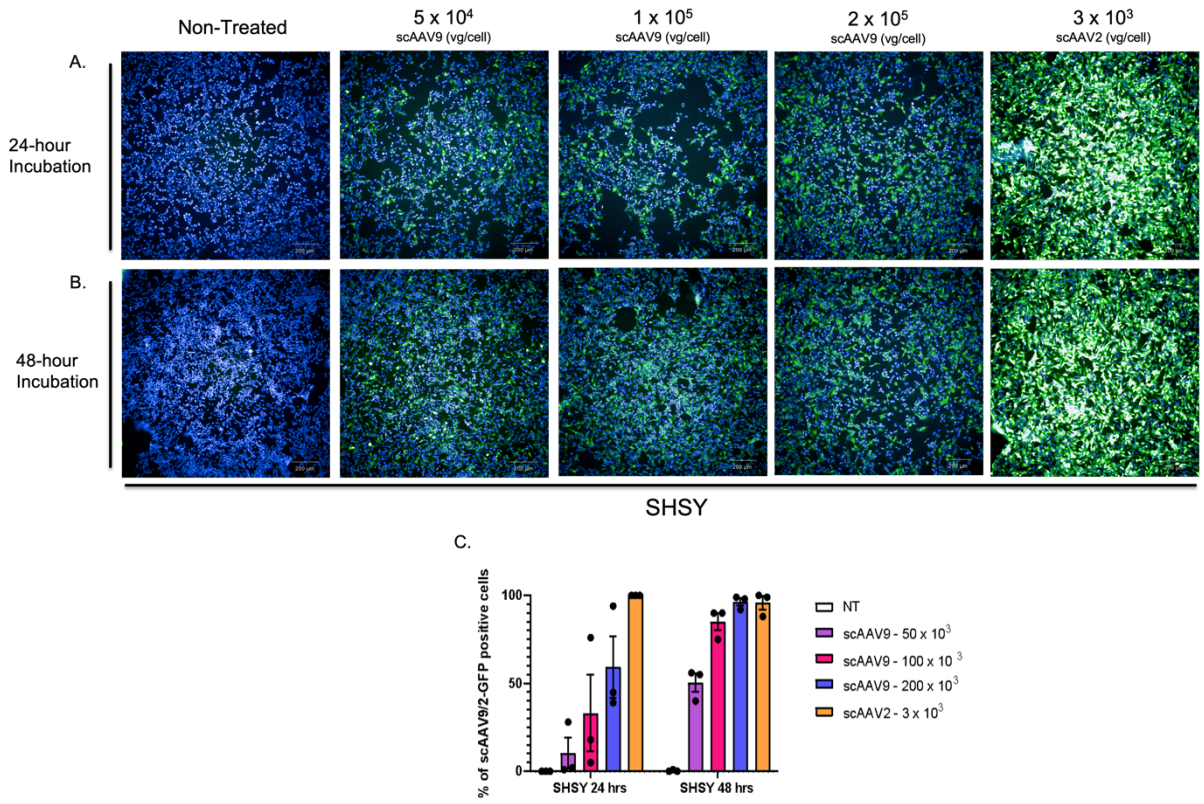

Figure 3.19: ***2 x 10^5 of scAAV9-GFP shows highest count of GFP positive cells in the SHSY cell line after 48 hours*** *– SHSY cells were transduced with scAAV9-GFP across a range of MOI's (5 x 10^4 – 2 x 10^5) over a (A). 24-hour and (B) 48-hour period. Cells were fixed with 4% paraformaldehyde before being imaged on the Incell microscope (10x). Scale bar is at 200 µm. (C) Percentage of scAAV-GFP positive cells was counted on Columbus software and percentage to that of total cells was plotted on the graph (biological N=3).*

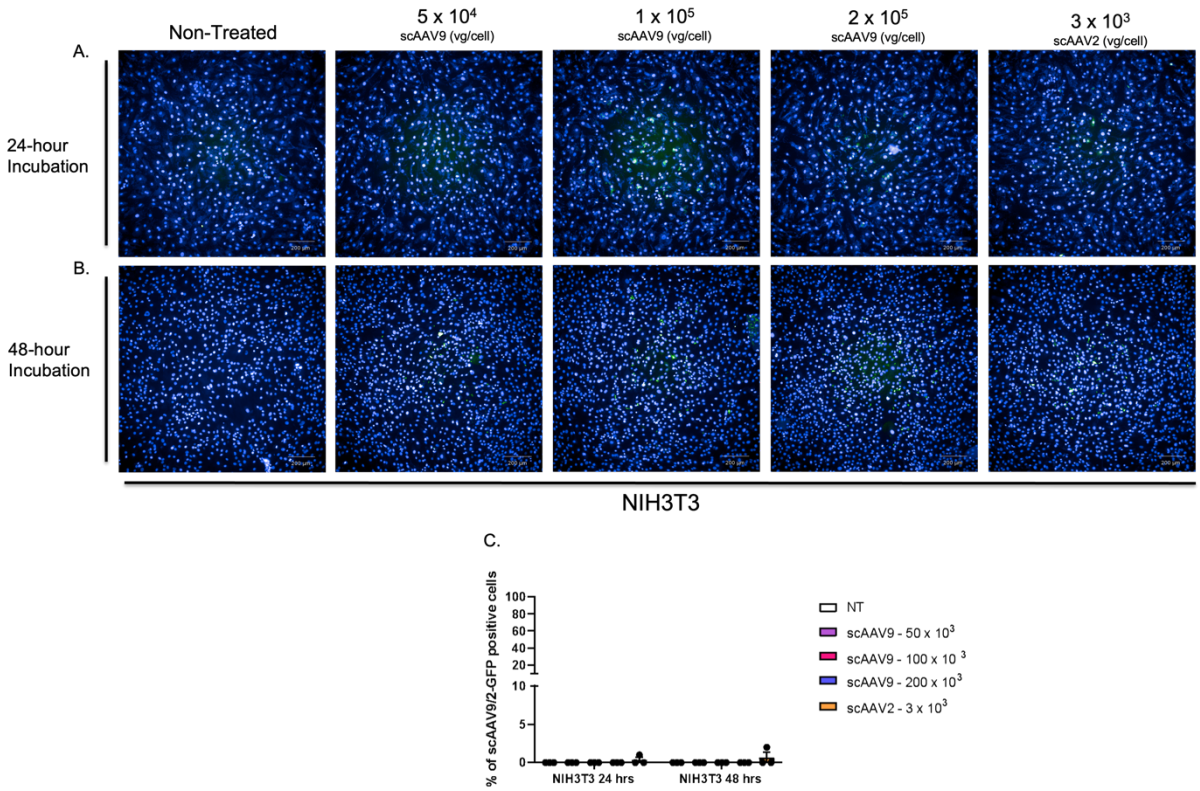

Figure 3.20: scAAV9-GFP transduction efficiency was limiting in NIH3T3 cell line across all conditions – *NIH3T3 cells were transduced with scAAV9-GFP across a range of MOI's (5 x 10^4 – 2 x 10^5) over a (A). 24-hour and (B) 48-hour period. Cells were fixed with 4% paraformaldehyde before being imaged on the Incell microscope (10x). Scale bar is at 200 µm. (C) Percentage of scAAV-GFP positive cells was counted on Columbus software and percentage to that of total cells was plotted on the graph (biological N=3).*

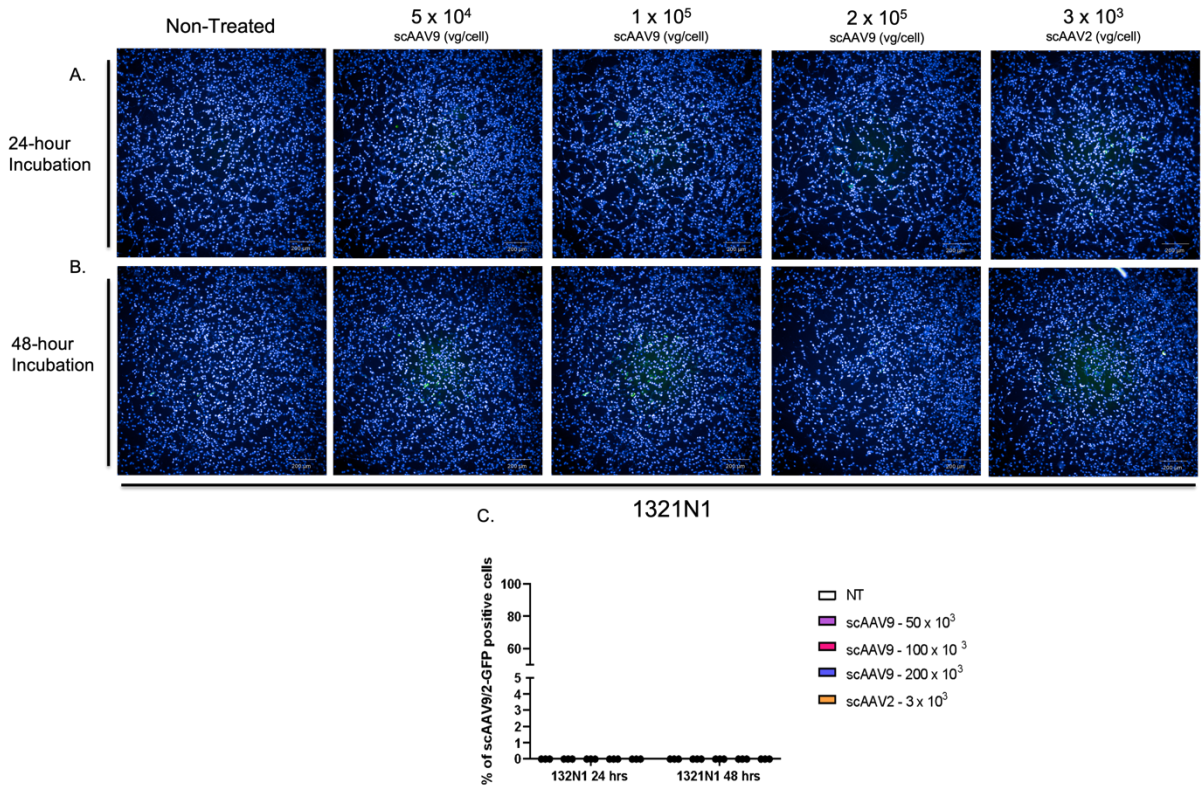

Figure 3.21: scAAV9-GFP transduction efficiency was limiting in 1321N1 cell line across all conditions *– 1321N1 cells were transduced with scAAV9-GFP across a range of MOI's (5 x 10^4 – 2 x 10^5) over a (A). 24-hour and (B) 48-hour period. Cells were fixed with 4% paraformaldehyde before being imaged on the Incell microscope (10x). Scale bar is at 200 µm. (C) Percentage of scAAV-GFP positive cells was counted on Columbus software and percentage to that of total cells was plotted on the graph (biological N=3).*

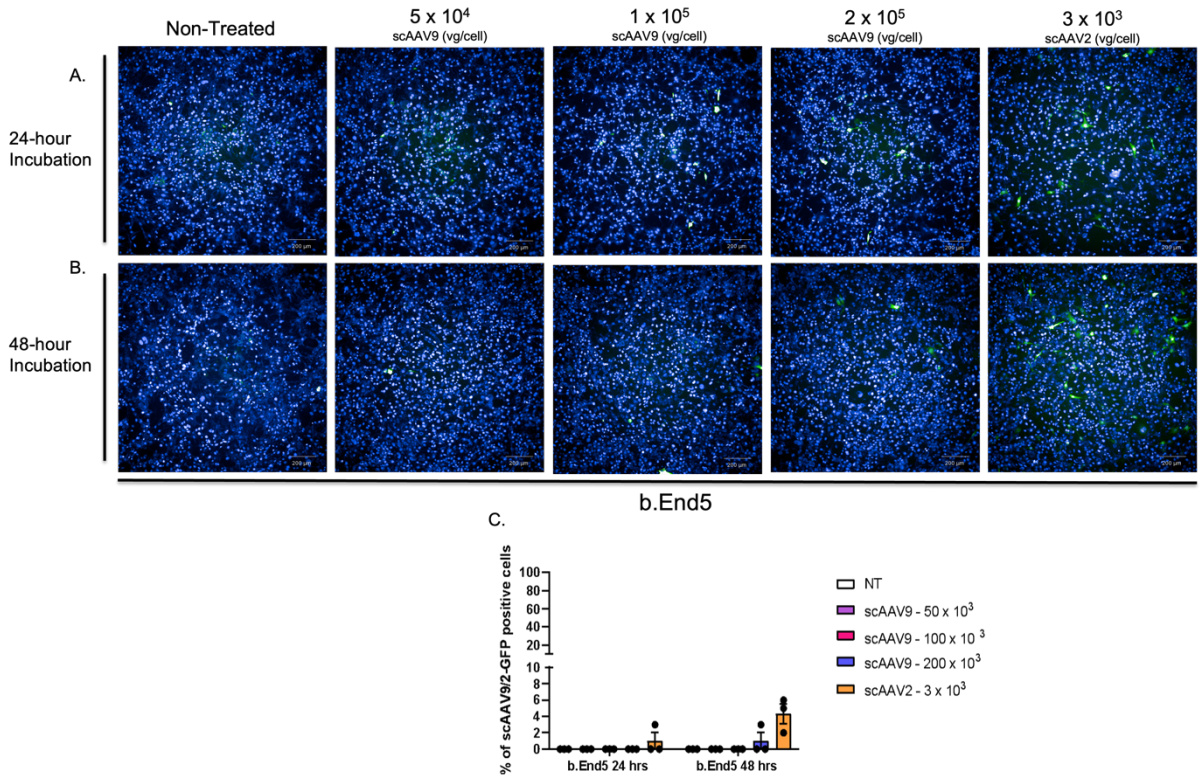

Figure 3.22: ***scAAV9-GFP transduction efficiency was limiting in b.End5 cell line and shows minor transduction in scAAV2*** – b.*End5 cells were transduced with scAAV9-GFP across a range of MOI's (5 x 10^4 – 2 x 10^5) over a (A). 24-hour and (B) 48-hour period. Cells were fixed with 4% paraformaldehyde before being imaged on the Incell microscope (10x). Scale bar is at 200 µm. (C) Percentage of scAAV-GFP positive cells was counted on Columbus software and percentage to that of total cells was plotted on the graph (biological N=3).*

3.3 Discussion

The aim of this chapter was to characterise potentially novel AAV9 target receptors, identified from preliminary data generated by our lab, in terms of their expression in neuronal cell lines. The selected neuronal lines were then used to validate AAV9 transduction efficiency. Along with the recently published AAVR receptor (Pillay, Meyer et al. 2016), preliminary data presented here identified SDC4, ICAM1 and SLC7A2 as potential AAV9 interactome targets, which were differentially regulated after AAV9 infection. This chapter has optimised, generated and tested the tools that would be required to further investigate these targets. Additionally, cell lines were screened to identify permissive and non-permissive lines to further investigate these targets in overexpression and knockdown studies.

Membrane proteins are notorious for being challenging proteins to characterise as a result of their hydrophobic regions, flexibility and lack of structural integrity (Carpenter, Beis et al. 2008, Wang, Zhang et al. 2022). Endogenous AAVR detection required limited optimisation with the Abcam AAVR antibody as it was reliable in both immunoblotting and immunofluorescence at the recommended dilutions (Figure 3.1). SLC7A2 and ICAM1 endogenous expression was detected by immunoblots in the HeLa cell line, however they were not effective for immunofluorescence labelling (Figure 3.6C and 3.8D). An optimisation step to suggest for potential immunofluorescence detection is the use of an alternate fixation methods as reagents like paraformaldehyde, although optimal for conserving cellular morphology due to being a chemical cross-linker, can denature proteins and affect antigen availability (Qin, Jiang et al. 2021). Alternate fixation reagents to test are methanol, acetone and glyoxal (Richter, Revelo et al. 2018). For the Santa Cruz SDC4 antibody, although mRNA levels of SDC4 showed successful knockdown of SDC4 expression as a result of SDC4-targetd siRNA, validating the effectiveness on a protein level and determining antibody specificity was a challenge due to the antibodies being ineffective in detecting endogenous SDC4 signal in any of the tested assays and cell lines (Figure 3.3). As a result, it prevented any form of characterisation of the neuronal cell lines in relation to SDC4 endogenous expression levels. Optimisation was attempted via the use of non-enzymatic disassociation reagents to preserve protein integrity and temperature conditioning to optimise protein folding favourable to the

antibody. However, again no SDC4 signal could be detected (Figure 3.11). Unexpectedly, analysis of tissue from mice indicated that the expression of endogenous SDC4 was capable of being detected via immunoblotting (Figure 3.14). As a result, it can be proposed that the lack of signal from the cell lines was as a result of the lines naturally having a low level of expression of SDC4. Literature has limited information on cell lines which express SDC4. Alternate antibodies to be tested for SDC4, such as in the Yang, Liu et al. (2021) study which used a Proteintech SDC4 antibody (11820-1-AP) could be validated in future studies for characterisation of cell lines. Intriguingly, the height of overexpressed SDC4 was higher (35 kDa) than what was predicted from literature (22kDa). This could be as a result of the protein being overexpressed undergoing post-translational modifications (PTMs) which results in an altered molecular weight. PTMs vary from oxidation of amino acids to form disulphide bonds to attachment of heavy oligosaccharide chains (Kumar, Narayanan et al. 2020). Due to being an alternate molecular weight, it could be suggested that the overexpressed SDC4 protein undergoes different PTMs due to excess protein synthesis.

Due to membrane proteins being challenging to isolate, lysis optimisation is required for effective transmembrane protein characterisation (Rampado, Giordano et al. 2022). The RIPA buffer used contained 1% Triton X-100 which is an effective lysis agent as it solubilises all membranes which is crucial for the analysis of membrane proteins (Koley and Bard 2010). It has been suggested that the detergent could be mis-folding the target protein of interest and obstructing the epitope region which will affect the binding of the antibody (Stangl, Veerappan et al. 2012). Future optimisation would be to test alternate detergents, such as NP-40 or CHAPs, to determine if the lysis agent is the causative agent for the lack of signal. An additional component to be optimised is the DTT reducing agent as the agent may be reducing bonds which are essential for the protein's stability and correct folding. As a result of this incorrect folding, the epitope of the SDC4 protein may be altered and as a result make the SDC4 antibody unable to bind. Tris(2-carboxyethyl)phosphine (TCEP) is a frequently used reducing agent which could act as a replacement (Liu, O'Mara et al. 2010). TCEP is a potent reducing agent and irreversible (as other agents, such as DTT, can decay allowing disulphide bonds to reform) which can be a factor for the detection of sensitive target proteins (Liu, Wang et al. 2016).

The data from the mouse tissue study suggest that the expression pattern of each target protein predominately increases with mouse age in all tissues analysed (Figure 3.13 – 3.16). This was interesting due to neonatal mice, having a known higher transduction efficiency of AAV9 to that of adult mice, having no detectable expression of AAVR in any of the CNS tissue. A reason for this result could be that due to the low levels of AAVR, AAV9 undergoes an alternate independent-AAVR transduction pathway which could increase the vectors efficiency. This would suggest that the capsid has a multimodal entry pathway, as suggested in the Dudek, Pillay et al. (2018) study. This could also support the findings of the lack of AAVR expression at all ages in the liver tissue which is known as one of the major off-target tissue in AAV9 *in vivo* research. Alternatively, a reason for the increased transduction to the CNS of neonates could be as a result of a more permeable blood-brain barrier (BBB) at the neonatal age, in turn allowing increased AAV9 delivery to the CNS. However, recent literature suggests that the neonatal BBB is developed and functional at a foetal stage (Saunders, Dreifuss et al. 2014, Mallard, Ek et al. 2018), meaning that both neonatal mice and adult mice BBB's are both functionally selective. Similarly, SDC4, ICAM1 and SLC7A2 expression increases with age with specific tissue conditions but appear to both peak in expression at the p15 age in liver tissue. This suggested that the protein expression level of neonatal and adult mice have a similar aged protein expression pattern in the liver. Overall, the data suggested that at a neonatal age, due to the lack of AAVR expression, AAV9 potentially undergoes an AAVR-independent entry pathway to the CNS and liver of neonatal mice.

Based on the fact that AAV9 has wide neuronal tropism, the screening of neuronal cell lines *in vitro* should, in theory, allow the identification of AAV9 permissive cell lines. From the neuronal cell lines selected, the SHSY cell line was identified as a novel permissive cell line (Figure 3.19). The endogenous expression level of AAVR in the SHSY and HeLa cell line did indicate that these lines would be more compatible for scAAV9 transduction based on what was shown in the Pillay et al. (2017) study. Intriguingly, the HeLa cell line was the only cell line to have endogenous expression of the other targets ICAM1 and SLC7A2. Given that these potential targets are the focus of this thesis, HeLa cells were therefore the more favourable permissive line to be used as an *in vitro* model for future studies, including siRNA-knockdown and CRISPR-knockout studies. Although this line had the broadest expression of these target proteins, SHSY's had the highest transduction efficiency in the same MOI and timeframe (at

100% GFP positive cells) which has never been stated in literature as being a permissive line. This could be as a result of having the highest endogenous expression of AAVR. It could be theorised that this cell line may be highly permissive because it also has a higher expression of other interactome targets which could enhance viral adsorption and entry. Determining if the HeLa and SHSY cell line have the highest expression of the other published interactors, such as galactose (Shen, Bryant et al. 2011) and laminin (Akache, Grimm et al. 2006), would enable a further protein screen to make identifying permissive lines for the vector easier for future studies. Due to the SHSY cell line having a strong AAV9 transduction efficiency, the cell line would be a suitable model for the identification of novel AAV9 interactors via an siRNA library screen which could be performed on a variety of targets using a 96-well or a 384-well plate in which SHSY's transfected with siRNA are then transduced with AAV9 to identify novel targets, similarly achieved in the Mano, Ippodrino et al. (2015) study. These results could be further supported with co-immunoprecipitation and other interaction studies. Except for these two cell lines, the other neuronal cell lines showed limited to no transduction. It can be assumed that the lack of endogenous expression of AAVR would have impeded viral entry. An alternate novel transduction technique shown in the Lee, Robinson et al. (2018) study, referred to as substrate-mediated gene delivery (reverse transduction), could have been used to increase the transduction efficiency of the viral vector. Because of this, attempting a reverse transduction of the cell lines in this study would be intriguing to determine if transduction in both permissive and non-permissive cell lines could be improved.

As a result of these transduction assays, HeLa and SHSY cell lines were identified as permissive cell lines to AAV9 while the N2A, NIH3T3, 1321N1 and b.End5 cell lines were classed as non-permissive cell lines. The permissive cell lines were carried over for an siRNA screen and CRISPR-KO generation while the non-permissive cell lines will be used for the overexpression study.

4 Modulation of novel target receptors in non-permissive cell lines had no effect on viral transduction

4.1 Introduction

Overexpression studies have become a prevalent genetic tool for investigating genes in relation to biological pathways (Parr-Brownlie, Bosch-Bouju et al. 2015). The main concept of this tool is the introduction of foreign DNA for a particular target protein which the cell naturally transcribes and translates resulting in an elevated production of the transfected target protein (Prelich 2012). In viral vector interactome validation studies, the overexpression tool is typically used to elevate transduction of viral vectors to particular *in vitro* models to determine the target proteins relevance to the vectors functional pathway (Meisen, Nejad et al. 2020) (Figure 4.0). This technique was achieved in the Pillay, Meyer et al. (2016) study which showed the overexpression of AAVR in non-permissive cell lines elevated the transduction efficiency of the majority of the AAV serotypes. In the previous chapter, the cell lines N2A, NIH3T3, 1321N1 and b.End5's were identified as non-permissive to AAV9 transduction. Given that the expression levels of ICAM1, SDC4 and SLC7A2 were dysregulated in response to AAV9 transduction, it was hypothesised that these targets could function as AAV9 receptors. The aim of this chapter was to design and optimise the overexpression tools required to determine if modulating these novel receptors would impact AAV9 transduction efficiency.

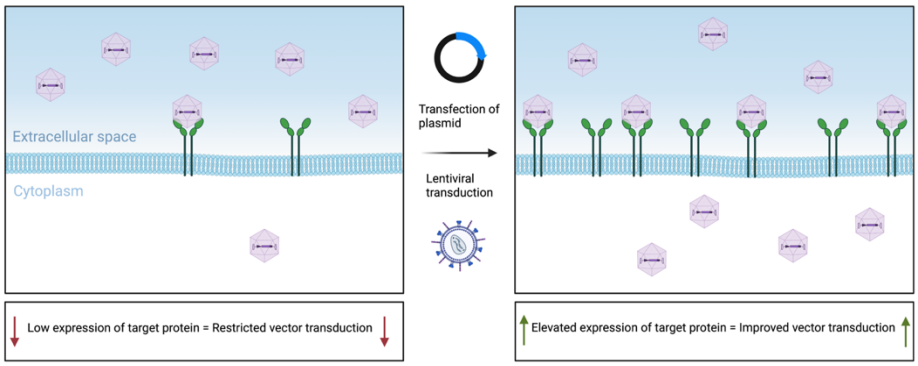

Figure 4.0: ***Model representation of overexpression studies*** *(Created with BioRender.com)*

4.2 Results

4.2.1 Effective transient overexpression was time-dependent and cell line transfection resistance was identified.

After generating overexpression constructs for AAVR, ICAM1, SDC4 and SLC7A2, the initial plan was to transiently transfect these vectors into non-permissive cells before performing the AAV9 transduction efficiency assay detailed in the previous chapter. However, there were concerns over the length of time the transient transfection would need to persist. Because scAAV9 transduction required 48-hours of incubation, and the transient transfection would need to be performed at least 24-hours prior, a time-course experiment was conducted to validate if overexpression remained consistent over a 72-hour period (24-hours for initial chemical transient transfection and 48-hours for scAAV9 transduction). This was validated in the HeLa cell line.

HeLa cells transfected with pCI_neo_HA_AAVR showed robust HA_AAVR overexpression 24 hours post transfection (Figure 4.1A). The level of overexpression increased 4.2-fold at 48-hours post transfection, but then waned by 72-hours. Cells transfected with pCI_neo_Myc_SDC4 showed strong Myc_SDC4 overexpression 24-hours post transfection. (Figure 4.1B). Transient overexpression peaked at 24-hours, then progressively decreased over the next 48 hours and 72-hours, reaching signal intensity 1.8-fold lower. Cells transfected with pCI_neo_ICAM1 showed strong over expression 24-hours post transfection and the signal remained consistent across all time points with a strong overexpressed signal of ICAM1 (Figure 4.1C). The 48-hour and 72-hour incubation periods showed a 1.3-fold increase in expression relative to that of the 24-hour intensity of signal. Cells transfected with pCI_neo_V5_SLC7A2 showed strong V5_SLC7A2 signal at 24-hours and the signal increased 2-fold at 48-hours (Figure 4.1D). By 72-hours, however, the signal showed only a 1.3-fold increase in expression relative to that of the 24-hour signal intensity.

Chemical transfection requires receptor-complex interactions on the cell surface and certain *in vitro* lines are difficult to transfect as a result of the lack of these complementary cell surface interactions (Maurisse, De Semir et al. 2010). Because of this, the transfection efficiencies of the non-permissive lines were investigated. The b.End5 non-permissive cell line

was not carried through due to their slow growth rate and difficult maintenance. Polyethylenimine (PEI) is the gold-standard chemical transfection reagent due to its high transfection efficiency in multiple cell lines, low toxicity and low cost. An alternate transfection reagent was Lipofectamine 2000 (Invitrogen, UK) which is a cation-lipid reagent which forms liposomes, referred to as lipoplexes, which results in efficient transfection delivery (Maurisse, De Semir et al. 2010). Both reagents were tested to determine transfection efficiency across the non-permissive cell lines and HeLa cells. Cells were transfected with the EGFP reporter plasmid pCMV-EGFP.

HeLa cells showed approximately 20% of cells per field of view were transfected with the PEI reagent while there was approximately 28% transfection efficiency with lipofectamine (Figure 4.2A). The N2A cells showed clusters of approximately 19% of cells GFP-positive with PEI while lipofectamine showed approximately 39% of GFP-positive cells per field of view (Figure 4.2B). The NIH3T3 cells showed no expression of GFP with either chemical reagent suggesting no transfection of pCMV-GFP (Figure 4.2C). Finally, the 1321N1 cell line showed approximately 7% of cells were GFP-positive after PEI transfection, while only approximately 1% of cells were GFP positive with Lipofectamine 2000 (Figure 4.2D).

Due to these non-permissive cell lines having limited transfection efficiency (Figure 4.2) and most of the transient expression decreasing over the experimental timeframe (Figure 4.1), it was decided to alter the experimental plan from transient transfection methods to the generation of stable cell lines using lentiviral transduction.

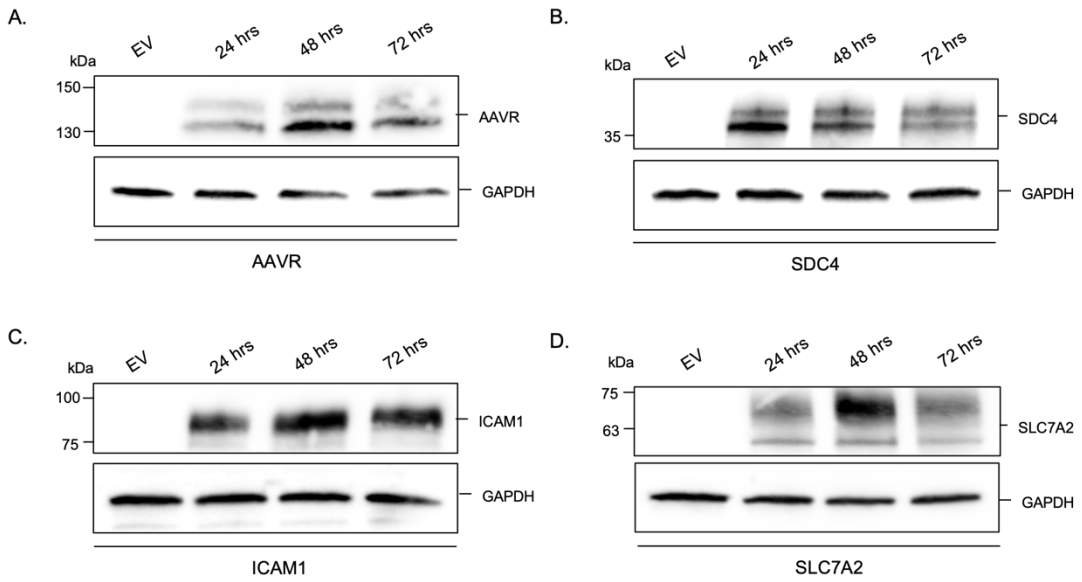

Figure 4.1: ***Transient overexpression of targets is limiting at 72 hours***–*HeLa cells were transfected with empty-vector (EV) and with (A) pCI_neo_Myc_SDC4 (B) pCI_neo_HA_AAVR and (C.) pCI_neo_ICAM1. Treated cells were subjected to SDS-PAGE and immunoblot. Blots were incubated with commercial primary antibodies using anti-Ha, anti-Myc, Abcam ICAM1 and anti-V5.*

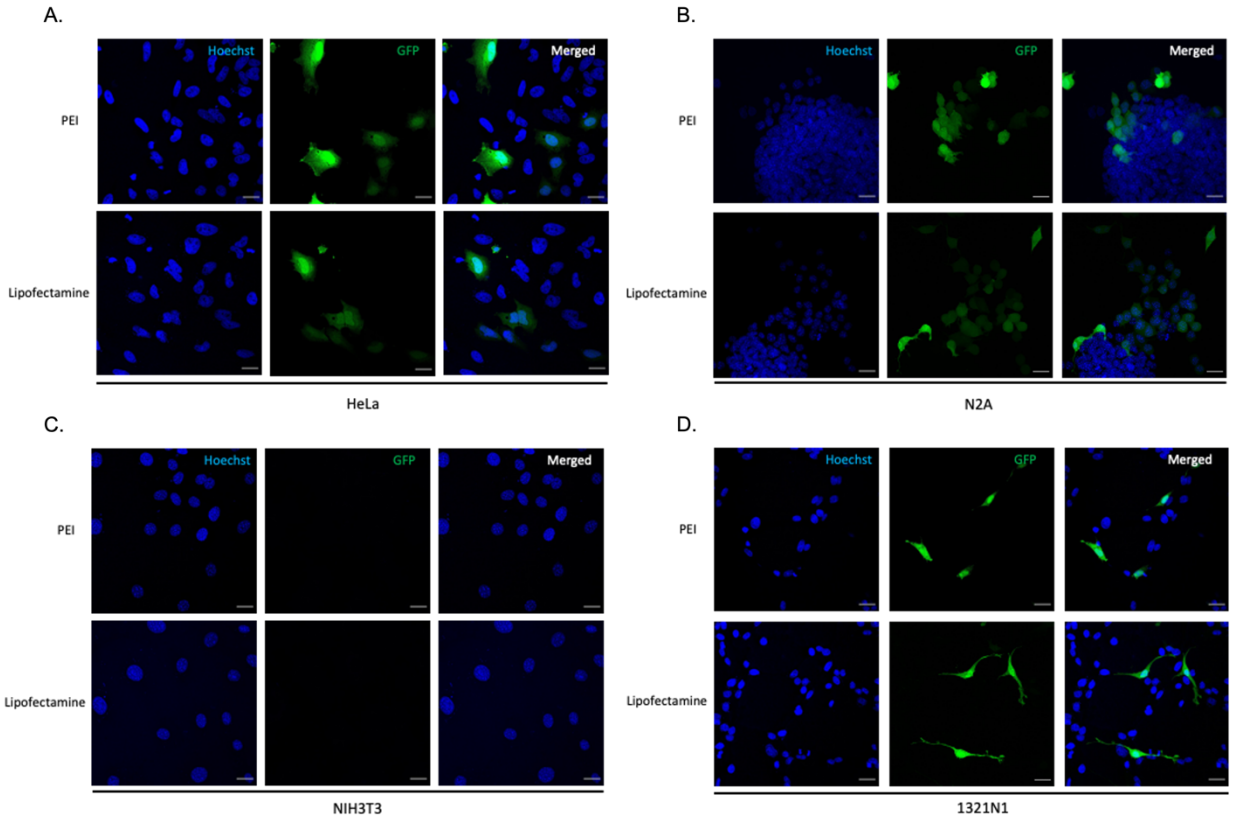

Figure 4.2: ***Transfection efficiency of non-permissive cell lines is restricted with both transfection reagents***– *HeLa cells were transfected with pCMV_GFP using both polyethyleneimine (PEI) and lipofectamine and left for 24 hours. Transfected cells were fixed with 4% paraformaldehyde before being imaged via confocal microscopy (63x). Scale bar is at 38 µm*

4.2.2 Generation of lentiviral vectors

Lentiviral plasmids were designed and purchased through VectorBuilder. Plasmids were designed to contain a puromycin resistance ORF to enable selection of transduced cells. To validate these plasmids prior to viral production, HeLa cells were transfected with these plasmids and left for 48-hours before overexpression was assessed by immunoblot. Overexpression of HA_AAVR, (Figure 4.3A), Myc_SDC4 (Figure 4.3B) and FLAG_ICAM1 (Figure 4.3C) was detected after transfection with the respective lentiviral plasmids. V5_SLC7A2 was also detected, but as a smeared signal across 75 kDa and 63 kDa in the LV_V5_SLC7A2 transfected cells (Figure 4.3D). This smear is likely a result of the protein being heavily glycosylated (Bensimon, Pizzagalli et al. 2020). Having confirmed that the designed plasmids are functional, lentiviral vectors for each target protein were generated. The titre of the viral vectors was quantified via qPCR, as shown in Table 4.1.

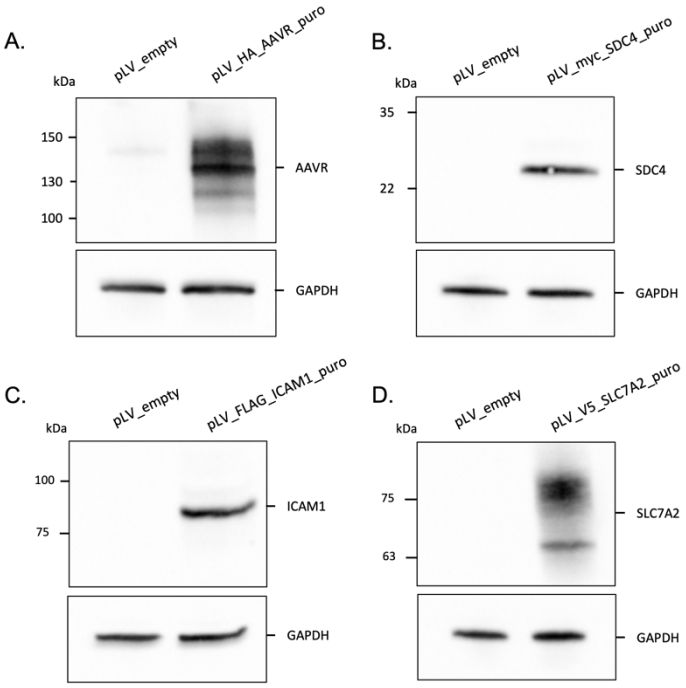

Figure 4.3: ***Validation of functionality of lentiviral plasmids*** *–HeLa cells were transfected with lentiviral empty-vector and with (A) pLV_Myc_SDC4_puro (B) pLV_HA_AAVR_puro (C.) pLV_FLAG_ICAM1_puro and (D) pLV_V5_SLC7A2_puro and left for 48 hours. Treated cells were subjected to an SDS-PAGE and immunoblot. Blots were incubated with commercial antibodies Anti-Myc, Anti-FLAG, Anti-V5 and Abcam AAVR).*

Table 4.1: ***Lentiviral titre for each lentiviral virus generated.***

Lentivirus	Titre (TU/ml)
HA_AAVR_puro	1.2×10^8
Myc_SDC4_puro	7.8×10^7
FLAG_ICAM1_puro	7.7 x 107
V5_SLC7A2_puro	7.5×10^7

4.2.3 Multiplicity of Infection (MOI) optimisation in non-permissive cell lines

The 3rd generation lentiviral system vesicular stomatitis virus G glycoprotein pseudotype (LV VSV-G) was used as the designed vector interacts with the ubiquitous cellular receptor phosphatidylserine which enables wide tropism of both dividing and non-dividing cells (Gutierrez-Guerrero, Cosset et al. 2020). LV vectors have been used as a tool to modify cells *in vitro* as a result of their capability to integrate their transgene, via the retroviral integrase enzyme, into the host genome of transduced cells resulting in stable transgene expression (Sanber, Knight et al. 2015). Although LV VSV-G has wide tropism, its transduction efficiency is varied across all cell lines as a result of varied cell surface interactions necessary for transduction. Because of this, an MOI optimisation step was required to determine the quantity of virions for effective transduction for each cell line. Once the optimal MOI was identified, this enabled the efficient generation of overexpressing stable cell lines for each target protein. The generated lentiviral vectors were tested at an MOI of 1, 5, 10 and 20 vg/cell over a 48-hour incubation.

Although HeLa cells are somewhat permissive to AAV9, the transduction efficiency of approximately 35% of total cells gives an obvious window for improvement. For this reason, HeLa cells were transduced with LV vectors containing the target proteins of interest and also used as a control stable line for which to compare with the other non-permissive cell lines that were to be generated. Overexpression of HA_AAVR was detectable in the expected golgi region in the MOI of 1 and higher MOI's had strong golgi signal as well as cytoplasmic signal (Figure 4.4A). Cytoplasmic overexpression of Myc_SDC4 was shown in all MOI conditions and signal remained consistently high with no noticeable difference in signal intensity (Figure 4.4B). Overexpression of FLAG_ICAM1 was detected in the cytoplasm of all transduced cells which appeared to increase with the progressive rise in MOI (Figure 4.4C). Similarly, to HA_AAVR, the overexpression of V5_SLC7A2 was particularly localised to the perinuclear region, possibly localising to the golgi apparatus. This staining was evident in the 1 and 5 MOI doses and signal appeared to become more cytoplasmic at the higher MOI's, particularly at an MOI of 20 (Figure 4.4D).

In the N2A cell line (Figure 4.5), there was a poor level of transduction across all LVs and all MOI's (Figure 4.5A – 4.5D). HA_AAVR was the only lentiviral vector to show effective expression which increased in MOI concentrations (Figure 4.5A). Similarly, to the N2A cell line, the NIH3T3 cell line exhibited poor transduction efficiency. A limited number of cells showed detectable overexpression of HA_AAVR and Myc_SDC4 in the 1 vg/cell MOI which increased with higher MOIs (Figure 4.6A and 4.6B). The optimal MOI titre for these targets was at 20 MOI. FLAG_ICAM1 and V5_SLC7A2 showed very low transduction efficiency across all MOIs (Figure 4.6C and Figure 4.6D).

Intriguingly, the 1321N1 cell line showed effective transduction across all targets and MOIs (Figure 4.7A – 4.7D). HA_AAVR transduction could be detected at 1 MOI and appeared to have the highest level of overexpression at 20 MOI as golgi staining was most evident. Overexpression of Myc_SDC4 expression could be detected in all cells at an MOI of 1 and in the MOI range up till 20 MOI. 1321N1 cell transduced with LV-FLAG_ICAM1 displayed cytoplasm labelling of all cells at an MOI of 1 and in the range up till MOI of 20. V5_SLC7A2 staining could be detected in the cytoplasm of transduced cells and signal appears to increase respectively with increasing MOI. Interestingly, as the MOI increased, the V5_SLC7A2 signal became more evidently punctate in the cytoplasm (Figure 4.7D).

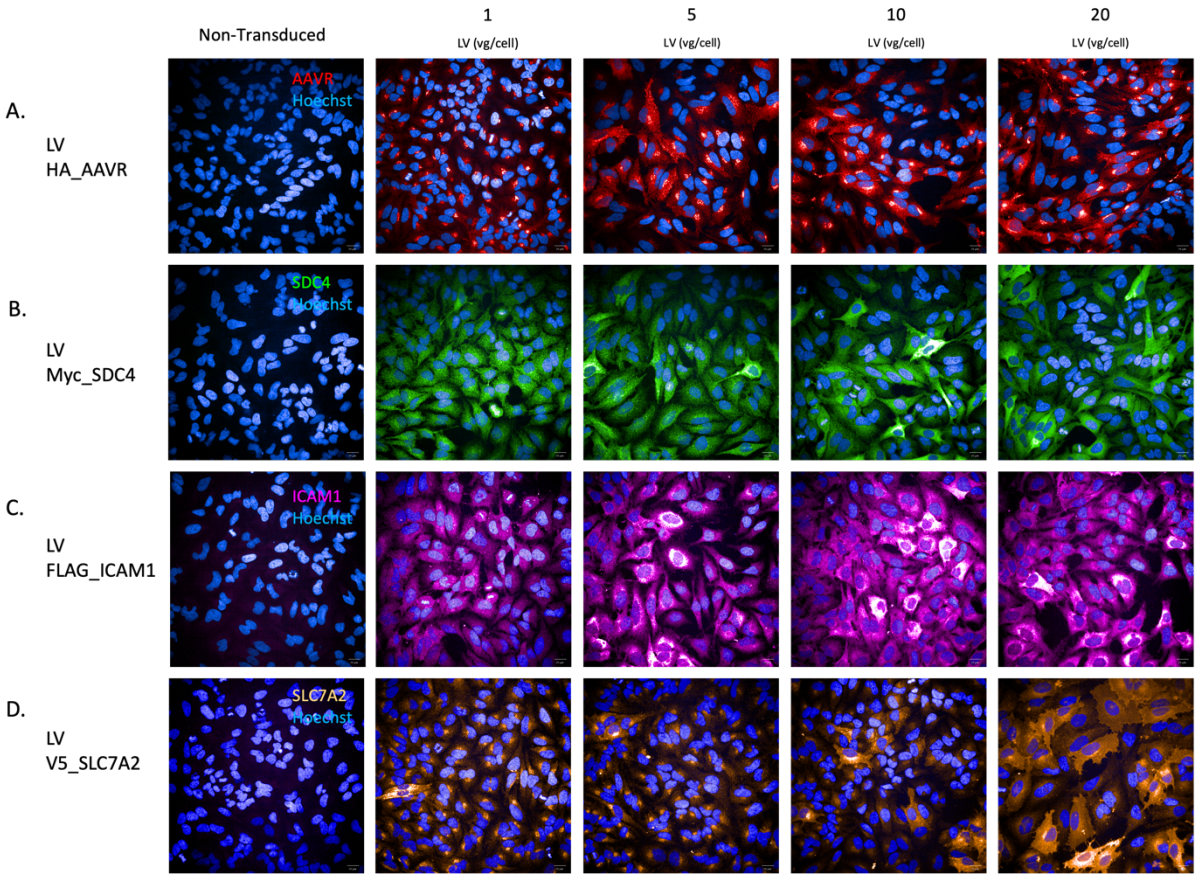

Figure 4.4: MOI optimisation of *lentiviral transduction in HeLa's* – *HeLa cells were transduced with (A) LV_HA_AAVR_puro (False-coloured red) (B) LV_Myc_SDC4_puro (C) LV_FLAG_ICAM1_puro (False-coloured magenta) or (D) LV_V5_SLC7A2_puro (false-coloured orange) and left for 48 hours at a range of MOIs (1– 20 vg/cell). Cells were fixed with 4% paraformaldehyde and incubated with their respective tagged antibodies (anti-Myc, Abcam AAVR, anti-FLAG and anti-V5) and imaged via the Phoenix OPERA (40x). Scale bar is at 100 µm.*

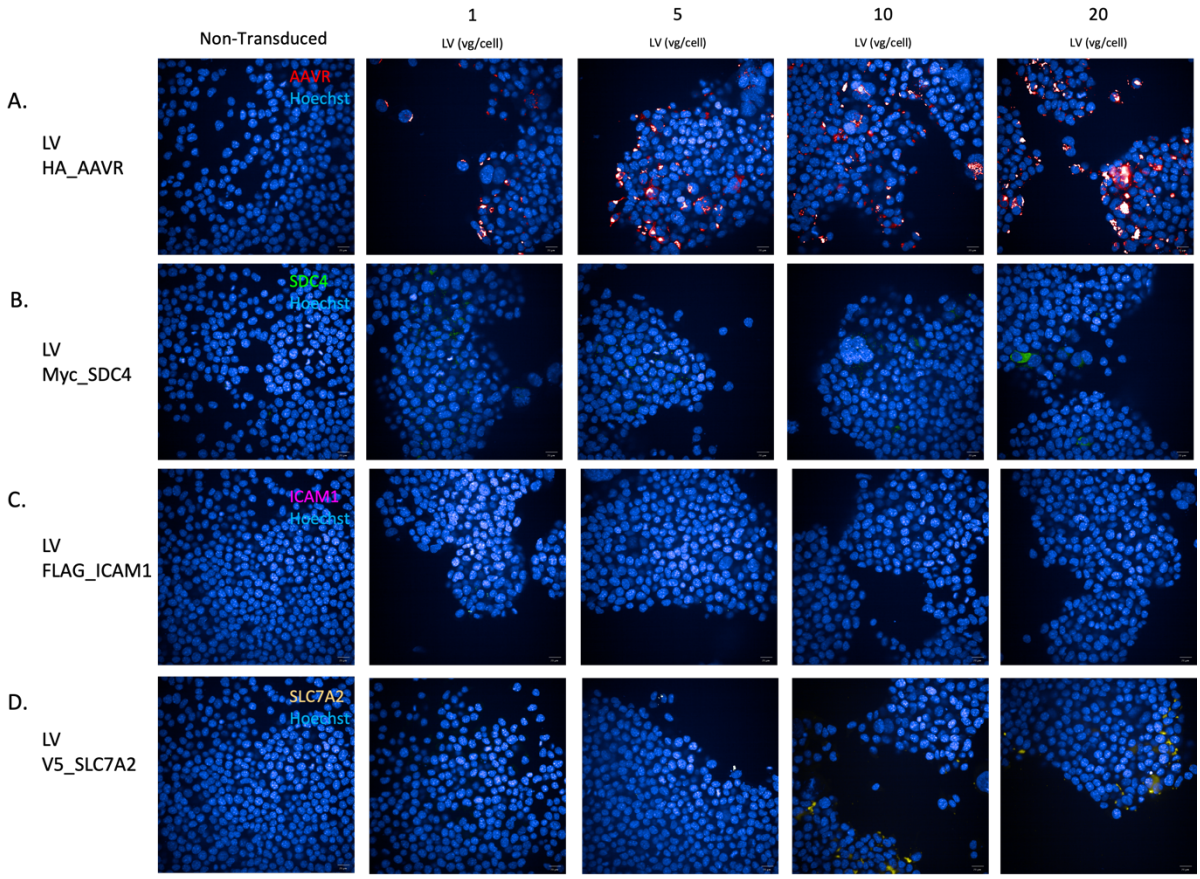

Figure 4.5: MOI optimisation of *lentiviral transduction in N2A's* *–N2A cells were transduced (A) LV_HA_AAVR_puro (False-coloured red) (B) LV_Myc_SDC4_puro (C.) LV_FLAG_ICAM1_puro (False-coloured magenta) and (D) LV_V5_SLC7A2_puro (False-coloured orange) and left for 48 hours at a range of MOIs (1-20 vg/cell). Cells were fixed with 4% paraformaldehyde and incubated with their respective tagged antibodies (anti-Myc, Abcam AAVR, anti-FLAG and anti-V5) and imaged via the Phoenix OPERA (40x). Scale bar is at 100 µm.*

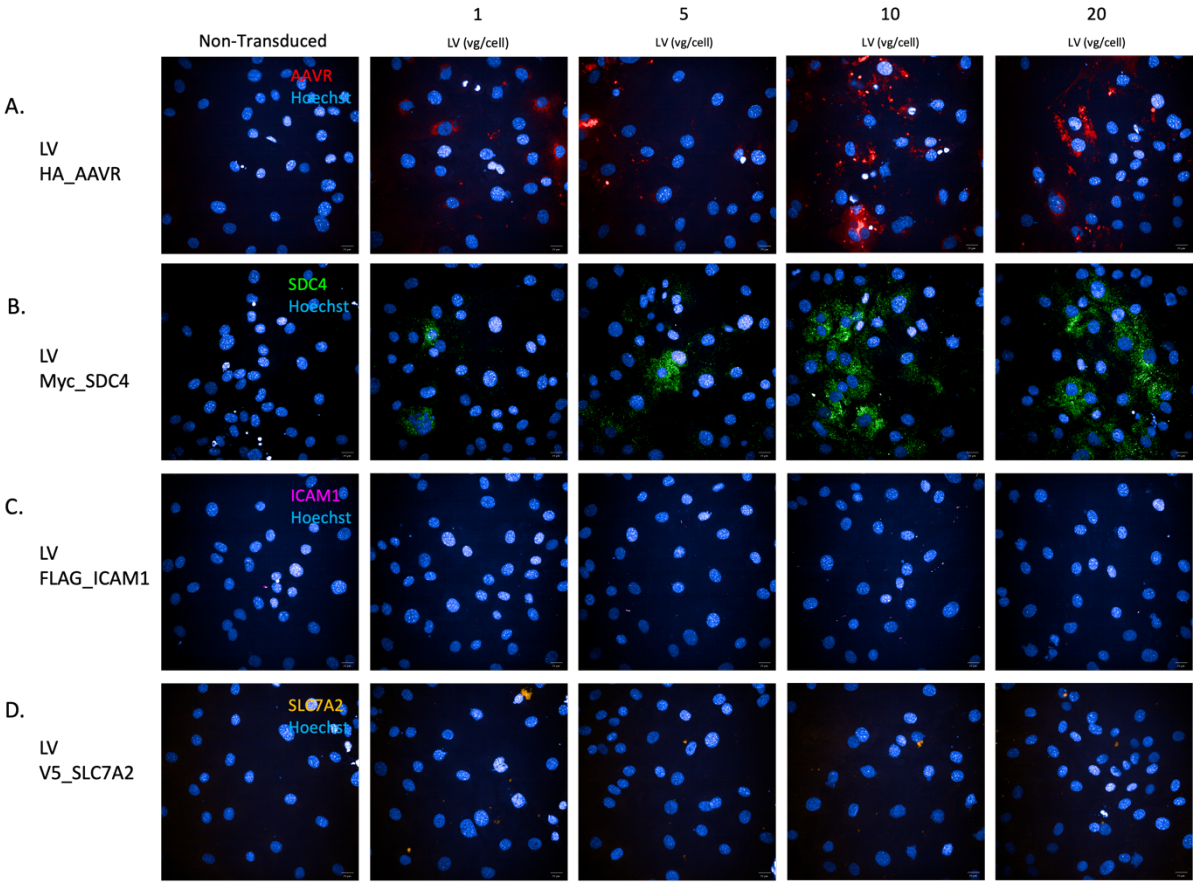

Figure 4.6: MOI optimisation of *lentiviral transduction in NIH3T3* *–NIH3T3 cells were transduced (A) LV_HA_AAVR_puro (False-coloured red) (B) LV_Myc_SDC4_puro (C.) LV_FLAG_ICAM1_puro (False-coloured magenta) and (D) LV_V5_SLC7A2_puro (False-coloured orange) and left for 48 hours at a range of MOIs (1-20 vg/cell). Cells were fixed with 4% paraformaldehyde and incubated with their respective tagged antibodies (anti-Myc, Abcam AAVR, anti-FLAG and anti-V5) and imaged via the Phoenix OPERA (40x). Scale bar is at 100 µm.*

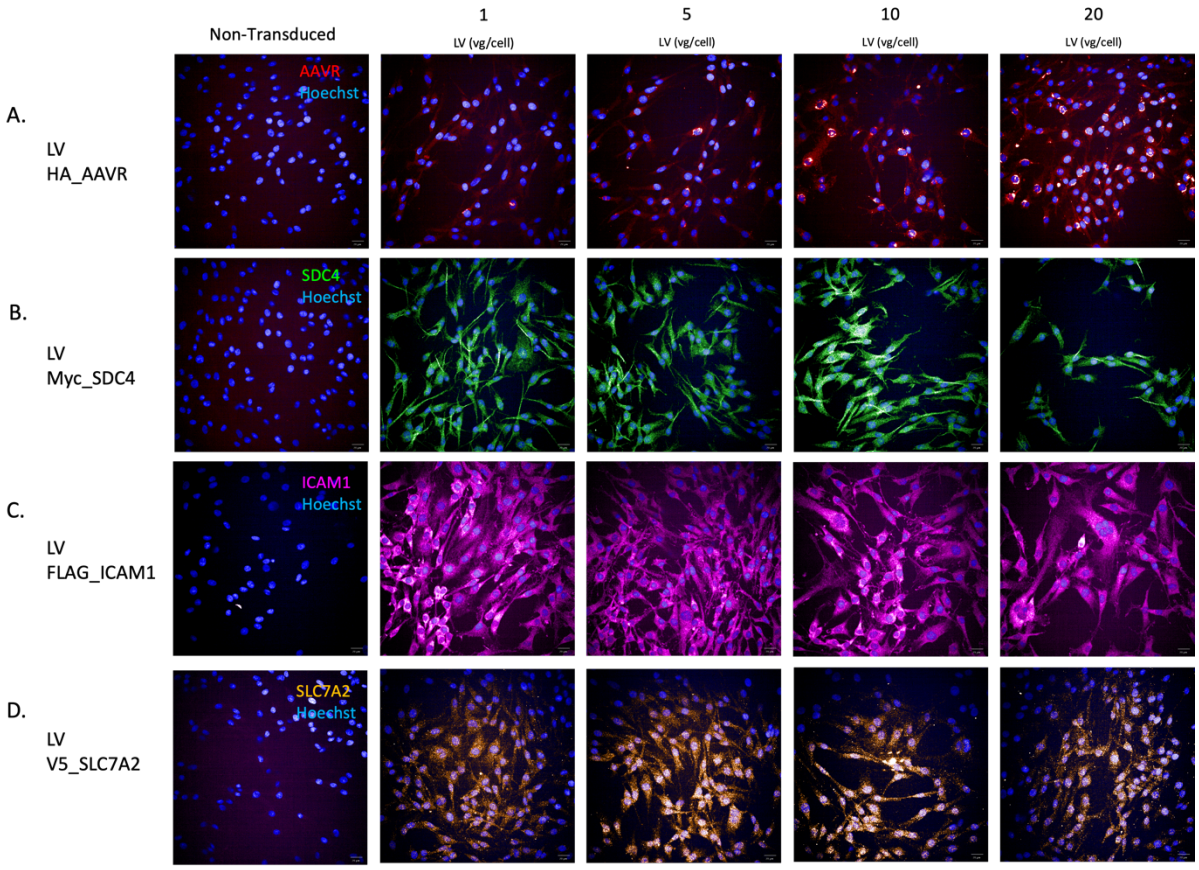

Figure 4.7: MOI optimisation of *lentiviral transduction in 1321N1* *–1321N1 cells were transduced (A) LV_HA_AAVR_puro (False-coloured red) (B) LV_Myc_SDC4_puro (C.) LV_FLAG_ICAM1_puro (False-coloured magenta) and (D) LV_V5_SLC7A2_puro (False-coloured orange) and left for 48 hours at a range of MOIs (1 -20 vg/cell). Cells were fixed with 4% paraformaldehyde and incubated with their respective tagged antibodies (anti-Myc, Abcam AAVR, anti-FLAG and anti-V5) and imaged via the Phoenix OPERA (40x). Scale bar is at 100 µm.*

4.2.4 Generation of HeLa stable cell lines

Following the MOI optimisation experiment, HeLa cells were transduced with each lentiviral vector at an MOI of 1. After 48-hours of transduction, the cells were replated in media containing an optimised concentration of 3 □g/□l puromycin for selective pressure of transduced cells. LV vectors integrate predominately at transcription start sites (TSSs) and CpG islands and multiple integration events can occur because of varied vector transduction per cell (Ballandras-Colas, Chivukula et al. 2022). In line with this, because single cells were not selected these stable lines consisted of a mixed pool of transduced cells meaning each cell had varied levels of stable expression due to varied quantity of integration events.

These HeLa stable lines were characterised for their level of target overexpression and distribution compared to controls. AAVR golgi signal could be detected in the wild-type cells, as shown in Figure 4.8A. Cells transduced with LV_HA_AAVR were shown to have elevated signal in the golgi regions and in the cytoplasm of selected cells. This was further validated via immunoblot which showed a strong signal in the HA_AAVR stable cell line at the expected height (Figure 4.8B). For SDC4, Myc_SDC4 HeLa stable cells showed strong signal in the cytoplasm of all transduced cells (Figure 4.9A). This was further confirmed via immunoblot which revealed signal at the predicted height in literature of 22 kDa (Figure 4.9B). For the ICAM1 stable cell line, the cell line had detectable signal unlike its wild-type condition and the labelling was localised at the cell membrane (Figure 4.10A). This overexpression was further confirmed via immunoblot. Overexpressed FLAG_ICAM1 band was displayed at the validated 80 kDa height (Figure 4.10B). Finally, for the SLC7A2 stable cell line, V5_SLC7A2 overexpression was demonstrated via cytoplasmic and membrane labelling (Figure 4.11A). Additionally, a change in cellular morphology could be observed in treated cells as well as a difference in overexpression levels per cell. This overexpression was further confirmed by immunoblot and overexpressed signal could be detected at the expected 70 kDa height (Figure 4.11B).

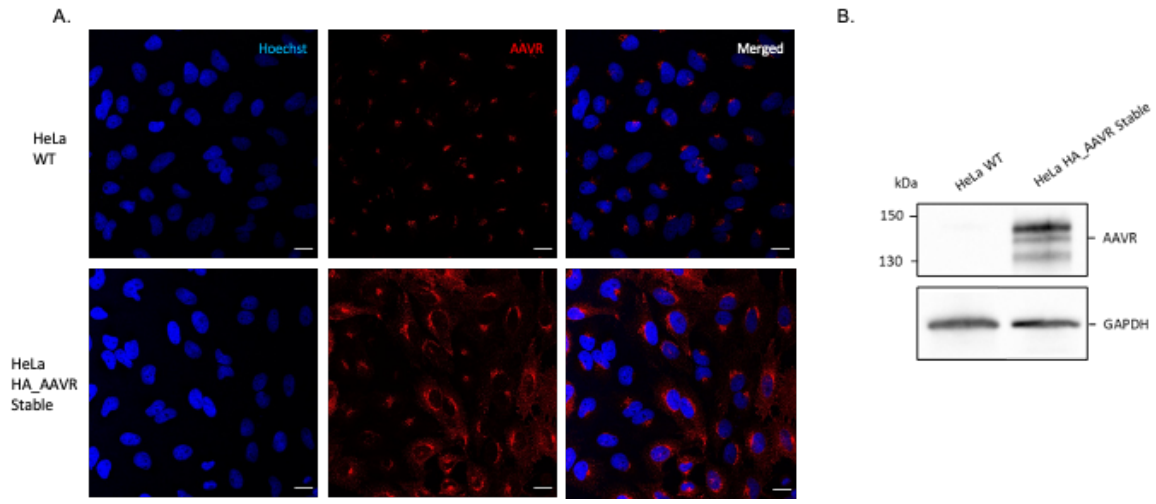

Figure 4.8: ***Generation of HeLa_HA_AAVR_puro stable cell line***–*(A) Puromycin-selected HeLa_HA_AAVR_puro was fixed with 4% paraformaldehyde and immunostained with Abcam AAVR before being imaged via confocal microscopy (63x) for anti-mouse Alexa 488) signal (False-coloured red). Scale bar is at 38 µm. (B) Stable cells were subjected to an SDS-PAGE and immunoblot. Blots were incubated with Abcam AAVR. GAPDH was used as a loading control.*

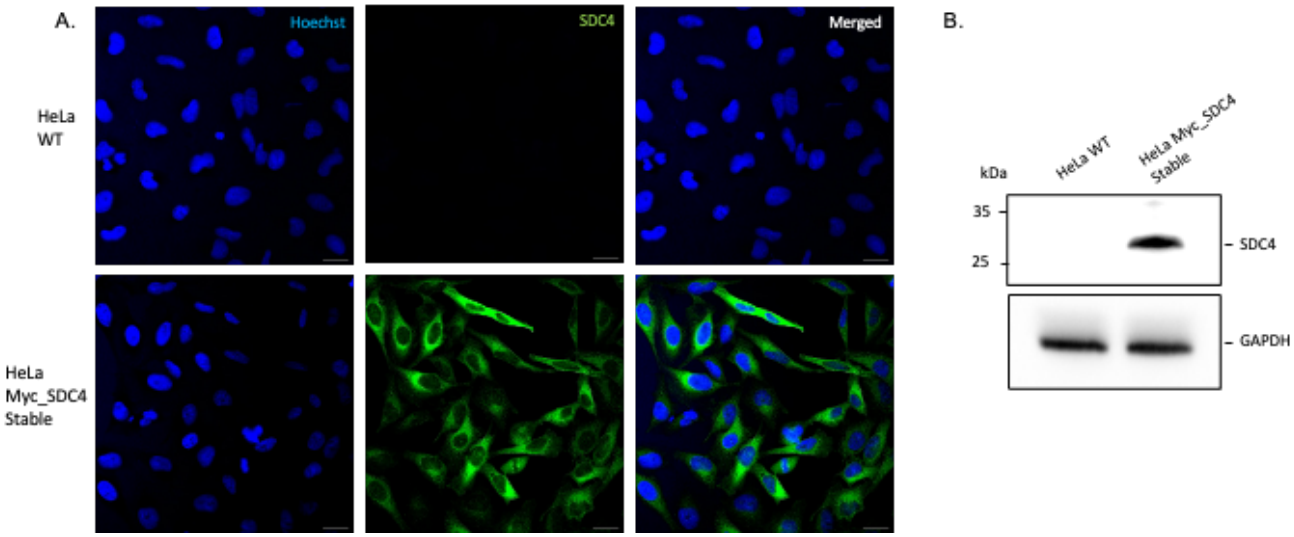

Figure 4.9: ***Generation of HeLa_Myc_SDC4_puro stable cell line***–*(A) Puromycin-selected HeLa_Myc_SDC4_puro were fixed with 4% paraformaldehyde and immunostained with Santa Cruz SDC4 before being imaged via confocal microscopy (63x) for anti-mouse Alexa488. Scale bar is at 38 µm. (B) Stable cells were subjected to an SDS-PAGE and immunoblot. Blot was incubated with Santa Cruz antibody. GAPDH was used as a loading control.*

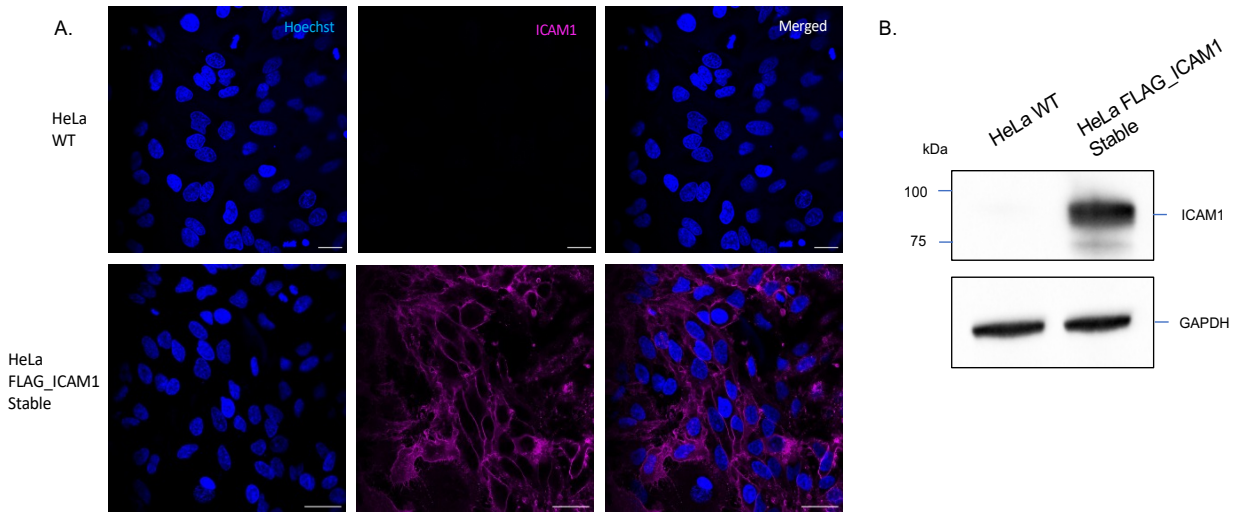

Figure 4.10: ***Generation of HeLa_FLAG_ICAM1_puro stable cell line***– *(A) Puromycin-selected HeLa_FLAG_ICAM1_puro were fixed and immunostained with Abcam ICAM1 before being imaged via confocal microscopy (63x) for anti-rabbit Alexa488 signal (false-coloured magenta) Scale bar is at 38 µm. (B) Stable cells were subjected to an SDS-PAGE and immunoblot. Blots were incubated with the primary antibody Abcam ICAM1.*

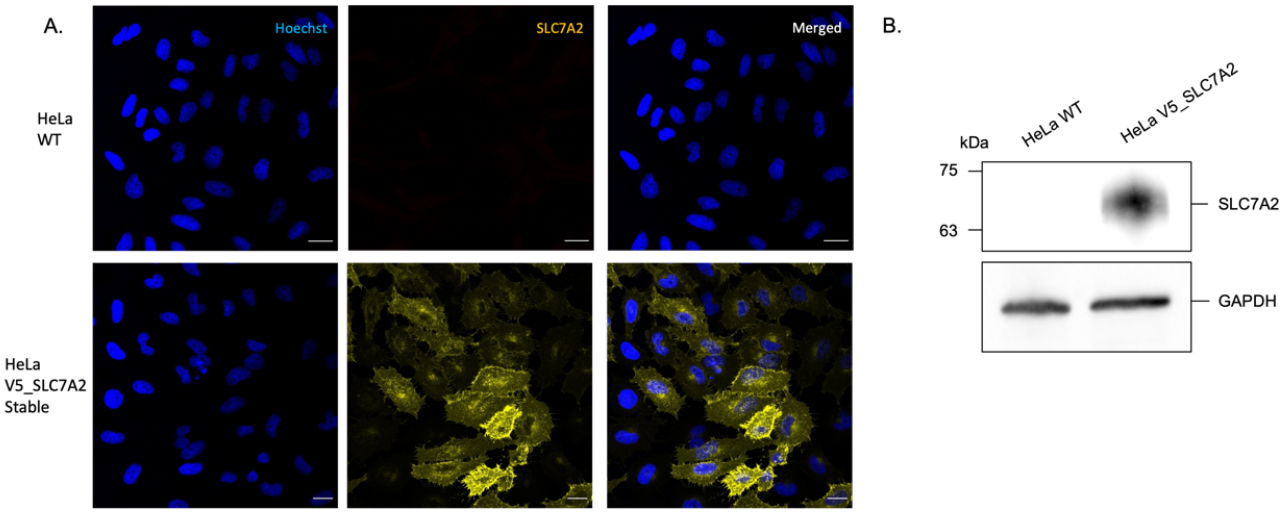

Figure 4.11: ***Generation of HeLa_V5_SLC7A2_puro stable cell line****–(A) Puromycin-selected HeLa_V5_SLC7A2_puro were fixed with 4% paraformaldehyde and immunostained with anti-V5 before being imaged via confocal microscopy (63x) for anti-rabbit Alexa 488 signal (false-coloured yellow) Scale bar is at 38 µm. (B) Stable cells were subjected to an SDS-PAGE and immunoblotted with the anti-V5 antibody.*

4.2.5 Overexpression of SLC7A2 increases transduction efficiency.

Having generated and characterised the stable cell lines for each target protein, we investigated if the overexpression of each target influenced viral transduction efficiency following the same transduction experimental process optimised in Chapter 3.

The HeLa wild-type transduction efficiency was maintained at an average of 35% of scAAV9-GFP positive cells relative to total cells, as shown previously. As expected from our positive control, the overexpression of HA_AAVR showed a significant increase to 100% of cells being scAAV9-GFP positive (a 70% increase relative to that of the control, p≤0.0001*)* (Figure 4.12A and 4.12B). The overexpression of Myc_SDC4 and FLAG_ICAM1 showed no significant difference to that of the wild-type transduction efficiency at an average of 36% and 39% of scAAV9-GFP positive cells relative to total cells, respectively. However, the overexpression of V5_SLC7A2 showed a significant increase to 72% of scAAV9-GFP positive cells (a 51% increase relative to that of the control, p ≤0.001*)*. This data initially indicated that the overexpression of SLC7A2 has a role in AAV9's transduction. Because of this, it was validated if the V5_SLC7A2 line had an elevated expression of the positive control AAVR which could influence the transduction efficiency assay. An immunoblot of the stable line showed a significant 7.6-fold-change in endogenous AAVR protein expression (Figure 4.12C and 4.12D).

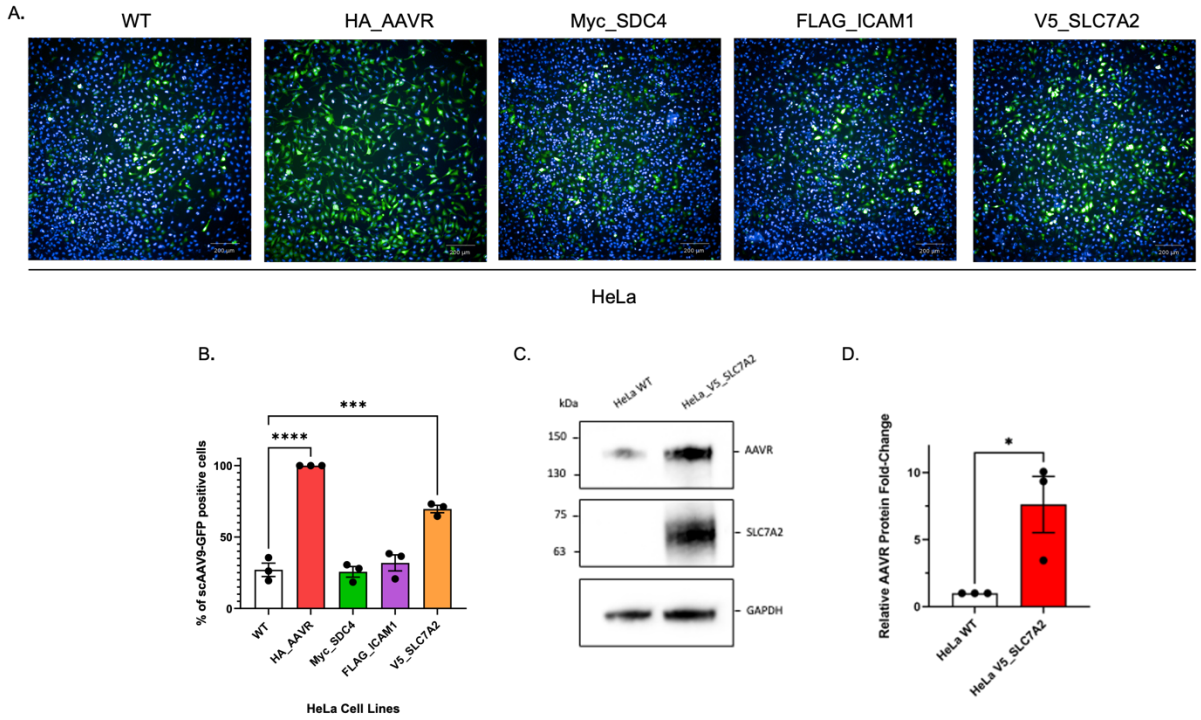

Figure 4.12: Overexpression of SLC7A2 increases scAAV9 transduction in HeLa cell line – *(A) scAAV9 transduction at 2 x 10^5 for 48-hour incubation for each stable cell line. Cells were fixed with 4% paraformaldehyde and imaged via the Incell system (10x). Scale bar is at 200 µm. (B) Graph represents mean relative number of scAAV9-GFP positive cells using Columbus analysis software. Normalised datasets are shown relative to the WT dataset. (Mean±SEM; ANOVA, * * * p≤0.001, * * * * p≤0.0001, biological N=3). (C) Stable cells were subjected to SDS-PAGE and immunoblot. Blots were incubated with mouse Abcam AAVR and rabbit anti-V5 antibody. GAPDH was used as loading control. (D) Graph represents mean relative AAVR signal using Fiji software. Normalised datasets are shown relative to the WT dataset. (Mean±SEM; T-test, * p≤0.05, biological N=3).*

4.2.6 Generation of 1321N1 stable cell lines

Due to the 1321N1 cell line having the highest lentiviral transduction efficiency for all the targets compared to the other non-permissive cell lines (Figure 4.7), the cell line was brought forward, and stable 1321N1 cell lines were generated for each respective target protein.

These 1321N1 stable lines were characterised for their level of target overexpression and distribution compared to controls. Cells transduced with LV_HA_AAVR were shown to have elevated signal in the cytoplasm (Figure 4.13A). Overexpressed signal was validated via immunoblot which showed a strong signal in the HA_AAVR stable cell line (Figure 4.13B). For the SDC4 stable cell line, Myc_SDC4 HeLa stable cells showed signal which was localised in the perinuclear region or in the cytoplasm of the cells (Figure 4.14A). This was further confirmed via immunoblot which showed signal at the expected height (Figure 4.14B). For the ICAM1 stable cell line, the cell line had detectable signal which was localised to the cell membrane and cytoplasm (Figure 4.15A). This overexpression was further confirmed via immunoblot where there is an overexpressed FLAG_ICAM1 signal at the validated height (Figure 4.15B). For the SLC7A2 stable cell line, V5_SLC7A2 overexpression was not detected via immunostaining and only background signal could be observed (Figure 4.16A). This could be due to the antibody requiring a specific level of expression to be detectable, as shown in the previous chapter. The overexpression was confirmed by immunoblot and overexpressed signal could be detected at the expected endogenous 170 kDa height (Figure 4.16B).

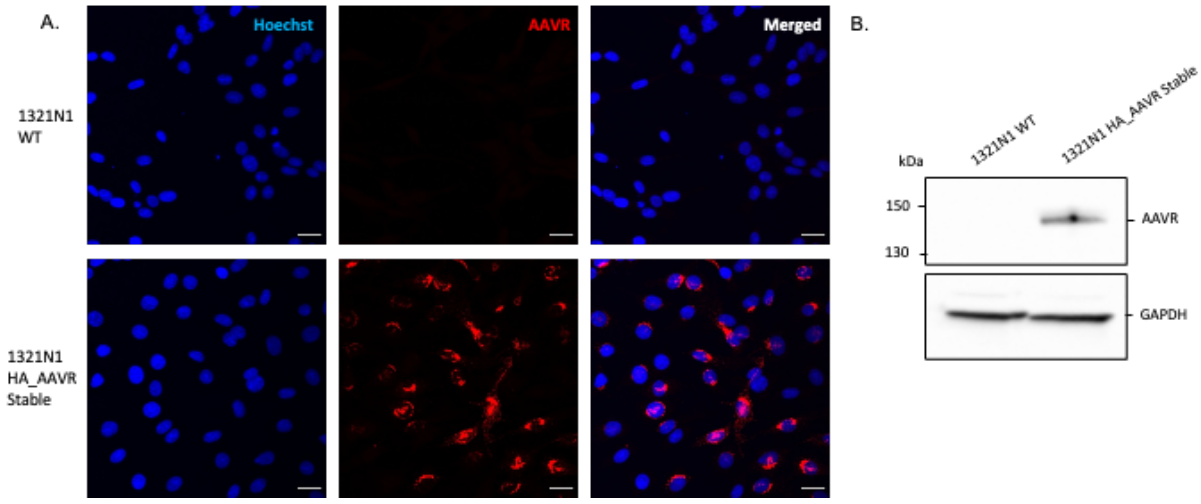

Figure 4.13: ***Generation of 1321N1_HA_AAVR_puro stable cell line***– *(A) Puromycin-selected 1321N1_HA_AAVR_puro was fixed and immunostained with Abcam AAVR before being imaged via confocal microscopy for Alexa 488 signal (false-colour red) (63x). Scale bar is at 38 µm. (B) Stable cells were subjected to an SDS-PAGE and immunoblotted with Abcam AAVR antibody. GAPDH was used as a loading control.*

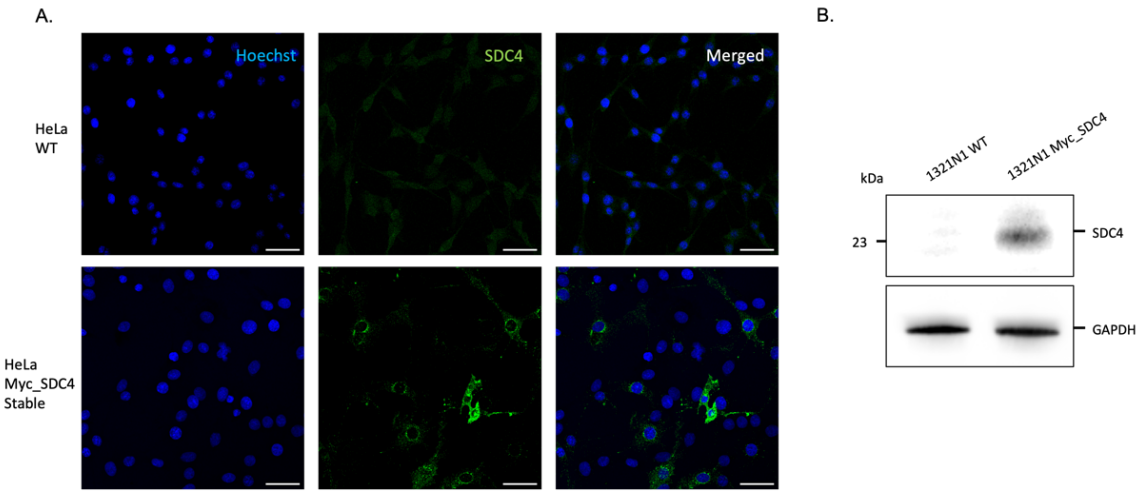

Figure 4.14: ***Generation of 1321N1_Myc_SDC4_puro stable cell line*** *– (A) Puromycin-selected 1321N1_Myc_SDC4 cells were fixed and immunostained with Abcam ICAM1 before being imaged via confocal microscopy for rabbit Alexa 488 signal (63x) Scale bar is at 38 µm. (B) Stable cells were subjected to an SDS-PAGE and immunoblotted with the Santa Cruz SDC4 antibody. GAPDH was used as a loading control.*

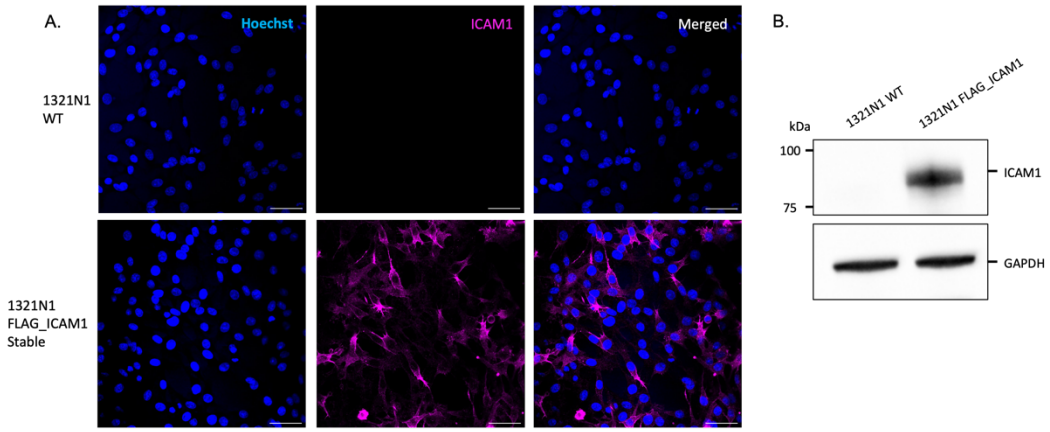

Figure 4.15: ***Generation of 1321N1_FLAG_ICAM1_puro stable cell line****–(A) Puromycin-selected 1321N1_FLAG_ICAM1_puro was fixed and immunostained with Abcam ICAM1 before being imaged via confocal microscopy for rabbit Alexa 488 signal (63x) (false-colouring magenta). Scale bar is at 38 µm. (B) Stable cells were subjected to an SDS-PAGE and immunoblotted with the Abcam ICAM1 antibody. GAPDH was used as a loading control.*

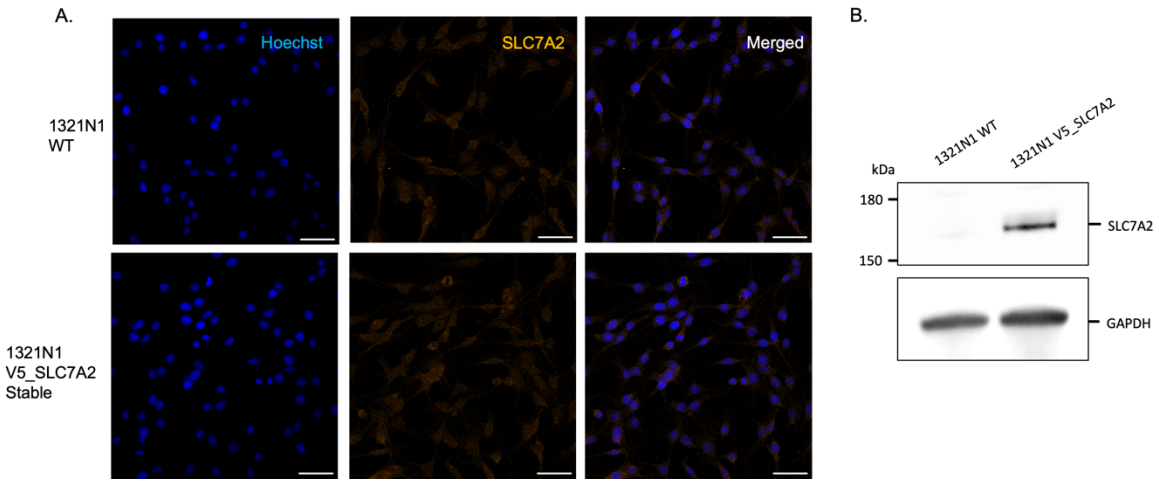

Figure 4.16: ***Generation of 1321N1_V5_SLC7A2_puro stable cell line*** *– (A) Puromycin-selected 1321N1_V5_SLC7A2_puro was fixed and immunostained with Abcam SLC7A2 before being imaged via confocal microscopy for rabbit Alexa488 signal (63x) (false-colouring orange). Scale bar is at 38 µm. (B) Stable cells were subjected to an SDS-PAGE and immunoblotted with the Abcam SLC7A2 antibody. GAPDH was used as a loading control.*

4.2.7 Viral transduction efficiency in 1321N1 stable cell lines

Similarly to the HeLa stable cell lines, the generated 1321N1 stable cell lines were incubated with 2 x 10^5 vg/cell of scAAV9 to determine if viral transduction was elevated in the overexpressed non-permissive cell line after 48-hours.

Wild-type cells showed no scAAV9-GFP positive cells as seen previously in our neuronal cell line screen. In the HA_AAVR 1321N1 stable cell line, GFP signal could be visualised which when quantified showed 7% of GFP positive cells relative to that of total cells (Figure 4.17A and 4.17B, $p \leq 0.01$). While the overexpression of Myc_SDC4, FLAG_ICAM1 and V5_SLC7A2 showed no positive GFP positive cells.

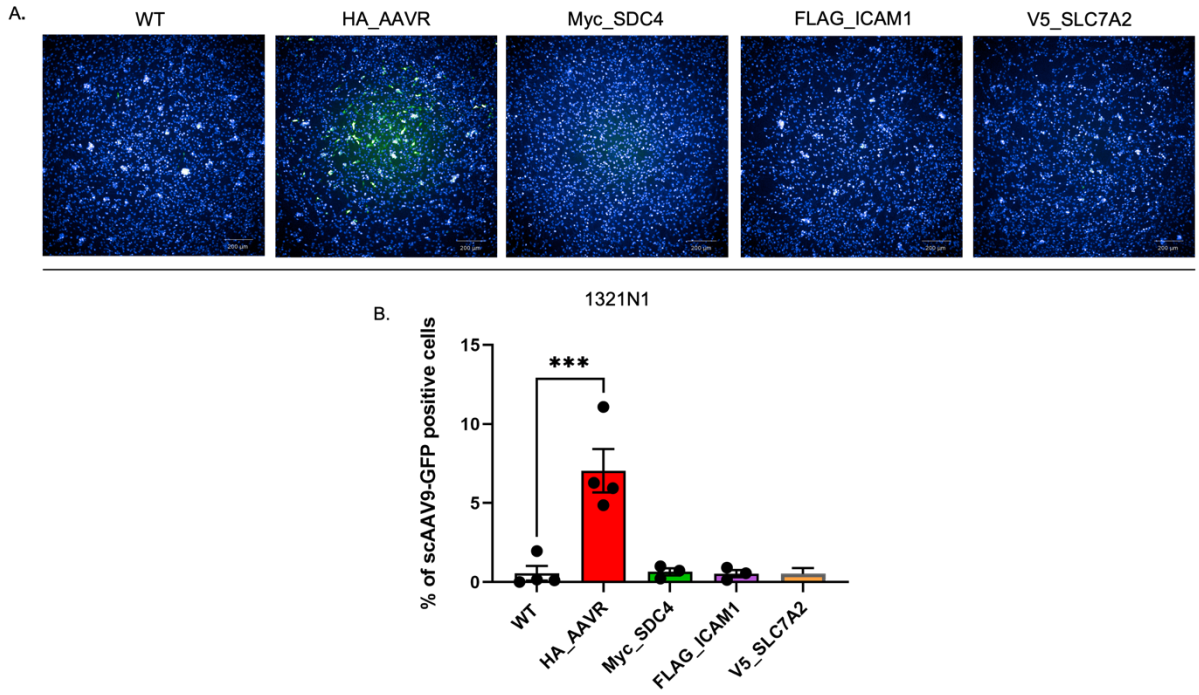

Figure 4.17: ***Overexpression of AAVR increases scAAV9 transduction in stable 1321N1 cell lines*** *– (A) scAAV9 transduction at 2 x 10^5 for 48-hour incubation for each stable cell line. Cells were fixed with 4% paraformaldehyde and imaged via the Incell system (10x). Scale bar is at 200 µm (B) Graph represents mean relative number of scAAV9-GFP positive cells using Columbus analysis software. Normalised datasets are shown relative to the WT dataset. (Mean±SEM; ANOVA, * * p≤0.01, biological N=4).*

4.2.8 AAVR and ICAM1 interact with AAV9

Given that viral capsid protein interactions with cell surface receptors can govern the method of viral infection or uptake (Maginnis 2018), it was hypothesised that these target proteins may interact with the AAV capsid to enable transduction. Due to the target proteins being located on the cell surface, it was theorised that the virus may require direct interaction with the proteins to enable access to a particular pathway. To investigate this, the HeLa overexpression lines were subjected to immunoprecipitation analysis. Whole cell lysates from each overexpression line and wild-type control were incubated with AAV9_mCherry viral capsids. Target proteins were then immunoprecipitated from these lysates using target or tag specific antibodies. Immune pellets were subjected to SDS-PAGE and immunoblot to determine if the viral capsid proteins were simultaneously co-precipitated after target protein pull down, indicating a protein-protein interaction.

Input samples of stable HA_AAVR showed a clear increase in AAVR expression compared to wild type control cells (Figure 4.18A). Immunoprecipitation with endogenous AAVR antibodies resulted in a strong enrichment of AAVR from both wild-type and HA_AAVR stable cells indicating successful capture of the target protein. Viral protein 1, 2 and 3 (VP1, VP2 and VP3) were detected in the input samples of both conditions as expected at 100 kDa, 75 kDa and 50 kDa respectively. Enrichment of AAVR from the stable lines led to the co-immunoprecipitation of VP1, VP2 and VP3. Due to the success in co-immunoprecipitating viral proteins with the AAVR positive control, the other stable lines for each target were investigated. Myc_SDC4 was efficiently immunoprecipitated with anti-SDC4 antibodies (Figure 4.18B). VP1, VP2 and VP3 proteins were detectable in the input samples but were not shown to co-immunoprecipitate with SDC4. ICAM1 signal was detectable in the stable cell line and in wild-type line input samples. ICAM1 protein was enriched in both cell lines after immunoprecipitation (Figure 4.18C) with anti-ICAM1 antibodies. Intriguingly, VP1 was shown to co-immunoprecipitate with ICAM1. The level of VP1 co-immunoprecipitate was higher in the overexpressed condition supporting the fact that ICAM1 interacts with VP1. Unfortunately, V5_SLC7A2 was undetectable in the wild-type and stable cell line input samples. (Figure 4.18D). Once immunoprecipitated however, overexpressed SLC7A2 was

readily detectable. VP1, VP2 and VP3 were detectable in both input samples but were not co-immunoprecipitated with SLC7A2.

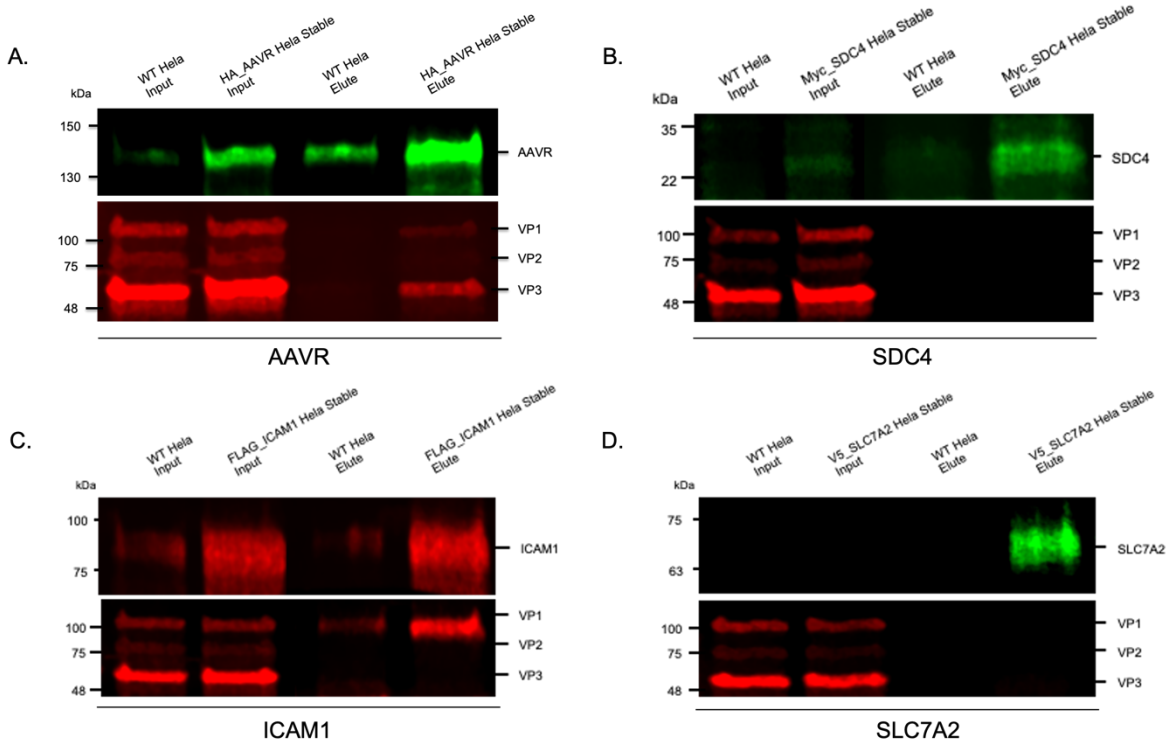

Figure 4.18: ***Overexpression of HA_AAVR and FLAG_ICAM1 precipitates viral proteins*** *–Stable cell lines were lysed and incubated with ssAAV9 and antibodies (Abcam AAVR, Santa Cruz SDC4, Abcam ICAM1 and anti-V5) before CO-IP elution was subjected to an SDS_PAGE and immunoblot. AAV9 was detected using – VP1/2/3 antibody (A) AAVR stable cell line was detected with Abcam AAVR) (B) SDC4 stable cell line was detected with Santa Cruz SDC4 antibody (C.) ICAM1 was detected using Abcam ICAM1 antibody. V5_SLC7A2 was detected using the anti-V5 antibody.*

4.3 Discussion

The purpose of this chapter was to validate if elevating the identified novel target proteins in non-permissive cell lines could increase viral transduction. This was achieved by generating stable overexpression cell lines to determine if AAV9 transduction was affected. Furthermore, the interaction between these targets and the viral capsid proteins was investigated to prove interaction.

Initially the experimental plan for the current chapter was to overexpress each target protein via transient transfection of the previously generated tagged mammalian expression constructs. Unfortunately, due to the experimental setup of the optimised transduction timeframe with scAAV9, CMV-promoter driven target protein expression was not maintained at peak protein expression across the necessary timeframe (Figure 4.1). In addition to this, the transfection efficiency of each non-permissive cell line was validated, as immortalised cell lines have varied transfection efficiencies (Kim and Eberwine 2010). While HeLa cells were readily transfected, the non-permissive cell lines were not (Figure 4.2), further strengthening the need to adjust the experimental plan. As a result, the generation of lentiviral vectors to deliver and integrate the transgenes of interest was chosen to create stable cell lines, similar to that of the Pillay, Meyer et al. (2016) study. The presence of a puromycin resistance gene within the LV vectors allowed for the selection of positively transduced cells. However, within this antibiotic-selected population, there is varied level of expression between cells, mainly due to alternate integration events, varied copy numbers per cell and specific chromosomal integration sites (Kaufman, Kocman et al. 2008, Biffi, Bartolomae et al. 2011, Ronen, Negre et al. 2011). If more time was applicable, selecting cell clones with the highest expression pattern would have been ideal to determine if transduction was affected based on a certain expression level of the target protein. For example, if the highest expressing clones of 1321N1 HA_AAVR were selected and expanded, then potentially more cells may have been transduced by scAAV9.

The non-permissive cell lines screened and selected for this study were difficult to transfect and transduce, making the generation of multiple stable overexpression lines experimentally challenging. Several ranges of lentiviral MOI's were tested in N2As and NIH3T3s and only the LV_HA_AAVR vector was shown to have consistent expression across all cell lines. Because of

this, these cell lines were not carried further to generate stable lines due to this lack of transduction and expression of all targets. A potential technique to improve lentiviral transduction is to incorporate positively charged polycations during the transduction protocol (Denning, Das et al. 2013). The polarity of the polycation reduces the cell membrane electrostatic repulsion forces which enhances the interaction of lentiviral particles. However, due to polybrene causing neuronal toxicity due to mitochondrial calcium overloading, it prevents its use in neuronal cell lines (Bao, Shi et al. 2018). The alternate cationic polymer DEAE-Dextran could be used which has less cell-specific toxicity. Additionally, an alternate experimental protocol for the transduction of lentivirus is by concentrating the lentivirus via ultracentrifugation and resuspending the cell line of interest before replating. This has been shown to yield improved transduction as a result of improved mass transport and virus-cell interactions (Pirona, Oktriani et al. 2020). A combination of the two techniques listed may have assisted in the generation of NIH3T3 and N2A stable cell lines. Literature states that mucin expression can inhibit lentiviral transduction (Seppen, Barry et al. 2000). Given that a number of these non-permissive cells could not be transduced with LV, screening these neuronal lines for mucin expression would be informative.

After generating the stable overexpression cell lines, it was validated if the overexpression of these targets could improve viral transduction due to the increased availability of potential entry factors which would make the cell more susceptible to viral transduction. As expected, the overexpression of AAVR in HeLa and 1321N1 significantly increased transduction efficiency (Figure 4.12 and Figure 4.17). Overexpression of SDC4 and ICAM1, on the other hand, had no significant effect on transduction efficiency. This therefore suggests that the increased availability of these target proteins on the cell surface has no effect on the vector's transduction pathway. Intriguingly, the overexpression of SLC7A2 did have a significant effect on AAV9 transduction in the HeLa cell line, suggesting that the target protein could be involved in AAV9's HeLa transduction pathway (Figure 4.12). Due to the elevated levels of transduction and the co-immunoprecipitation assay showing no evidence of interaction (Figure 4.18), it is therefore more likely that the increased expression and increased function of the target protein was what was altering the viral transduction efficiency. In the Madigan, Berry et al. (2020) study it was shown that the knockout of the calcium pump ATPC1 resulted in decreased viral transduction due to alternate intracellular trafficking and defective

conformational capsid changes which were essential to support AAV gene transcription. Amino acids have been shown to regulate gene expression (Kimball and Jefferson 2004), so it could be the case that the amino acids regulated by SLC7A2, like L-arginine, are effecting AAV9's transgene expression. It could be hypothesised that the overexpression of V5_SLC7A2 was having a similar affect as shown in the ATPC1 study and increased gene transcription due to the elevated uptake of amino acids. To validate this, inhibiting the solute carrier's function via pharmokinetics would determine if the potentially elevated transport of these molecules may be the cause of elevated scAAV9 transduction or transcription. The compound N-ethylmaleimide (NEM) could be used due its inhibitory interaction with SLC7A2 by binding to Cys-33 and Cys-273 residues located on the N-terminus which inhibits transport function, as shown in the Beyer, Mallmann et al. (2013) study.

Due to elevated transduction in the V5_SLC7A2 HeLa cell line, it was also validated if the dysregulation of V5_SLC7A2 simultaneously dysregulated the positive control AAVR. The stable overexpression of SLC7A2 in HeLa cells resulted in elevated levels of AAVR (Figure 4.12C), potentially suggesting that the increased transduction may be as a result of the elevation in AAVR levels rather than the elevated function of SLC7A2 alone. The fact that overexpression of SLC7A2 affects AAVR levels is, itself, intriguing, suggesting altered expression of AAVR upon SLC7A2 overexpression or even changes in AAVR stability. These data also suggest some form of possible interaction or relationship. Future studies are warranted to investigate any potential interaction or shared common pathway which could result in simultaneous elevated expression of AAVR. Due to AAVR's localisation to the golgi, it could be proposed that AAVR functions in either transporting SLC7A2 from the golgi after PTMs to the cell membrane or AAVR functions in the recycling pathway of SLC7A2. Because of SLC7A2 overexpression, the cell may require more AAVR to process the elevated levels of SLC7A2. A future experiment would be to validate if AAVR dysregulation, via loss of function studies, affects the localisation of SLC7A2 or to determine if the overexpression of SLC7A2 alters the localisation of AAVR to determine if they are dependent on one another.

The overexpression of Myc_SDC4, FLAG_ICAM1, and V5_SLC7A2 was shown to have no effect on viral transduction in the 1321N1 cell line. Due to the overexpression of HA_AAVR in 1321N1 cells only leading to 7% of transduction efficiency, the overexpression effects of the other targets was likely to be limited as given that AAVR is clearly a crucial interacting partner

necessary for AAV9 transduction, as shown in Figure 4.12 in the HeLa cell line. Therefore, the lack of effect seen with overexpression of the other targets was to be expected, as they could not compensate for the lack of AAVR endogenous expression in the 1321N1 cell line. Even in the HA_AAVR 1321N1 stable cell line, there was limited transduced cells relative to the total. It would therefore be interesting to determine if the cells that were transduced in this line had the highest expression of AAVR, given the variability in transgene expression in these pooled stable lines. This would clarify if the level of expression of AAVR was the determining factor for effective transduction. The localisation of AAVR in the HA_AAVR stable 1321N1 cell line (Figure 4.13) showed irregular localisation compared to the localisation of AAVR in the HeLa cell line (Figure 4.8). If the localisation of AAVR was being affected due to the biology of the *in vitro* model, it may affect the transduction efficiency of AAV9. This would explain why there was significant variation between the overexpression of AAVR in the HeLa cell line compared to the 1321N1 cell line. This was observed also in the overexpression of SDC4 which appeared to localise predominately perinuclear region of the cell (Figure 4.14). Additionally, AAVR may require alternate protein interactions for effective *trans*-golgi transport which may not be present in the 1321N1 cell line. These experiments therefore unveiled an unexpected limitation which was that the non-permissive lines selected would require a form of expression of AAVR to enable investigative studies into the functional relevance of other targets in AAV9's entry pathway. Dual overexpression stable lines with simultaneous AAVR and the target protein of interest overexpression would go some way to enable investigation of whether these target proteins can increase viral transduction in non-permissive cell lines. Alternatively, the use of different cell lines like that of the HeLa cell line, which the virus has average transduction efficiency and enables a range for improvement, would enable a detectable enhancement in transduction. In the Meisen, Nejad et al. (2020) study, the cell lines used were U2-OS cells to determine GPR108 as a target protein for viral transduction and in the Ellis, Hirsch et al. (2013) cell line screen, other cell lines identified were HEK293T and HUVEC cell lines which could transduce scAAV9 with similar efficiency to that of Hela's. Generating overexpression cell lines in these *in vitro* models may provide further insight into the functional nature of these targets due to their capability of being transduced prior to protein dysregulation. Although the 1321N1 cell line was shown to not transduce scAAV9 (Figure 3.21) the HeLa AAVR knockout cell line internalises the viral vector (Figure 5.23), but transduction is not detectable (Figure 5.8). Because of this, investigating if the identified non-

permissive cell lines in Chapter 3 (N2A, NIH3T3, 1321N1 and b.End5) were similarly internalising the viral vector but lacking the necessary proteins required for transgene expression. In the Turkki, Makkonen et al. (2013) study, it was shown that non-permissive cell lines to the human enterovirus echovirus 1 (EV1) impaired viral infection post-internalisation as a result of differential expression of proteins, such as vimentin and filamentous actin. By investigating this in the non-permissive cell lines identified in this study, this would provide further insight into whether the cell lines lack specific surface protein expression preventing entry or if they lack the intracellular proteins necessary for transgene expression.

Due to the target proteins of interest being potential interactome partners with AAV9, their functional nature could be theorised to require direct interaction with the viral capsid on the cell membrane surface in relation to early stages of the transduction pathway. Enrichment of overexpressed AAVR was shown to co-immunoprecipitate VP1, VP2 and VP3 proteins which has not been shown in literature but supports the findings of the Pillay, Meyer et al. (2016) study. Intriguingly, no viral proteins were precipitated with endogenous AAVR capture in the wild-type control, suggesting that a concentrated expression of the target protein was required to confirm interaction. To better understand AAV9s interaction with AAVR, validating the virus-protein region of interaction would enlighten what domains are necessary for viral transduction. This would be achieved by designing truncated versions of AAVR using site-directed mutagenesis which would generate mutated AAVR proteins. Each protein variant will lack specific domains which would enable the identifications of the domains which are necessary for viral interaction. This was shown in the Pillay, Meyer et al. (2016) study which proved that PKD1-3 domains are the interacting domains for AAV2 transduction.

SDC4 was found not to interact with AAV9 capsid proteins in these experiments. Although no interaction could be proven, the experiment may require optimisation as the potential interaction between SDC4 and the viral proteins may demand less stringent IP lysis buffer. Literature suggests that a lower concentration of NP40, 0.05% rather than the 1% used, could be optimal to minimise non-specific binding and increase the recovery of the antigen (Yang, Zhang et al. 2009). It is also stated that higher stringency of detergents has less of an effect at higher protein concentrations, which supports the fact that enriched overexpressed AAVR precipitated viral protein compared to enriched endogenous levels of AAVR.

The enrichment of ICAM1 revealed the co-immunoprecipitation of VP1 in both endogenous ICAM1 and overexpressed conditions. This implies that not only does ICAM1 interact with the viral capsid, but VP1 has also been identified to be the specific viral protein of the viral capsid which binds with the target protein. An experiment to further validate this direct interaction would be a cell-free *in vitro* binding assay which would require the development of recombinant GST-tagged ICAM1 which would be incubated with *in vitro* translated VP1 (Louche, Salcedo et al. 2017). In the absence of other cellular components, this would determine if the co-immunoprecipitation of ICAM1 and VP1 is a direct protein interaction. Following this supportive finding, peptides can be designed to interact with specific amino acid clusters to block interactions in these areas (Opie, Warrington et al. 2003). Using this method, inserting peptide sequences into a variety of regions in VP1 will determine if interaction with ICAM1 is affected via co-immunoprecipitation assay. This would determine if any of these peptides, which are bound to and block specific amino acid regions, abolish ICAM1 binding and enable the identification of the binding loci. An alternate validation method, which was used in the Dudek, Zabaleta et al. (2020) study, was the generation of chimeric capsids to identify the motif on the VP1 domain for the GPR108 target. It has been shown previously that the VP1 and VP2 domains of AAV serotypes are capable of domain grafting to other AAV serotypes to prove unique interactions (Mays, Wang et al. 2013). It would be intriguing to determine if AAV2 interacts with ICAM1 similarly to that of AAV9. If not, the generation of a AAV2 chimeric capsid containing AAV9's VP1 domain would be suggested as it would confirm if interaction were adopted. Alternatively in relation to ICAM1, to identify the protein domain binding region, generating truncated versions of ICAM1 via site-directed mutagenesis would assist in understanding the interacting process. By removing the N-terminus domain of ICAM1, it would enable analysis into viral interaction and function on the cell surface while the removal of the C-terminal domain would provide insight into whether the protein functions in internalisation.

Although ICAM1 interacts with the VP1 domain of AAV9, the overexpression of the target localised on the cell surface in both the HeLa and 1321N1 stable cells showed no improvement in viral transduction (Figure 4.12 and 4.17). This indicates that ICAM1 is not functionally relevant in the transduction pathway of either cell lines. Due to ICAM1 being a known transmembrane glycoprotein which plays a role in immune responses (Bui, Wiesolek et al.

2020), it could be investigated if AAV9's infectivity in immune cells is affected by the dysregulation of ICAM1 which would enable insight into the protein function in this particular immune *in vitro* model. Additionally, the target was identified in a blood-brain barrier cell line and has been shown to have a function in transcytosis (Hsu, Rappaport et al. 2014) so the target could be related to that of the transcytosis pathway, independent of transduction. Following a similar methodology to that of the Merkel, Andrews et al. (2017) study, a trans-well models could determine if the quantity of virions transported across from the apical side to the basolateral side of blood-brain barrier cell lines are affected as a result of protein dysregulation of ICAM1.

Following the investigation of these novel targets in non-permissive cell lines, the targets were further validated in loss-of-function studies with the previously identified permissive cell lines: Hela and SHSYs.

5 Loss of novel targets impacts AAV9 transduction efficiency

5.1 Introduction

Experimental techniques involved in loss-of-function (LOF) methods have become a widely used application in all research fields (Zimmer, Pan et al. 2019). LOF is usually generated in two ways: inhibiting translational expression and genetic knockout experiments. In Chapter 3, the HeLa and SHSY cell lines were identified as being permissive to AAV9 transduction. Furthermore, HeLa cells also expressed AAVR, ICAM1 and SLC7A2 at the highest endogenous levels compared to the other lines being studied. Given that AAV9 interaction with cell surface receptors is necessary for transduction to occur (Bell, Vandenberghe et al. 2011), the aim of this chapter was to determine if reduction of our novel protein targets could impact viral transduction efficiency. This would identify them as important interaction partners and potential regulators of AAV9 transduction. To validate these targets involvement in AAV9 transduction, the HeLa and SHSY cell lines were used in an siRNA-mediated modulation of all the targets. Following this screen, the CRISPR-Cas9 systems (Cas9-D10 nickase and Cas9-ribonucleoprotein complex) were used to generate knockout cell populations in HeLa and SHSY cell lines to validate transduction efficiency on a genomic level. Finally, rescue overexpression of the CRISPR-edited cell lines were generated to confirm the specificity of the findings. Using all generated cell lines, the entry mechanism of these targets was investigated via an internalisation assay.

5.2 Results

5.2.1 siRNA knockdown of target proteins in permissive cell lines

To investigate the effect of targeted siRNA knockdown of AAVR, SDC4, ICAM1 and SLC7A2 on AAV9 transduction efficiency, HeLa and SHSY cells were treated with the siRNA's characterised previously (Figure 3.1, 3.3, 3.6, 3.8) before performing the scAAV9-GFP transduction efficiency assay, as described in Chapter 3. HeLa and SHSY cells were treated with siRNA for 72 hours before incubation with scAAV9-GFP. 48-hours post transduction cells were fixed, nuclei stained, and the percentage of GFP-positive cells quantified by microscopy. Transduction efficiency was quantified as the number of GFP-positive cells relative to total cells and expressed relative to the non-targeting control (NTC) siRNA cells.

The level of target mRNA knockdown was confirmed via quantitative PCR in HeLa cells. The AAVR mRNA levels were significantly reduced by 88%, SDC4 levels by 69%, ICAM1 levels by 68% and SLC7A2 levels by 66% (Figure 5.1AI-AIV). The reduction in AAVR completely prevented transduction of AAV9, with zero GFP-positive cells detected (Figure 5.1B). Targeted siRNA of SDC4 and ICAM1 led to a significant reduction in scAAV9-GFP positive cells (44% and 76% average decrease, respectively) (*p≤0.01*, *p≤0.0001,* respectively). The targeted siRNA of SLC7A2 showed no significant GFP difference between that and the NTC control.

Due to the successful knockdown of mRNA in the HeLa cell line, the SHSY permissive line was also validated. The level of target mRNA knockdown was confirmed via quantitive PCR. The AAVR mRNA levels were significantly reduced by 61%, SDC4 mRNA levels by 58% and SLC7A2 mRNA levels by 55% (Figure 5.2AI, 5.2AII and 5.2AIV). The depletion in AAVR led to a significant reduction in GFP positive cells (*p≤0.01)* (Figure 5.2B) while the knockdown of SDC4 and SLC7A2 showed no significant difference *(*Figure 5.2C). Unexpectedly, ICAM1 siRNA led to an upregulation in mRNA expression in SHSYs (Figure 5.2AIII) despite giving strong and efficient knockdown in HeLa cells. For this reason, a second siRNA targeting ICAM1 was tested. Unfortunately, the second siRNA failed to knockdown ICAM1 in SHSY but also in the HeLa cell line (Figure 5.3A and 5.3B).

A limitation of siRNA knockdown is the potential for off-target effects due to sequence homology (Neumeier and Meister 2020). To have confidence in the effects in this siRNA screen, the mRNA and protein expression of each target was investigated in each siRNA condition to determine if effects on scAAV9 transduction were a result of off-target mRNA/protein dysregulation. Due to the lack of a functional SDC4 antibody for endogenous expression, this target was not investigated in the protein analysis. Targeted siRNA-knockdown of AAVR, SDC4, ICAM1 or SLC7A2 showed no significant mRNA dysregulation in any of the targets (Figure 5.4A - 5.4D). Similarly, protein quantification showed efficient protein knockdown after targeted siRNA, but no off-target effects on AAVR or ICAM1 levels (Figure 5.5A-5.5D). However, SLC7A2 protein levels were significantly elevated after ICAM1 siRNA knockdown (Figure 5.5C and 5.5D). These data suggest that SDC4 and ICAM1 could potentially be targets for viral transduction.

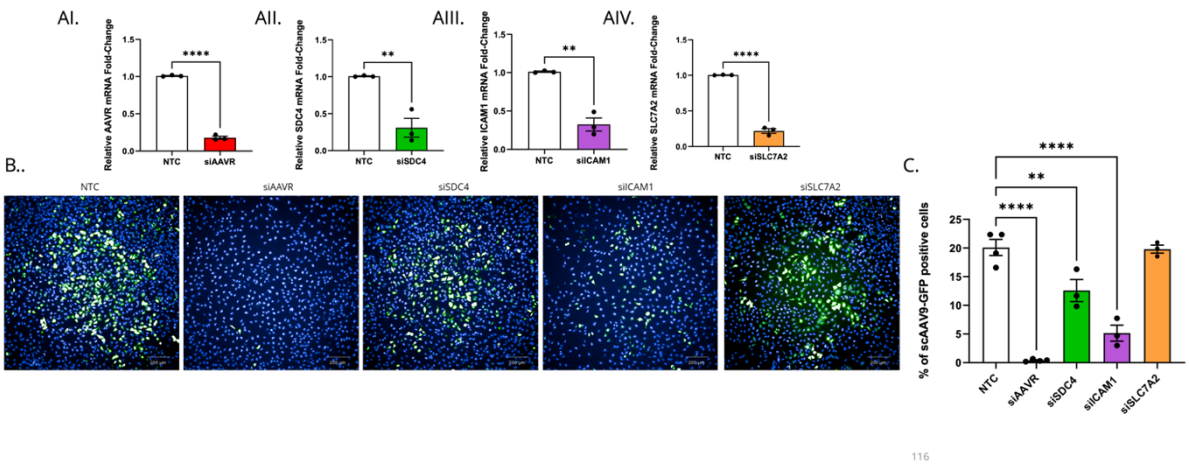

Figure 5.1: ***Knockdown of SDC4 and ICAM1 reduces scAAV9 transduction in HeLa cell line*** *–siRNA targeting each target protein was transfected into HeLa cells. (AI-AIV) Transfected cells RNA for each targeted siRNA was collected for cDNA conversion which was used for qPCR analysis using optimised primers to validate knockdown. Graph represents mean mRNA levels after siRNA transfection relative to that of the NTC dataset (Mean*±SEM; *t-*test, * * p≤0.01, ** * * p≤0.001, * * * * p≤0.0001 biological N=3). (B) scAAV9 transduction at 2 x 10^5 for 48-hour incubation for each siRNA condition. Cells were fixed with 4% paraformaldehyde and imaged via the Incell system (10x). Scale bar is at 200 µm. (C) Graph represents mean relative number of scAAV9-GFP positive cells using Columbus analysis software. Normalised datasets are shown relative to the NTC dataset. (Mean±SEM; ANOVA, * * * * p≤0.0001 * * * p≤0.001, biological N=3).*

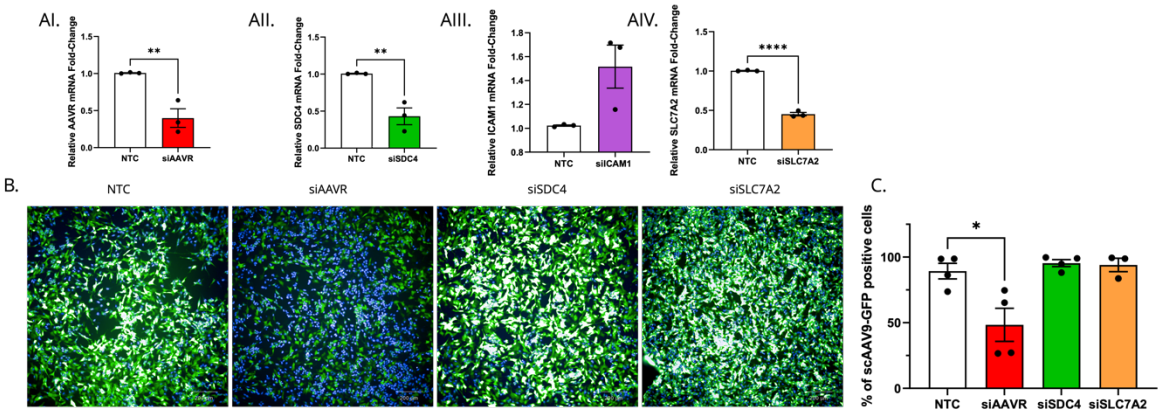

Figure 5.2: ***Knockdown of AAVR significantly reduces scAAV9-GFP positive SHSY cells***– *siRNA targeting each target protein was transfected into HeLa cells. (AI-AIV) Transfected cells RNA for each targeted siRNA was collected for cDNA conversion which was used for qPCR analysis using optimised primers to validate knockdown. Graph represents mean relative level of mRNA levels after siRNA transfection relative to that of the NTC dataset (Mean*±SEM; *t*-test, * * p≤0.01, ** * * p≤0.001, * * * * p≤0.0001 biological N=3). (B) scAAV9 transduction at 2 x 10^5 for 48-hour incubation for each siRNA condition. Cells were fixed with 4% paraformaldehyde and imaged via the Incell system (10x). Scale bar is at 200 µm.(C) Graph represents mean relative number of scAAV9-GFP positive cells using Columbus analysis software. Normalised datasets are shown relative to the NTC dataset. (Mean±SEM; ANOVA, * p≤0.05, biological N=3).*

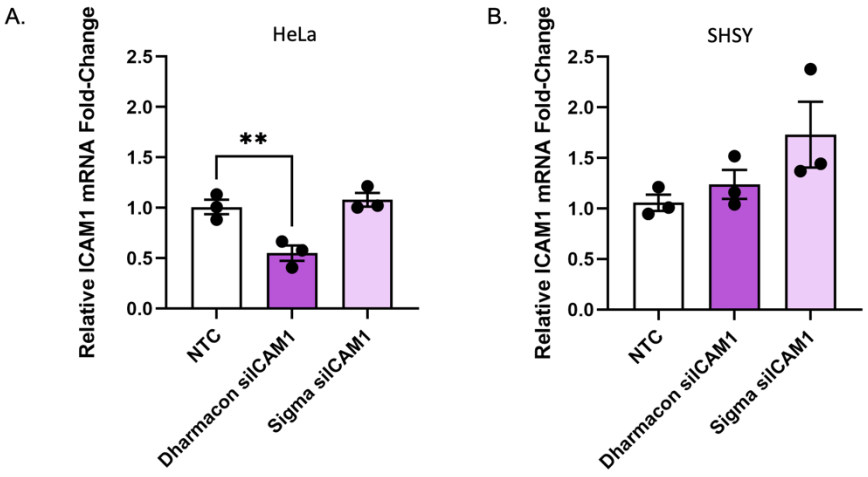

Figure 5.3: ***Knockdown of ICAM1 could not be achieved in the SHSY cell line*** – *(A) siICAM1 treated HeLa cells RNA was collected for cDNA conversion and used for qPCR analysis to validate knockdown. Graph represents mean of mRNA levels after siRNA transfection relative to that of the NTC dataset (Mean*±SEM; *t*-test, * * p≤0.01, *biological N=3). (B) siICAM1 treated SHSY cells RNA was collected for cDNA conversion and used for qPCR analysis to validate knockdown. Graph represents mean relative level of mRNA levels after siRNA transfection relative to that of the NTC dataset (Mean*±SEM; *t*-test, *biological N=3).*

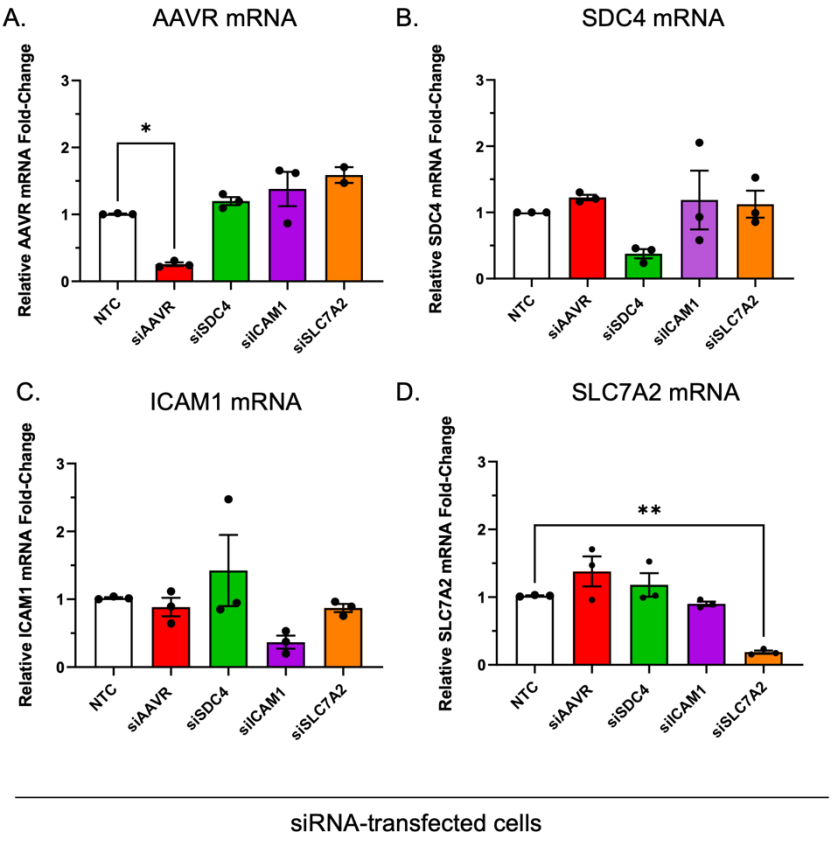

Figure 5.4: ***siRNA knockdown has no off-target effects on mRNA levels across all targets–*** *siRNA targeting each target protein was transfected into HeLa cells. (A-E) Transfected cells RNA for each targeted siRNA was collected for cDNA conversion which was used for qPCR analysis using optimised primers to validate knockdown. Graph represents mean relative level of mRNA levels of each target (A) AAVR (B) SDC4) (C) ICAM1 and (D) SLC7A2 for each siRNA target. Datasets are relative to that of the NTC dataset (Mean*±SEM; *ANOVA, * p≤0.5 * * p≤0.01, biological N=3).*

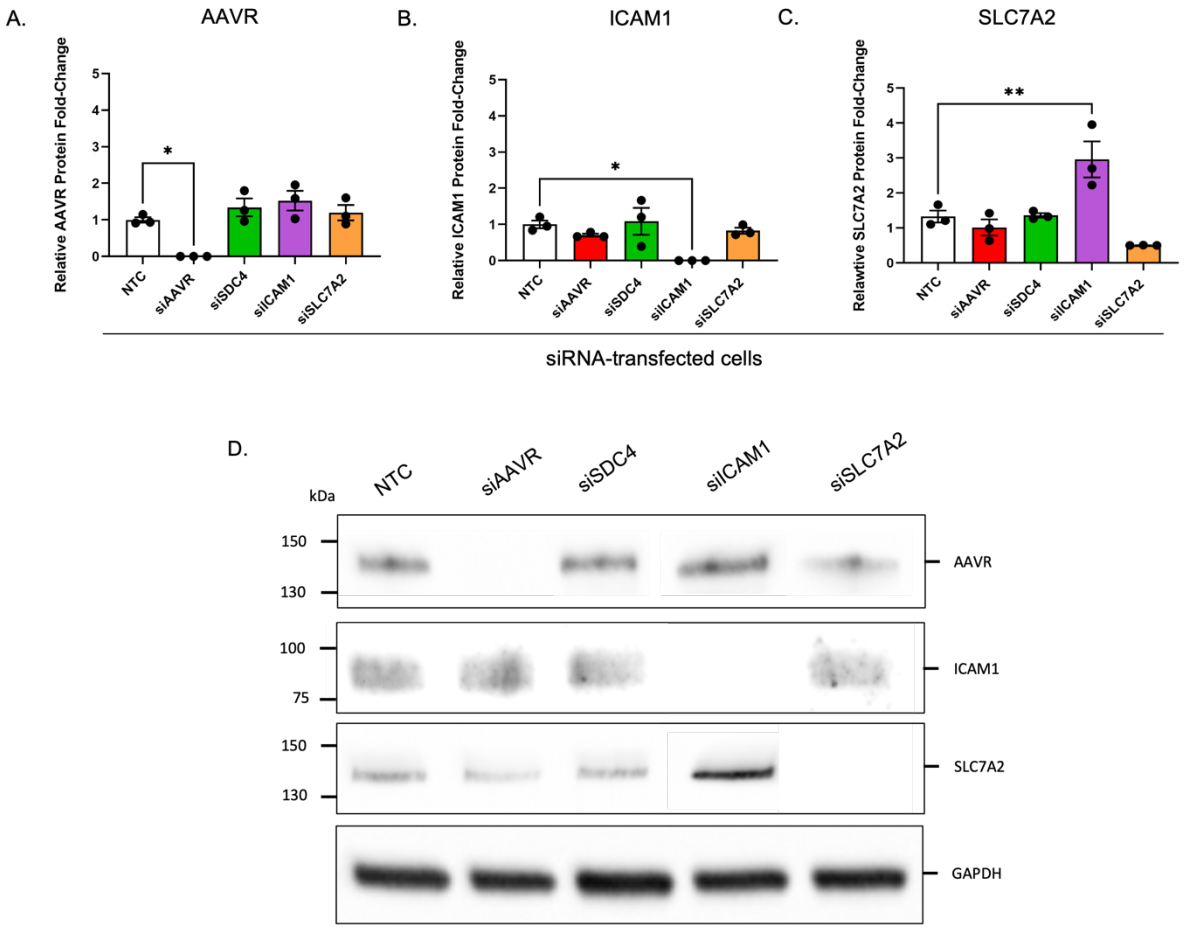

Figure 5.5: ***A significant increase in SLC7A2 protein level in siRNA-ICAM1–*** *siRNA targeting each target protein was transfected into HeLa cells. (A-D) Transfected cells were subjected to an SDS-PAGE and immunoblot. Blots were incubated with Abcam AAVR, Abcam ICAM1 or Abcam SLC7A2. Signal was quantified and graphed datasets of each condition are relative to that of the NTC dataset (Mean*±SEM; *ANOVA, * p≤0.5 * * p≤0.01, biological N=3).*

5.2.2 AAV9 transduction was AAVR-dependent.

Recent publications demonstrate that AAVR is essential for AAV2 transduction (Pillay, Meyer et al. 2016). This study utilised a HeLa AAVR-KO cell line generated via CRISPR/Cas9 to show that loss of AAVR severely impacts on AAV transduction efficiency across a range of AAV serotypes. This cell line was therefore a perfect positive control in the current studies to evaluate the role of newly identified targets on AAV9 transduction efficiency. For the purpose of this study, this cell line was therefore characterised in-house via immunofluorescence and immunoblotting to validate knockout of AAVR relative to its isotype control.

Immunofluorescence staining showed endogenous AAVR signal in the golgi region of the wild-type cell line while this specific signal was abolished in the AAVR-knockout cell line (Figure 5.6A). This endogenous expression pattern was confirmed via immunoblot with the expected endogenous expression at the validated 140 kDa height which was depleted in the knockout line (Figure 5.6B). Due to the confirmed knockout of endogenous AAVR expression, an AAVR stable overexpression cell line of the AAVR-knockout cells, referred to as AAVR-Rescue, was generated using the lentivirus HA_AAVR. Overexpression of AAVR was clearly detected in the golgi region of the AAVR-Rescue cell line with some cells showing golgi labelling and cytoplasmic distribution compared to that of the knockout cell line (Figure 5.7A). This was supported via immunoblot with intense overexpression detected in the AAVR-Rescue cell line (Figure 5.7B).

Following the generation and characterisation of these cell lines, the cell lines were transduced with scAAV9-GFP to assess (i) impact of knockout of AAVR on % of cells GFP positive; (ii) lentiviral-AAVR ability to rescue dysregulated transduction efficiency in the knockout line. scAAV9 gave a transduction efficiency of 35% of GFP-positive cells in the wild-type cell line while the knockout cell line showed no detectable GFP signal ($p \leq 0.0001$) (Figure 5.8A-B). As expected, restoration of AAVR protein levels with LV-HA-AAVR completely rescued the transduction efficiency to 100% of GFP positive cells ($p \leq 0.0001$). Due to this success, CRISPR-knockout lines for other targets were generated and characterised before validating their effects via transduction assays.

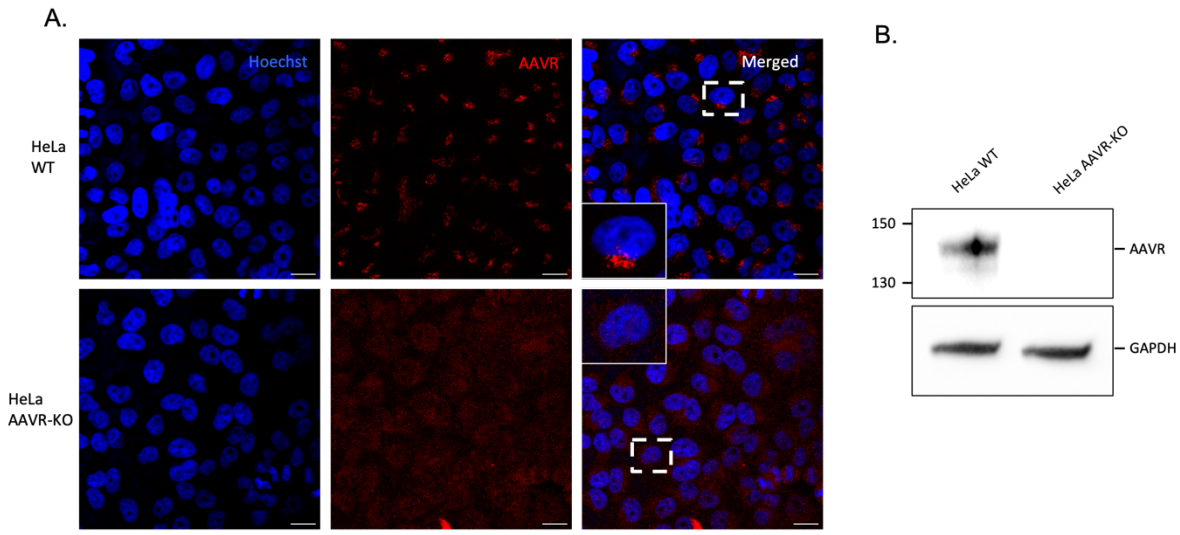

Figure 5.6: ***No endogenous signal can be detected in the AAVR-KO cell line -*** *(A) CRISPR cells were fixed with 4% paraformaldehyde and immunostained with Abcam AAVR antibody and Anti-Mouse Alexa488. Images vis confocal microscopy (63x). Scale bar is at 25 µm. (B) Treated cells were analysed by SDS-PAGE and immunoblotted with Abcam AAVR antibody at the recommended dilution. GAPDH was used as a loading control.*

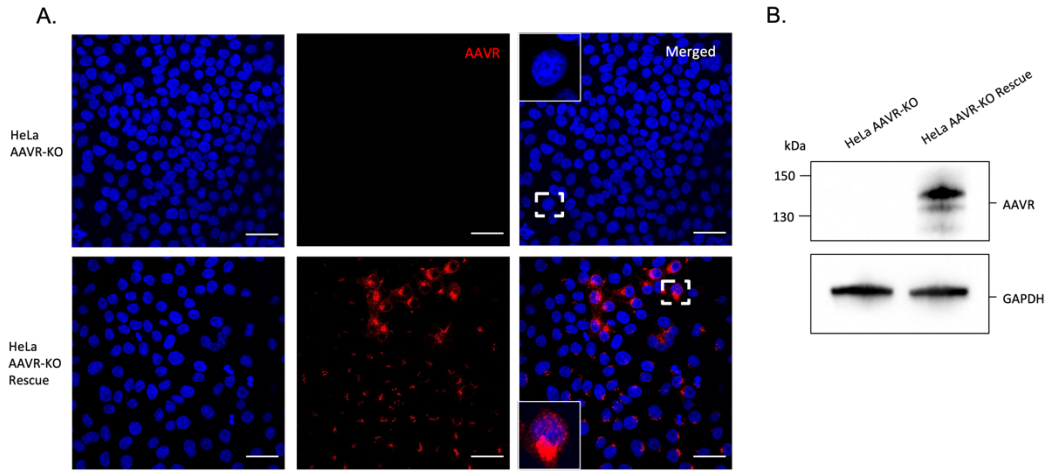

Figure 5.7: ***Lentiviral-mediated AAVR overexpression of in the AAVR-KO cell line*** *- (A) CRISPR AAVR-KO cells were fixed with 4% paraformaldehyde and immunostained with Abcam AAVR antibody and Anti-Mouse Alexa488. Images vis confocal microscopy (63x). Scale bar is at 38 µm. (B) Treated cells were analysed by SDS-PAGE and immunoblotted with Abcam AAVR antibody at the recommended dilution. GAPDH was used as a loading control.*

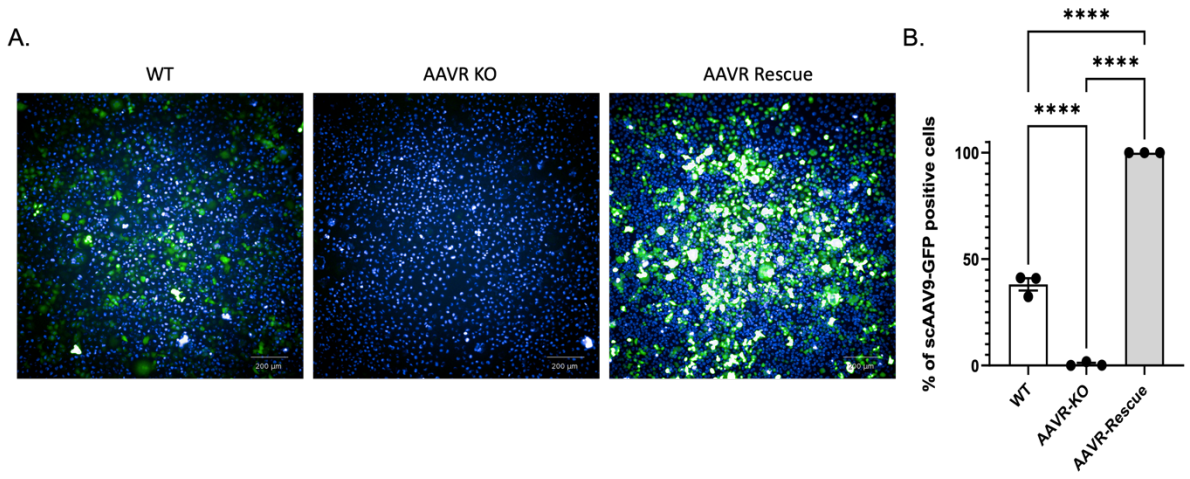

Figure 5.8: ***CRISPR knockout of AAVR abolishes transduction and is rescued by AAVR overexpression*** *– (A) scAAV9 transduction at 2 x 10^5 for 48-hour incubation for each siRNA condition. Cells were fixed with 4% paraformaldehyde and imaged via the Incell system (10x). Scale bar is at 200 µm (B) Graph represents mean relative number of scAAV9-GFP positive cells using Columbus analysis software. Normalised datasets are shown relative to the NTC dataset. (Mean±SEM; ANOVA, * * * * p≤0.0001, biological N=3).*

5.2.3 Generation of SDC4 CRISPR edited HeLa cell line.

To generate SDC4-KO HeLa cells, SDC4-specfiic guides were cloned into the AIO-puro Cas9-D10A nickase plasmid (Figure 2.1). The plasmid contains dual gRNA scaffolding sites which enables the cloning of both sense and antisense guides into a single construct. The sense guide recognises an upstream sequence in the target exon compared to that of the antisense guide. This enables the nickase to recognise and edit two different exon loci resulting in the generation of an indel (Ran, Hsu et al. 2013). Because of this, this method was very accurate. Additionally, the plasmid contains a puromycin-selection marker which enables the selection of successfully transfected cells which are expressing the guides and nickase (Chiang, le Sage et al. 2016). Puromycin resistant cells were then single seeded and expanded to CRISPR clones before determining SDC4 mRNA levels via quantitative PCR and further characterisation.

Quantitative PCR analysis revealed varied levels of mRNA knockdown in the seven CRISPR clones selected (Figure 5.9A). Clone □1 and Clone □7 had the strongest mRNA knockdown (52% and 51%, respectively, p≤*0.01*). Clone □7 was characterised via sequencing and Synthego ICE analysis which indicated specific indel mutations, ranging from a 10-base pair insertion (approximately 25% of population) to a 30-base pair deletion (approximately 3% of cell population) and 40% of unedited cells/alleles (Figure 5.9B). Whether this suggests the cell population was 40% unedited or if this was due to HeLa cells being polypoid, and therefore suggesting that the unedited percentage related to unedited alleles, was unclear. The discordance graph shows clear base-by-base differences after the cut site of the Cas9 in comparison between the reference sanger sequence (orange line) and the Cas9 sanger sequence (green line) (Figure 5.9C). The indel was shown via sequencing data locating the gRNA sequence (horizontal black line) and PAM site (horizontal red dashed line) which clearly shows a scrambled sequence following the homologous end-joining repair site (vertical black dashed line) (Figure 5.9D).

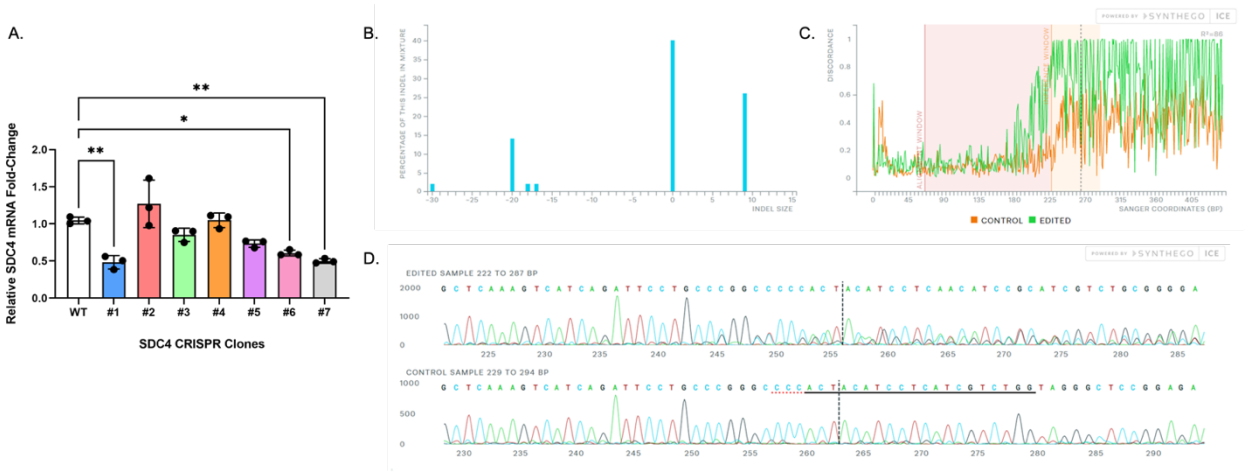

Figure 5.9: ***Generation and validation of HeLa SDC4-CRISPR cell line clones*** – *(A) HeLa SDC4 CRISPR edited clones RNA was collected for cDNA conversion and used for qPCR analysis to validate knockdown. Graph represents mean relative level of mRNA levels relative to that of the WT dataset (Mean*±SEM; *ANOVA*, * p≤0.05 * * p≤0.01, *N=3). (B) Indel plot generated from Sythego ICE which identifies the distribution of indels in the entire population of genomes and the percentage of genomes that contain it. (C) A discordance plot generated from Synthego ICE which shows the average amount of unaligned base sequences between the wild-type (orange line) and the mutant (green line) after the cut site. (D) Sanger sequence which shows edited sequence and wild-type sequence, and the black underline region is the guide sequence while the horizontal red line represents the PAM site. The vertical black dotted line represents the actual cut site.*

5.2.4 AAV9 gene transfer in SDC4-CRISPR HeLa cell lines

SDC4-CRISPR clone 7 was next characterised via both immunofluorescence and immunoblotting. Additionally, this SDC4-CRISPR line was then transduced with LV-Myc-SDC4, as described previously, to generate a rescue line of the CRISPR edited cells, termed SDC4-Rescue.

No expression of SDC4 could be detected in either the wild-type HeLa or SDC4 CRISPR-edited HeLa lines (Figure 5.10A). As a result, all future characterisation experiments in relation to endogenous SDC4 were achieved using quantitive PCR. The endogenous mRNA levels of SDC4 revealed 54% depletion in the SDC4-CRISPR line relative to the wild-type expression levels ($p \leq 0.01$) (Figure 5.10B). Characterisation of the SDC4-Rescue line showed strong overexpression, localised primarily in the cytoplasm (Figure 5.11A). In addition, SDC4 overexpression was readily detected via immunoblot (Figure 5.11B).

Once fully characterised, the SDC4-CRISPR line was transduced with scAAV9-GFP to determine if SDC4 depletion would affect AAV9 transduction efficiency and if LV-mediated SDC4 restoration rescues it. The HeLa wild-type condition showed an average of 38% GFP-positive cells, while the HeLa SDC4-CRISPR line had consistently elevated transduction efficiency with an average of 72% of GFP positive cells (a 90% increase relative to that of the wild-type, $p \leq 0.0001$) (Figure 5.11A), indicating that loss of SDC4 was enhancing transduction efficiency. Intriguingly, the SDC4-Rescue line revealed a rescue of this altered transduction by decreasing the transduction efficiency to 36%, back to that of the wild-type GFP levels ($p \leq 0.0001$) (Figure 5.11B).

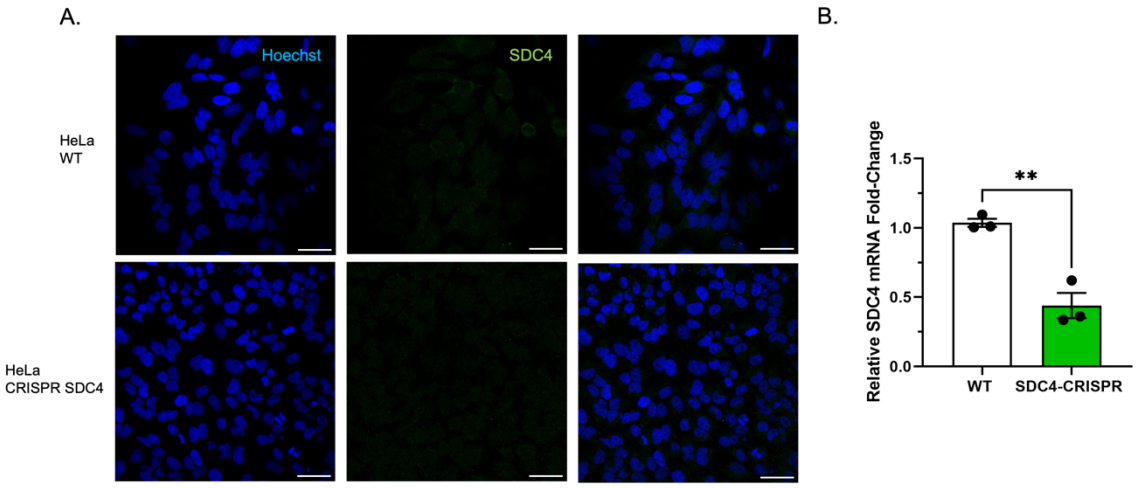

Figure 5.10: ***SDC4 mRNA levels were significantly reduced in the SDC4-CRISPR HeLa cell line –*** *(A) CRISPR cells were fixed with 4% paraformaldehyde and immunostained with Santa Cruz SDC4 antibody and Anti-Mouse Alexa488. Images vis confocal microscopy (63x). Scale bar is at 25 µm. (B) Treated cells RNA was collected enabling cDNA to be generated and used in a qPCR with optimised primers. Graph represents mean relative level of SDC4 mRNA levels relative to WT dataset (Mean*±SEM; *t*-test, * * p≤0.01, *biological* N=3).

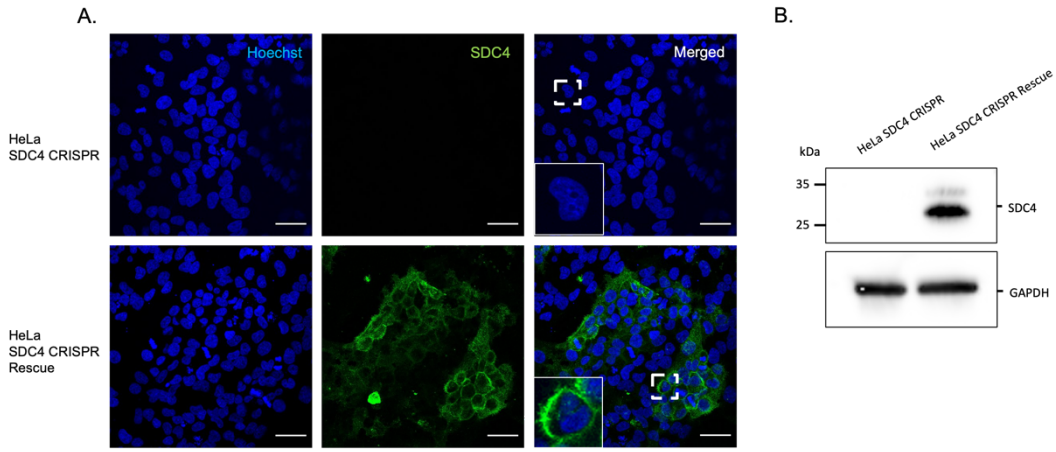

Figure **5.11:** ***LV-mediated stable restoration of SDC4 expression in CRISPR-SDC4 HeLa cell line-*** *(A) CRISPR cells were fixed with 4% paraformaldehyde and immunostained with SDC4 R&D antibody and Anti-Mouse Alexa488. Images vis confocal microscopy (63x). Scale bar is at 38 µm. (B) Treated cells were analysed by SDS-PAGE and immunoblotted with SDC4 R&D antibody at the recommended dilution. GAPDH was used as a loading control.*

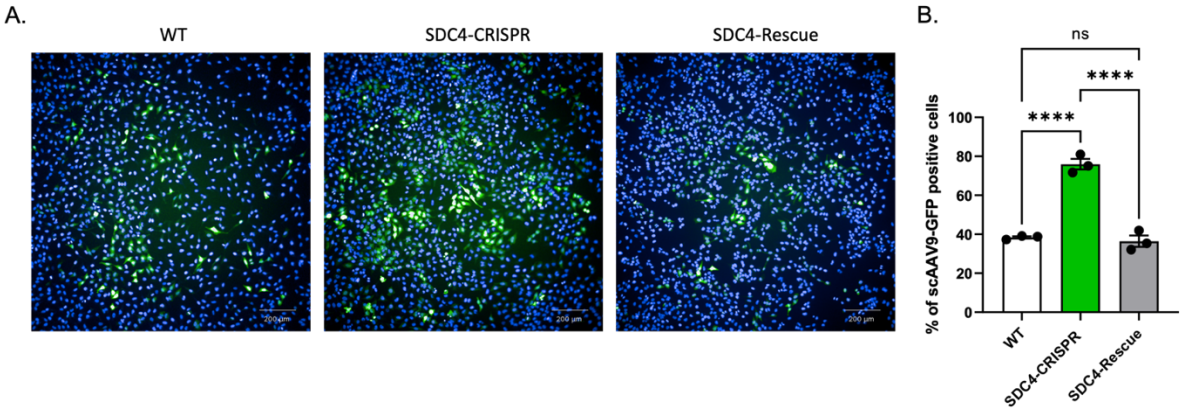

Figure 5.12: ***CRISPR knockdown of SDC4 significantly elevates transduction and is rescued by SDC4 overexpression*** *– (A) scAAV9 transduction at 2 x 10^5 for 48-hour incubation for each siRNA condition. Cells were fixed with 4% paraformaldehyde and imaged via the Incell system (10x). Scale bar is at 200 µm. (B) Graph represents mean relative number of scAAV9-GFP positive cells using Columbus analysis software. Normalised datasets are shown relative to the NTC dataset. (Mean±SEM; ANOVA, * * * * p≤0.0001, biological N=3).*

5.2.5 AAV9 gene transfer in ICAM1-CRISPR HeLa cell lines

A commercially available ICAM1-knockout cell line and its respective isotype wild-type were purchased from Abcam and characterised to validate their ICAM1 expression levels. Immunofluorescence and immunoblotting characterisation were performed to determine if endogenous signal could be observed in the isotype line and if signal was abolished in the CRISPR-knockout line. Additionally, a rescue cell line was generated using LV-FLAG_ICAM1 previously produced, termed ICAM1-Rescue.

No fluorescent signal of ICAM1 could be detected in either the isotype wild-type or ICAM1-CRISPR cells (Figure 5.13A). However, immunoblots confirmed complete depletion of ICAM1 protein in the ICAM1-CRISPR line (Figure 5.13B). The stable ICAM1-Rescue line on the other hand displayed clear overexpression of FLAG_ICAM1 within the cytoplasm but predominately localised at the cell membrane (Figure 5.14A). Furthermore, the ICAM1-Rescue line showed intense FLAG_ICAM1 signal via immunoblotting (Figure 5.14B). Following the characterisation and generating of ICAM1 HeLa cell lines, the cell lines underwent a transduction efficiency assay with scAAV9-GFP to determine if the knockout of ICAM1 affected transduction efficiency and if overexpression could rescue it. The wild-type isotype had an average of 17% of GFP positive cells while the ICAM1-KO cell line had an average of 33% of GFP positive cells, indicating significant increase AAV9 transduction efficiency (a 64% increase in transduction, $p \leq 0.05$) (Figure 5.15A). In the ICAM1-Rescue cell line, viral susceptibility was reduced to an average of 9% of GFP positive cells ($p \leq 0.001$), thus significantly rescuing the altered transduction efficiency observed in the ICAM1-KO cells (Figure 5.15B).

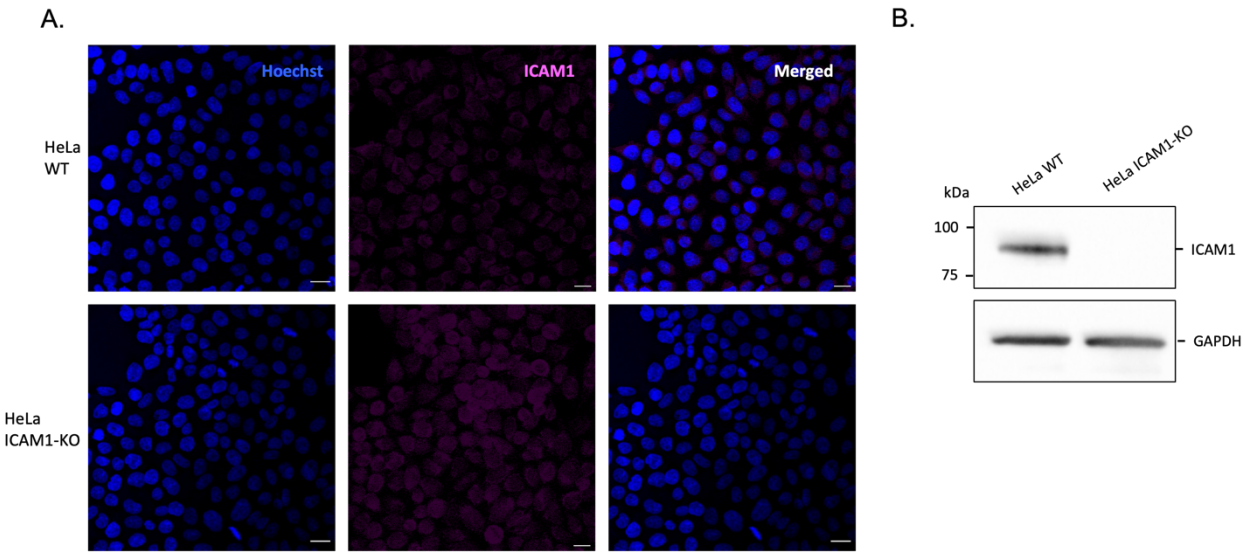

Figure 5.13: ***Knockout of ICAM1 was detectable via western analysis*** - (*A) CRISPR cells were fixed with 4% paraformaldehyde and immunostained with Abcam ICAM1 antibody and Anti-Mouse Alexa488. Images vis confocal microscopy (63x). Scale bar is at 25 µm. (B) Treated cells were analysed by SDS-PAGE and immunoblotted with Abcam ICAM1 antibody at the recommended dilution. GAPDH was used as a loading control.*

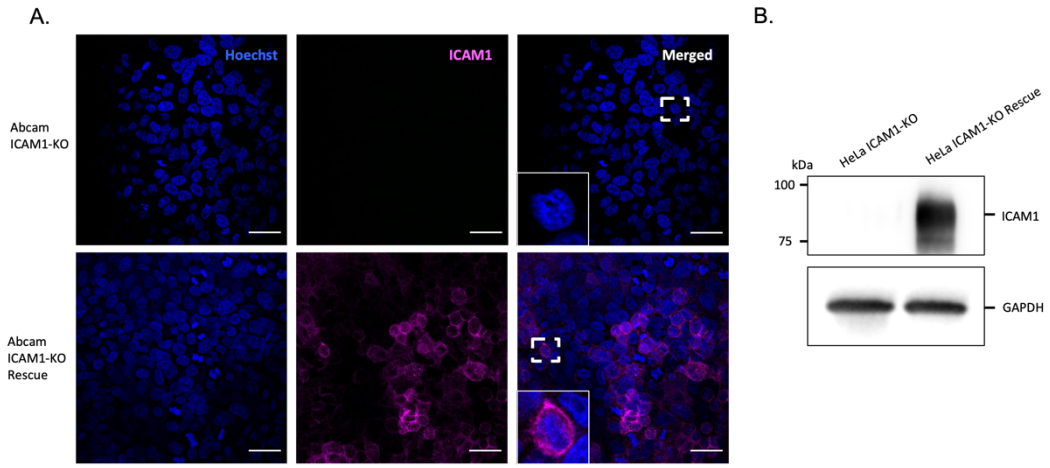

Figure 5.14: ***Overexpressed rescue levels of ICAM1 be detected in the ICAM1-KO cell line*** *- (A) CRISPR cells were fixed with 4% paraformaldehyde and immunostained with Abcam ICAM1 antibody and Anti-Mouse Alexa488. Images vis confocal microscopy (63x). Scale bar is at 38 µm. (B) Treated cells were analysed by SDS-PAGE and immunoblotted with Abcam ICAM1 antibody at the recommended dilution. GAPDH was used as a loading control.*

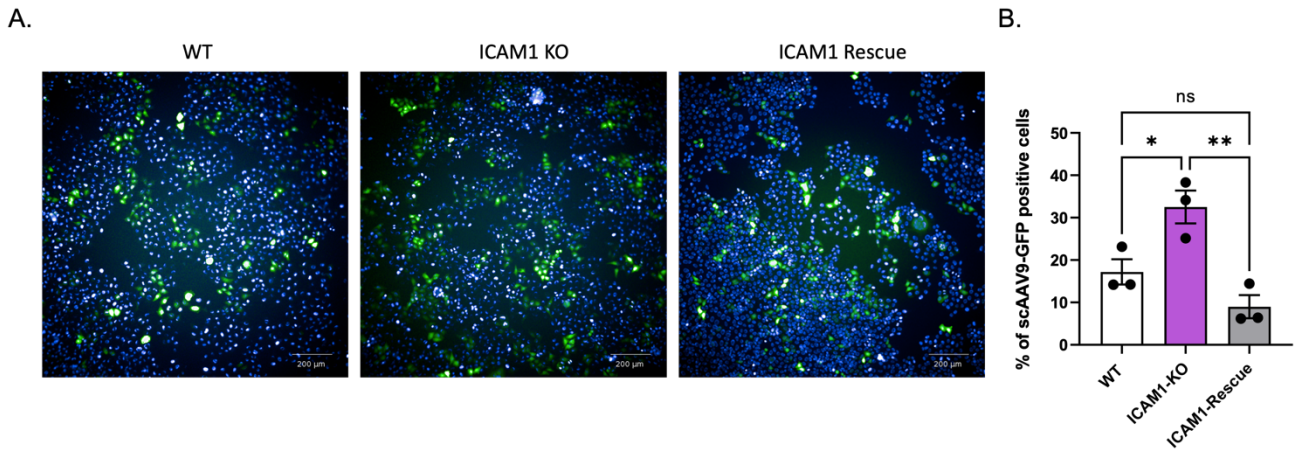

Figure 5.15: ***CRISPR knockout of ICAM1 elevates transduction and is rescued by ICAM1 overexpression***– (*A) scAAV9 transduction at 2 x 10*^{5} *for 48-hour incubation for each siRNA condition. Cells were fixed with 4% paraformaldehyde and imaged via the Incell system (10x). Scale bar is at 200 µm. (B) Graph represents mean relative number of scAAV9-GFP positive cells using Columbus analysis software. Normalised datasets are shown relative to the NTC dataset. (Mean±SEM; ANOVA, * p≤0.05, * * p≤0.01, biological N=3).*

5.2.6 AAV9 gene transfer of SLC7A2 CRISPR edited HeLa cell line

In order to generate an SLC7A2 CRISPR-edited cell line, guides were designed for a ribonucleoprotein-Cas9 method. The guides and Cas9 complex were transfected into HeLa cells via electropermeabilization. As a control, a population of HeLa cells were electroporated in the presence of ribonucleoprotein Cas9 complex alone, in the absence of gRNA's. These cells were referred to as CRISPR-Control. The edited population of cells which survived electropermeabilization were expanded and SLC7A2-CRISPR DNA was analysed by sequencing.

Sequencing data analysis software showed mutations in the HeLa SLC7A2-CRISPR mixed population with an estimated 1-base pair mutations (approximately 25% of the cell population) and variety of alternate base-pair mutations each at around 2% of the cell population (Figure 5.16A). An estimated 43% of the cell population were unedited but similarly to the HeLa SDC4-CRISPR line, this could be as a result of the HeLa line not being diploid in nature. The discordance graph shows a distinct difference between the control reference sequence and that of the edited sequence which suggests clear frameshift movement even before the cut site (Figure 5.16B). This could have been as a result of using two gRNA sequences to target exon 2, potentially resulting in a simultaneous dual edit. The predictive software identifies the gRNA reference sequence between the edited and the control sanger sequence and the PAM site shows the cut-site resulting in the scrambled read-out in the edited sample (Figure 5.16C).

Following the generation of the SLC7A2-CRISPR cell line, characterisation of SLC7A2 expression was conducted. Immunofluorescence of the CRISPR-Control cell line and the SLC7A2-CRISPR line revealed only background signal in either cell line (Figure 5.17A). Immunoblot analysis demonstrated approximately 63% knockdown in SLC7A2 protein levels in the SLC7A2-CRISPR HeLa cell line compared to that of the CRISPR-Control cell line (Figure 5.17B). This was additionally supported with the mRNA expression level of the SLC7A2 CRISPR line being reduced by 65% relative to that of the CRISPR-Control ($p \leq 0.001$) (Figure 5.17C).

Following the generation and characterisation of the cell lines for SLC7A2 expression, the cell lines were transduced with scAAV9-GFP to determine if genetic depletion of SLC7A2 dysregulated viral transduction efficiency. The CRISPR-Control HeLa cell line showed an

average of 34% of GFP positive cells while the CRISPR_SLC7A2 showed a reduced quantity of GFP cells at 26% (Figure 5.18A), potentially indicating that loss of SLC7A2 reduces AAV9 transduction efficiency. However, due to variation in the wild-type control, the reduction was not significant ($p \leq 0.298$) (Figure 5.18B).

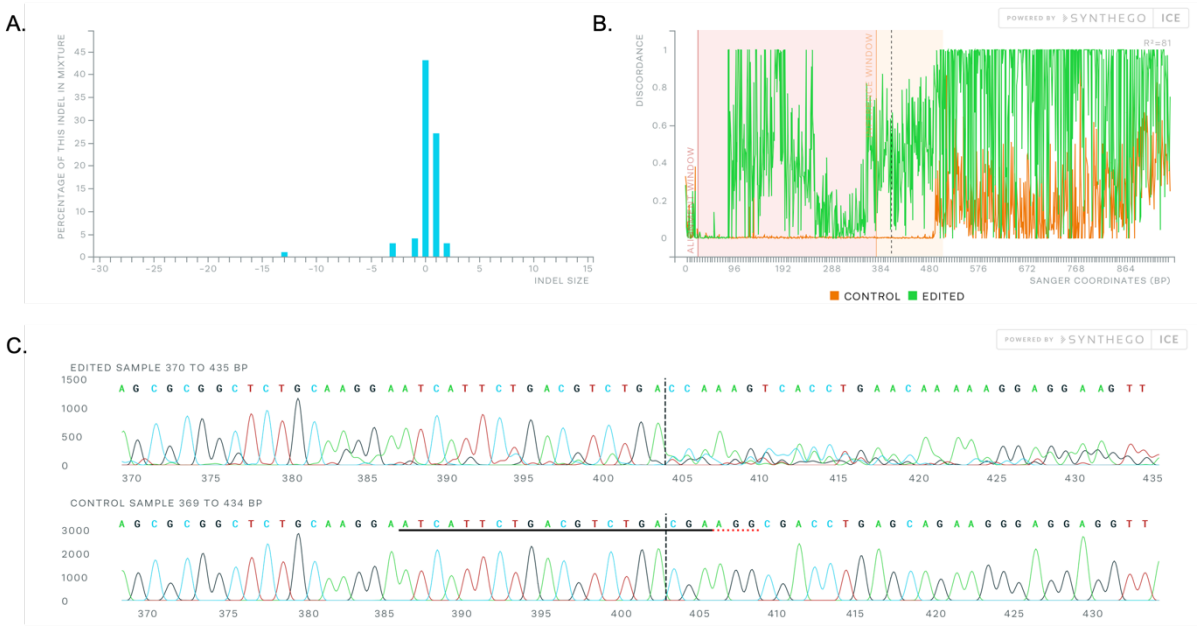

Figure 5.16: ***Generation and validation of HeLa SLC7A2-CRISPR mixed population cell line*** – *(A) Indel plot generated from Sythego ICE which identifies the distribution of indels in the entire population of genomes and the percentage of genomes that contain it. (B.) A discordance plot generated from Synthego ICE which shows the average amount of unaligned base sequences between the wild-type (orange line) and the mutant (green line) after the cut site. (C). Sanger sequence which shows edited sequence and wild-type sequence, and the black underline region is the guide sequence while the horizontal red line represents the PAM site. The vertical black dotted line represents the actual cut site.*

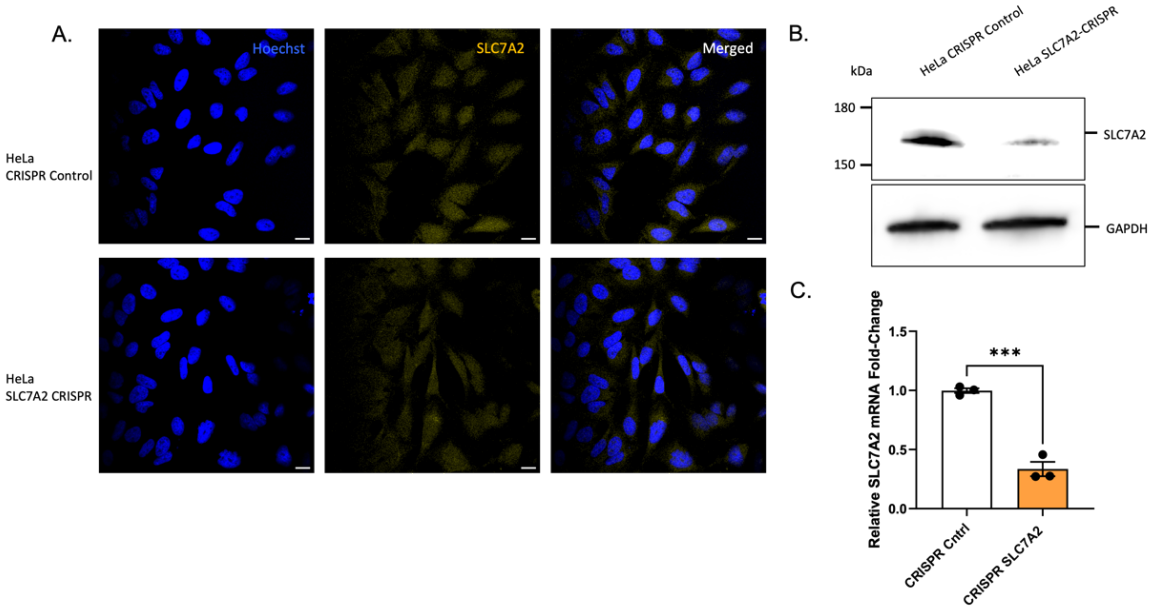

Figure 5.17: ***CRISPR knockdown of SLC7A2 was detectable via western analysis and qPCR*** **-** **(***A) CRISPR cells were fixed with 4% paraformaldehyde and immunostained with Abcam SLC7A2 antibody (Reference) and Anti-Mouse Alexa488. Images vis confocal microscopy (63x). Scale bar is at 25 µm. (B) Treated cells were analysed by SDS-PAGE and immunoblotted with Abcam SLC7A2 antibody at the recommended dilution. GAPDH was used as a loading control. (C.) CRISPR cells RNA was collected enabling cDNA to be generated and used in a qPCR with optimised primers. Graph represents mean relative level of SLC7A2 mRNA levels relative to CRISPR Control (Cntrl) dataset (*Mean*±SEM; *t*-test, * * * p≤0.001, *biological* N=3).

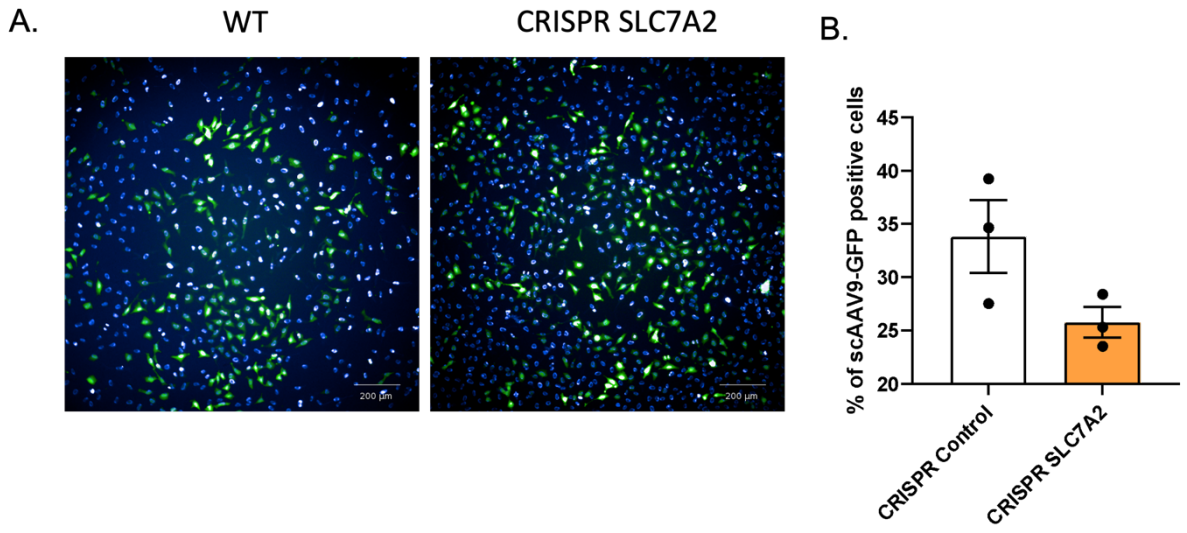

Figure 5.18: ***CRISPR knockdown of SLC7A2 reduces scAAV9 transduction*** *– (A) (A) scAAV9 transduction at 2 x* 10^5 *for 48-hour incubation for each siRNA condition. Cells were fixed with 4% paraformaldehyde and imaged via the Incell system (10x). Scale bar is at 200 µm. (B) Graph represents mean relative number of scAAV9-GFP positive cells using Columbus analysis software. Normalised datasets are shown relative to the NTC dataset. (Mean±SEM; t-test, biological N=3).*

5.2.7 Protein off-target screen across all HeLa CRISPR lines

Although CRISPR is a precise genetic tool, off-targeted effects and dysregulation of cellular pathways can still occur (Atkins, Chung et al. 2021). As a method to validate the effects observed in the transduction efficiency, each target protein was screened to validate if any of the proteins of interest were simultaneously dysregulated. Due to the lack of a functional antibody for SDC4, this target was unable to be investigated via immunoblot.

The levels of the four target proteins in the CRISPR-edited and knockout cell lines were analysed via immunoblot. Loss of AAVR in the AAVR knockout line significantly decreased ICAM1 protein signal ($p<0.05$) but did not show any dysregulation of SLC7A2 protein levels (Figure 5.19A). The downregulation of SDC4 in the SDC4-CRISPR line showed an increase in AAVR protein levels by 1.5-fold and a major reduction in SLC7A2 protein levels (Figure 5.20A). No dysregulation was observed with ICAM1 protein levels with SDC4-CRISPR cells. The loss of ICAM1 in the ICAM1 knockout cells showed unchanged levels of AAVR protein levels however revealed a non-significant decrease in SLC7A2 protein levels which had varied downregulated expression (Figure 5.21A). While the CRISPR-SLC7A2 cell line showed no dysregulation of protein expression of ICAM1 or AAVR (Figure 5.22A).

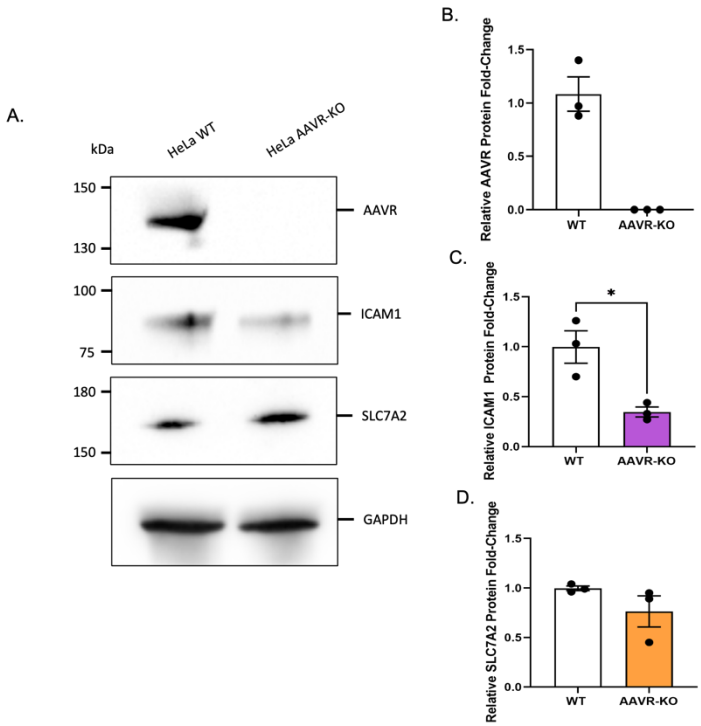

Figure 5.19: ***AAVR-knockout cell line displays a significant decrease in ICAM1 protein level*** – *(A) Wild-type isotype/CRISPR Control cell lines and CRISPR edited cell lines were lysed and subjected to an SDS-PAGE and immunoblot. Blots were incubated with Abcam AAVR, Abcam ICAM1 and Abcam SLC7A2. Normalised datasets are shown relative to the NTC dataset - (B) AAVR (C) ICAM1 and (D) SLC7A2. (Mean±SEM; t-test, * p≤0.05, biological N=3).*

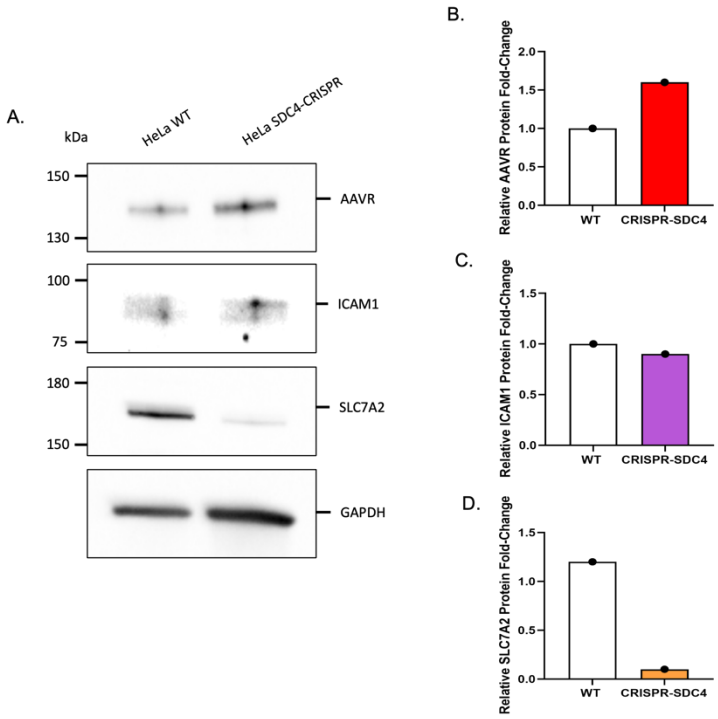

Figure 5.20: ***A major decrease in SLC7A2 protein level in the HeLa SDC4-CRISPR cell -*** *(A) Wild-type isotype/CRISPR Control cell lines and CRISPR edited cell lines were lysed and subjected to an SDS-PAGE and immunoblot. Blots were incubated with Abcam AAVR, Abcam ICAM1 and Abcam SLC7A2. Normalised datasets are shown relative to the NTC dataset - (B) AAVR (C) ICAM1 and (D) SLC7A2 (biological N=1).*

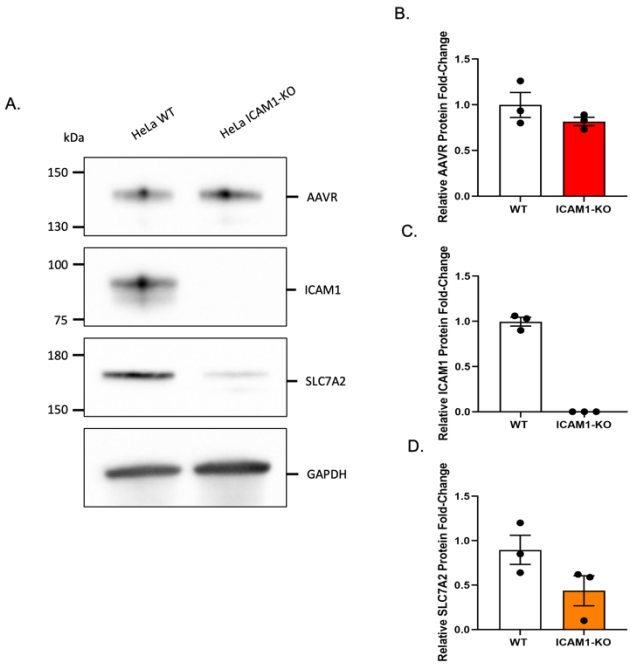

Figure 5.21: ***Knockout of ICAM1 may impact SLC7A2 protein level in ICAM1 knockout cell line –*** *(A) Wild-type isotype/CRISPR Control cell lines and CRISPR edited cell lines were lysed and subjected to an SDS-PAGE and immunoblot. Blots were incubated with Abcam AAVR, Abcam ICAM1 and Abcam SLC7A2. Normalised datasets are shown relative to the NTC dataset - (B) AAVR (C) ICAM1 and (D) SLC7A2. (Mean±SEM; t-test, biological N=3).*

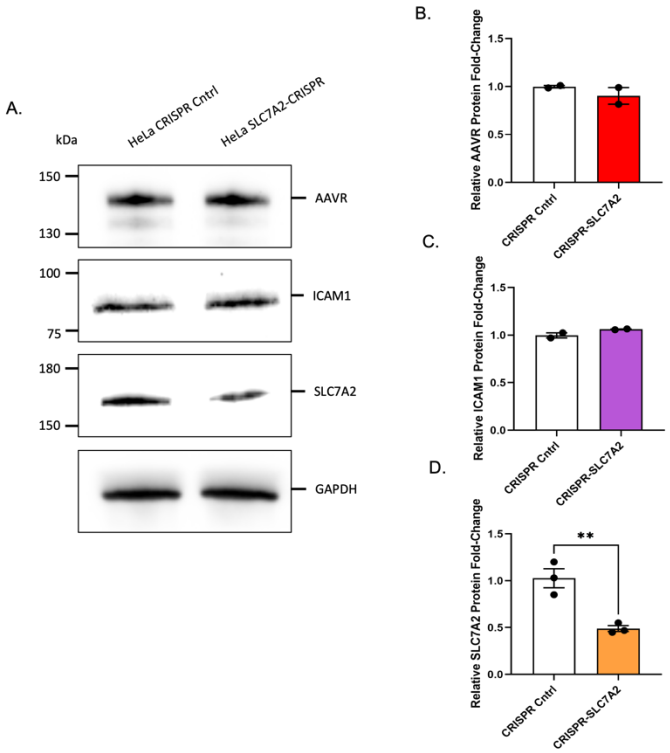

Figure 5.22: ***No indirect dysregulation was observed in the HeLa CRISPR-SLC7A2 line*** *– (A) Wild-type isotype/CRISPR control cell lines and CRISPR edited cell liens were lysed and subjected to an SDS-PAGE and immunoblot. Blots were incubated with Abcam AAVR, Abcam ICAM1 and Abcam SLC7a2. Normalised datasets are shown relative to the NTC dataset – (B) AAVR (C) ICAM1 and (D) SLC7A2 (Mean±SEM; t-test, ** p<0.01, biological N=3).*

5.2.8 Internalisation Assay of AAV9 in CRISPR-edited HeLa cell lines

AAVR, SDC4, ICAM1 and SLC7A2 all localise to the cell membrane (Anbarasan, Bavanilatha et al. 2015, Pillay, Meyer et al. 2016, Xia, Wu et al. 2021, Hudak, Roach et al. 2023). Having shown that alteration to their expression and their potential interactions with the AAV9 capsid proteins, it was theorised that these targets could be involved in the early stages of the AAV transduction pathway. To validate this, the HeLa knockout and CRISPR-edited cells, with their respective isotype and rescue lines, were incubated with AAV9-mCherry for 24-hours to determine if AAV9 entry was affected. Trypsin was used prior to DNA extraction to remove any extracellularly attached virions, meaning all transgenes quantified via quantitative PCR, were internalised virions only (Madigan, Berry et al. 2020).

The removal of the C-tail of AAVR was shown to affect the internalisation of AAV2 via immunostaining, so the knockout of the target was expected to have a similar effect in this assay with AAV9 (Pillay, Meyer et al. 2016). However, wild-type isotype and AAVR knockout cell line showed no difference comparatively in transgene signal, suggesting no difference in the rate of entry (Figure 5.23A). On the other hand, the AAVR-Rescue cell line showed a significant increase in transgene signal (a 58-fold increase, $p \leq 0.0001$). In the HeLa SDC4 cell lines, the SDC4-CRISPR cell line and the SDC4-Rescue line had a reduced transgene signal relative to that of the HeLa wild-type (33% and 27% reduction, respectively) (Figure 5.23B). In the HeLa ICAM1 cell lines, the wild-type isotype and ICAM1 knockout cell lines showed a 35% upregulation in transgene signal (Figure 5.23C). Alternatively, the rescue cell line showed a non-significant rescue by having transgene signal like that of the wild-type isotype cell line. In the SLC7A2 CRISPR cell line, the level of transgene signal was shown to have no difference between the CRISPR-Control and the CRISPR SLC7A2 cell lines (Figure 5.23D). This is similar to that of the transduction efficiency results which supports the fact that the CRISPR knockdown of SLC7A2 has no effect on the entry rate of AAV9.

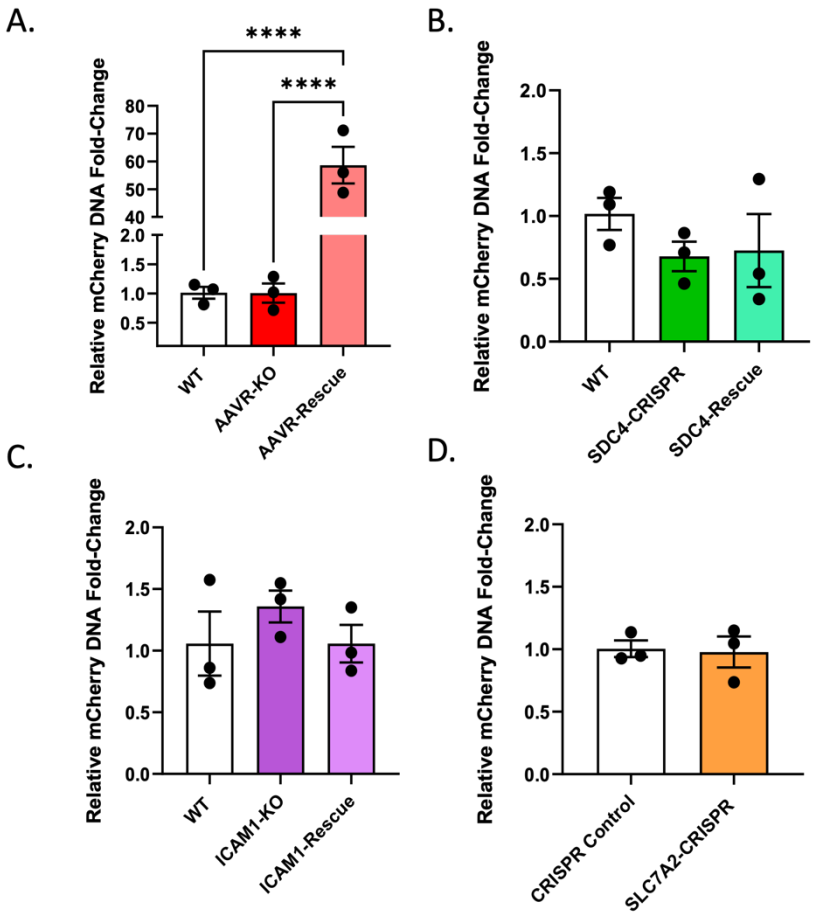

Figure 5.23: ***AAVR rescue increases viral internalisation*** *– Cells were seeded and incubated with 5 x 10^4 ssAAV9_mCherry for 24 hours before being lifted with trypsin. DNA was collected and used for qPCR analysis using optimised mCherry primers to validate internalisation. GAPDH was used as a housekeeping gene. Normalised datasets are shown relative to the wild type/CRISPR Control dataset for (A) AAVR, (B) SDC4, (C) ICAM1 and (D) SLC7A2. (Mean±SEM; ANOVA, * * * * p≤0.0001, biological N=3).*

5.2.9 Generation of SHSY CRISPR cell lines

In Chapter 3, SHSY's were characterised as the most permissive neuronal cell line to AAV9 transduction. To determine if loss of AAVR, SDC4, ICAM1 or SLC7A2 could affect transduction efficiency in these cells, SHSY CRISPR edited lines were generated. Although SHSY's do not express the target proteins on a detectable level via immunoblotting, as screened previously, the proteins could still have functional relevance in AAV9's SHSY transduction pathway at very low levels. As a result, CRISPR-KO lines of SHSYs were attempted to be generated due to being the strongest permissive cell line and due to the cell line having a near-diploid karyotype (1.8% polyploidy) which may result in fewer varied indels post Cas9 cleavage and therefore fewer genetic variation events (Yusuf, Leung et al. 2013). Like the HeLa SLC7A2 CRISPR edited line described previously, SHSY cells were treated with ribonucleoprotein-Cas9 and designed guides and transfected via electroporation. Viable cells were then expanded, and then single cell seeded. Confluent clones DNA were sent for sanger sequencing and analysed via Synthego ICE software.

The SHSY AAVR-CRISPR cell line clones showed varied AAVR mRNA depletion with clone 1 and clone 6 having the highest knockdown (72% and 76%, respectively, $p \leq 0.0001$ (Figure 5.24A). Clone 6 was sent off for sanger sequencing and the data shows varied indels in the cell population ranging from a 39 base-pair deletion (1% of cell population) and a 15 base-pair insertion (5% of cell population) (Figure 5.24B). Only 1% of the cell's population are estimated to be unedited. The discordance graph shows a distinct difference between the control reference sequence and that of the edited sequence after the cut site (Figure 5.24C). The sanger sequence shows following the cut site and PAM sequence a scrambled base pair read-out compared to the control sample sequence (Figure 5.24D).

The SHSY SDC4-CRISPR cell line clones showed a varied SDC4 mRNA knockdown of each clone, with clone 6 showing the highest mRNA knockdown at 71% ($p \leq 0.0001$) (Figure 5.25A). This clone was sent for sanger sequencing which revealed a range of indels in exon 2 from 2 base-pair deletions (10% of the population) to 17-base pair insertions (2% of the population) (Figure 5.25B). Only 3% of the cell population are predicted to be unedited. The discordance graph and the sanger sequence data show scrambled and altered sequence following the cut

site (Figure 5.25C). Even before the cut site, the base-pair read-out was in disorder relative to the control sequence suggesting frameshift movement in certain alleles (Figure 5.25D).

The SHSY ICAM1-CRISPR cell population showed no indels were introduced (Figure 5.26A). The indel graph shows 100% of cell unedited and the discordance graph shows no dissimilarity between the CRISPR-edited and the control sequence (Figure 5.26B). Additionally, the sanger sequence showed complete similarity between the base-pairs detected between the CRISPR-edited and the control sequence (Figure 5.26C). As a result, these cells were not single seeded like the other edited populations.

The SHSY SLC7A2-CRISPR cell populations showed a varied SLC7A2 mRNA knockdown of each clone. Several clones appear to have no expression of SLC7A2 mRNA suggesting they are complete knockouts of the target protein (*p≤0.0001)* (Figure 5.27A). The indel graph showed a wide range of alternate indels ranging from 24-base pair deletions (6% of the population) to 13-base pair insertions (3% of the population) (Figure 5.27B). Only 4% of the population was predicted to be unedited. The discordance graph showed a clear difference in base-pairs between following the Cas9 cut site (Figure 5.27C). The sanger sequence comparison showed a complete scramble of base-pair read-out following the cut site, supporting further the success in the introduction of an indel (Figure 5.27D).

Although the CRISPR SHSY cell lines were generated, due to time constraints, investigating if AAV9's transduction efficiency was dysregulated was planned for future studies.

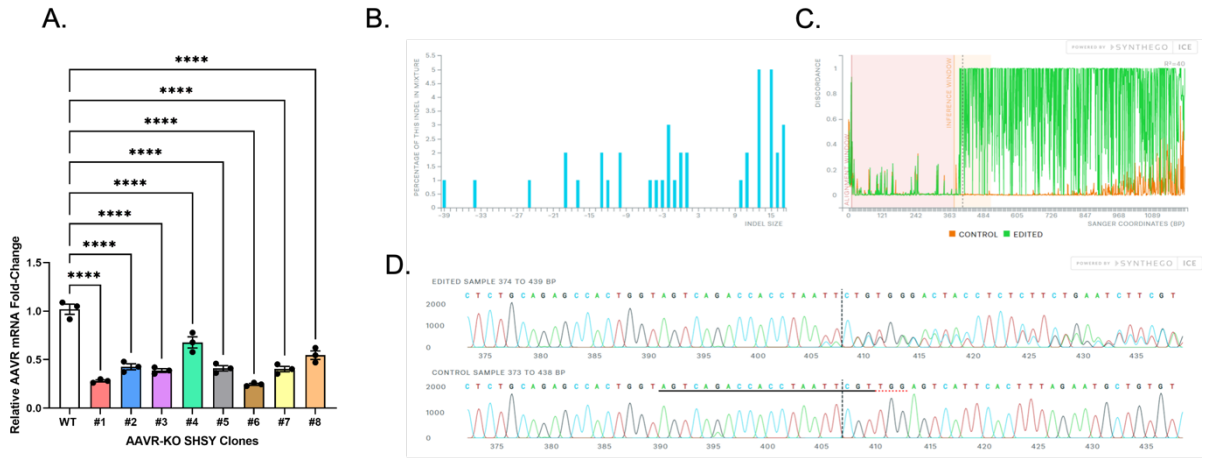

Figure 5.24: Generation ***and validation of SHSY AAVR-CRISPR cell line clones*** – *(A) SHSY AAVR CRISPR edited clones RNA was collected for cDNA conversion and used for qPCR analysis to validate knockdown. Graph represents mean relative level of mRNA levels relative to that of the WT dataset (Mean*±SEM; *ANOVA, * * * * p≤0.0001, biological N=1). (B) Indel plot generated from Sythego ICE which identifies the distribution of indels in the entire population of genomes and the percentage of genomes that contain it. (C). A discordance plot generated from Synthego ICE which shows the average amount of unaligned base sequences between the wild-type (orange line) and the mutant (green line) after the cut site. (D). Sanger sequence which shows edited sequence and wild-type sequence, and the black underline region is the guide sequence while the horizontal red line represents the PAM site. The vertical black dotted line represents the actual cut site.*

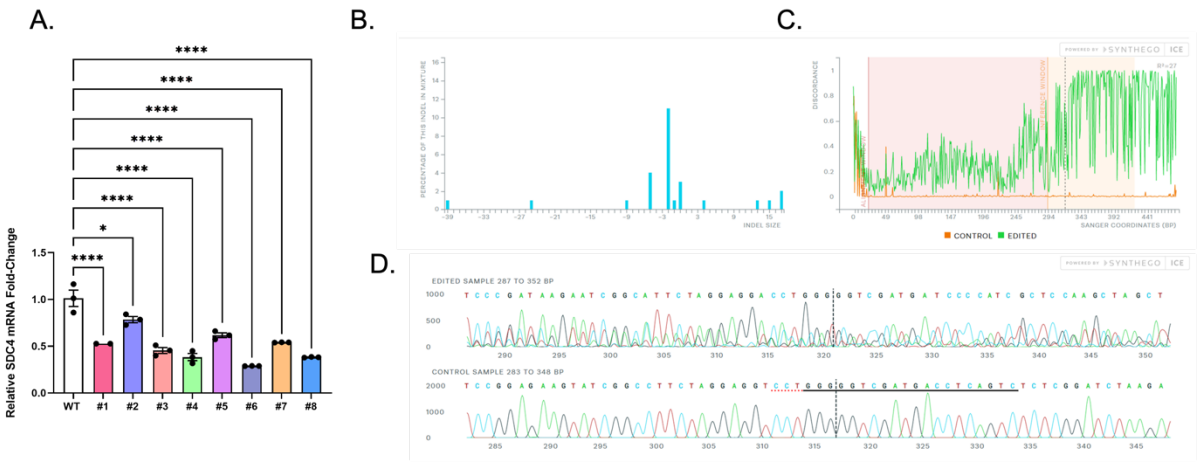

Figure 5.25: ***Generation and validation of SHSY SDC4-CRISPR cell line clones*** *– (A) SHSY SDC4 CRISPR edited clones RNA was collected for cDNA conversion and used for qPCR analysis to validate knockdown. Graph represents mean relative level of mRNA levels relative to that of the WT dataset (Mean*±SEM; *ANOVA, * p≤0.05, * * * * p≤0.0001, biological N=1).((B) Indel plot generated from Sythego ICE which identifies the distribution of indels in the entire population of genomes and the percentage of genomes that contain it. (C) A discordance plot generated from Synthego ICE which shows the average amount of unaligned base sequences between the wild-type (orange line) and the mutant (green line) after the cut site. (D). Sanger sequence which shows edited sequence and wild type sequence, and the black underline region is the guide sequence while the horizontal red line represents the PAM site. The vertical black dotted line represents the actual cut site.*

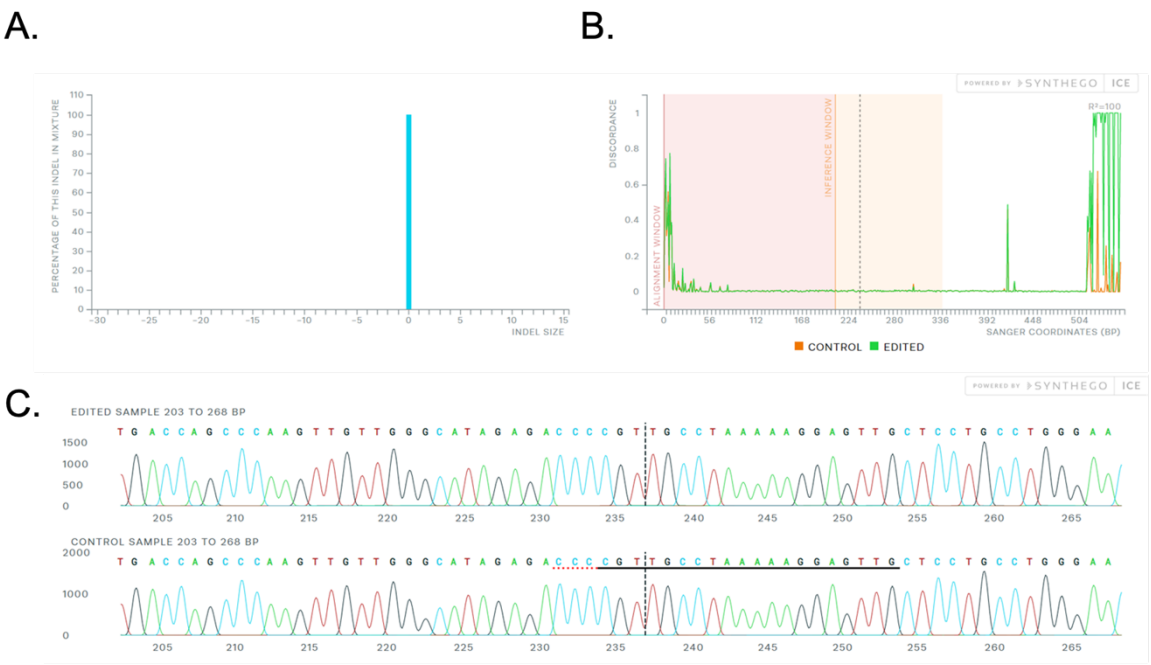

Figure 5.26: ***No indel confirmation of SHSY ICAM1-CRISPR edited mixed population*** *– (A) Indel plot generated from Sythego ICE which identifies the distribution of indels in the entire population of genomes and the percentage of genomes that contain it. (B) A discordance plot generated from Synthego ICE which shows the average amount of unaligned base sequences between the wild-type (orange line) and the mutant (green line) after the cut site. (C). Sanger sequence which shows edited sequence and wild-type sequence, and the black underline region is the guide sequence while the horizontal red line represents the PAM site. The vertical black dotted line represents the actual cut site.*

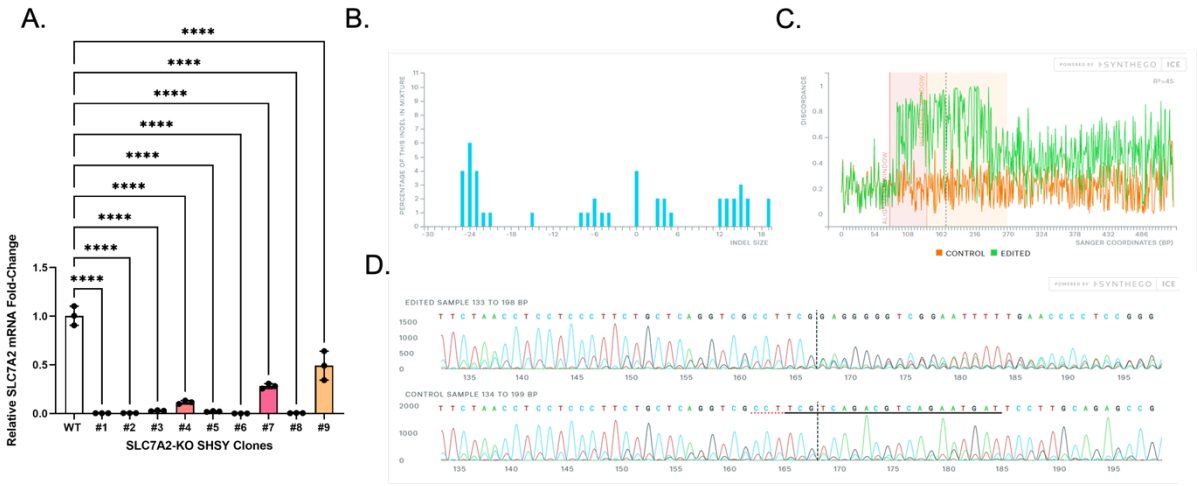

Figure 5.27: ***Generation and validation of SHSY SLC7A2-CRISPR cell line clones*** *– (A) SHSY SLC7A2 CRISPR edited clones RNA was collected for cDNA conversion and used for qPCR analysis to validate knockdown. Graph represents mean relative level of mRNA levels relative to that of the WT dataset (Mean*±SEM; *ANOVA, * * * * p≤0.0001, biological N=1).B) Indel plot generated from Synthego ICE which identifies the distribution of indels in the entire population of genomes and the percentage of genomes that contain it. (C.) A discordance plot generated from Synthego ICE which shows the average amount of unaligned base sequences between the wild-type (orange line) and the mutant (green line) after the cut site. (D). Sanger sequence which shows edited sequence and wild-type sequence, and the black underline region is the guide sequence while the horizontal red line represents the PAM site. The vertical black dotted line represents the actual cut site.*

5.3 Discussion

The purpose of this chapter was to determine if loss of AAVR, ICAM1, SDC4 or SLC7A2 affected AAV9 transduction efficiency. This was tested via two LOF experiments: an siRNA screen to knockdown mRNA expression of each target and the generation of CRISPR-edited cell lines in identified permissive cell lines. The siRNA knockdown screen showed reduced transduction efficiency with AAVR, SDC4 and ICAM1 but siRNA was limited by potential off-targeted effects due to sequence homology. As a result, CRISPR lines of the HeLa cell line were generated and showed reduced transduction efficiency in the AAVR-KO cell lines. However, the ICAM1-KO and SDC4 CRISPR cell lines showed an increase in transduction efficiency. The specificity of these findings was confirmed by overexpressing each target with their respective CRISPR-knockout lines which revealed restoration of the levels when compared to the wild-type isotype levels. Additionally, it was investigated if these targets are involved in the vector's entry pathway via an internalisation assay which showed no difference between the wild-type and AAVR-knockout lines except for the AAVR-Rescue line showed a significant increase in transgene delivery.

The CRISPR knockout of the target proteins was hypothesised to decrease viral transduction due to the lack of the theorised entry factor. This was shown to be an effective method with our positive control AAVR target as the knockout elicited no transduction while its rescue resulted in heightened transduction (Figure 5.7). Although this was successful, the CRISPR knockout of ICAM1 and CRISPR-edit of SDC4 increased viral transduction, suggesting that these targets act as restriction factors to scAAV9 in the HeLa cell line (Figure 5.11 and 5.14, respectively). This was further supported as overexpressing the respective target proteins in their knockout line showed reduced scAAV9 transduction. Similar results have been shown in the Madigan, Tyson et al. (2019) study which identified the cell polarity determinant Crumbs 3 protein, referred to as Crb3, as a AAV restriction factor in hepatocytes. This was proven by knocking out the protein resulting in elevated transduction and stable expression of the target in these lines decreased transduction. Previous studies have shown that altering cell surface glycan availability can affect AAV9 transduction efficiency (Meyer and Chapman 2022). In the Shen, Bryant et al. (2011) study, AAV9 transduction efficiency increased by increasing the availability of interacting proteins via neuraminidase treatment to selectively

remove alternate glycans. The data presented here indicated that loss of SDC4 and ICAM1 could be acting in a similar way, enabling greater access to sugars and proteins at the lipid bilayer which are part of AAV9's interactome, thus leading to increased transduction efficiency. ICAM1 as a potential restriction factor is supported by the findings in Chapter 4 that show ICAM1 is capable of interacting with the VP1 capsid protein. Given that they interact, yet its loss increases efficiency, it is possible ICAM1 has an inhibitory function to AAV9 transduction. ICAM1 may guide AAV9 into a dead-end pathway and by removing the proteins membrane involvement results in the virions reaching productive trafficking routes resulting in improved transduction (Riyad and Weber 2021). Due to being an interacting partner and ICAM1's known function in immune cells (Bui, Wiesolek et al. 2020), ICAM1 could be suggested to have an alternate function, for example in relation to an immune cell pathway. ICAM1 has been shown previously to have a function as a regulator of macrophage phagocytosis and co-stimulate T-cell activation with leucocyte function-associated antigen-1 (LFA-1) (Kohlmeier, Rumsey et al. 2003, Zhong, Lin et al. 2021). Because of this, it would be suggested to determine the expression level of ICAM1 in T-cells and macrophages and whether AAV9 viral clearance and AAV9-induced T-cell activation is affected when ICAM1 is inhibited in both immune cell types.

The Cas9-D10A nickase strategy minimises the chances of off-targeted genome editing, which is a potential limitation with wild type Cas9 (Zhang and Jiang 2022). Furthermore, the construct was designed in such a way that dual gRNA can be cloned into a single vector, meaning only a single transfection step was required unlike previous methods which required a dual transfection of two separate Cas9 constructs each with a separate gRNA (Adikusuma, Pfitzner et al. 2017). For these reasons, the Cas9-D10A system was initially used to generate the CRISPR knockouts of the novel targets detailed here. The presence of a puromycin marker within this construct was also beneficial as it enabled the antibiotic-selection of transfected cells, and therefore potentially edited cell populations. The AIO_Puro_SDC4 construct was shown to successfully introduce an indel in the generated SDC4-CRISPR HeLa cell line (Figure 5.9D). Although this was a success, the predicted sequencing data showed that around 40% of the alleles amplified were unedited (Figure 5.9B). This could be as a result of during the manual single-seeding step, the clone selected had an unedited cell in its population resulting in a mixed edit population over time. This seems unlikely as the cells underwent antibiotic-

selection, but the unedited cells transduced with the construct may not of had an indel introduced potentially due to repair of the strand break. These repaired cells may have survived in the presence of puromycin due to retaining the transfected construct. To validate this, designing primers across the exon of interest and cloning these amplified sequences into blunt-end constructs would enable identification of edited and non-edited exons in alternate alleles. An improvement to this method was used in the Chiang, le Sage et al. (2016) study in which the AIO_puro constructs designed contained a 2A peptide-linker to a EGFP and mCherry fluorescent marker which enabled quantification of transfection efficiency and easier selection of Cas9-D10A expressing cells resulting in a very high editing efficiency. The use of electroporation for the AIO_puro construct could also be considered to improve the transfection efficiency, however due to the permeabilization of the membranes, antibiotic selection would be unable to be attempted. An alternative reason for the high percentage of unedited cells could be as a result of the HeLa cell line having a polyploid genotype. Due to the cell line having multiple copies of alleles, high efficiency in genetic edit was required as cells which are identified as edited may still contain alleles which have no indels and are functional in expression (Yin, Liu et al. 2018). In both CRISPR-edited cell lines generated, the mRNA expression was significantly knocked down. However, they could not be identified as a genetic knockout due to maintaining expression. Although this was not a major limitation, the retained expression may mask the deregulatory effects being investigated. Due to the level of CRISPR-induced knockdown being similar to that of the siRNA-induced knockdown, the difference in their effects on viral transduction could be as a result of chronic reduction in the CRISPR lines which gives the cells time to adapt and alter protein expression. While the transient acute knockdown of siRNA may not provide enough time for the cells to adapt and therefore results in a dysregulated cell surface, altering protein-virus interactions.

Other permissive cell lines which have fewer genetic-edit variability could be suggested for future use. This will still be a challenge as alternate cell lines which are known to be permissive for scAAV9, for example HEK293T, U2-OS and HUVEC cell lines, are all polyploid in genetic nature (Ellis, Hirsch et al. 2013). Intriguingly, the SHSY cell line has a near-diploid karyotype consisting of 47 chromosomes which would be an ideal model in respect to being a more stable genotype cell line (Shipley, Mangold et al. 2016). Unfortunately, due to time constraints, the CRISPR method was adapted and the use of electroporation of CRISPR-Cas9/gRNA

ribonucleoprotein complexes were used due to its high efficiency. The RNP system was preferred as following electroporation, the RNP complex cleaves the target sequences while rapidly being degraded via intracellular degradation pathways (Bloomer, Khirallah et al. 2022). Due to this high turnover rate, the limitations of off targeting were minimised. Additionally, two guides targeting two different regions of the same exon were transfected, per target protein, to increase the chances of introducing an indel in the targeted exon. The SHSY clones of each target showed effective knockdown in expression except for that in the ICAM1 condition. Reasons for the ICAM1 population having had no indels identified could be as a result of the guides designed may not have been efficient. To improve efficiency of edit, newly designed guides could be optimised and validated. In the Mei, Gu et al. (2022) study, the CRISPR-Surfaceome online tool and database was created for the design of gRNA's specifically focused on cell surface proteins. Within this study, ICAM1 was targeted with guides generated from the CRISPR-Surfaceome tool which led to the development of ICAM1 knockout H1-HeLa cells to investigate rhinovirus infectivity. It would be suggested to use the same guides designed in the study or to use the software to design new guides against ICAM1 and potentially future targets. The single cell selected clones in the other targets showed a variety of indels within each cell population. This variety of indels could be as a result of reasons mentioned previously and the use of a more accurate single seeding method, such as flow cytometry, would be recommended (Chiang, le Sage et al. 2016). Although there is a variety of indels, the predictive software detected fewer unedited cell populations in the SHSY cell lines, suggesting the increased effectiveness in this method. It will be intriguing in future studies to investigate how these edited cell populations dysregulate scAAV9 transduction efficiency in the permissive SHSY cell line. The use of electroporated RNP was used to generate the CRISPR-SLC7A2 HeLa cell line and showed successful indel introduction. However, the predictive software still predicted 40% of unedited cells in the HeLa population which highlights the difficulty in the generation of knockout lines in the HeLa cell line compared to more stable karyotypes, such as the SHSY cell line, in both CRISPR techniques.

RNAi-interference, via the use of siRNA, was an effective functional screening process to validate the potential affiliation between the targets and the viral vector, as used in previous studies (Song, Pekrun et al. 2022). siRNA was effective in silencing the expression of each target in the permissive HeLa cell line before scAAV9 transduction, as clearly shown with the

positive control siRNA-AAVR condition (Figure 5.1). Intriguingly, the knockdown in mRNA of SDC4 and ICAM1 showed a significant decrease in scAAV9 transduction in the HeLa cell line which initially suggested that the targets are necessary for the transduction entry pathway. On the other hand, siRNA knockdown of SLC7A2 had no effect on the transduction pathway. Due to the potential off-target silencing due to homology sequencing and the siRNA being a mixed pool of siRNA per target which increases this risk, it was shown on both an mRNA and protein level that each target was not dysregulated except for SLC7A2 gene expression increasing with ICAM1-targeting siRNA (Figure 5.4). Due to this elevated expression of SLC7A2 with ICAM1-targeting siRNA, this could potentially suggest that there may be a shared pathway or function between ICAM1 and SLC7A2. This phenomenon of transcriptional and protein adaptation is proposed in the El-Brolosy, Kontarakis et al. (2019) study. Supporting this theory, the ICAM1 knockout cell line showed a major decrease in SLC7A2 protein levels. Intriguingly, this downregulated effect was also observed in the CRISPR-SDC4 cell line, so could additionally suggest a shared membrane-protein pathway or localised receptor clustering. Although this was only an mRNA screen of the relevant target genes of this study, transcriptome sequencing via RNA-profiling methods would be required for high-throughput and detailed analysis on the transcriptomes stability in relation to the presence of each siRNA pool (Kukurba and Montgomery 2015). In the previous chapter, it was shown that the overexpression of SLC7A2 upregulated AAVR protein expression. However, the introduction of siRNA or the generation of CRISPR SLC7A2 showed no effect on AAVR expression. This supports the previously suggested hypothesis that the increased expression of SLC7A2 could require elevated levels of AAVR to shuttle the overexpressed SLC7A2 to the plasma membrane or to assist in a potential recycling pathway. Although siRNA is known to have potential off-targeting, the use of a mixed pool of siRNA has been suggested to reduce the effects of off-targeting as the mixed pool dilutes the concentration of siRNA (Neumeier and Meister 2020). This was because each duplex worked synergistically with one another to knockdown the mRNA expression of its target protein and the off-target frequency was reduced due to the dilution of the siRNA duplexes. Because of this, it supports the idea that the effects seen may be more relevant to the proteins sharing a particular pathway which results in a compensatory response such as dysregulated protein expression.

An experimental challenge in the siRNA screen was the consistent elevation in ICAM1 mRNA expression when the SHSY cell line was incubated with the siRNA targeting pool for ICAM1 (Figure 5.2). It was shown to clearly be functional in the HeLa cell line therefore suggesting this is a cell-type specific response. This phenomenon could be as a result of the oligonucleotide sequences not causing mRNA degradation but blocks translation in the SHSY cell line (Scacheri, Rozenblatt-Rosen et al. 2004). Because of this, a positive feedback loop may be stimulated, resulting in increased transcription of the *ICAM1* gene. Alternatively, the SHSY cell line may be dependent on the ICAM1 protein for cell attachment. As a result, attempting to knockdown the protein may elicit a response resulting in the previously suggested phenomenon. Although the viability of the cells showed no noticeable difference between the NTC-siRNA and ICAM1-siRNA, a lactate dehydrogenase (LDH) assay would indicate if the cells viability was affected. Additionally, the upregulation may be as a result of a specific splice variant which is increasing in expression due to the knockdown of the full-length variant. To determine this, a quantitative PCR with primers designed for each splice variant would inform if one of the variants are upregulated which masks the knockdown of the other variants.

Although this was challenging, the SHSY cell line showed a significant decrease in GFP positive cells in the positive control siRNA targeting AAVR treated cells (Figure 5.2E). Although this is a similar result to the HeLa cell line, the mRNA knockdown of SDC4 showed no effect on viral transduction in this cell line. Due to being the strongest permissive cell line, it could be suggested the SHSY cell line may have a higher expression or a broader expression range of AAV9 transduction pathway proteins which enables easier cellular entry (Maginnis 2018). Because of this, these other entry factors may mask the effects seen in the HeLa line. Alternatively, the higher transduction could be as a result of an alternate entry pathway used in the SHSY cell line relative to that of SDC4-dependent pathway AAV9 potentially uses in the HeLa cell line. An example of a technique to infer this characterisation of each pathway would be to block ATP to validate if both transduction pathways are passive or active (Merkel, Andrews et al. 2017). Although the results showed a significant effect in the HeLa cell line during siRNA-induced knockdown, the overexpression of the target protein in the same cell line showed no effect on viral transduction (Figure 4.12). Although this is contradicted when the protein was knocked down on a genetic level with CRISPR-SDC4 line showing elevated

transduction efficiency (Figure 5.11). This result was further supported as the genetic rescue of the target in the CRISPR line resulted in a rescue in transduction. It can be theorised that the siRNA or CRISPR-edited cells were causing an unintentional change on the cell surface which was causing lower/heightened transduction. Because of this, an SDC4-siRNA screen in other permissive cell lines would enlighten if downregulated transduction were consistent in other cell types. In the Madigan, Tyson et al. (2019) study it was shown that the knockout of pical polarity determinant Crumbs 3 (Crb3) resulted in a major increase in galactose expression. Due to seeing an elevation in transduction after CRISPR-edit, it can be suggested that although AAVR was not affected in siRNA-targeting SDC4 knockdown, other interacting partners, such as galactose and laminin, may be dysregulated.

Although the loss of AAVR, ICAM1 and SDC4 affected AAV9 transduction efficiency, there was no apparent effect on AAV9 internalisation. The internalisation assay showed no difference between the wild-type isotype HeLa line and the AAVR-KO cell line while the rescue of AAVR significantly increased the number of viral genomes internalised (Figure 5.19A). Due to the transduction efficiency of the AAVR knockout cell line yielding no GFP positive cells, it suggested that the virus was being internalised, but the transgene expression was being inhibited. In the Turkki, Makkonen et al. (2013) study, it was shown that non-permissive lines to the human enterovirus echovirus 1 (EV1) were incapable of transgene expression post-internalisation due to the differential expression of intracellular proteins, such as vimentin. Because of this, it would be intriguing to investigate if the cell lines screened previously for scAAV9 optimisation (N2A, NIH3T3, 1321N1 and b.End5) were internalising the vector but ineffectively processing the transgene. The CRISPR-ICAM1 and Rescue-ICAM1 lines showed a similar internalisation pattern to that of the transduction results in which the CRISPR-ICAM1 line resulted in increased transgene delivery compared to its wild-type isotype. The overexpression of the target returned its levels back down to the control wild type (Figure 5.19C). The CRISPR-SDC4 and Rescue-SDC4 lines showed a non-significant difference of transgene delivered compared to the wild-type (Figure 5.19B). This is intriguing as the CRISPR-SDC4 line had a significantly higher transduction pattern (Figure 5.11B), suggesting the knockdown in expression may stimulate more efficiently the pathways necessary for transduction. Although the protein screen of the SDC4-CRISPR line indicated an elevated protein expression of AAVR which would indirectly increase its transduction efficiency. On the

other hand, the SLC7A2-CRISPR cell line showed no difference in internalisation rate to that of the CRISPR-Control line (Figure 5.19D). To validate if the binding efficiency of the viral vector is affected due to the CRISPR-knockout, a binding assay should be conducted, similar to that of the Madigan, Berry et al. (2020) study which used temperature to block internalisation and validate if vector binding on the cell surface is affected. Additionally, it would also be proposed to conduct a nuclear uptake assay to investigate if the dysregulation of the target proteins alters the transport of the transgene to the nuclear regions to initiate transcription, which is a key stage to the transduction pathway (Berry and Asokan 2016).

In conclusion, the CRISPR knockout lines of the novel target proteins predominately showed an upregulation in transduction efficiency, which was supported via lentiviral rescue studies. This suggests the targets either have an alternate vector binding function, which is inhibitory in the transduction pathway, or the removal of the targets enhances viral binding due to greater access to other cell surface interactors. The chapter showed that CRISPR generated lines can have dysregulated protein expression levels of other targets and the screening of a variety of validated AAV9 interactome protein targets in generated lines should be a necessity.

6 Discussion

6.1 Summary

AAV9 is the gold-standard viral vector for neurological gene therapy (Bell, Vandenberghe et al. 2011). In recent years, the vectorolgy field has sought to expand the understanding of AAV9's interactome by the identification and validation of novel targets via loss-of-function and overexpression screening studies (Madigan, Tyson et al. 2019, Dudek, Zabaleta et al. 2020, Meisen, Nejad et al. 2020). Surface protein interactions with the viral capsid are known to be essential entry factors in relation to the binding and internalisation of AAV (Meyer and Chapman 2022). By developing our understanding of these interactions and pathways, the aim is to improve future vector design for next-generation vector studies. As a result, this will enhance the therapeutic efficiency of the viral capsid and potentially improving the efficacy and safety of treatment across multiple monogenic disorders.

The aim of this thesis was to validate the functional relevance of the novel target proteins identified in a preliminary gene expression screen. The targets, which were shown to have upregulated gene expression after cells were incubated with AAV9, were ICAM1, SDC4 and SLC7A2 (Figure 1.6). Due to these targets sharing characteristics similar to previously identified interactome targets (in terms of their cell surface localisation and protein structure suggestive of functional relevance to the viral transduction pathway), these targets were taken forward for characterisation and validation. To increase confidence in our findings, the AAVR protein identified in the Pillay, Meyer et al. (2016) study was used as a positive control. The data presented in Chapter 3 identified and characterised the *in vitro* models required for future studies as well as designing and generating the tools required for characterisation of all the targets. The data identified SH-SY5Y (SHSY) and HeLa cells as being permissive to AAV9 transduction while the other *in vitro* lines tested (N2A, NIH3T3, 1321N1 and b.End5) were identified as non-permissive due to limited transduction efficiency (Figure 3.17 – 3.22). Challenges with sub optimal commercially available antibodies led to difficulties with certain target characterisations. As a result, multiple optimisation experiments were required as well as the generation of overexpression constructs to help confirm specificity and localisation of

each target. Finally, Chapter 3 also characterised the temporal change in expression of these novel targets within AAV9 permissive mouse tissues. This study presented an intriguing finding which was that the majority of the targets, including AAVR, had no endogenous expression at a neonatal time points, bringing into question the pathway that AAV9 utilises to transduce the neonatal CNS *in vivo* (Figure 3.13 – 3.16).

Based on the hypothesis that these novel target proteins could function as entry factors for AAV9, Chapter 4 utilised the non-permissive cell lines identified previously to investigate if overexpression of these targets could impact transduction efficiency. The HeLa and 1321N1 cell lines were used as the overexpression models to validate each target due to the limited transduction efficiency and stability of NIH3T3 and N2A overexpression stable lines (Figure 4.4 – 4.7). The stable 1321N1 cells showed improved AAV9 transduction efficiency in the AAVR positive control line, while the HeLa stable cell lines showed an increase in transduction efficiency with the AAVR and the SLC7A2 stable cell lines (Figure 4.12). Although the overexpression of SLC7A2 was shown to improve viral transduction, suggesting a functional role in the transduction pathway in the HeLa cell line, the expression of AAVR was shown to simultaneously increase (Figure 4.12D). The other stable lines in both cell types showed no improvement in transduction efficiency after overexpression, suggesting they are not functional in the transduction pathway when overexpressed. Following on from this, a co-immunoprecipitation experiment was conducted to investigate the interaction between the target proteins and the AAV9 capsid proteins. From these studies VP1, VP2 and VP3 was shown to interact with AAVR, while VP1 alone was shown to interact with ICAM1. (Figure 4.17).

Given that AAVR and SLC7A2 overexpression were able to affect AAV9 transduction efficiency, the aim of Chapter 5 was to further validate the role of these targets in the AAV9 transduction pathway *in vitro* via reducing the expression of each novel target protein and investigating AAV9-medaited gene transfer. The RNAi screen using siRNA in the HeLa cell line showed a significant reduction in viral transduction with SDC4- and ICAM1-targeting siRNA (Figure 5.1). Due to the overexpression results of SLC7A2 indicating to have an affect with viral transduction, all the targets were taken forward for a CRISPR-edit screen. HeLa cells were chosen to generate CRISPR-edited lines because the cell line displayed endogenous expression of most targets (Figure 3.10), CRISPR-edited cell lines were generated.

Upregulation in viral transduction was observed in the SDC4- and ICAM1-CRISPR edited cell lines (Figure 5.12 and 5.15). These effects could be rescued via the generation of LV-overexpression HeLa lines, demonstrating the relevance of these findings. Because of these findings, the internalisation rate of the viral vector was investigated in these generated lines. Intriguingly, no difference was observed between the wild-type and the AAVR knockout cell line while the rescue cell line showed a significant increase in transgene signal (Figure 5.23). The CRISPR lines for other targets showed no significant difference in gene transgene signal suggesting no difference in rate of internalisation.

6.2 ICAM1's involvement in the AAV9 lifecycle

ICAM1 was shown to interact with capsid protein VP1, indicating a potential interaction between ICAM1 and the viral capsid. The interaction between AAV viral particles and AAVR is facilitated via AAVR's ectodomain, specifically the Ig-like polycystic kidney domains (PKDs) (Pillay, Meyer et al. 2016). Given the potential interaction with VP1 and the fact that ICAM1 also localises to the plasma membrane and contains five extracellular Ig superfamily (IgSF) domains (Yang, Jun et al. 2004, Kang, Kim et al. 2012), it could be hypothesised that ICAM1 could also function as an adsorption or internalisation factor for AAV9. Surprisingly, the stable overexpression of ICAM1 showed no difference in viral transduction efficiency compared to the wild-type cells (Figure 4.12), while the knockout of ICAM1 showed significantly elevated viral transduction efficiency (Figure 5.15). These data suggests that ICAM1 can negatively regulate AAV9's transduction pathway, as its removal enhances AAV9 entry. This suggests ICAM1 could be more functionally relevant as a restriction factor in the transduction pathway, similarly to the identified restriction factors in an RNAi screen in the Mano, Ippodrino et al. (2015) study. By functioning as a so-called decoy receptor, ICAM1 could cause viral capsids to remain anchored to the cell surface, inhibiting their internalisation and cellular transduction (Figure 6.1A). By removing the target protein via genetic knockout, one would expect improved localisation and frequency of interaction with known functional pathways, leading to increased transduction efficiency, as was observed with ICAM1 knockout. However, this theory would suggest that the overexpression of ICAM1 would have an inhibitory effect on transduction due to the increased availability of these 'dead-end' pathways. This was not

observed in the transduction efficiency study with the ICAM1 overexpression cells (Figure 4.12). The increased transduction efficiency in ICAM1 knockout cells could instead be related to effects on other known entry factors, such as galactose (Shen, Bryant et al. 2011). For example, in the Madigan, Tyson et al. (2019) study it was reported that the knockout of the restriction factor protein Crumbs3 resulted in a significant increase in galactose expression. As a result, screening ICAM1 knockouts for galactose expression changes could give further insight into whether this was the cause for the elevated transduction. A similar finding was described in our current study, as the overexpression of SLC7A2 resulted in the elevated expression of AAVR (Figure 4.12C). Therefore, it may be a necessary screening process in studies such as this to characterise other known protein targets after genetic manipulation to ensure protein expression of these targets is not also dysregulated prior to viral transduction efficiency validation.

Although an interaction between ICAM1 and AAV9 was demonstrated, the functional nature of this interaction is still unknown. ICAM1 functions as a signalling receptor in epithelial and endothelial cells in relation to transendothelial migration to sites of inflammation and activation of lymphocytes (Bui, Wiesolek et al. 2020). As a result, it could be suggested to have a role in the immune clearance of the vector. Vector immunogenicity is a clinical challenge in gene therapy and affects transgene stability and efficacy as well as being linked to liver toxicity (Ronzitti, Gross et al. 2020, Bing, Justesen et al. 2022). It could be theorised that ICAM1 may be an interacting partner between immune cells and the viral vector, which would explain why the protein is capable of binding to the viral capsid but not assisting in viral transduction (Figure 6.1B). Following the experimental protocol of Melgaco, Azamor et al. (2021), AAV9's cellular immune response could be investigated using peripheral blood mononuclear cells (PEBCs) for cytokine expression. Additionally, ICAM1 has been shown to be a downstream regulator of MyD88, associated with the TLR9-MyD88 pathway which is known immune pathway in relation to adaptive immune responses to AAV (Ahmed, Khan et al. 2021). Determining if genes related to the TLR9-MyD88 pathway are dysregulated would provide insight into whether ICAM1 is linked to AAV immunogenicity (Rogers, Martino et al. 2011, Israelow, Mao et al. 2021). To validate the viral clearance rate requires *in vivo* analysis with ICAM1 knockout mice. By determining if the viral load is elevated in serum and if transduction in target tissue is improved, as conducted in the Israelow, Mao et al. (2021) study, it will give

evidence towards its identification as a potential restriction factor. If ICAM1 is indeed involved in AAV clearance, then altering the viral capsid to decrease interactions with ICAM1 would help to reduce vector immunogenicity. As it appears to be specific to VP1, identifying and mutating the amino acid cluster in VP1 which binds to ICAM1, the interaction could be modulated. Such experiments could help to further improve the therapeutic efficiency of the vector via avoiding immune clearance. Similar experiments were performed in the Tse, Klinc et al. (2017) study, where AAV1 capsid variants were designed to specifically evade neutralising antibodies from mouse, NHP and human sera. This shows that capsid function can be maintained while altering AAV antigenicity stimulated by the viral capsid.

However, ICAM1 may have other supportive roles in the AAV lifecycle independent of transduction. Extracellular ligands are essential for transcytosis (Pulgar 2019) and ICAM1 was recently shown to have a role in transcytosis in hepatic epithelial cells to help regulate adhesion and migration of lymphocytes (Cacho-Navas, Reglero-Real et al. 2022). Furthermore, ICAM1 positive nanoparticles are capable of crossing the BBB (Hsu, Rappaport et al. 2014). Given that ICAM1 was identified from a BBB model in our initial preliminary data, it could be hypothesised that ICAM1 functions in AAV transcytosis and has no impact on transduction (Figure 6.1C). Because of this, an *in vitro* assay using a trans-well model, similar to that of the Song, Pekrun et al. (2022) study, will enable an investigation into whether overexpressing and knocking out ICAM1 in a human blood brain barrier cell model, such as hCMEC/D3, dysregulates the rate of transcytosis. It would also be interesting to investigate if AAV9 is AAVR-dependent or independent in relation to its transcytosis pathway as literature has only shown its functionality in the viral transduction pathway. By identifying the target proteins necessary for AAV9 transcytosis, the pathway the vector hijacks could be exploited for drug delivery and future vector design, promising to enhance therapeutic potential for the treatment of neurological disorders.

A.

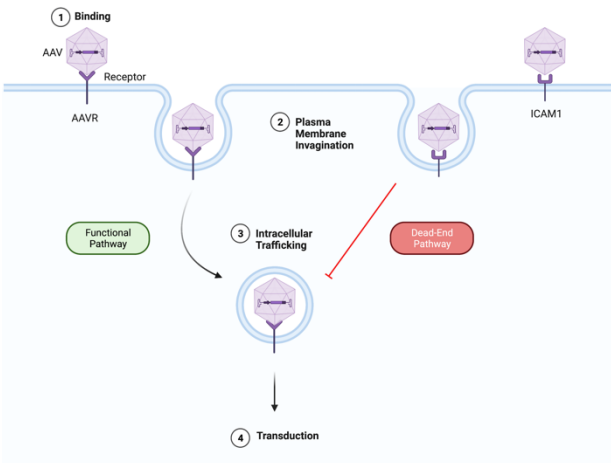

B.

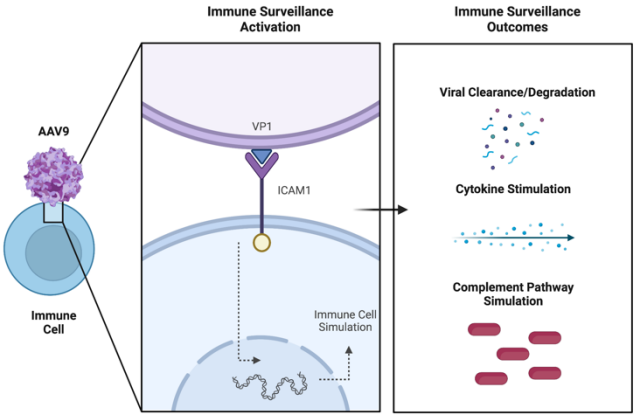

C.

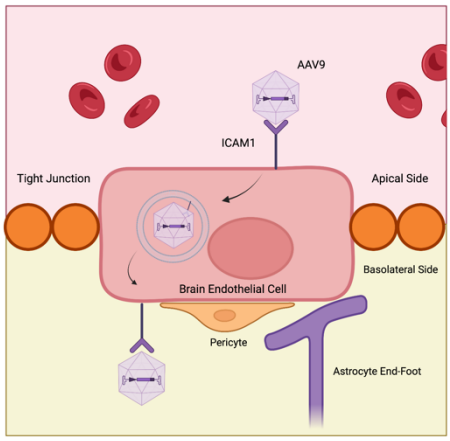

Figure 6.1: ***Model of ICAM1's potential functions–*** *(A) ICAM1 acting as a binding partner for a transduction-independent pathway. (B) ICAM1 on the immune cell interacting with the viral capsid and stimulating an immune response. (C.) ICAM1 binding to the viral capsid and assisting in its transcytosis pathway (Created in Biorender.com).*

6.3 Internalisation of AAV9 is AAVR-independent.

As previously reported, AAVR was found to regulate viral transduction efficiency, with overexpression and the loss-of-function studies increasing and decreasing AAV9 transduction respectively (Figure 4.12 and 5.8) (Pillay et al 2016). Importantly, this study also indicated that AAVR interacts with VP1, 2 and 3 on the AAV capsid proteins VP1, VP2 and VP3 (Figure 4.18), a novel finding which supports the findings of the Pillay, Meyer et al. (2016) study. However, the internalisation of AAV9 in AAVR knockout cells was unaffected, while overexpression of AAVR significantly increased AAV9 internalisation (Figure 5.23). The ability of AAVR overexpression to increase transduction independent of increased internalisation could indicate that AAVR functions elsewhere within the AAV9 lifecycle, aside from vector adsorption and internalisation. Indeed, in the Pillay, Meyer et al. (2016) study, AAVR was found to localise exclusively to the Golgi apparatus. Given the importance of AAVR in AAV9 transduction, this localisation could lead to the hypothesis that delivery of AAV9 to the Golgi is an essential and necessary step in the transduction pathway, suggesting AAVR is required post-internalisation. In the Madigan, Berry et al. (2020) study it was shown that dysregulated intracellular calcium homeostasis led to inefficient vector processing via the Golgi, which resulted in transduction-deficient vectors. This study indicates that conformational changes in the AAV9 capsid are essential for transgene delivery and transduction, which has also been described by others in relation to the binding of galactose and the stimulation of pH (Penzes, Chipman et al. 2021). It could therefore be speculated that AAVR is required for a conformational change of the AAV9 capsid within the Golgi thus enabling transgene delivery and expression. To validate if this indeed the case in AAVR-knockout cells, the use monoclonal antibodies for different epitopes located on the capsid (for example: A69, A1 and B1 monoclonal antibodies), would enable identification of epitopes which are externalised following AAV capsid conformational change as achieved in the Madigan, Berry et al. (2020) study. This is important as understanding how the viral vector changes through the transduction pathway is necessary as more information in relation to the vectors functional requirements will enable additional screening processes to validate the functional nature of any future generated vectors.

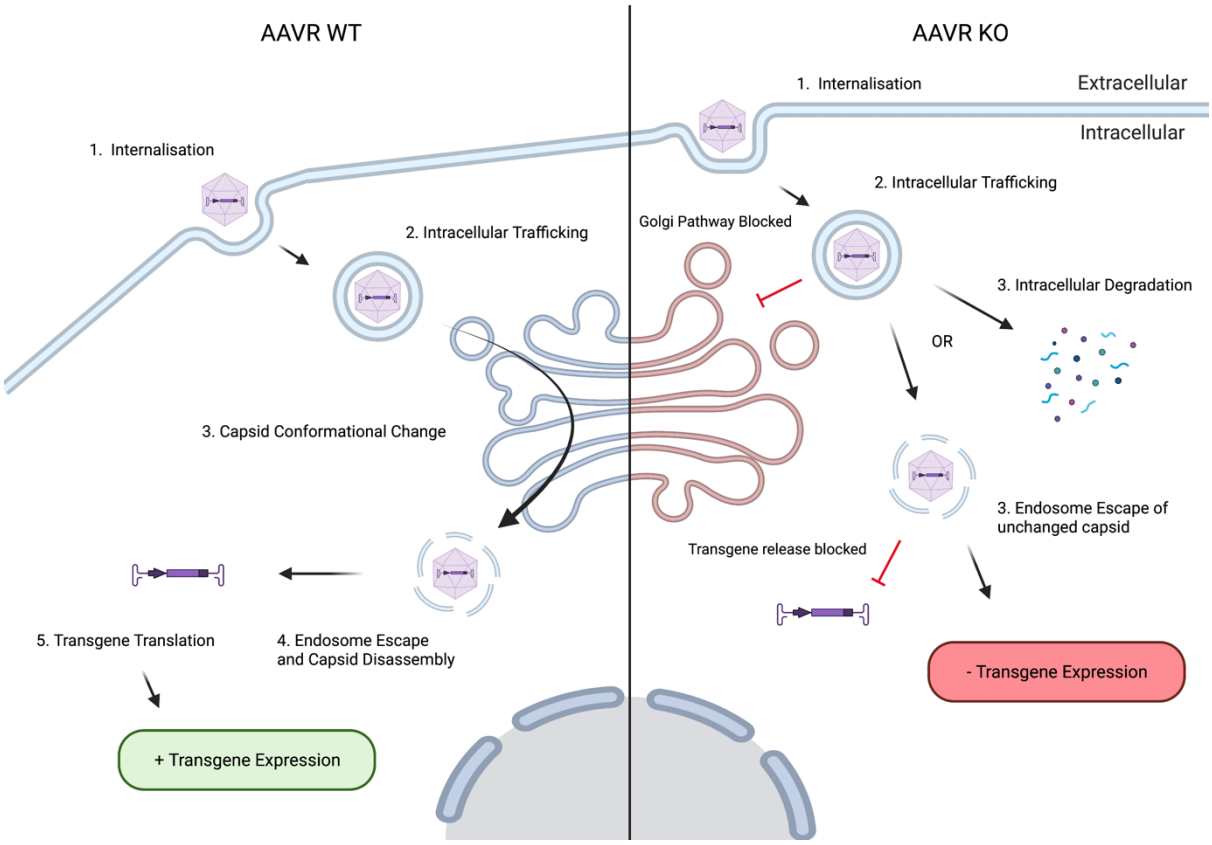

Figure 6.2: ***Model of AAV9 transduction pathway in relation to AAVR-Golgi pathway*** **–** *(Left side) the target cell internalises the viral vector and transports the vector-contained vesicle to the golgi in which the vector is processed and undergoes a conformational change. The vector is released from the golgi and the capsid undergoes capsid disassembly to release the therapeutic transgene to enable transcription and translation. (Right side) – the vector is internalised however does not translocate to the golgi and as a result either undergoes degradation or the capsid does not release the transgene, resulting in inhibited transgene expression. (Created in Biorender.com).*

6.4 Interrelationship between AAV9 receptors

In Chapter 2, it was shown that the overexpression of SLC7A2 in the HeLa cell line upregulated AAV9 transduction efficiency (Figure 4.12), suggesting SLC7A2 had a functional role in AAV9s transduction pathway. However, SLC7A2 overexpression led to a significant increase in AAVR expression which could have significantly contributed to the elevated SLC7A2-mediated transduction efficiency observed. This was an interesting finding as the knockdown of SLC7A2 via siRNA (Figure 5.3 – 5.4) and CRISPR-edit (Figure 5.22) showed no significant effect on endogenous AAVR expression. These data suggest the increased expression of SLC7A2 led to the elevated expression of AAVR. This would imply that AAVR is required in a particular pathway in the processing of SLC7A2. AAVRs natural cellular function is largely unknown except for the fact that it is a target receptor for the majority of AAV serotypes and that it localises in the plasma membrane and golgi. Therefore, determining AAVR's true cellular function would provide further insight into its role in the AAV transduction pathway. Because AAVR is localised to the plasma membrane and the Golgi network, a possible pathway of relevance for its function could be the endosomal transport pathway between the plasma membrane and the *trans*-golgi network (Pillay, Meyer et al. 2016, Summerford, Johnson et al. 2016). As a result, AAVR may transport SLC7A2 after PTMs in the golgi to the plasma membrane. Whether AAVR has a bidirectional mechanistic transport function, however, is unknown. To investigate this hypothesis, generating an SLC7A2 overexpression line from the AAVR knockout HeLa cell lines would enable an investigation into whether the lack of AAVR expression alters SLC7A2's localisation and expression. If AAVR is associated with the *trans*-Golgi network and involved in PTMs, it would be interesting to determine if the processing of glycosylated molecules such as galactose, is also affected and if the golgi is morphologically different due to the lack of AAVR.

An alternate suggested pathway is that due to the stable overexpression of SLC7A2, the cell might require increased expression in recycling proteins. Many trans-Golgi proteins are associated with the recycling pathway from the plasma membrane as a result of their C-tail which functions in endocytosis and intracellular trafficking (Maxfield and McGraw 2004). Trans-golgi proteins, such as AAVR, may elevate in expression due to SLC7A2 overexpression requiring simultaneous elevated recycling functions, as observed in our study. Because of this,

investigating lysosomal expression would provide insight into whether there is a simultaneous elevation in expression between AAVR and lysosomal pathways in the stable SLC7A2 HeLa cells to support this theory. To validate this, investigating the expression levels of recycling endosomes, via markers such as Arf6 and Rab11, in response to the increased expression of AAVR could indicate a potential association with this pathway (Kobayashi and Fukuda 2013).

Similarly, the knockdown of SLC7A2 via siRNA showed an upregulation in ICAM1 protein expression and the CRISPR cell lines ICAM1 and SDC4 also displayed a reduced protein expression of SLC7A2. Due to the identified targets exhibiting these effects, it could be suggested that the cell surface being dysregulated was the causative factor for several of the investigated targets being affected which indicates the complexity of investigating membrane proteins *in vitro*. Additionally, the overexpression of the targets has been shown to alter the cells morphology which could be indicative of the dysregulated membrane. Membrane receptors, glycans and signalling molecules have been proposed to localise together on a cell membrane, referred to as receptor clustering, which regulate signalling activity (Chen, Oh et al. 2021). Because of this, it could be theorised that the dysregulation between the target proteins could be occurring due to each target being associated in each other's cell surface clusters. In support of this, disruption of cytoskeletal proteins has been shown to dysregulate cell surface clusters localisation (Boggara, Athmakuri et al. 2013) and cell surface cluster dysregulation has been shown to alter molecular mechanisms (Villaseñor, Schilling et al. 2017). To validate this in relation to the target proteins identified in this study, a proximity ligation assay would highlight if the targets were localised in close proximity to one another. Additionally, the targets may interact with one another. As a result, a co-immunoprecipitation assay of each target would validate if direct interactions were occurring on the cell surface.

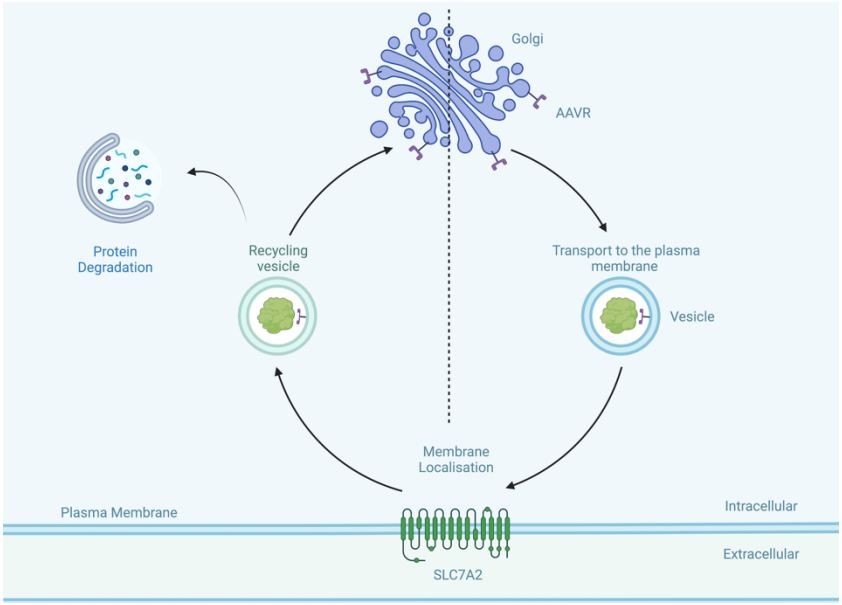

Figure 6.3: ***AAVRs potential pathways in relation to SLC7A2 –*** *AAVR transporting the SLC7A2 protein to the plasma membrane after PTMs or transporting SLC7A2 from the plasma membrane to either be degraded or to be processed before degradation (Created in Biorender.com).*

6.5 Future Directions

The SHSY knockout lines generated for SDC4, SLC7A2 and AAVR were unable to be validated for AAV9 transduction efficiency due to time constraints caused by the COVID-19 pandemic. Future work would include investigating if AAV9 transduction efficiency is affected due to these genetically edited lines. This will enlighten if there is an alternate transduction pattern to that of the HeLa cell line, similar to that of the siRNA data (Figure 5.1 – 5.2). If so, this could suggest an alternate transduction pathway. Unfortunately, the SHSY ICAM1 knockout cell line showed no indel insertion with the guides designed. Because of this, the guides generated from the CRISPR-surfaceome software in the Mei, Gu et al. (2022) study should be used as they were reported to have high editing efficiency by generating ICAM1 knockout cell lines. This altered the tropism of rhinovirus infection which uses ICAM1 as a primary receptor. By generating this cell line, it would further assess if AAV9s transduction pathway is ICAM1-independent, as shown in the HeLa cell line. Additionally, the SHSY cell line was identified as to have the highest AAV9 transduction efficiency when compared to all the cell lines screened (Figure 3.19). Because of this high transduction efficiency, it could be suggested to use this novel permissive ell line to identify new targets. This could be achieved by pulling down the AAV viral proteins incubated in SHSY lysate and assessing the precipitated proteins using mass spectrometry sequencing to identify targets, as described in the Liu, Van Voorhis et al. (2021) article. Other cell lines which are permissive to AAV9, such as the HeLa and U2-OS cell lines, can also undergo this experimental process to cross-examine the results to more accurately validate potential targets.

The next stage of this project is to validate the identified targets *in vivo*. Due to ICAM1 being shown as an interacting partner and having an unknown function, this target would be carried forward for *in vivo* studies. Following the Pillay, Meyer et al. (2016) study, AAVR would still be used as a positive control as it has been throughout this project. Using knockout mice of each target, AAV9 would be injected intravascularly to validate if biodistribution and gene transfer of the vector is affected from the knockout of the target protein. This would require tissue analysis of GFP signal from a variety of tissue including brain, spine, liver, muscle and heart. The *in vivo* studies will determine if cell/tissue tropism is affected as well as determining if the transcytosis pathway to the CNS is impacted. Additionally, direct delivery to the CNS

would be used to assess neurotropism in the absence of the target receptors. Viral clearance could also be investigated, as described previously.

In conclusion, understanding and developing methods to identify AAV9's interactome is an expanding research area. Exploring the viral vectors interactions and pathways will enhance our understanding of the vector's requirements for therapeutic efficiency. By doing this, the generation of novel capsid variants, via the use of predictive artificial intelligence software, will more accurately design vectors considering the interactions essential for improved cell specific targeting.

7 Reference List

Abbott, N. J., A. A. K. Patabendige, D. E. M. Dolman, S. R. Yusof and D. J. Begley (2010). "Structure and function of the blood–brain barrier." Neurobiology of Disease **37**(1): 13-25.

Adikusuma, F., C. Pfitzner and P. Q. Thomas (2017). "Versatile single-step-assembly CRISPR/Cas9 vectors for dual gRNA expression." PLoS One **12**(12): e0187236.

Ahmed, H., M. A. Khan, U. D. Kahlert, M. Niemela, D. Hanggi, S. R. Chaudhry and S. Muhammad (2021). "Role of Adaptor Protein Myeloid Differentiation 88 (MyD88) in Post-Subarachnoid Hemorrhage Inflammation: A Systematic Review." Int J Mol Sci **22**(8).

Akache, B., D. Grimm, K. Pandey, S. R. Yant, H. Xu and M. A. Kay (2006). "The 37/67-kilodalton laminin receptor is a receptor for adeno-associated virus serotypes 8, 2, 3, and 9." Journal of virology **80**(19): 9831-9836.

Alfonso-Dunn, R., A. W. Turner, P. M. Jean Beltran, J. H. Arbuckle, H. G. Budayeva, I. M. Cristea and T. M. Kristie (2017). "Transcriptional Elongation of HSV Immediate Early Genes by the Super Elongation Complex Drives Lytic Infection and Reactivation from Latency." Cell Host Microbe **21**(4): 507-517 e505.

Alvarez, J. I., T. Katayama and A. Prat (2013). "Glial influence on the blood brain barrier." Glia **61**(12): 1939-1958.

Anbarasan, C., M. Bavanilatha, K. Latchumanadhas and S. Ajit Mullasari (2015). "ICAM-1 molecular mechanism and genome wide SNP's association studies." Indian Heart J **67**(3): 282-287.

Anderson, J. L. and T. J. Hope (2005). "Intracellular trafficking of retroviral vectors: obstacles and advances." Gene Ther **12**(23): 1667-1678.

Antoniou, P., A. Miccio and M. Brusson (2021). "Base and Prime Editing Technologies for Blood Disorders." Front Genome Ed **3**: 618406.

Arotcarena, M. L., S. Dovero, N. Biendon, N. Dutheil, V. Planche, E. Bezard and B. Dehay (2021). "Pilot Study Assessing the Impact of Intrathecal Administration of Variants AAV-PHP.B and AAV-PHP.eB on Brain Transduction in Adult Rhesus Macaques." Front Bioeng Biotechnol **9**: 762209.

Asmamaw, M. and B. Zawdie (2021). "Mechanism and Applications of CRISPR/Cas-9-Mediated Genome Editing." Biologics **15**: 353-361.

Atkins, A., C. H. Chung, A. G. Allen, W. Dampier, T. E. Gurrola, I. K. Sariyer, M. R. Nonnemacher and B. Wigdahl (2021). "Off-Target Analysis in Gene Editing and Applications for Clinical Translation of CRISPR/Cas9 in HIV-1 Therapy." Front Genome Ed **3**: 673022.

Ballandras-Colas, A., V. Chivukula, D. T. Gruszka, Z. Shan, P. K. Singh, V. E. Pye, R. K. McLean, G. J. Bedwell, W. Li, A. Nans, N. J. Cook, H. J. Fadel, E. M. Poeschla, D. J. Griffiths, J. Vargas, I. A. Taylor, D. Lyumkis, H. Yardimci, A. N. Engelman and P. Cherepanov (2022). "Multivalent interactions essential for lentiviral integrase function." Nat Commun **13**(1): 2416.

Bao, F., H. Shi, M. Gao, L. Yang, L. Zhou, Q. Zhao, Y. Wu, K. Chen, G. Xiang, Q. Long, J. Guo, J. Zhang and X. Liu (2018). "Polybrene induces neural degeneration by bidirectional Ca(2+) influx-dependent mitochondrial and ER-mitochondrial dynamics." Cell Death Dis **9**(10): 966.

Batista, A. R., O. D. King, C. P. Reardon, C. Davis, Shankaracharya, V. Philip, H. Gray-Edwards, N. Aronin, C. Lutz, J. Landers and M. Sena-Esteves (2020). "Ly6a Differential Expression in Blood-Brain Barrier Is Responsible for Strain Specific Central Nervous System Transduction Profile of AAV-PHP.B." Human Gene Therapy **31**(1-2): 90-102.

Beharry, A., Y. Gong, J. C. Kim, K. S. Hanlon, J. Nammour, K. Hieber, F. Eichler, M. Cheng, A. Stemmer-Rachamimov, K. M. Stankovic, D. B. Welling, C. Ng and C. A. Maguire (2022). "The AAV9 Variant Capsid AAV-F Mediates Widespread Transgene Expression in Nonhuman Primate Spinal Cord After Intrathecal Administration." Hum Gene Ther **33**(1-2): 61-75.

Bell, C. L., B. L. Gurda, K. Van Vliet, M. Agbandje-McKenna and J. M. Wilson (2012). "Identification of the galactose binding domain of the adeno-associated virus serotype 9 capsid." Journal of virology **86**(13): 7326-7333.

Bell, C. L., L. H. Vandenberghe, P. Bell, M. P. Limberis, G.-P. Gao, K. Van Vliet, M. Agbandje-McKenna and J. M. Wilson (2011). "The AAV9 receptor and its modification to improve in vivo lung gene transfer in mice." The Journal of clinical investigation **121**(6): 2427-2435.

Bellettato, C. M. and M. Scarpa (2018). "Possible strategies to cross the blood–brain barrier." Italian Journal of Pediatrics **44**(Suppl 2).

Bello-Morales, R., S. Andreu and J. A. Lopez-Guerrero (2020). "The Role of Herpes Simplex Virus Type 1 Infection in Demyelination of the Central Nervous System." Int J Mol Sci **21**(14).

Bensimon, A., M. D. Pizzagalli, F. Kartnig, V. Dvorak, P. Essletzbichler, G. E. Winter and G. Superti-Furga (2020). "Targeted Degradation of SLC Transporters Reveals Amenability of Multi-Pass Transmembrane Proteins to Ligand-Induced Proteolysis." Cell Chem Biol **27**(6): 728-739 e729.

Bergers, G. and S. Song (2005). "The role of pericytes in blood-vessel formation and maintenance." Neuro-oncology **7**(4): 452-464.

Berges, B. K., J. H. Wolfe and N. W. Fraser (2005). "Stable levels of long-term transgene expression driven by the latency-associated transcript promoter in a herpes simplex virus type 1 vector." Mol Ther **12**(6): 1111-1119.

Berry, G. E. and A. Asokan (2016). "Chemical Modulation of Endocytic Sorting Augments Adeno-associated Viral Transduction." The Journal of biological chemistry **291**(2): 939-947.

Bevington, J. M., P. G. Needham, K. C. Verrill, R. F. Collaco, V. Basrur and J. P. Trempe (2007). "Adeno-associated virus interactions with B23/Nucleophosmin: identification of sub-nucleolar virion regions." Virology **357**(1): 102-113.

Beyer, S. R., R. T. Mallmann, I. Jaenecke, A. Habermeier, J. P. Boissel and E. I. Closs (2013). "Identification of cysteine residues in human cationic amino acid transporter hCAT-2A that are targets for inhibition by N-ethylmaleimide." J Biol Chem **288**(42): 30411-30419.

Bian, F., B. Xiong, X. Yang and S. Jin (2016). "Lipid rafts, ceramide and molecular transcytosis." Frontiers in bioscience (Landmark edition) **21**: 806-838.

Biffi, A., C. C. Bartolomae, D. Cesana, N. Cartier, P. Aubourg, M. Ranzani, M. Cesani, F. Benedicenti, T. Plati, E. Rubagotti, S. Merella, A. Capotondo, J. Sgualdino, G. Zanetti, C. von Kalle, M. Schmidt, L. Naldini and E. Montini (2011). "Lentiviral vector common integration sites in preclinical models and a clinical trial reflect a benign integration bias and not oncogenic selection." Blood **117**(20): 5332-5339.

Bing, S. J., S. Justesen, W. W. Wu, A. M. Sajib, S. Warrington, A. Baer, S. Thorgrimsen, R. F. Shen and R. Mazor (2022). "Differential T cell immune responses to deamidated adeno-associated virus vector." Mol Ther Methods Clin Dev **24**: 255-267.

Bloomer, H., J. Khirallah, Y. Li and Q. Xu (2022). "CRISPR/Cas9 ribonucleoprotein-mediated genome and epigenome editing in mammalian cells." Adv Drug Deliv Rev **181**: 114087.

Boggara, M., K. Athmakuri, S. Srivastava, R. Cole and R. S. Kane (2013). "Characterization of the diffusion of epidermal growth factor receptor clusters by single particle tracking." Biochim Biophys Acta **1828**(2): 419-426.

Bravo-Hernandez, M., T. Tadokoro, M. R. Navarro, O. Platoshyn, Y. Kobayashi, S. Marsala, A. Miyanohara, S. Juhas, J. Juhasova, H. Skalnikova, Z. Tomori, I. Vanicky, H. Studenovska, V. Proks, P. Chen, N. Govea-Perez, D. Ditsworth, J. D. Ciacci, S. Gao, W. Zhu, E. T. Ahrens, S. P. Driscoll, T. D. Glenn, M. McAlonis-Downes, S. Da Cruz, S. L. Pfaff, B. K. Kaspar, D. W. Cleveland and M. Marsala (2020). "Spinal subpial delivery of AAV9 enables widespread gene silencing and blocks motoneuron degeneration in ALS." Nat Med **26**(1): 118-130.

Brockman, M. A. and D. M. Knipe (2002). "Herpes simplex virus vectors elicit durable immune responses in the presence of preexisting host immunity." J Virol **76**(8): 3678-3687.

Bui, T. M., H. L. Wiesolek and R. Sumagin (2020). "ICAM-1: A master regulator of cellular responses in inflammation, injury resolution, and tumorigenesis." J Leukoc Biol **108**(3): 787-799.

Bulgakova, N. A. and E. Knust (2009). "The Crumbs complex: from epithelial-cell polarity to retinal degeneration." J Cell Sci **122**(Pt 15): 2587-2596.

Cabezas, R., M. Ávila, J. Gonzalez, R. S. El-Bachá, E. Báez, L. M. García-Segura, J. C. J. Coronel, F. Capani, G. P. Cardona-Gomez and G. E. Barreto (2014). "Astrocytic modulation of blood brain barrier: perspectives on Parkinson's disease." Frontiers in Cellular Neuroscience **8**.

Cacho-Navas, C., N. Reglero-Real, N. Colas-Algora, S. Barroso, G. de Rivas, K. Stamatakis, J. Feito, G. Andres, M. Fresno, L. Kremer, I. Correas, M. A. Alonso and J. Millan (2022). "Plasmolipin regulates basolateral-to-apical transcytosis of ICAM-1 and leukocyte adhesion in polarized hepatic epithelial cells." Cell Mol Life Sci **79**(1): 61.

Carpenter, E. P., K. Beis, A. D. Cameron and S. Iwata (2008). "Overcoming the challenges of membrane protein crystallography." Current Opinion in Structural Biology **18**(5): 581-581.

Carson, J., D. Haddad, M. Bressman and Y. Fong (2010). "Oncolytic Herpes Simplex Virus 1 (Hsv-1) Vectors: Increasing Treatment Efficacy and Range through Strategic Virus Design." Drugs Future **35**(3): 183-195.

Carvalho, L. S., H. T. Turunen, S. J. Wassmer, M. V. Luna-Velez, R. Xiao, J. Bennett and L. H. Vandenberghe (2017). "Evaluating Efficiencies of Dual AAV Approaches for Retinal Targeting." Frontiers in neuroscience **11**: 503-503.

Chan, K. Y., M. J. Jang, B. B. Yoo, A. Greenbaum, N. Ravi, W.-L. Wu, L. Sánchez-Guardado, C. Lois, S. K. Mazmanian, B. E. Deverman and V. Gradinaru (2017). "Engineered AAVs for efficient noninvasive gene delivery to the central and peripheral nervous systems." Nature Neuroscience **20**(8): 1172-1179.

Chand, D., F. Mohr, H. McMillan, F. F. Tukov, K. Montgomery, A. Kleyn, R. Sun, S. Tauscher-Wisniewski, P. Kaufmann and G. Kullak-Ublick (2021). "Hepatotoxicity following administration of onasemnogene abeparvovec (AVXS-101) for the treatment of spinal muscular atrophy." J Hepatol **74**(3): 560-566.

Chen, Z., D. Oh, K. H. Biswas, R. Zaidel-Bar and J. T. Groves (2021). "Probing the effect of clustering on EphA2 receptor signaling efficiency by subcellular control of ligand-receptor mobility." Elife **10**.

Chiang, T. W., C. le Sage, D. Larrieu, M. Demir and S. P. Jackson (2016). "CRISPR-Cas9(D10A) nickase-based genotypic and phenotypic screening to enhance genome editing." Sci Rep **6**: 24356.

Christian, M., T. Cermak, E. L. Doyle, C. Schmidt, F. Zhang, A. Hummel, A. J. Bogdanove and D. F. Voytas (2010). "Targeting DNA double-strand breaks with TAL effector nucleases." Genetics **186**(2): 757-761.

Colella, P., G. Ronzitti and F. Mingozzi (2018). "Emerging Issues in AAV-Mediated In Vivo Gene Therapy." Molecular therapy. Methods & clinical development **8**: 87-104.

Cook, A. M., G. Morgan Jones, G. W. J. Hawryluk, P. Mailloux, D. McLaughlin, A. Papangelou, S. Samuel, S. Tokumaru, C. Venkatasubramanian, C. Zacko, L. L. Zimmermann, K. Hirsch and L. Shutter (2020). "Guidelines for the Acute Treatment of Cerebral Edema in Neurocritical Care Patients." Neurocrit Care **32**(3): 647-666.

Cooper, R. S. and E. E. Heldwein (2015). "Herpesvirus gB: A Finely Tuned Fusion Machine." Viruses **7**(12): 6552-6569.

Coroadinha, A. S. (2023). "Host Cell Restriction Factors Blocking Efficient Vector Transduction: Challenges in Lentiviral and Adeno-Associated Vector Based Gene Therapies." Cells **12**(5).

Czarnek, M., K. Sarad, A. Karas, J. Kochan and J. Bereta (2021). "Non-targeting control for MISSION shRNA library silences SNRPD3 leading to cell death or permanent growth arrest." Mol Ther Nucleic Acids **26**: 711-731.

Dana, H., G. M. Chalbatani, H. Mahmoodzadeh, R. Karimloo, O. Rezaiean, A. Moradzadeh, N. Mehmandoost, F. Moazzen, A. Mazraeh, V. Marmari, M. Ebrahimi, M. M. Rashno, S. J. Abadi and E. Gharagouzlo (2017). "Molecular Mechanisms and Biological Functions of siRNA." Int J Biomed Sci **13**(2): 48-57.

Daneman, R. and A. Prat (2015). "The blood-brain barrier." Cold Spring Harbor perspectives in biology **7**(1): a020412-a020412.

Daneman, R. and A. Prat (2015). "The blood–brain barrier." Cold Spring Harbor Perspectives in Biology **7**(1).

de Jong, Y. P. and R. W. Herzog (2021). "Liver gene therapy and hepatocellular carcinoma: A complex web." Mol Ther **29**(4): 1353-1354.

Denise, H., S. A. Moschos, B. Sidders, F. Burden, H. Perkins, N. Carter, T. Stroud, M. Kennedy, S. A. Fancy, C. Lapthorn, H. Lavender, R. Kinloch, D. Suhy and R. Corbau (2014). "Deep Sequencing Insights in Therapeutic shRNA Processing and siRNA Target Cleavage Precision." Mol Ther Nucleic Acids **3**(2): e145.

Denning, W., S. Das, S. Guo, J. Xu, J. C. Kappes and Z. Hel (2013). "Optimization of the transductional efficiency of lentiviral vectors: effect of sera and polycations." Mol Biotechnol **53**(3): 308-314.

Deverman, B. E., P. L. Pravdo, B. P. Simpson, S. R. Kumar, K. Y. Chan, A. Banerjee, W.-L. Wu, B. Yang, N. Huber, S. P. Pasca and V. Gradinaru (2016). "Cre-dependent selection yields AAV variants for widespread gene transfer to the adult brain." Nature biotechnology **34**(2): 204-209.

DiGiacomo, V. and D. Meruelo (2016). "Looking into laminin receptor: critical discussion regarding the non-integrin 37/67-kDa laminin receptor/RPSA protein." Biological reviews of the Cambridge Philosophical Society **91**(2): 288-288.

DiMattia, M. A., H.-J. Nam, K. V. Vliet, M. Mitchell, A. Bennett, B. L. Gurda, R. McKenna, N. H. Olson, R. S. Sinkovits, M. Potter, B. J. Byrne, G. Aslanidi, S. Zolotukhin, N. Muzyczka, T. S. Baker and M. Agbandje-McKenna (2012). "Structural Insight into the Unique Properties of Adeno-Associated Virus Serotype 9." Journal of Virology **86**(12): 6947-6958.

Dominguez, E., T. Marais, N. Chatauret, S. Benkhelifa-Ziyyat, S. Duque, P. Ravassard, R. Carcenac, S. Astord, A. Pereira de Moura, T. Voit and M. Barkats (2011). "Intravenous scAAV9 delivery of a codon-optimized SMN1 sequence rescues SMA mice." Hum Mol Genet **20**(4): 681-693.

Dong, D., H. Zhou, S.-Y. Na, R. Niedra, Y. Peng, H. Wang, B. Seed and G. L. Zhou (2018). "GPR108, an NF-κB activator suppressed by TIRAP, negatively regulates TLR-triggered immune responses." PLOS ONE **13**(10): e0205303-e0205303.

Dong, W. and B. Kantor (2021). "Lentiviral Vectors for Delivery of Gene-Editing Systems Based on CRISPR/Cas: Current State and Perspectives." Viruses **13**(7).

Drouin, L. M. and M. Agbandje-McKenna (2013). "Adeno-associated virus structural biology as a tool in vector development." Future virology **8**(12): 1183-1199.

Duan, W., M. Guo, L. Yi, Y. Liu, Z. Li, Y. Ma, G. Zhang, Y. Liu, H. Bu, X. Song and C. Li (2019). "The deletion of mutant SOD1 via CRISPR/Cas9/sgRNA prolongs survival in an amyotrophic lateral sclerosis mouse model." Gene Therapy 2019 27:3 **27**(3): 157-169.

Duarte, F. and N. Deglon (2020). "Genome Editing for CNS Disorders." Front Neurosci **14**: 579062.

Dudek, A. M., S. Pillay, A. S. Puschnik, C. M. Nagamine, F. Cheng, J. Qiu, J. E. Carette and L. H. Vandenberghe (2018). "An Alternate Route for Adeno-associated Virus (AAV) Entry Independent of AAV Receptor." Journal of virology **92**(7).

Dudek, A. M., N. Zabaleta, E. Zinn, S. Pillay, J. Zengel, C. Porter, J. S. Franceschini, R. Estelien, J. E. Carette, G. L. Zhou and L. H. Vandenberghe (2020). "GPR108 Is a Highly Conserved AAV Entry Factor." Molecular Therapy **28**(2): 367-381.

Durand, S. and A. Cimarelli (2011). "The inside out of lentiviral vectors." Viruses **3**(2): 132-159.

Earley, L. F., J. M. Powers, K. Adachi, J. T. Baumgart, N. L. Meyer, Q. Xie, M. S. Chapman and H. Nakai (2017). "Adeno-associated Virus (AAV) Assembly-Activating Protein Is Not an Essential Requirement for Capsid Assembly of AAV Serotypes 4, 5, and 11." Journal of virology **91**(3): e01980-01916.

Eichler, F., C. Duncan, P. L. Musolino, P. J. Orchard, S. De Oliveira, A. J. Thrasher, M. Armant, C. Dansereau, T. C. Lund, W. P. Miller, G. V. Raymond, R. Sankar, A. J. Shah, C. Sevin, H. B. Gaspar, P. Gissen, H. Amartino, D. Bratkovic, N. J. C. Smith, A. M. Paker, E. Shamir, T. O'Meara, D. Davidson, P. Aubourg and D. A. Williams (2017). "Hematopoietic Stem-Cell Gene Therapy for Cerebral Adrenoleukodystrophy." N Engl J Med **377**(17): 1630-1638.

El-Brolosy, M. A., Z. Kontarakis, A. Rossi, C. Kuenne, S. Gunther, N. Fukuda, K. Kikhi, G. L. M. Boezio, C. M. Takacs, S. L. Lai, R. Fukuda, C. Gerri, A. J. Giraldez and D. Y. R. Stainier (2019). "Genetic compensation triggered by mutant mRNA degradation." Nature **568**(7751): 193-197.

Ellis, B. L., M. L. Hirsch, J. C. Barker, J. P. Connelly, R. J. Steininger and M. H. Porteus (2013). A survey of ex vivo/in vitro transduction efficiency of mammalian primary cells and cell lines with Nine natural adeno-associated virus (AAV1-9) and one engineered adeno-associated virus serotype. Virology Journal, BioMed Central. **10:** 74-74.

Elmen, J., H. Thonberg, K. Ljungberg, M. Frieden, M. Westergaard, Y. Xu, B. Wahren, Z. Liang, H. Orum, T. Koch and C. Wahlestedt (2005). "Locked nucleic acid (LNA) mediated improvements in siRNA stability and functionality." Nucleic Acids Res **33**(1): 439-447.

Emmanuel, S. N., J. K. Smith, J. Hsi, Y. S. Tseng, M. Kaplan, M. Mietzsch, P. Chipman, A. Asokan, R. McKenna and M. Agbandje-McKenna (2022). "Structurally Mapping Antigenic Epitopes of Adeno-associated Virus 9: Development of Antibody Escape Variants." J Virol **96**(3): e0125121.

Endsley, M. A., A. D. Somasunderam, G. Li, N. Oezguen, V. Thiviyanathan, J. L. Murray, D. H. Rubin, T. W. Hodge, W. A. O'Brien, B. Lewis and M. R. Ferguson (2014). "Nuclear trafficking of the HIV-1 pre-integration complex depends on the ADAM10 intracellular domain." Virology **454-455**: 60-66.

Ferrucci, P. F., L. Pala, F. Conforti and E. Cocorocchio (2021). "Talimogene Laherparepvec (T-VEC): An Intralesional Cancer Immunotherapy for Advanced Melanoma." Cancers (Basel) **13**(6).

Figenschau, S. L., E. Knutsen, I. Urbarova, C. Fenton, B. Elston, M. Perander, E. S. Mortensen and K. A. Fenton (2018). "ICAM1 expression is induced by proinflammatory cytokines and associated with TLS formation in aggressive breast cancer subtypes." Sci Rep **8**(1): 11720.

Finkelshtein, D., A. Werman, D. Novick, S. Barak and M. Rubinstein (2013). "LDL receptor and its family members serve as the cellular receptors for vesicular stomatitis virus." Proc Natl Acad Sci U S A **110**(18): 7306-7311.

Foust, K. D., E. Nurre, C. L. Montgomery, A. Hernandez, C. M. Chan and B. K. Kaspar (2009). "Intravascular AAV9 preferentially targets neonatal-neurons and adult-astrocytes in CNS." Nature biotechnology **27**(1): 59-59.

Foust, K. D., D. L. Salazar, S. Likhite, L. Ferraiuolo, D. Ditsworth, H. Ilieva, K. Meyer, L. Schmelzer, L. Braun, D. W. Cleveland and B. K. Kaspar (2013). "Therapeutic AAV9-mediated suppression of mutant

SOD1 slows disease progression and extends survival in models of inherited ALS." Mol Ther **21**(12): 2148-2159.

Fragkos, M., M. Breuleux, N. Clément and P. Beard (2008). "Recombinant adeno-associated viral vectors are deficient in provoking a DNA damage response." Journal of virology **82**(15): 7379-7387.

Froelich, S., A. Tai and P. Wang (2010). "Lentiviral vectors for immune cells targeting." Immunopharmacol Immunotoxicol **32**(2): 208-218.

Fujimura, Y., K. Yamada and H. Tachibana (2005). "A lipid raft-associated 67 kDa laminin receptor mediates suppressive effect of epigallocatechin-3-O-gallate on FcεRI expression." Biochemical and Biophysical Research Communications **336**(2): 674-681.

Gaj, T., D. S. Ojala, F. K. Ekman, L. C. Byrne, P. Limsirichai and D. V. Schaffer (2017). "In vivo genome editing improves motor function and extends survival in a mouse model of ALS." Science Advances **3**(12): 3952-3952.

Galvan, A., T. L. Petkau, A. M. Hill, A. J. Korecki, G. Lu, D. Choi, K. Rahman, E. M. Simpson, B. R. Leavitt and Y. Smith (2021). "Intracerebroventricular Administration of AAV9-PHP.B SYN1-EmGFP Induces Widespread Transgene Expression in the Mouse and Monkey Central Nervous System." Hum Gene Ther **32**(11-12): 599-615.

Garba, A. O. and S. A. Mousa (2010). "Bevasiranib for the treatment of wet, age-related macular degeneration." Ophthalmol Eye Dis **2**: 75-83.

Gerasimavicius, L., B. J. Livesey and J. A. Marsh (2022). "Loss-of-function, gain-of-function and dominant-negative mutations have profoundly different effects on protein structure." Nat Commun **13**(1): 3895.

Gibeault, R. L., K. L. Conn, M. D. Bildersheim and L. M. Schang (2016). "An Essential Viral Transcription Activator Modulates Chromatin Dynamics." PLoS Pathog **12**(8): e1005842.

Giovannelli, I., A. Higginbottom, J. Kirby, M. Azzouz and P. J. Shaw (2023). "Prospects for gene replacement therapies in amyotrophic lateral sclerosis." Nat Rev Neurol **19**(1): 39-52.

Girod, A., C. E. Wobus, Z. Zadori, M. Ried, K. Leike, P. Tijssen, J. A. Kleinschmidt and M. Hallek (2002). "The VP1 capsid protein of adeno-associated virus type 2 is carrying a phospholipase A2 domain required for virus infectivity." J Gen Virol **83**(Pt 5): 973-978.

Goertsen, D., N. C. Flytzanis, N. Goeden, M. R. Chuapoco, A. Cummins, Y. Chen, Y. Fan, Q. Zhang, J. Sharma, Y. Duan, L. Wang, G. Feng, Y. Chen, N. Y. Ip, J. Pickel and V. Gradinaru (2022). "AAV capsid variants with brain-wide transgene expression and decreased liver targeting after intravenous delivery in mouse and marmoset." Nat Neurosci **25**(1): 106-115.

Gopalappa, R., B. Suresh, S. Ramakrishna and H. H. Kim (2018). "Paired D10A Cas9 nickases are sometimes more efficient than individual nucleases for gene disruption." Nucleic Acids Res **46**(12): e71.

Gowing, G., S. Svendsen and C. N. Svendsen (2017). "Ex vivo gene therapy for the treatment of neurological disorders." Prog Brain Res **230**: 99-132.

Greene, C. and M. Campbell (2016). "Tight junction modulation of the blood brain barrier: CNS delivery of small molecules." Tissue Barriers **4**(1): e1138017-e1138017.

Gruntman, A. M. and T. R. Flotte (2015). "Delivery of Adeno-Associated Virus Gene Therapy by Intravascular Limb Infusion Methods." Hum Gene Ther Clin Dev **26**(3): 159-164.

Guide, S. V., M. E. Gonzalez, I. S. Bagci, B. Agostini, H. Chen, G. Feeney, M. Steimer, B. Kapadia, K. Sridhar, L. Quesada Sanchez, F. Gonzalez, M. Van Ligten, T. J. Parry, S. Chitra, L. A. Kammerman, S. Krishnan and M. P. Marinkovich (2022). "Trial of Beremagene Geperpavec (B-VEC) for Dystrophic Epidermolysis Bullosa." N Engl J Med **387**(24): 2211-2219.

Guo, H., S. Shen, L. Wang and H. Deng (2010). "Role of tegument proteins in herpesvirus assembly and egress." Protein Cell **1**(11): 987-998.

Guo, J., S. Chen, C. Huang, L. Chen, D. J. Studholme, S. Zhao and L. Yu (2004). "MANSC: a seven-cysteine-containing domain present in animal membrane and extracellular proteins." Trends in Biochemical Sciences **29**(4): 172-174.

Gutierrez-Guerrero, A., F. L. Cosset and E. Verhoeyen (2020). "Lentiviral Vector Pseudotypes: Precious Tools to Improve Gene Modification of Hematopoietic Cells for Research and Gene Therapy." Viruses **12**(9).

Ha, J., H. Park, J. Park and S. B. Park (2021). "Recent advances in identifying protein targets in drug discovery." Cell Chemical Biology **28**(3): 394-423.

Hamill, K. J., K. Kligys, S. B. Hopkinson and J. C. R. Jones (2009). "Laminin deposition in the extracellular matrix: a complex picture emerges." Journal of cell science **122**(Pt 24): 4409-4417.

Hanlon, K. S., B. P. Kleinstiver, S. P. Garcia, M. P. Zaborowski, A. Volak, S. E. Spirig, A. Muller, A. A. Sousa, S. Q. Tsai, N. E. Bengtsson, C. Loov, M. Ingelsson, J. S. Chamberlain, D. P. Corey, M. J. Aryee, J. K. Joung, X. O. Breakefield, C. A. Maguire and B. Gyorgy (2019). "High levels of AAV vector integration into CRISPR-induced DNA breaks." Nat Commun **10**(1): 4439.

Hanlon, K. S., J. C. Meltzer, T. Buzhdygan, M. J. Cheng, M. Sena-Esteves, R. E. Bennett, T. P. Sullivan, R. Razmpour, Y. Gong, C. Ng, J. Nammour, D. Maiz, S. Dujardin, S. H. Ramirez, E. Hudry and C. A. Maguire

(2019). "Selection of an Efficient AAV Vector for Robust CNS Transgene Expression." Molecular Therapy - Methods and Clinical Development **15**: 320-332.

Hauck, B., W. Zhao, K. High and W. Xiao (2004). "Intracellular viral processing, not single-stranded DNA accumulation, is crucial for recombinant adeno-associated virus transduction." J Virol **78**(24): 13678-13686.

Heming, J. D., J. F. Conway and F. L. Homa (2017). "Herpesvirus Capsid Assembly and DNA Packaging." Adv Anat Embryol Cell Biol **223**: 119-142.

Hervé, F., N. Ghinea and J.-M. Scherrmann (2008). "CNS delivery via adsorptive transcytosis." The AAPS journal **10**(3): 455-472.

Hordeaux, J., E. L. Buza, C. Dyer, T. Goode, T. W. Mitchell, L. Richman, N. Denton, C. Hinderer, N. Katz, R. Schmid, R. Miller, G. R. Choudhury, M. Horiuchi, K. Nambiar, H. Yan, M. Li and J. M. Wilson (2020). "Adeno-Associated Virus-Induced Dorsal Root Ganglion Pathology." Hum Gene Ther **31**(15-16): 808-818.

Hordeaux, J., Q. Wang, N. Katz, E. L. Buza, P. Bell and J. M. Wilson (2018). "The Neurotropic Properties of AAV-PHP.B Are Limited to C57BL/6J Mice." Mol Ther **26**(3): 664-668.

Hordeaux, J., Y. Yuan, P. M. Clark, Q. Wang, R. A. Martino, J. J. Sims, P. Bell, A. Raymond, W. L. Stanford and J. M. Wilson (2019). "The GPI-Linked Protein LY6A Drives AAV-PHP.B Transport across the Blood-Brain Barrier."

Hsu, J., J. Rappaport and S. Muro (2014). "Specific binding, uptake, and transport of ICAM-1-targeted nanocarriers across endothelial and subendothelial cell components of the blood-brain barrier." Pharmaceutical Research **31**(7): 1855-1866.

Hu, B., L. Zhong, Y. Weng, L. Peng, Y. Huang, Y. Zhao and X. J. Liang (2020). "Therapeutic siRNA: state of the art." Signal Transduct Target Ther **5**(1): 101.

Huang, H. L., H. W. Hsing, T. C. Lai, Y. W. Chen, T. R. Lee, H. T. Chan, P. C. Lyu, C. L. Wu, Y. C. Lu, S. T. Lin, C. W. Lin, C. H. Lai, H. T. Chang, H. C. Chou and H. L. Chan (2010). "Trypsin-induced proteome alteration during cell subculture in mammalian cells." Journal of Biomedical Science **17**(1): 1-10.

Huang, L. Y., S. Halder and M. Agbandje-McKenna (2014). "Parvovirus glycan interactions." Curr Opin Virol **7**: 108-118.

Huang, Q., K. Y. Chan, I. G. Tobey, Y. A. Chan, T. Poterba, C. L. Boutros, A. B. Balazs, R. Daneman, J. M. Bloom, C. Seed and B. E. Deverman (2019). "Delivering genes across the blood-brain barrier: LY6A, a novel cellular receptor for AAV-PHP.B capsids." bioRxiv: 538421-538421.

Hudak, A., M. Roach, D. Pusztai, A. Pettko-Szandtner, A. Letoha, L. Szilak, M. Azzouz and T. Letoha (2023). "Syndecan-4 Mediates the Cellular Entry of Adeno-Associated Virus 9." Int J Mol Sci **24**(4).

Iannitti, T., J. M. Scarrott, S. Likhite, I. R. P. Coldicott, K. E. Lewis, P. R. Heath, A. Higginbottom, M. A. Myszczynska, M. Milo, G. M. Hautbergue, K. Meyer, B. K. Kaspar, L. Ferraiuolo, P. J. Shaw and M. Azzouz (2018). "Translating SOD1 Gene Silencing toward the Clinic: A Highly Efficacious, Off-Target-free, and Biomarker-Supported Strategy for fALS." Molecular Therapy. Nucleic Acids **12**: 75-75.

Islam, M. M. and Z. Mohamed (2015). "Computational and Pharmacological Target of Neurovascular Unit for Drug Design and Delivery." BioMed Research International **2015**: 1-10.

Israelow, B., T. Mao, J. Klein, E. Song, B. Menasche, S. B. Omer and A. Iwasaki (2021). "Adaptive immune determinants of viral clearance and protection in mouse models of SARS-CoV-2." Sci Immunol **6**(64): eabl4509.

Jamieson, J. J., P. C. Searson and S. Gerecht (2017). "Engineering the human blood-brain barrier in vitro." Journal of Biological Engineering **11**(1): 37-37.

Jiang, J., Q. Zhu, T. F. Gendron, S. Saberi, M. McAlonis-Downes, A. Seelman, J. E. Stauffer, P. Jafar-Nejad, K. Drenner, D. Schulte, S. Chun, S. Sun, S. C. Ling, B. Myers, J. Engelhardt, M. Katz, M. Baughn, O. Platoshyn, M. Marsala, A. Watt, C. J. Heyser, M. C. Ard, L. De Muynck, L. M. Daughrity, D. A. Swing, L. Tessarollo, C. J. Jung, A. Delpoux, D. T. Utzschneider, S. M. Hedrick, P. J. de Jong, D. Edbauer, P. Van Damme, L. Petrucelli, C. E. Shaw, C. F. Bennett, S. Da Cruz, J. Ravits, F. Rigo, D. W. Cleveland and C. Lagier-Tourenne (2016). "Gain of Toxicity from ALS/FTD-Linked Repeat Expansions in C9ORF72 Is Alleviated by Antisense Oligonucleotides Targeting GGGGCC-Containing RNAs." Neuron **90**(3): 535-550.

Kang, S., C. U. Kim, X. Gu, R. M. Owens, S. J. van Rijn, V. Boonyaleepun, Y. Mao, T. A. Springer and M. M. Jin (2012). "Complex structure of engineered modular domains defining molecular interaction between ICAM-1 and integrin LFA-1." PLoS One **7**(8): e44124.

Kanter, J., M. C. Walters, L. Krishnamurti, M. Y. Mapara, J. L. Kwiatkowski, S. Rifkin-Zenenberg, B. Aygun, K. A. Kasow, F. J. Pierciey, Jr., M. Bonner, A. Miller, X. Zhang, J. Lynch, D. Kim, J. A. Ribeil, M. Asmal, S. Goyal, A. A. Thompson and J. F. Tisdale (2022). "Biologic and Clinical Efficacy of LentiGlobin for Sickle Cell Disease." N Engl J Med **386**(7): 617-628.

Kantor, A., M. E. McClements and R. E. MacLaren (2020). "CRISPR-Cas9 DNA Base-Editing and Prime-Editing." Int J Mol Sci **21**(17).

Kaufman, W. L., I. Kocman, V. Agrawal, H. P. Rahn, D. Besser and M. Gossen (2008). "Homogeneity and persistence of transgene expression by omitting antibiotic selection in cell line isolation." Nucleic Acids Res **36**(17): e111.

Kawamata, M., H. I. Suzuki, R. Kimura and A. Suzuki (2023). "Optimization of Cas9 activity through the addition of cytosine extensions to single-guide RNAs." Nat Biomed Eng.

Kim, I. J., V. N. Chouljenko, J. D. Walker and K. G. Kousoulas (2013). "Herpes simplex virus 1 glycoprotein M and the membrane-associated protein UL11 are required for virus-induced cell fusion and efficient virus entry." J Virol **87**(14): 8029-8037.

Kim, T. K. and J. H. Eberwine (2010). "Mammalian cell transfection: the present and the future." Anal Bioanal Chem **397**(8): 3173-3178.

Kimball, S. R. and L. S. Jefferson (2004). "Amino acids as regulators of gene expression." Nutr Metab (Lond) **1**(1): 3.

Kobayashi, H. and M. Fukuda (2013). "Arf6, Rab11 and transferrin receptor define distinct populations of recycling endosomes." Commun Integr Biol **6**(5): e25036.

Kohlmeier, J. E., L. M. Rumsey, M. A. Chan and S. H. Benedict (2003). "The outcome of T-cell costimulation through intercellular adhesion molecule-1 differs from costimulation through leucocyte function-associated antigen-1." Immunology **108**(2): 152-157.

Koley, D. and A. J. Bard (2010). "Triton X-100 concentration effects on membrane permeability of a single HeLa cell by scanning electrochemical microscopy (SECM)." Proc Natl Acad Sci U S A **107**(39): 16783-16787.

Komarova, Y. and A. B. Malik (2010). "Regulation of Endothelial Permeability via Paracellular and Transcellular Transport Pathways." Annual Review of Physiology **72**(1): 463-493.

Korobeynikov, V. A., A. K. Lyashchenko, B. Blanco-Redondo, P. Jafar-Nejad and N. A. Shneider (2022). "Antisense oligonucleotide silencing of FUS expression as a therapeutic approach in amyotrophic lateral sclerosis." Nat Med **28**(1): 104-116.

Kubotera, H., H. Ikeshima-Kataoka, Y. Hatashita, A. L. Allegra Mascaro, F. S. Pavone and T. Inoue (2019). "Astrocytic endfeet re-cover blood vessels after removal by laser ablation." Scientific Reports **9**(1): 1263-1263.

Kukurba, K. R. and S. B. Montgomery (2015). "RNA Sequencing and Analysis." Cold Spring Harb Protoc **2015**(11): 951-969.

Kumar, A., V. Narayanan and A. Sekhar (2020). "Characterizing Post-Translational Modifications and Their Effects on Protein Conformation Using NMR Spectroscopy." Biochemistry **59**(1): 57-73.

Lahr, W. S., C. J. Sipe, J. G. Skeate, B. R. Webber and B. S. Moriarity (2023). "CRISPR-Cas9 base editors and their current role in human therapeutics." Cytotherapy **25**(3): 270-276.

Lang, M. A., S. A. Jenkins, P. Balzano, A. Owoyele, A. Patel and A. K. Bamezai (2017). "Engaging Ly-6A/Sca-1 triggers lipid raft-dependent and -independent responses in CD4 ⁺ T-cell lines." Immunity, Inflammation and Disease **5**(4): 448-460.

Lee, E. J., T. M. Robinson, J. J. Tabor, A. G. Mikos and J. Suh (2018). "Reverse Transduction Can Improve Efficiency of AAV Vectors in Transduction-Resistant Cells." Biotechnology and bioengineering **115**(12): 3042-3042.

Lefevre, M., D. J. Felmlee, M. Parnot, T. F. Baumert and C. Schuster (2014). "Syndecan 4 is involved in mediating HCV entry through interaction with lipoviral particle-associated apolipoprotein E." PLoS One **9**(4): e95550.

Li, C. and R. J. Samulski (2020). "Engineering adeno-associated virus vectors for gene therapy." Nat Rev Genet **21**(4): 255-272.

Lim, C. K. W., M. Gapinske, A. K. Brooks, W. S. Woods, J. E. Powell, M. A. Zeballos C, J. Winter, P. Perez-Pinera and T. Gaj (2020). "Treatment of a Mouse Model of ALS by In Vivo Base Editing." Molecular Therapy **28**(4): 1177-1189.

Ling, Q., M. Rioux, Y. Hu, M. Lee and S. J. Gray (2021). "Adeno-associated viral vector serotype 9-based gene replacement therapy for SURF1-related Leigh syndrome." Mol Ther Methods Clin Dev **23**: 158-168.

Liu, M., W. C. Van Voorhis and R. J. Quinn (2021). "Development of a target identification approach using native mass spectrometry." Sci Rep **11**(1): 2387.

Liu, P., B. W. O'Mara, B. M. Warrack, W. Wu, Y. Huang, Y. Zhang, R. Zhao, M. Lin, M. S. Ackerman, P. K. Hocknell, G. Chen, L. Tao, S. Rieble, J. Wang, D. B. Wang-Iverson, A. A. Tymiak, M. J. Grace and R. J. Russell (2010). "A tris (2-carboxyethyl) phosphine (TCEP) related cleavage on cysteine-containing proteins." J Am Soc Mass Spectrom **21**(5): 837-844.

Liu, T., Y. Wang, X. Luo, J. Li, S. A. Reed, H. Xiao, T. S. Young and P. G. Schultz (2016). "Enhancing protein stability with extended disulfide bonds." Proc Natl Acad Sci U S A **113**(21): 5910-5915.

Livak, K. J. and T. D. Schmittgen (2001). "Analysis of relative gene expression data using real-time quantitative PCR and the 2(-Delta Delta C(T)) Method." Methods **25**(4): 402-408.

Louche, A., S. P. Salcedo and S. Bigot (2017). "Protein-Protein Interactions: Pull-Down Assays." Methods Mol Biol **1615**: 247-255.

Lu, C.-T., Y.-Z. Zhao, H. L. Wong, J. Cai, L. Peng and X.-Q. Tian (2014). "Current approaches to enhance CNS delivery of drugs across the brain barriers." International journal of nanomedicine **9**: 2241-2257.

Luissint, A.-C., C. Artus, F. Glacial, K. Ganeshamoorthy and P.-O. Couraud (2012). "Tight junctions at the blood brain barrier: physiological architecture and disease-associated dysregulation." Fluids and barriers of the CNS **9**(1): 23-23.

Lundstrom, K. (2018). "Viral Vectors in Gene Therapy." Diseases **6**(2): 42-42.

Lykken, E. A., C. Shyng, R. J. Edwards, A. Rozenberg and S. J. Gray (2018). "Recent progress and considerations for AAV gene therapies targeting the central nervous system." Journal of neurodevelopmental disorders **10**(1): 16-16.

Madigan, V. J., G. E. Berry, T. O. Tyson, D. Nardone-White, J. Ark, Z. C. Elmore, G. Murlidharan, H. A. Vincent and A. Asokan (2020). "The Golgi Calcium ATPase Pump Plays an Essential Role in Adeno-associated Virus Trafficking and Transduction." J Virol **94**(21).

Madigan, V. J., T. O. Tyson, J. A. Yuziuk, M. Pillai, S. Moller-Tank and A. Asokan (2019). "A CRISPR Screen Identifies the Cell Polarity Determinant Crumbs 3 as an Adeno-associated Virus Restriction Factor in Hepatocytes." J Virol **93**(21).

Maginnis, M. S. (2018). "Virus-Receptor Interactions: The Key to Cellular Invasion." J Mol Biol **430**(17): 2590-2611.

Mahmoodi Chalbatani, G., H. Dana, E. Gharagouzloo, S. Grijalvo, R. Eritja, C. D. Logsdon, F. Memari, S. R. Miri, M. R. Rad and V. Marmari (2019). "Small interfering RNAs (siRNAs) in cancer therapy: a nano-based approach." Int J Nanomedicine **14**: 3111-3128.

Mallard, C., C. J. Ek and Z. S. Vexler (2018). "The myth of the immature barrier systems in the developing brain: role in perinatal brain injury." J Physiol **596**(23): 5655-5664.

Manini, A., E. Abati, A. Nuredini, S. Corti and G. P. Comi (2021). "Adeno-Associated Virus (AAV)-Mediated Gene Therapy for Duchenne Muscular Dystrophy: The Issue of Transgene Persistence." Front Neurol **12**: 814174.

Mano, M., R. Ippodrino, L. Zentilin, S. Zacchigna and M. Giacca (2015). "Genome-wide RNAi screening identifies host restriction factors critical for in vivo AAV transduction." Proc Natl Acad Sci U S A **112**(36): 11276-11281.

Marchand, C., G. Lemay and D. Archambault (2019). "The Jembrana disease virus Rev protein: Identification of nuclear and novel lentiviral nucleolar localization and nuclear export signals." PLoS One **14**(8): e0221505.

Maroui, M. A., A. Calle, C. Cohen, N. Streichenberger, P. Texier, J. Takissian, A. Rousseau, N. Poccardi, J. Welsch, A. Corpet, L. Schaeffer, M. Labetoulle and P. Lomonte (2016). "Latency Entry of Herpes Simplex Virus 1 Is Determined by the Interaction of Its Genome with the Nuclear Environment." PLoS Pathog **12**(9): e1005834.

Mathiesen, S. N., J. L. Lock, L. Schoderboeck, W. C. Abraham and S. M. Hughes (2020). "CNS Transduction Benefits of AAV-PHP.eB over AAV9 Are Dependent on Administration Route and Mouse Strain." Mol Ther Methods Clin Dev **19**: 447-458.

Matsushita, T., T. Okada, T. Inaba, H. Mizukami, K. Ozawa and P. Colosi (2004). "The adenovirus E1A and E1B19K genes provide a helper function for transfection-based adeno-associated virus vector production." Journal of General Virology **85**(8): 2209-2214.

Matsuzaki, Y., A. Konno, R. Mochizuki, Y. Shinohara, K. Nitta, Y. Okada and H. Hirai (2018). "Intravenous administration of the adeno-associated virus-PHP.B capsid fails to upregulate transduction efficiency in the marmoset brain." Neurosci Lett **665**: 182-188.

Maurisse, R., D. De Semir, H. Emamekhoo, B. Bedayat, A. Abdolmohammadi, H. Parsi and D. C. Gruenert (2010). "Comparative transfection of DNA into primary and transformed mammalian cells from different lineages." BMC Biotechnol **10**: 9.

Maxfield, F. R. and T. E. McGraw (2004). "Endocytic recycling." Nat Rev Mol Cell Biol **5**(2): 121-132.

Mays, L. E., L. Wang, R. Tenney, P. Bell, H. J. Nam, J. Lin, B. Gurda, K. Van Vliet, K. Mikals, M. Agbandje-McKenna and J. M. Wilson (2013). "Mapping the structural determinants responsible for enhanced T cell activation to the immunogenic adeno-associated virus capsid from isolate rhesus 32.33." J Virol **87**(17): 9473-9485.

McCarty, D. M., P. E. Monahan and R. J. Samulski (2001). "Self-complementary recombinant adeno-associated virus (scAAV) vectors promote efficient transduction independently of DNA synthesis." Gene Ther **8**(16): 1248-1254.

McElwee, M., S. Vijayakrishnan, F. Rixon and D. Bhella (2018). "Structure of the herpes simplex virus portal-vertex." PLoS Biol **16**(6): e2006191.

McGarrity, G. J., G. Hoyah, A. Winemiller, K. Andre, D. Stein, G. Blick, R. N. Greenberg, C. Kinder, A. Zolopa, G. Binder-Scholl, P. Tebas, C. H. June, L. M. Humeau and T. Rebello (2013). "Patient monitoring and follow-up in lentiviral clinical trials." J Gene Med **15**(2): 78-82.

Mei, H., Q. Gu, W. Wang, Y. Meng, L. Jiang and J. Liu (2022). "CRISPR-surfaceome: An online tool for designing highly efficient sgRNAs targeting cell surface proteins." Comput Struct Biotechnol J **20**: 3833-3838.

Meisen, W. H., Z. B. Nejad, M. Hardy, H. Zhao, O. Oliverio, S. Wang, C. Hale, M. M. Ollmann and P. J. Collins (2020). "Pooled Screens Identify GPR108 and TM9SF2 as Host Cell Factors Critical for AAV Transduction." Molecular Therapy - Methods and Clinical Development **17**: 601-611.

Melgaco, J. G., T. Azamor, A. M. V. Silva, J. H. R. Linhares, T. P. Dos Santos, Y. S. Mendes, S. M. B. de Lima, C. B. Fernandes, J. da Silva, A. F. de Souza, L. N. Tubarao, E. C. D. Brito, T. B. S. Pereira, C. E. L. Menezes, M. D. Miranda, A. R. Matos, B. C. Caetano, J. Martins, T. L. Calvo, N. F. Rodrigues, C. Q. Sacramento, M. M. Siqueira, M. O. Moraes, S. Missailidis, P. C. C. Neves and A. P. D. Ano Bom (2021). "Two-Step In Vitro Model to Evaluate the Cellular Immune Response to SARS-CoV-2." Cells **10**(9).

Mendell, J. R., S. A. Al-Zaidy, K. J. Lehman, M. McColly, L. P. Lowes, L. N. Alfano, N. F. Reash, M. A. Iammarino, K. R. Church, A. Kleyn, M. N. Meriggioli and R. Shell (2021). "Five-Year Extension Results of the Phase 1 START Trial of Onasemnogene Abeparvovec in Spinal Muscular Atrophy." JAMA Neurol **78**(7): 834-841.

Mercuri, E., B. T. Darras, C. A. Chiriboga, J. W. Day, C. Campbell, A. M. Connolly, S. T. Iannaccone, J. Kirschner, N. L. Kuntz, K. Saito, P. B. Shieh, M. Tulinius, E. S. Mazzone, J. Montes, K. M. Bishop, Q. Yang, R. Foster, S. Gheuens, C. F. Bennett, W. Farwell, E. Schneider, D. C. De Vivo, R. S. Finkel and C. S. Group (2018). "Nusinersen versus Sham Control in Later-Onset Spinal Muscular Atrophy." N Engl J Med **378**(7): 625-635.

Merkel, S. F., A. M. Andrews, E. M. Lutton, D. Mu, E. Hudry, B. T. Hyman, C. A. Maguire and S. H. Ramirez (2017). "Trafficking of adeno-associated virus vectors across a model of the blood-brain barrier; a comparative study of transcytosis and transduction using primary human brain endothelial cells." Journal of neurochemistry **140**(2): 216-230.

Meyer, N. L. and M. S. Chapman (2022). "Adeno-associated virus (AAV) cell entry: structural insights." Trends Microbiol **30**(5): 432-451.

Micaroni, M., G. Giacchetti, R. Plebani, G. G. Xiao and L. Federici (2016). "ATP2C1 gene mutations in Hailey-Hailey disease and possible roles of SPCA1 isoforms in membrane trafficking." Cell Death Dis **7**(6): e2259.

Mietzsch, M., F. Broecker, A. Reinhardt, P. H. Seeberger and R. Heilbronn (2014). "Differential adeno-associated virus serotype-specific interaction patterns with synthetic heparins and other glycans." Journal of virology **88**(5): 2991-3003.

Milone, M. C. and U. O'Doherty (2018). "Clinical use of lentiviral vectors." Leukemia **32**(7): 1529-1541.

Mizukami, H., N. S. Young and K. E. Brown (1996). "Adeno-Associated Virus Type 2 Binds to a 150-Kilodalton Cell Membrane Glycoprotein." Virology **217**(1): 124-130.

Mocellin, S. and M. Provenzano (2004). "RNA interference: learning gene knock-down from cell physiology." J Transl Med **2**(1): 39.

Modlich, U. and C. Baum (2009). "Preventing and exploiting the oncogenic potential of integrating gene vectors." J Clin Invest **119**(4): 755-758.

Musarrat, F., V. Chouljenko and K. G. Kousoulas (2021). "Cellular and Viral Determinants of HSV-1 Entry and Intracellular Transport towards Nucleus of Infected Cells." J Virol **95**(7).

Muylaert, I., K. W. Tang and P. Elias (2011). "Replication and recombination of herpes simplex virus DNA." J Biol Chem **286**(18): 15619-15624.

Nabi, I. R. and P. U. Le (2003). "Caveolae/raft-dependent endocytosis." The Journal of Cell Biology **161**(4): 673-677.

Naso, M. F., B. Tomkowicz, W. L. Perry, W. R. Strohl and W. R. Strohl (2017). "Adeno-Associated Virus (AAV) as a Vector for Gene Therapy." BioDrugs : clinical immunotherapeutics, biopharmaceuticals and gene therapy **31**(4): 317-334.

Nayerossadat, N., T. Maedeh and P. A. Ali (2012). "Viral and nonviral delivery systems for gene delivery." Advanced biomedical research **1**: 27-27.

Neumeier, J. and G. Meister (2020). "siRNA Specificity: RNAi Mechanisms and Strategies to Reduce Off-Target Effects." Front Plant Sci **11**: 526455.

Newsom, S., H. P. Parameshwaran, L. Martin and R. Rajan (2020). "The CRISPR-Cas Mechanism for Adaptive Immunity and Alternate Bacterial Functions Fuels Diverse Biotechnologies." Front Cell Infect Microbiol **10**: 619763.

Nonnenmacher, M. and T. Weber (2011). "Adeno-Associated Virus 2 Infection Requires Endocytosis through the CLIC/GEEC Pathway." Cell Host & Microbe **10**(6): 563-576.

Nonnenmacher, M. and T. Weber (2012). "Intracellular transport of recombinant adeno-associated virus vectors." Gene Ther **19**(6): 649-658.

Nonnenmacher, M. E., J. C. Cintrat, D. Gillet and T. Weber (2015). "Syntaxin 5-dependent retrograde transport to the trans-Golgi network is required for adeno-associated virus transduction." J Virol **89**(3): 1673-1687.

Ohtsuki, S. and T. Terasaki (2007). "Contribution of Carrier-Mediated Transport Systems to the Blood–Brain Barrier as a Supporting and Protecting Interface for the Brain; Importance for CNS Drug Discovery and Development." Pharmaceutical Research **24**(9): 1745-1758.

Opie, S. R., K. H. Warrington, Jr., M. Agbandje-McKenna, S. Zolotukhin and N. Muzyczka (2003). "Identification of amino acid residues in the capsid proteins of adeno-associated virus type 2 that contribute to heparan sulfate proteoglycan binding." J Virol **77**(12): 6995-7006.

Owen, D. J., C. M. Crump and S. C. Graham (2015). "Tegument Assembly and Secondary Envelopment of Alphaherpesviruses." Viruses **7**(9): 5084-5114.

Pardridge, W. M. (2005). "The blood-brain barrier: bottleneck in brain drug development." NeuroRx : the journal of the American Society for Experimental NeuroTherapeutics **2**(1): 3-14.

Parr-Brownlie, L. C., C. Bosch-Bouju, L. Schoderboeck, R. J. Sizemore, W. C. Abraham and S. M. Hughes (2015). "Lentiviral vectors as tools to understand central nervous system biology in mammalian model organisms." Front Mol Neurosci **8**: 14.

Penzes, J. J., P. Chipman, N. Bhattacharya, A. Zeher, R. Huang, R. McKenna and M. Agbandje-McKenna (2021). "Adeno-associated Virus 9 Structural Rearrangements Induced by Endosomal Trafficking pH and Glycan Attachment." J Virol **95**(19): e0084321.

Petrich, J., D. Marchese, C. Jenkins, M. Storey and J. Blind (2020). "Gene Replacement Therapy: A Primer for the Health-system Pharmacist." J Pharm Pract **33**(6): 846-855.

Pillay, S. and J. E. Carette (2017). "Host determinants of adeno-associated viral vector entry." Current opinion in virology **24**: 124-131.

Pillay, S., N. L. Meyer, A. S. Puschnik, O. Davulcu, J. Diep, Y. Ishikawa, L. T. Jae, J. E. Wosen, C. M. Nagamine, M. S. Chapman and J. E. Carette (2016). "An essential receptor for adeno-associated virus infection." Nature **530**(7588): 108-112.

Pirona, A. C., R. Oktriani, M. Boettcher and J. D. Hoheisel (2020). "Process for an efficient lentiviral cell transduction." Biol Methods Protoc **5**(1): bpaa005.

Poletti, V. and F. Mavilio (2021). "Designing Lentiviral Vectors for Gene Therapy of Genetic Diseases." Viruses **13**(8).

Prelich, G. (2012). "Gene overexpression: uses, mechanisms, and interpretation." Genetics **190**(3): 841-854.

Pryadkina, M., W. Lostal, N. Bourg, K. Charton, C. Roudaut, M. L. Hirsch and I. Richard (2015). "A comparison of AAV strategies distinguishes overlapping vectors for efficient systemic delivery of the 6.2 kb Dysferlin coding sequence." Molecular Therapy - Methods & Clinical Development **2**: 15009-15009.

Pulgar, V. M. (2019). "Transcytosis to Cross the Blood Brain Barrier, New Advancements and Challenges." Frontiers in Neuroscience **12**: 1019-1019.

Qin, Y., W. Jiang, A. Li, M. Gao, H. Liu, Y. Gao, X. Tian and G. Gong (2021). "The Combination of Paraformaldehyde and Glutaraldehyde Is a Potential Fixative for Mitochondria." Biomolecules **11**(5).

Raj, D., A. M. Davidoff and A. C. Nathwani (2011). "Self-complementary adeno-associated viral vectors for gene therapy of hemophilia B: progress and challenges." Expert Rev Hematol **4**(5): 539-549.

Rampado, R., F. Giordano, L. Moracci, S. Crotti, P. Caliceti, M. Agostini and F. Taraballi (2022). "Optimization of a detergent-based protocol for membrane proteins purification from mammalian cells." J Pharm Biomed Anal **219**: 114926.

Ran, F. A., P. D. Hsu, C. Y. Lin, J. S. Gootenberg, S. Konermann, A. E. Trevino, D. A. Scott, A. Inoue, S. Matoba, Y. Zhang and F. Zhang (2013). "Double nicking by RNA-guided CRISPR Cas9 for enhanced genome editing specificity." Cell **154**(6): 1380-1389.

Ravindra Kumar, S., T. F. Miles, X. Chen, D. Brown, T. Dobreva, Q. Huang, X. Ding, Y. Luo, P. H. Einarsson, A. Greenbaum, M. J. Jang, B. E. Deverman and V. Gradinaru (2020). "Multiplexed Cre-dependent selection yields systemic AAVs for targeting distinct brain cell types." Nat Methods **17**(5): 541-550.

Recchia, A. and F. Mavilio (2011). "Site-specific integration by the adeno-associated virus rep protein." Curr Gene Ther **11**(5): 399-405.

Richter, K. N., N. H. Revelo, K. J. Seitz, M. S. Helm, D. Sarkar, R. S. Saleeb, E. D'Este, J. Eberle, E. Wagner, C. Vogl, D. F. Lazaro, F. Richter, J. Coy-Vergara, G. Coceano, E. S. Boyden, R. R. Duncan, S. W. Hell, M. A. Lauterbach, S. E. Lehnart, T. Moser, T. F. Outeiro, P. Rehling, B. Schwappach, I. Testa, B. Zapiec and S. O. Rizzoli (2018). "Glyoxal as an alternative fixative to formaldehyde in immunostaining and super-resolution microscopy." EMBO J **37**(1): 139-159.

Rinaldi, C. and M. J. A. Wood (2018). "Antisense oligonucleotides: the next frontier for treatment of neurological disorders." Nat Rev Neurol **14**(1): 9-21.

Riyad, J. M. and T. Weber (2021). "Correction: Intracellular trafficking of adeno-associated virus (AAV) vectors: challenges and future directions." Gene Ther **28**(12): 771.

Riyad, J. M. and T. Weber (2021). "Intracellular trafficking of adeno-associated virus (AAV) vectors: challenges and future directions." Gene Ther **28**(12): 683-696.

Rodriguez, A., S. Tatter, W. Debinski, A. Rodriguez, S. B. Tatter and W. Debinski (2015). "Neurosurgical Techniques for Disruption of the Blood–Brain Barrier for Glioblastoma Treatment." Pharmaceutics **7**(3): 175-187.

Rogers, G. L., A. T. Martino, G. V. Aslanidi, G. R. Jayandharan, A. Srivastava and R. W. Herzog (2011). "Innate Immune Responses to AAV Vectors." Front Microbiol **2**: 194.

Ronen, K., O. Negre, S. Roth, C. Colomb, N. Malani, M. Denaro, T. Brady, F. Fusil, B. Gillet-Legrand, K. Hehir, Y. Beuzard, P. Leboulch, J. D. Down, E. Payen and F. D. Bushman (2011). "Distribution of lentiviral vector integration sites in mice following therapeutic gene transfer to treat beta-thalassemia." Mol Ther **19**(7): 1273-1286.

Ronzitti, G., D. A. Gross and F. Mingozzi (2020). "Human Immune Responses to Adeno-Associated Virus (AAV) Vectors." Front Immunol **11**: 670.

Sanber, K. S., S. B. Knight, S. L. Stephen, R. Bailey, D. Escors, J. Minshull, G. Santilli, A. J. Thrasher, M. K. Collins and Y. Takeuchi (2015). "Construction of stable packaging cell lines for clinical lentiviral vector production." Sci Rep **5**: 9021.

Sander, J. D., E. J. Dahlborg, M. J. Goodwin, L. Cade, F. Zhang, D. Cifuentes, S. J. Curtin, J. S. Blackburn, S. Thibodeau-Beganny, Y. Qi, C. J. Pierick, E. Hoffman, M. L. Maeder, C. Khayter, D. Reyon, D. Dobbs, D. M. Langenau, R. M. Stupar, A. J. Giraldez, D. F. Voytas, R. T. Peterson, J. R. Yeh and J. K. Joung (2011). "Selection-free zinc-finger-nuclease engineering by context-dependent assembly (CoDA)." Nat Methods **8**(1): 67-69.

Saunders, N. R., J. J. Dreifuss, K. M. Dziegielewska, P. A. Johansson, M. D. Habgood, K. Mollgard and H. C. Bauer (2014). "The rights and wrongs of blood-brain barrier permeability studies: a walk through 100 years of history." Front Neurosci **8**: 404.

Scacheri, P. C., O. Rozenblatt-Rosen, N. J. Caplen, T. G. Wolfsberg, L. Umayam, J. C. Lee, C. M. Hughes, K. S. Shanmugam, A. Bhattacharjee, M. Meyerson and F. S. Collins (2004). "Short interfering RNAs can induce unexpected and divergent changes in the levels of untargeted proteins in mammalian cells." Proc Natl Acad Sci U S A **101**(7): 1892-1897.

Schön, A., B. R. Clarkson, M. Jaime and E. Freire (2017). "Temperature stability of proteins: Analysis of irreversible denaturation using isothermal calorimetry." Proteins **85**(11): 2009-2009.

Seppen, J., S. C. Barry, J. H. Klinkspoor, L. J. Katen, S. P. Lee, J. V. Garcia and W. R. Osborne (2000). "Apical gene transfer into quiescent human and canine polarized intestinal epithelial cells by lentivirus vectors." J Virol **74**(16): 7642-7645.

Serlin, Y., I. Shelef, B. Knyazer and A. Friedman (2015). "Anatomy and physiology of the blood-brain barrier." Seminars in cell & developmental biology **38**: 2-6.

Shen, B., W. Zhang, J. Zhang, J. Zhou, J. Wang, L. Chen, L. Wang, A. Hodgkins, V. Iyer, X. Huang and W. C. Skarnes (2014). "Efficient genome modification by CRISPR-Cas9 nickase with minimal off-target effects." Nat Methods **11**(4): 399-402.

Shen, S., K. D. Bryant, S. M. Brown, S. H. Randell and A. Asokan (2011). "Terminal N-linked galactose is the primary receptor for adeno-associated virus 9." The Journal of biological chemistry **286**(15): 13532-13540.

Shen, S., K. D. Bryant, J. Sun, S. M. Brown, A. Troupes, N. Pulicherla and A. Asokan (2012). "Glycan binding avidity determines the systemic fate of adeno-associated virus type 9." J Virol **86**(19): 10408-10417.

Shen, S., A. N. Troupes, N. Pulicherla and A. Asokan (2013). "Multiple roles for sialylated glycans in determining the cardiopulmonary tropism of adeno-associated virus 4." Journal of virology **87**(24): 13206-13213.

Shen, X. and D. R. Corey (2018). "Chemistry, mechanism and clinical status of antisense oligonucleotides and duplex RNAs." Nucleic Acids Res **46**(4): 1584-1600.

Sheng, P., K. A. Flood and M. Xie (2020). "Short Hairpin RNAs for Strand-Specific Small Interfering RNA Production." Frontiers in Bioengineering and Biotechnology **8**: 940-940.

Shipley, M. M., C. A. Mangold and M. L. Szpara (2016). "Differentiation of the SH-SY5Y Human Neuroblastoma Cell Line." J Vis Exp(108): 53193.

Sofroniew, M. V. and H. V. Vinters (2010). "Astrocytes: biology and pathology." Acta neuropathologica **119**(1): 7-35.

Song, J., C. Lu, J. Leszek and J. Zhang (2021). "Design and Development of Nanomaterial-Based Drug Carriers to Overcome the Blood-Brain Barrier by Using Different Transport Mechanisms." Int J Mol Sci **22**(18).

Song, R., K. Pekrun, T. A. Khan, F. Zhang, S. P. Pasca and M. A. Kay (2022). "Selection of rAAV vectors that cross the human blood-brain barrier and target the central nervous system using a transwell model." Mol Ther Methods Clin Dev **27**: 73-88.

Sonntag, F., S. Bleker, B. Leuchs, R. Fischer and J. A. Kleinschmidt (2006). "Adeno-associated virus type 2 capsids with externalized VP1/VP2 trafficking domains are generated prior to passage through the cytoplasm and are maintained until uncoating occurs in the nucleus." J Virol **80**(22): 11040-11054.

Stamatovic, S. M., R. F. Keep and A. V. Andjelkovic (2008). "Brain endothelial cell-cell junctions: how to "open" the blood brain barrier." Current neuropharmacology **6**(3): 179-192.

Stangl, M., A. Veerappan, A. Kroeger, P. Vogel and D. Schneider (2012). "Detergent properties influence the stability of the glycophorin A transmembrane helix dimer in lysophosphatidylcholine micelles." Biophys J **103**(12): 2455-2464.

Stanimirovic, D. B., J. K. Sandhu and W. J. Costain (2018). "Emerging Technologies for Delivery of Biotherapeutics and Gene Therapy Across the Blood-Brain Barrier." BioDrugs : clinical immunotherapeutics, biopharmaceuticals and gene therapy **32**(6): 547-559.

Stracker, T. H., G. D. Cassell, P. Ward, Y.-M. Loo, B. v. Breukelen, S. D. Carrington-Lawrence, R. K. Hamatake, P. C. v. d. Vliet, S. K. Weller, T. Melendy and M. D. Weitzman (2004). "The Rep Protein of Adeno-Associated Virus Type 2 Interacts with Single-Stranded DNA-Binding Proteins That Enhance Viral Replication." Journal of Virology **78**(1): 441-453.

Strang, B. L. and N. D. Stow (2005). "Circularization of the herpes simplex virus type 1 genome upon lytic infection." J Virol **79**(19): 12487-12494.

Summerford, C., J. S. Johnson and R. J. Samulski (2016). "AAVR: A Multi-Serotype Receptor for AAV." Mol Ther **24**(4): 663-666.

Sung, Y. K. and S. W. Kim (2019). "Recent advances in the development of gene delivery systems." Biomaterials Research 2019 23:1 **23**(1): 1-7.

Takeshima, K., J. Arii, Y. Maruzuru, N. Koyanagi, A. Kato and Y. Kawaguchi (2019). "Identification of the Capsid Binding Site in the Herpes Simplex Virus 1 Nuclear Egress Complex and Its Role in Viral Primary Envelopment and Replication." J Virol **93**(21).

Tan, J., F. Zhang, D. Karcher and R. Bock (2019). "Engineering of high-precision base editors for site-specific single nucleotide replacement." Nat Commun **10**(1): 439.

Thomsen, G. M., G. Gowing, J. Latter, M. Chen, J. P. Vit, K. Staggenborg, P. Avalos, M. Alkaslasi, L. Ferraiuolo, S. Likhite, B. K. Kaspar and C. N. Svendsen (2014). "Delayed Disease Onset and Extended Survival in the SOD1G93A Rat Model of Amyotrophic Lateral Sclerosis after Suppression of Mutant SOD1 in the Motor Cortex." Journal of Neuroscience **34**(47): 15587-15600.

Tosolini, A. P. and J. N. Sleigh (2020). "Intramuscular Delivery of Gene Therapy for Targeting the Nervous System." Front Mol Neurosci **13**: 129.

Tran, H., M. P. Moazami, H. Yang, D. McKenna-Yasek, C. L. Douthwright, C. Pinto, J. Metterville, M. Shin, N. Sanil, C. Dooley, A. Puri, A. Weiss, N. Wightman, H. Gray-Edwards, M. Marosfoi, R. M. King, T. Kenderdine, D. Fabris, R. Bowser, J. K. Watts and R. H. Brown, Jr. (2022). "Suppression of mutant C9orf72 expression by a potent mixed backbone antisense oligonucleotide." Nat Med **28**(1): 117-124.

Tse, L. V., K. A. Klinc, V. J. Madigan, R. M. Castellanos Rivera, L. F. Wells, L. P. Havlik, J. K. Smith, M. Agbandje-McKenna and A. Asokan (2017). "Structure-guided evolution of antigenically distinct adeno-associated virus variants for immune evasion." Proc Natl Acad Sci U S A **114**(24): E4812-E4821.

Tsuji, Y. (2020). "Transmembrane protein western blotting: Impact of sample preparation on detection of SLC11A2 (DMT1) and SLC40A1 (ferroportin)." PLoS One **15**(7): e0235563.

Turkki, P., K. E. Makkonen, M. Huttunen, J. P. Laakkonen, S. Yla-Herttuala, K. J. Airenne and V. Marjomaki (2013). "Cell susceptibility to baculovirus transduction and echovirus infection is modified by protein kinase C phosphorylation and vimentin organization." J Virol **87**(17): 9822-9835.

Villaseñor, R., J. Lampe, M. Schwaninger and L. Collin (2019). "Intracellular transport and regulation of transcytosis across the blood–brain barrier." Cellular and Molecular Life Sciences **76**(6): 1081-1092.

Villaseñor, R., M. Schilling, J. Sundaresan, Y. Lutz and L. Collin (2017). "Sorting Tubules Regulate Blood-Brain Barrier Transcytosis." Cell Reports **21**(11): 3256-3270.

Vink, C. A., J. R. Counsell, D. P. Perocheau, R. Karda, S. M. K. Buckley, M. H. Brugman, M. Galla, A. Schambach, T. R. McKay, S. N. Waddington and S. J. Howe (2017). "Eliminating HIV-1 Packaging Sequences from Lentiviral Vector Proviruses Enhances Safety and Expedites Gene Transfer for Gene Therapy." Mol Ther **25**(8): 1790-1804.

Wang, L., J. Zhang, D. Wang and C. Song (2022). "Membrane contact probability: An essential and predictive character for the structural and functional studies of membrane proteins." PLoS Comput Biol **18**(3): e1009972.

Weinberg, M. S., R. J. Samulski and T. J. McCown (2013). "Adeno-associated virus (AAV) gene therapy for neurological disease." Neuropharmacology **69**: 82-88.

Westerman, K. A., Z. Ao, E. A. Cohen and P. Leboulch (2007). "Design of a trans protease lentiviral packaging system that produces high titer virus." Retrovirology **4**: 96.

Westhaus, A., M. Cabanes-Creus, A. Rybicki, G. Baltazar, R. G. Navarro, E. Zhu, M. Drouyer, M. Knight, R. F. Albu, B. H. Ng, P. Kalajdzic, M. Kwiatek, K. Hsu, G. Santilli, W. Gold, B. Kramer, A. Gonzalez-Cordero, A. J. Thrasher, I. E. Alexander and L. Lisowski (2020). "High-Throughput In Vitro, Ex Vivo, and In Vivo Screen of Adeno-Associated Virus Vectors Based on Physical and Functional Transduction." Hum Gene Ther **31**(9-10): 575-589.

Wu, Z., H. Yang and P. Colosi (2010). "Effect of Genome Size on AAV Vector Packaging." Molecular Therapy **18**(1): 80-86.

Wysocka, J. and W. Herr (2003). "The herpes simplex virus VP16-induced complex: the makings of a regulatory switch." Trends Biochem Sci **28**(6): 294-304.

Xia, S., J. Wu, W. Zhou, M. Zhang, K. Zhao, J. Liu, D. Tian and J. Liao (2021). "SLC7A2 deficiency promotes hepatocellular carcinoma progression by enhancing recruitment of myeloid-derived suppressors cells." Cell Death Dis **12**(6): 570.

Xiao, C., C. M. Bator, V. D. Bowman, E. Rieder, Y. He, B. Hebert, J. Bella, T. S. Baker, E. Wimmer, R. J. Kuhn and M. G. Rossmann (2001). "Interaction of coxsackievirus A21 with its cellular receptor, ICAM-1." J Virol **75**(5): 2444-2451.

Yang, B., S. Li, H. Wang, Y. Guo, D. J. Gessler, C. Cao, Q. Su, J. Kramer, L. Zhong, S. S. Ahmed, H. Zhang, R. He, R. C. Desrosiers, R. Brown, Z. Xu and G. Gao (2014). "Global CNS Transduction of Adult Mice by Intravenously Delivered rAAVrh.8 and rAAVrh.10 and Nonhuman Primates by rAAVrh.10." Molecular Therapy **22**(7): 1299-1299.

Yang, H., Y. Liu, M. M. Zhao, Q. Guo, X. K. Zheng, D. Liu, K. W. Zeng and P. F. Tu (2021). "Therapeutic potential of targeting membrane-spanning proteoglycan SDC4 in hepatocellular carcinoma." Cell Death & Disease 2021 12:5 **12**(5): 1-16.

Yang, H., S. Ren, S. Yu, H. Pan, T. Li, S. Ge, J. Zhang and N. Xia (2020). "Methods Favoring Homology-Directed Repair Choice in Response to CRISPR/Cas9 Induced-Double Strand Breaks." Int J Mol Sci **21**(18).

Yang, L., L. Bailey, D. Baltimore and P. Wang (2006). "Targeting lentiviral vectors to specific cell types in vivo." Proc Natl Acad Sci U S A **103**(31): 11479-11484.

Yang, L., H. Zhang and J. E. Bruce (2009). "Optimizing the detergent concentration conditions for immunoprecipitation (IP) coupled with LC-MS/MS identification of interacting proteins." Analyst **134**(4): 755-762.

Yang, Y., C. D. Jun, J. H. Liu, R. Zhang, A. Joachimiak, T. A. Springer and J. H. Wang (2004). "Structural basis for dimerization of ICAM-1 on the cell surface." Mol Cell **14**(2): 269-276.

Yew, C. T., N. Gurumoorthy, F. Nordin, G. J. Tye, W. S. Wan Kamarul Zaman, J. J. Tan and M. H. Ng (2022). "Integrase deficient lentiviral vector: prospects for safe clinical applications." PeerJ **10**: e13704.

Yin, F., W. Liu, J. Chai, B. Lu, R. W. Murphy and J. Luo (2018). "CRISPR/Cas9 Application for Gene Copy Fate Survey of Polyploid Vertebrates." Front Genet **9**: 260.

Yusuf, M., K. Leung, K. J. Morris and E. V. Volpi (2013). "Comprehensive cytogenomic profile of the in vitro neuronal model SH-SY5Y." Neurogenetics **14**(1): 63-70.

Zaragoza, R. (2020). "Transport of Amino Acids Across the Blood-Brain Barrier." Front Physiol **11**: 973.

Zhang, H., B. Yang, X. Mu, S. S. Ahmed, Q. Su, R. He, H. Wang, C. Mueller, M. Sena-Esteves, R. Brown, Z. Xu and G. Gao (2011). "Several rAAV vectors efficiently cross the blood-brain barrier and transduce neurons and astrocytes in the neonatal mouse central nervous system." Molecular therapy : the journal of the American Society of Gene Therapy **19**(8): 1440-1448.

Zhang, Z. R. and Z. R. Jiang (2022). "Effective use of sequence information to predict CRISPR-Cas9 off-target." Comput Struct Biotechnol J **20**: 650-661.

Zheng, Z., M. Chopp and J. Chen (2020). "Multifaceted roles of pericytes in central nervous system homeostasis and disease." J Cereb Blood Flow Metab **40**(7): 1381-1401.

Zhong, H., H. Lin, Q. Pang, J. Zhuang, X. Liu, X. Li, J. Liu and J. Tang (2021). "Macrophage ICAM-1 functions as a regulator of phagocytosis in LPS induced endotoxemia." Inflamm Res **70**(2): 193-203.

Zhu, L., B. Tan, S. S. Dwight, B. Beahm, M. Wilsey, B. E. Crawford, B. Schweighardt, J. W. Cook, T. Wechsler and W. F. Mueller (2022). "AAV9-NGLY1 gene replacement therapy improves phenotypic and biomarker endpoints in a rat model of NGLY1 Deficiency." Mol Ther Methods Clin Dev **27**: 259-271.

Zimmer, A. M., Y. K. Pan, T. Chandrapalan, R. W. M. Kwong and S. F. Perry (2019). "Loss-of-function approaches in comparative physiology: is there a future for knockdown experiments in the era of genome editing?" J Exp Biol **222**(Pt 7).

Research Output from PhD:

Oral Platform Communications:

1. Poster presentation at the American Society of Gene and Cell Therapy (ASGCT, 2022)

   Roach, M. Webster, C. Azzouz, M. *Identification and Validation of Target Receptors/Transporters for AAV9.*

   Presented in Washington D.C., United States, at the ASGCT conference in May 2022.

   Awarded an 'Outstanding Poster Presentation Award' for my poster at the ASGCT's 25th Annual Meeting.

   Awarded a grant by the Guarantors of Brain Trust to attend the ASGCT's 25th Annual Meeting in Washington.

2. Poster presentation at the European Society of Gene and Cell Therapy (ESGCT, 2022)

   Roach, M. Webster, C. Azzouz, M. *Identification and Validation of Target Receptors/Transporters for AAV9.*

Presented in Edinburgh., United Kingdom at the ESGCT conference in October 2022.

Conferences Attended:

1. The American Society of Gene and Cell Therapy (2020, 2021, 2022)
2. The European Society of Gene and Cell Therapy (2022)
3. Innovative Medicine Initiative (IMI) (2019, 2021, 2022).

Courses Attended:

MED629 Neuro-Anatomy (2021)